NATURAL CONVECTION IN LIQUID METALS

by

MURRAY JOHN STEWART

B.A.Sc. (Honours), University of British Columbia, 1967

A THESIS SUBMITTED IN PARTIAL FULFILMENT OF

THE REQUIREMENTS FOR THE DEGREE OF

DOCTOR OF PHILOSOPHY

in the Department

of

METALLURGY

We accept this thesis as conforming to the

required standard

THE UNIVERSITY OF BRITISH COLUMBIA

December, 1970

In presenting this thesis in partial fulfilment of the requirements for an advanced degree at the University of British Columbia, I agree that the Library shall make it freely available for reference and study. I further agree tha permission for extensive copying of this thesis for scholarly purposes may be granted by the Head of my Department or by his representatives. It is understood that copying or publication of this thesis for financial gain shall not be allowed without my written permission.

Department of Metallurgy

The University of British Columbia
Vancouver 8, Canada

Date December 7, 1970

Acknowledgement

The author would like to express thanks to his research director, Dr. Fred Weinberg, for his continuing advice and encouragement throughout the course of this project.

Financial assistance was given by the H. R. MacMillan Family Fellowship and the Shell Canada Fellowship in Engineering and special thanks are thus accorded.

Abstract

Natural convection in liquid metals has been studied by direct observation of the fluid flow, using radioactive tracer techniques. The study is of importance in understanding the solidification of metals since fluid flow strongly influences the heat and mass transfer in the system which in turn strongly influences the structure, homogeneity, and mechanical properties of the solid metal produced.

The system examined in this investigation was a rectangular liquid cell of variable thickness, positioned on edge. A small driving force for natural convection was imposed across the liquid cell and when steady state conditions were reached, a small amount of the same material containing a radioactive isotope was added to the top of the cell. The tracer material was picked up by the flow and after a given time interval the liquid was quenched to fix the tracer position. The resultant solid block was autoradiographed to determine the distribution of the added radioactive material.

Thermal convection was observed in liquid tin and liquid lead using radioactive Sn^{113} and radioactive Tl^{204} respectively. The results show that the flow rates increase with increasing temperature difference across the liquid cell, increasing average temperature, and increasing

liquid cell thickness. Flow rates with Grashof numbers from 10^6 to 10^8 were experimentally observed.

A finite difference numerical solution for the problem of thermal convection is presented for Prandtl numbers of 10.0, 1.0, 0.1, and 0.0127 with Grashof numbers from 2×10^3 to 2×10^7. The experimental results for liquid tin (Pr = 0.0127) are found to approach the theoretical analysis for large cell thicknesses and large temperature differences. The flow behavior of various types of fluids is compared with liquid metals to show that non-metallic analogies to metallic flow problems have very limited value.

Solute convection is experimentally considered from three different viewpoints; a) independent solute convection, b) the influence of solute convection on thermal convection, and c) the thermal and solute conditions for complete liquid mixing. It was found that there must be a horizontal density inversion across the whole liquid cell for complete mixing to occur throughout the liquid zone.

Interdendritic liquid flow resulting from the natural convection in the residual liquid pool was observed in lead-tin alloys. The flow penetrated into the solid-liquid zone to a point of approximately 12 - 22 % solid for primary dendrite spacings of from 700 to 1000 microns. Several experimental models are presented for interdendritic flow. A three dimensional wire mesh model predicts that

the finer the dendrite structure, the greater the flow penetration into the solid-liquid zone. The experimental results for the lead-tin alloys compared favorably with the model.

As an extension of the fluid flow considerations, an investigation was carried out to determine macrosegregation in castings which have imposed fluid flow patterns. The macrosegregation present in stationary, rotated, and oscillated castings of Al - 3 wt. % Ag was determined by measuring the distribution of radioactive silver added to the melt. It was found that no significant macrosegregation was present in the stationary and rotated castings. Extensive macrosegregation was detected in the oscillated casting. For the oscillated case the macrosegregation can be accounted for on the basis of the long range movement of dendrite fragments which break and/or melt off in the solid-liquid interface region. This movement is a direct result of turbulent waves associated with the oscillation. The maximum silver concentration is shown to be related to the columnar-to-equiaxed transition.

TABLE OF CONTENTS

List of Figures

Page

Page

Page

Page

Page

List of Tables

1. Introduction

The structure and properties of castings are determined, in part, by natural convection of the residual liquid metal during solidification. Natural or free convection, as used in this thsis, can be defined as the motion of a fluid due to density changes resulting from any temperature or compositional differences in the fluid. This introduction will discuss the reasons why the study of natural convection is vital to a true understanding of many solidification phenomena.

1.1. The importance of liquid metal flow

The importance of liquid metal flow due to natural convection has only recently been realised. The flow of the liquid metal during solidification affects the heat transfer, the mass transfer, and the final cast structure.

The heat transfer rate in a system in which heat transfer occurs by convection is greater than that which would result from conduction alone. With convection there

are two modes of heat transfer; by the conduction of heat between two points at different temperatures, and by mass transport in the liquid. The more rapid heat removal by convection in a closed system, such as the residual liquid metal in a casting, results in more rapid a lowering of temperature gradients in the liquid metal and a more rapid removal of superheat from the liquid. The thermal profile in a convecting system will have a different shape than the thermal profile in a system transferring heat by conduction alone. To illustrate, consider the closed rectangular fluid system shown in Figure 1.

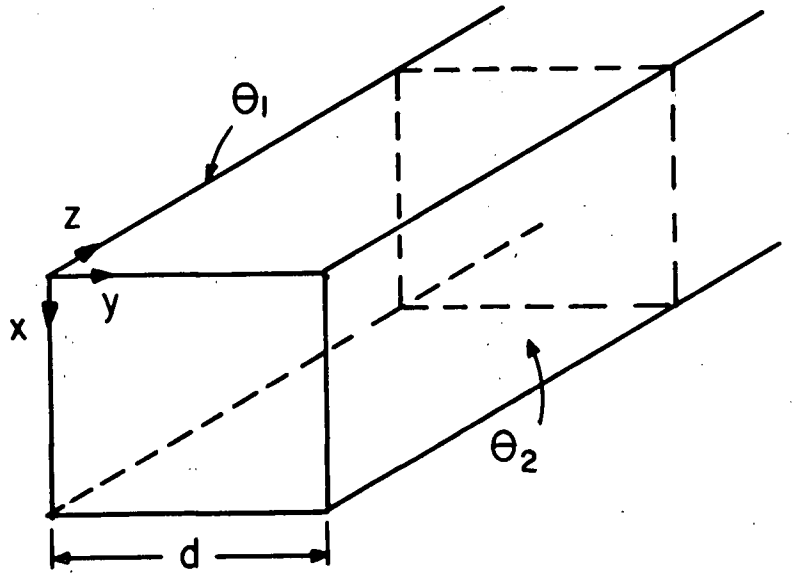

Figure 1. A closed rectangular fluid system of infinite length in the z direction.

One long vertical side is maintained at a temperature θ_1, and the opposite vertical wall is maintained at temperature θ_2, such that θ_2 is greater than θ_1. Let the upper and lower horizontal surfaces be perfectly insulated and let the cell be infinitely long in the z direction. Thus, in this system, all the heat transfer is across the cell from y = 0 to y = d. If the fluid system is not allowed to flow, the heat transfer is governed by the general three dimensional heat conduction equation (1):

$$\frac{\partial}{\partial x}\left(k\frac{\partial \theta}{\partial x}\right) + \frac{\partial}{\partial y}\left(k\frac{\partial \theta}{\partial y}\right) + \frac{\partial}{\partial z}\left(k\frac{\partial \theta}{\partial z}\right) = -\dot{q} + \rho C_p \frac{\partial \theta}{\partial t} \qquad (1.1)$$

where: k = thermal conductivity

q = heat transfer rate

ρ = fluid density

C_p = fluid specific heat

t = time

θ = temperature

Assuming from Figure 1a that all the heat transfer is in the y direction, all material properties are constants and the system has reached steady-state conditions, equation (1.1) reduces to:

$$\frac{d^2\theta}{dy^2} = 0 \qquad (1.2)$$

with the boundary conditions that

at $y = 0$: $\theta = \theta_1$

$y = d$: $\theta = \theta_2$

Solving equation (1.2) for the resulting thermal profile with the use of conditions (1.3) results in:

$$\theta = \left(\frac{\theta_2 - \theta_1}{d}\right) y + \theta_1 \qquad (1.4)$$

Figure 2a shows the isothermal lines that result from equation (1.4). The isotherms are vertical lines and the temperature gradient is linear in y across the cell and is equal to $(\theta_2 - \theta_1) / d$. It should be noted that the temperature is not a function of the vertical x direction.

In a system that the fluid is allowed to flow by natural thermal convection the system becomes much more complex. This is because the motion of the fluid alters the thermal profile, and since the fluid motion is determined by the thermal profile, the flow and the temperature in the cell are coupled. They must therefore be solved together for the general thermal convection case. This problem has been solved numerically for non-metals by Wilkes and Churchill (2). The details of their solution will be discussed in Chapter 3. Qualitatively, the isothermal profile that results from the flowing system is shown in Figure 2b. The isotherms are seen to bend towards the hot side along the bottom of the cell and towards the cold side along the top of the cell. This is caused by the fluid near the cold wall being cooled, becoming more dense, and thus flowing down the cold wall and along the bottom of the cell from left to right. Similarly the fluid rises

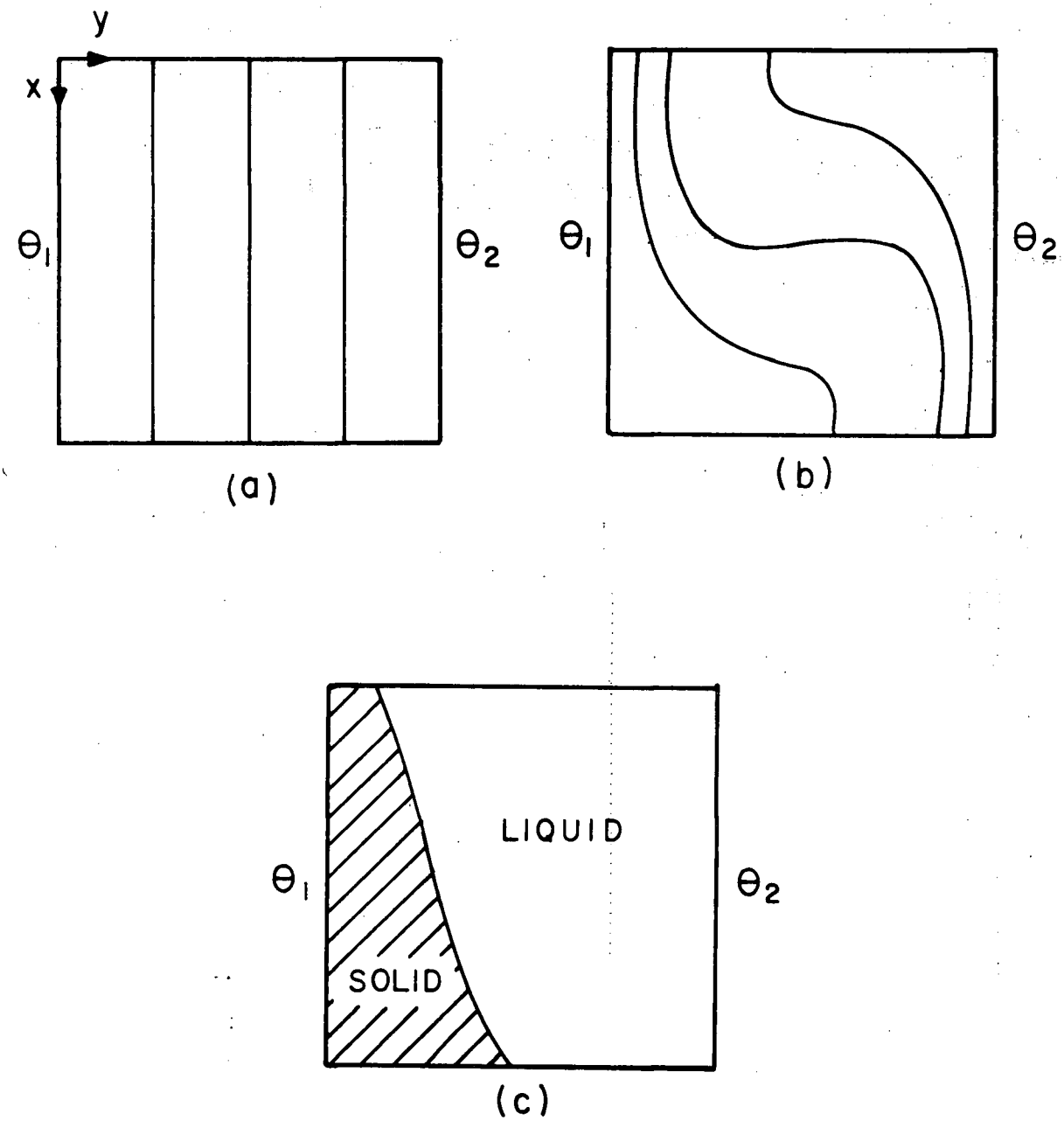

Figure 2. A cross section view of the system of Figure 1 showing (a) the steady-state conduction isotherms, (b) the steady-state convection isotherms, and (c) the solid-liquid interface advancing across the system.

on the hot side of the cell as its density decreases and it moves across the top of the cell from the right to the left. This fluid movement causes the isotherms to bend as in Figure 2b.

The shape of the solid-liquid interface, during solidification, is altered by the thermal convection isotherms in the residual liquid pool. If the vertical wall at temperature θ_1 is a solidification front and it is allowed to move into the liquid pool the interface will not remain in a vertical plane. It will take up a shape as shown in Figure 2c, if θ_1 is below the melting point of the liquid metal. This shape has been observed by Szekely and Chhabra (3) in a pure lead system. The shape is reasonable when consideration is given to the shape of the isotherms in Figure 2b. A solid-liquid interface will move more rapidly into a liquid with a lower thermal gradient since there is less heat to be conducted away through the solid in order for the interface to advance. The lower regions of the cell have a lower temperature gradient near the cold wall than the upper regions of the cell, and hence the interface will advance more quickly in the lower regions resulting in the interface shown in Figure 1d.

In a convecting system where there is a rapid rate of heat removal, there is a corresponding rapid lowering of the temperature gradients in the liquid. In a normal casting, in which no additional heat is added to

the system as solidification progresses, the rate of removal of the liquid superheat will depend on the rate of convection. As the gradients decrease the possibility of interface breakdown occurring, changing the structure, is enhanced by constitutional supercooling occurring sooner. Also, due to the difference in the temperature gradientalong the cold wall, interface breakdown can occur in some regions of the interface and not others. From Figure 2b the lowest temperature gradients, and thus the most favourable position for constitutional supercooling, occurs at the upper and lower regions of the vertical wall. It would thus be expected that the interface breakdown would occur in these regions first. This phenomenon has been observed by Weinberg (4) who showed experimentally that a cellular structure occurred near the upper and lower edges of the interface indicating breakdown and a planar region occurred in the central area indicating no breakdown in unidirectionally solidified rods.

Natural convection can affect both the macrosegregation and the microsegregation in a casting. The longitudinal macrosegregation resulting from the unidirectional solidification of a metal rod, with a planar interface, is very sensitive to flow in the liquid ahead of the advancing interface. The macrosegregation resulting from unidirectional solidification with (a) complete convective mixing in the liquid (b) mixing in the liquid by

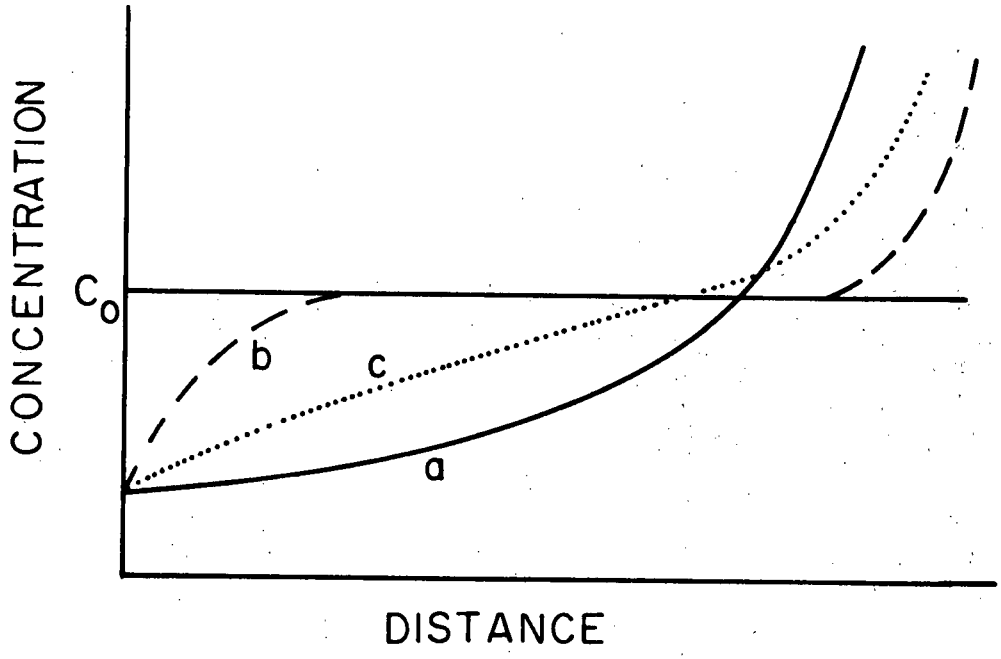

Figure 3. The longitudinal macrosegregation from unidirectional growth with (a) complete convective mixing in the liquid, (b) mixing by diffusion only in the liquid, and (c) incomplete convective mixing in the liquid.

diffusion only or (c) incomplete convective mixing in the liquid, is shown in Figure 3. This is a plot of solute concentration as a function of the distance along the solidified rod, with an average composition in the rod of C_o. The shape of the solute concentration curves are seen to be greatly altered by the extent of the mixing.

Macrosegregation can also occur if the solid-liquid interface is of a dendritic nature. The most commonly observed example of this is inverse segregation (5). Due to a volume change on freezing of the metal, solute rich liquid is pulled back into the dendritic network to cause solute enrichment in the initial stages of the casting. This is in contrast to the solute depletion

which would be expected from Figure 2. The cause of this fluid flow, volume contraction in the dendritic zone causing a pressure gradient and pulling new fluid into the zone, does not fall within the definition of natural convection considered here. Detailed analysis of this type of flow has been developed by Flemings and his co-workers (6,7,8,9). Their analysis includes thermal and solute convection in the dendritic zone but does not consider the flow in the residual liquid outside the interface region.

Macrosegregation can also be caused by the flow cutting across the dendrites and the formation of flow channels at right angles to the dendrites (10). This flow causes segregation by displacing interdendritic liquid, which is enriched by the solute rejection on solidification. The temperature of the liquid in the interdendritic region will be lower than that of the liquid in the central pool and hence the thermal convective forces will be in the vertical downwards direction in the mushy zone. The solute convective forces will depend on the relative density of the elements being segregated. If the rejected solute is denser than the solvent the solute convection will be downwards and hence enhance the natural thermal convection. If the rejected solute is less dense the solute convection will be upwards and counteract the thermal convection forces. Although the driving forces for the interdendritic fluid flow are known, the analysis is greatly hampered by

the very complex nature of the solid-liquid interface.

The phenomena of solute banding in a casting has been shown to be caused by convection in the liquid metal (11, 12, 13). For very large temperature gradients, the flow rates in a system with convective flow can be such that the system will become turbulent or oscillatory in nature. Accompanying this turbulent flow will be thermal fluctuations at any particular point in the liquid. When the thermal fluctuations occur near a solid-liquid interface a growth rate perturbation will occur. This will result in the effective solute distribution coefficient changing and a band of solute different in composition being produced. Previous workers have shown a direct correlation between the rate of temperature fluctuations and the rate of band formation.

The manner in which natural convection affects a cast structure is still open to much controversy. The most widely investigated aspect of structure change is the columnar to equiaxed transition which occurs in alloy systems. There have been a number of theories developed to account for the onset of the equiaxed structure, particularly the source of the nuclei resulting in this structure. These include (a) partial remelting of dendrites leaving solid dendrite fragments (14, 15), (b) breaking or shearing of dendrites with or without remelting producing solid particles (16), (c) survival of nuclei from the

initial chill of the casting (17), (d) nucleation at the upper surface of the casting, the nuclei subsequently moving into the casting (18), (e) the bending of dendrite arms causing adiabatic local melting, and producing solid dendrite fragments (19). Almost all of the above theories require some motion of the liquid metal for the transition to occur. The remelting and breaking of dendrite arms is enhanced by thermal fluctuations in the liquid and the fluctuating mechanical forces exerted on the dendrites by a turbulent flow. Also, due to convection, the thermal gradients ahead of the solid-liquid interface are reduced and hence the probability of nuclei surviving and growing into an equiaxed grain is increased. The liquid metal flow also facilitates the movement of the nuclei from the position at which they are formed to where they grow as equiaxed grains to stop the further growth of the columnar grains.

1.2. The driving forces for liquid metal flow

The presence and extent of fluid flow by natural convection is dependent on the driving forces present and the resistance of the metal to flow. There are a number of driving forces which produce fluid motion in liquid metals, including thermal gradients, concentration gradients, mechanical mixing, and imposed magnetic fields.

Thermal gradients are perhaps the most common

driving force for liquid motion in the casting of metals. In all solidification processes, some temperature gradient is present in the liquid at some time during the process. The temperature differences produce a force resulting from the temperature dependence of the liquid metal density. As temperature gradients can readily be altered experimentally, many of the effects of fluid flow are examined by altering the gradient and corresponding thermal convection. The actual flow velocities are quite sensitive to the thermal gradients (20, 21).

There are two important dimensionless parameters which are used when discussing thermal convection: the Prandtl number and the Grashof number. The Prandtl number is the ratio of the momentum diffusivity to the thermal diffusivity of the fluid and is written as:

$$Pr = \frac{\nu}{\alpha} = \frac{\mu/\rho}{k/\rho C_p} = \frac{C_p \mu}{k} \qquad (1.5)$$

where: Pr = Prandtl number

ν = kinematic viscosity, cm.^{2} / sec.

α = thermal diffusivity, cm.^{2} / sec.

μ = absolute viscosity, poise, gm. / cm.-sec.

ρ = density, gm. / cm.^{3}

k = thermal conductivity, cal. / cm.-sec.-°C

C_p = specific heat, cal. / gm.-°C

The magnitude of the Prandtl number for a fluid relates the way the flow and thermal profiles are related in natural

convection. Table I lists various fluids and their respective Prandtl numbers. The values for liquid metals are generally lower than those for other types of fluids by as much as several orders of magnitude and hence the thermal convection behaviour will be very different. Generally liquid metals have values of the order of 10^{-2}, gases have values close to 1, and water has a value near 10.

The Grashof number is a dimensionless parameter relating the buoyancy forces in the fluid due to the temperature differences to the viscous forces in the fluid and is written:

$$Gr = \frac{g\beta\Delta\theta d^3}{\nu^2} \qquad (1.6)$$

where: Gr = Grashof number

g = acceleration due to gravity, cm. / sec.^{2}

β = coefficient of volume expansion, 1 / °C

$\Delta\theta = \theta_2 - \theta_1$ = temperature difference between the hot and the cold walls, °C

d = distance between the hot and the cold walls, cm.

Another dimensionless parameter used in thermal convection is the Rayleigh number defined as:

$$Ra = Gr \cdot Pr \qquad (1.7)$$

Solute gradients cause fluid motion in a similar manner to thermal gradients. Solute concentration

TABLE I.

Selected Fluid Properties

Fluid	Viscosity centipoise	Specific Heat cal/gm-°C	Thermal Conductivity cal/cm-sec-°C	Density gm/cm^3	Kinematic Viscosity cm^2/sec	Prandtl Number	$\frac{Grashof}{\Delta T}$ 1/°C
Tin (37, 38, 39)	1.88	0.054	0.08	6.95	0.0027	0.013	3.6×10^6
Lead (37, 38, 39)	2.39	0.038	0.039	10.62	0.0022	0.024	5.8×10^6
NH_3 (gas) (1)	0.0094	0.52	0.000052	0.0079	0.012	0.9	0.32×10^6
Steel (40)	6.5	0.12	0.07	6.95	0.0093	0.11	0.6×10^6
NaCl (liquid) (41)	1.27	0.27	0.03	1.54	0.0083	0.12	1.3×10^6
Water (1)	1.38	1.0	0.0014	1.0	0.0138	10.0	1.3×10^6

differences may arise from solute rejection at a solid-liquid interface or any other inhomogeneities present in the liquid metal alloy. The relative importance between thermal and solute convection in a particular system is dependent on the relative density differences produced by the thermal and solute gradients and also whether the effects are additive or subtractive. Cole and Winegard (22) have shown that for large thermal gradients (5 - 30 °C / cm.) and dilute alloys (0.01 wt. % lead-tin alloys) that the mixing due to solute convection is negligible compared with the thermal convection.

External mechanical mixing to induce fluid flow gives rise to forced convection rather than natural convection. Mechanical mixing can develop flows which can go against the flow that would result from the natural driving forces. Enhancement of flow is used to intensify the effects of natural convection to produce, for example, finer and more controllable grain sizes. Control of the grain structure has been extensively investigated by various oscillations and rotations of the mould to enhance or suppress the fluid motion (15, 16, 23). An investigation into the effects of forced convection on the macrosegregation will be discussed in Chapter 8.

Magnetic fields can be used to either enhance or suppress the natural convection in a liquid metal. Since metals are electrical conductors they can be induced to

move under a rotating magnetic field (24), or a constant magnetic field if a direct electrical current is passed through the liquid metal at right angles to the magnetic field (25). A magnetic field can also be used to reduce the natural convection as there is a retarding force to motion of a conductor in a constant magnetic field. This behavior can be visualized as an increase in the viscosity of the liquid. The reducing of natural convection will suppress the thermal oscillations (12), reduce the solute banding (13), change the macrosegregation along a unidirectionally solidified rod (26), and suppress the columnar to equiaxed transition by reducing convection and increasing the thermal gradient (27).

1.3. The detection of fluid flow

The detection and analysis of natural convection can be divided into two general classes of techniques: direct and indirect. The indirect methods involve the analysis of an effect of convection, to deduce the flow that was occurring at the time the effect was produced. The direct method involves the actual measuring of the flow or some property associated with the flow, while the flow is occurring.

The effects of convection discussed in section 1.1., such as segregation, can be used to deduce the liquid flow that occurs during the formation of the effect.

Generally, this type of analysis will only give a relative degree of mixing or a very approximate idea of the direction of the flow. Unidirectional growth experiments can be done at various temperature gradients and specimen sizes and configurations to determine their effect on the flow rates using the final solute distribution for the comparison. Quenched interface shapes and diffusion boundary layer shapes ahead of the interface can be used to deduce the flow in that region. However, quantitative values of the flow rates are not possible by these methods.

Direct methods of observing the fluid flow are very easily accomplished in non-metallic transparent liquids. Ammonium chloride - water systems (16, 28, 29, 30), sodium chloride - water systems (31), and molten sodium chloride (26) have all been studied. The main drawbacks of relating these observations to liquid metal situations is the differences in the basic flow behavior between the non-metallic and metallic systems or the differences in the way they solidify. This subject will be discussed further in Chapter 3.

Temperature measurements can be used as a direct method to determine the flow rates in liquid metals. The time for a thermal oscillation to travel between two near points can be measured with two thermocouples in the melt (26) and hence the local velocity between the two points determined. This procedure, however, requires large temperature fluctuations and hence has limited use at the

lower flow rates without turbulent flow. Also the local effect of the thermocouple on the flow is not known. The shape of the isothermal lines can also be used to deduce the fluid flow directions in the melt. For example, the profile in Figure 2b is obviously for a one cell flow around the liquid cell.

Direct observation of flow in liquid metals can also be made using radioactive tracer techniques. The flow can be observed using "in situ" monitoring of the movement of the tracers in the melt (21) or by using a quenching technique (20). The quenching technique has been used exclusively in the present work and is fully discussed in the following chapter.

1.4 Purpose of the present investigation

Many factors of solidification are greatly altered by natural convection, as described in the previous section. For a basic understanding of the effect of liquid metal flow on casting structures and properties, the details of the flow itself must be known. Very little research, either experimental or analytical, has been done to discover the exact behavior of natural convection of liquid metals in a closed system. A great deal of work has been done both analytically and experimentally on non-metallic natural convection, but generally this cannot, with any degree of accuracy, be applied to liquid metal flow. The reasons

for this will become evident in the theoretical sections to follow. Direct observation of the cell flow patterns in liquid metals has previously not been achieved. It is for these reasons a research program was undertaken to observe experimentally, and compute theoretically, the thermal convection behavior of a liquid metal.

Using the experimetal technique developed to observe the fluid flow, several other areas of fluid effects were observed. Flows resulting from solute convection and the volume change on freezing were observed as was the interdendritic flow caused by the convection in the outer liquid pool.

During the course of this work an auxiliary research study was conducted jointly with Mr. L. C. MacAulay under the direction of Professor F. Weinberg. This study was on the macrosegregation in aluminum - 3 wt. % silver castings rotated and oscillated during solidification. This work is presented in Chapter 7 of this thesis in an identical form as it is to appear in the forthcoming thesis of Mr. MacAulay. This work has been accepted for publication in Metallurgical Transactions and will appear in the same form as presented here.

2. General Experimental Apparatus and Procedures

2.1. Apparatus

The technique used in the present investigations was that of using radioactive elements to trace out the flow patterns in the liquid metal pool under various boundary restrictions. The experimental apparatus is shown in Figures 4a and 4b. The molten metal is contained in an aluminum or copper mould that is assembled as shown in Figure 5. The central U shaped piece is machined from aluminum or copper plate and a number of various thicknesses and cell lengths were produced. The mould is open on the upper surface. The sides of the mould are 1/16 inch thick sheets of the same material as the U shaped piece. A number of stainless steel bolts are used to assemble the mould. All surfaces of the mould are coated with a collodial graphite wash to prevent any attack on the mould by the liquid metal. The graphite layer between the flat side plates and the U piece also stops any leakage of the liquid metal out of the mould even if a good contact in the mould assembly is not obtained. After quenching the solid metal

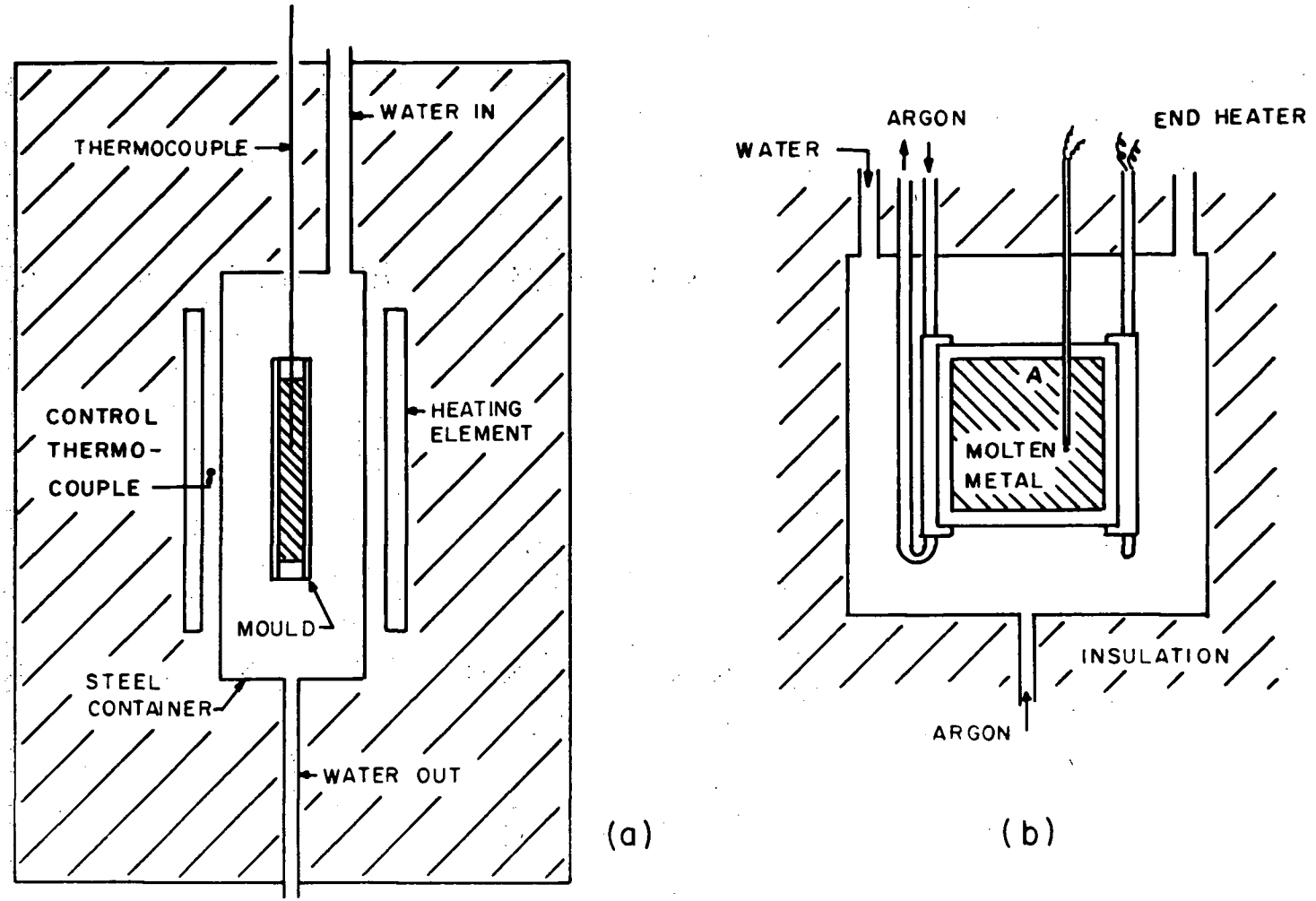

Figure 4. The experimental apparatus for observing natural convection showing (a) the side section view of the overall furnace and (b) the front section view of the inner furnace details.

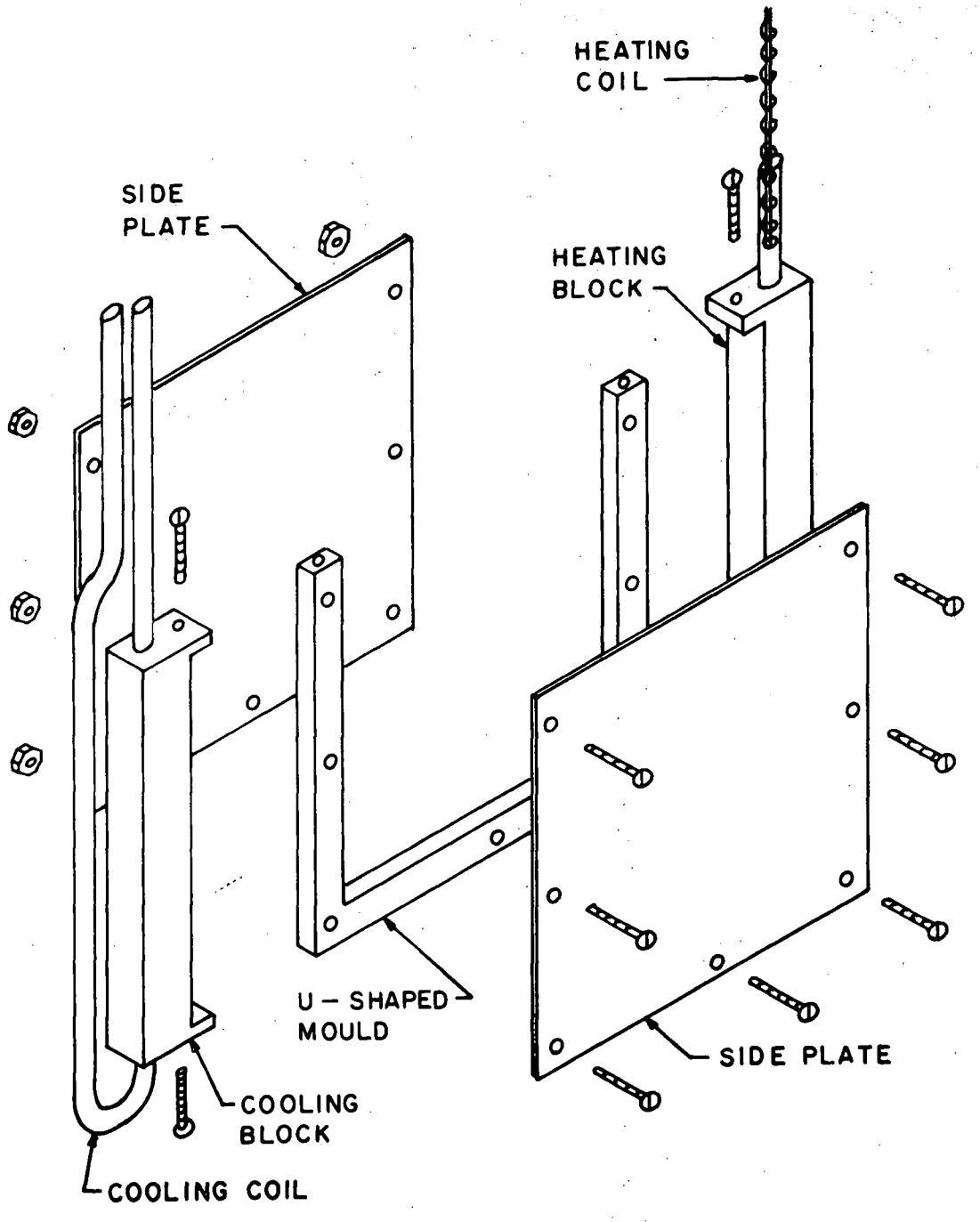

Figure 5. Exploded view of the copper or aluminum mould used in observing natural convection.

is removed by disassembling the mould. On one end of the mould a heating block is attached. A chromel winding is contained in a quartz tube and this is lowered into a hole passing through the copper heating block. The power to the heating coil is supplied from a variable autotransformer connected to a Sola constant voltage transformer giving a stable applied power up to 80 watts during the experiment. On the opposite end of the mould is a cooling block of similar construction to the heating block. A copper tube is passed through the block for the passage of argon or water to give a variable rate of heat removal. Both the blocks are bolted to the U shaped piece and a tight fit is maintained for good heat transfer by the use of .002 inch spacers.

The composite mould is suspended in a covered stainless steel container 6 x 6 x 2 inches with stainless steel straps. During an experiment the container is filled with argon to reduce oxidation, and for quenching the container is rapidly filled with water. A large flat heating element is placed on either side of the steel container for raising and maintaining the overall furnace temperature. A Honeywell temperature controller connected to the plate heaters is used to maintain a constant furnace temperature. The control thermocouple is between the heating plate and the stainless steel tank. This controller maintains a temperature within ± 1/2 °C at the control thermocouple.

The whole assembly is contained in a brick insulated outer aluminum case, constructed to allow direct visual observation of the melt from above the furnace.

Temperature measurements of the molten bath are made with long thermocouple probes inserted into the melt from the top of the furnace. Two types of thermocouples are used. For simple temperature monitoring of the bath iron-constantan thermocouples, sheathed by 1.5 mm. diameter quartz tubing, are used. The end of the sheath is left open and the thermocouple bead which is 0.5 mm. in diameter, positioned outside the tube for good temperature response and accuracy. For accurate temperature profile measurements for the bath, a commercially made iron-constantan thermocouple contained in a 0.5 mm. stainless steel tube is used. The very small diameter of the tube causes minimum disturbance in the melt. Either of these thermocouple probes can be positioned to any location in the melt with the aid of a horizontal and vertical calibrated traverse mechanism on top of the furnace. The thermocouples are connected via an ice water cold junction to a Honeywell Electronic 194 temperature recorder. Full scale deflections of between 20 millivolts (360°C) and 0.1 millivolts (1.8°C) were used in this work.

2.2. Experimental procedure

The liquid metals used in this study were tin,

lead, lead-tin alloys and lead-bismuth alloys. All materials were specified as 99.999% pure for metallic impurities. The radioactive tracers used were tin (Sn^{113}) with K and e^- radiation and thallium (Tl^{204}) a pure beta emitter. The tracers were obtained from the Atomic Energy of Canada Limited. Various combinations of melt material and tracer element were used to investigate various aspects of natural convection.

The general procedure for an experimental run is as follows:

(a) The mould is assembled and the material to be investigated is cast into the mould. The filled mould is placed in the furnace and the temperature of the system is raised by means of the heating plates. With the use of the heating and cooling blocks a prescribed temperature difference is imposed and maintained across the molten or semi-molten region. During this time an argon atmosphere is maintained in the steel container.

(b) A temperature traverse is made of the molten zone when the system has reached equilibrium conditions. The system is assumed to be in equilibrium when the average temperature and the temperature difference across the melt are both constant for a period of approximately one-half hour. The 0.5 mm. diameter thermocouple is used.

(c) To observe the flow pattern, a small sphere of radioactive material is added to the melt. The

material added is approximately 0.1 gms. For the tin tracer the particle added is 25 wt. % Sn^{113} as received from The Atomic Energy of Canada Ltd. For the thallium tracer the particle added is 1.5 wt. % Tl^{204} as received. The tracer is added at the top of the melt and is allowed to flow for a certain period of time. The whole system is then quenched very rapidly by filling the stainless steel container with cold water.

(d) The resultant solid block containing the radioactive material is removed from the mould and placed on a sheet of either X-Ray or Contrast Process Ortho film. The presence of radioactive material adjacent to the film will effectively expose the film locally. An examination of the developed film then reveals the flow pattern in the liquid prior to the quench. The penetration distances of the radiation in the metal casting is relatively short (20 microns for the thallium in tin), so that for observing the internal flow pattern the surface layers can be progressively machined off and autoradiographed.

All the autoradiographs presented in this thesis are printed from negatives made from the original autoradiographs. The position of the tracer will show as a darkened region as in the original autoradiograph. All pictures will be shown, where applicable, with the flow in the counterclockwise direction, and are also shown actual size.

2.3. Validity of technique

The most important question to be resolved in this experimental technique is whether the autoradiographs are representative of the flow that occurs prior to the quench, or the quench process itself causes significant fluid motion.

It is reasonable to assume that the more rapid the quench, the greater is the likelihood that the tracer will be fixed in its position prior to quenching. To quench the stainless steel tank is completely filled with cold water in two seconds. The quench rate is estimated from the temperature response of a thermocouple left in the melt during the quench. A typical temperature vs. time curve is shown in Figure 6, for a pure tin melt with a starting temperature of 268°C (melting point 231.9°C). The temperature response indicates that the tin starts to solidify in approximately one second and that the casting is completely solid after three seconds from the start of the quench.

A zero temperature gradient in a molten bath of pure tin should produce no fluid flow. A test was conducted in which radioactive tin was added to liquid tin in which there was no detectable temperature gradient, then quenched thirty seconds after the addition. The sample size was 6.4 cm. by 6.4 cm. by 0.32 cm. thick. Figure 7 shows the

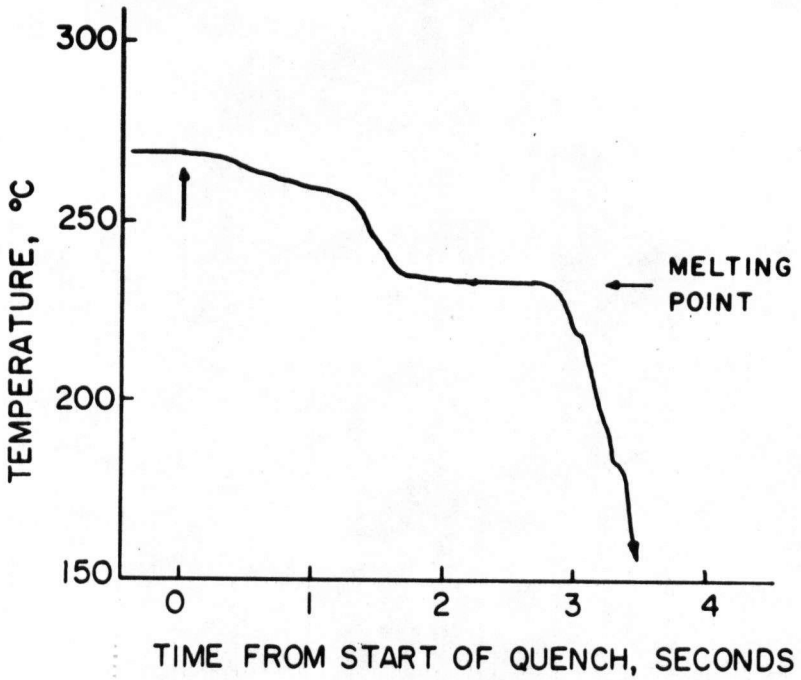

Figure 6. The temperature versus time curve in the liquid tin during rapid water quenching.

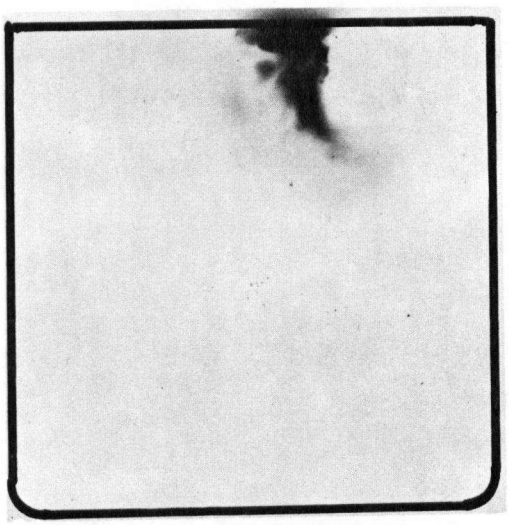

Figure 7. The tracer movement in a liquid tin melt (Sn^{113} tracer) with a 0°C temperature difference, left 30 seconds before quenching. (Actual size)

resulting flow as the darkened region of the autoradiograph. The tracer is seen to have remained essentially in the region in which it was added, with some slight downward flow due to the addition containing the radioactive tin being colder than the liquid.

The change in the flow pattern at different positions within the casting can also be used to determine to what extent the autoradiographs are representative of the fluid flow before quenching. The outer surface of the liquid cell should solidify extremely rapidly so that little tracer movement would be anticipated. In the central region there is a three second elapse from the start of quenching to complete solidification; some extraneous flow might occur during this interval. The tracer profile at various positions in the solid block is shown in Figure 8. This sample had a 3°C temperature difference across the liquid cell, an average temperature of 260°C, and is pure tin with tin tracer. The casting was made in the 6.4 by 6.4 by 0.32 cm. mould. It should be noted that a temperature difference is used to describe the thermal conditions rather than a temperature gradient. From Figure 2b it is evident that the temperature gradient is not a constant but a function of the vertical position in the cell and hence is not a unique parameter for a certain thermal condition. The three autoradiographs in Figure 8a, 8b and 8c represent the tracer position at the as cast surface, 13% below the surface, and

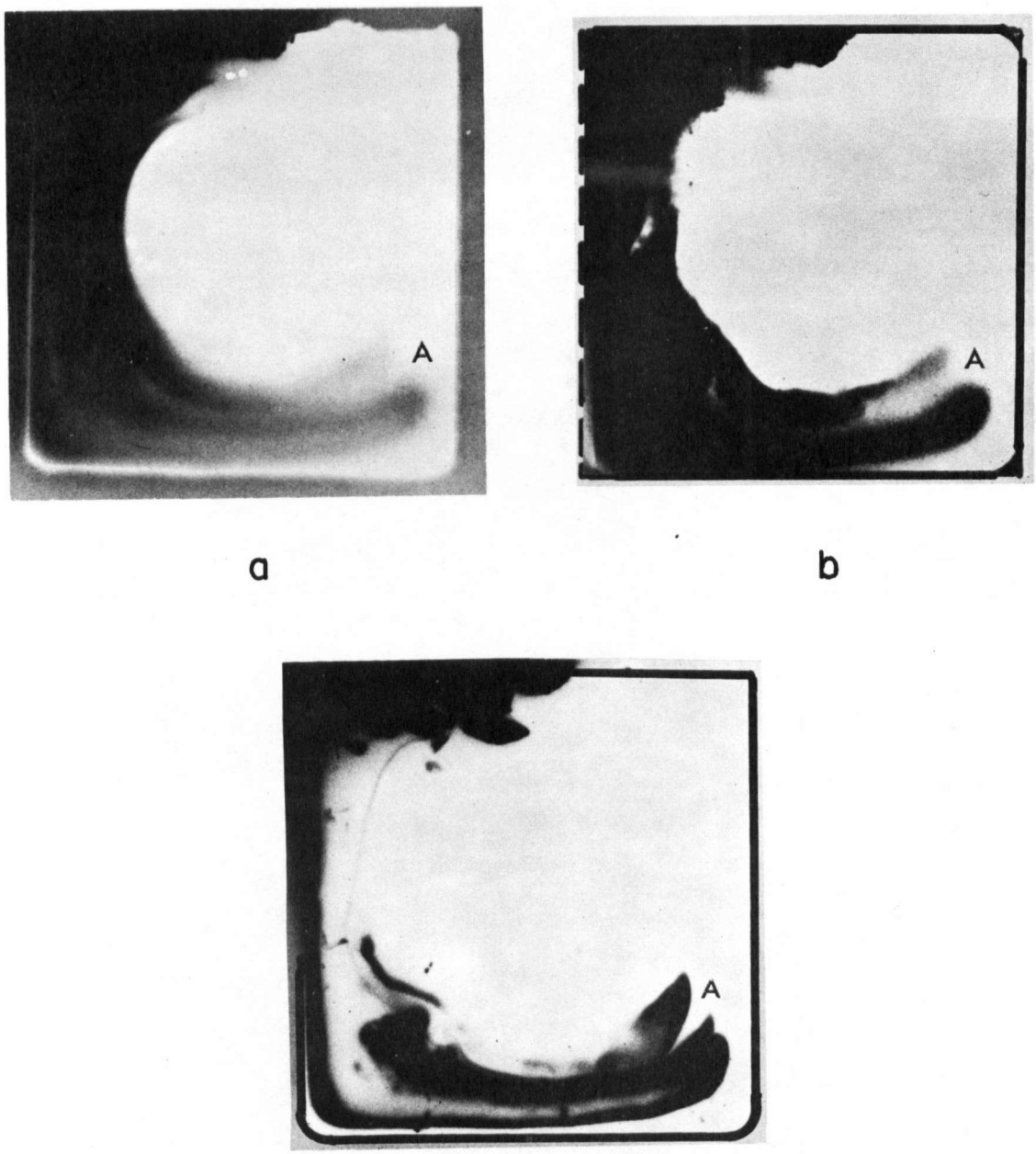

Figure 8. The tracer profile in a tin melt (Sn^{113} tracer, 260°C average temperature) with a 3.0°C temperature difference left 30 seconds before quenching, (a) on the as cast surface, (b) 13% into the tin block, and (c) 44% into the tin block.

44% below the surface. It is apparent that the limit of flow around the liquid cell (point A) is nearly the same throughout the casting which would not be the case if there were internal flow after the surface layers were solid.

From the observations presented in this section it is very reasonable to assume that the quenching operation does not cause any significant disturbance of the overall flow pattern.

3. Thermal Convection

3.1. Experimental investigations

Thermal convection is perhaps the most important form of convection in standard casting processes and will therefore receive the greatest study in this work. The experimental results of the present investigation will be presented under the following divisions:

(a) temperature difference across the liquid and average temperature

(b) liquid metal thickness

(c) temperature distribution in the liquid

(d) liquid zone height

(e) double cell flows

(f) liquid metal investigated

(g) thermal fluctuations

For a melt of pure tin, radioactive tin was used as the tracer and for melts of pure lead, radioactive thallium was used as the tracer. Both of these systems will be representative of thermal convection only.

3.1.1. Variable applied temperature difference and average temperature

The thermal convective flow is very dependent on the thermal boundary conditions present in the melt. The liquid cell used in the experiments described in this section is 6.4 cm. by 6.4 cm. by 0.32 cm. thick. The effect of changing the liquid cell thickness is discussed in the next section. The flow pattern as a function of temperature difference across the pure tin melt is shown in the autoradiographs in Figure 9. All these samples had an average temperature of 260 ± 1°C. The eight flow patterns shown have temperature differences from 0.23°C to 9.1°C across the liquid zone. Comparing the samples shows that the flow rate increases greatly with increasing temperature difference, but the shape of the flow pattern remains essentially constant over the range of temperature differences considered here. All flow occurs in single cellular patterns and appears to be laminar in nature as no small turbulent eddy currents are apparent.

The effect of changing the average temperature of the tin melt can be seen in Figure 10. Three different average temperatures have been studied, 237°C, 260°C and 305°C. Figures 10a and 10b compare the flow rates at 237°C and 305°C with a 2°C temperature difference and Figures 10c and 10d compare the flow rates for a 3°C temperature difference. It should be noted when comparing that the

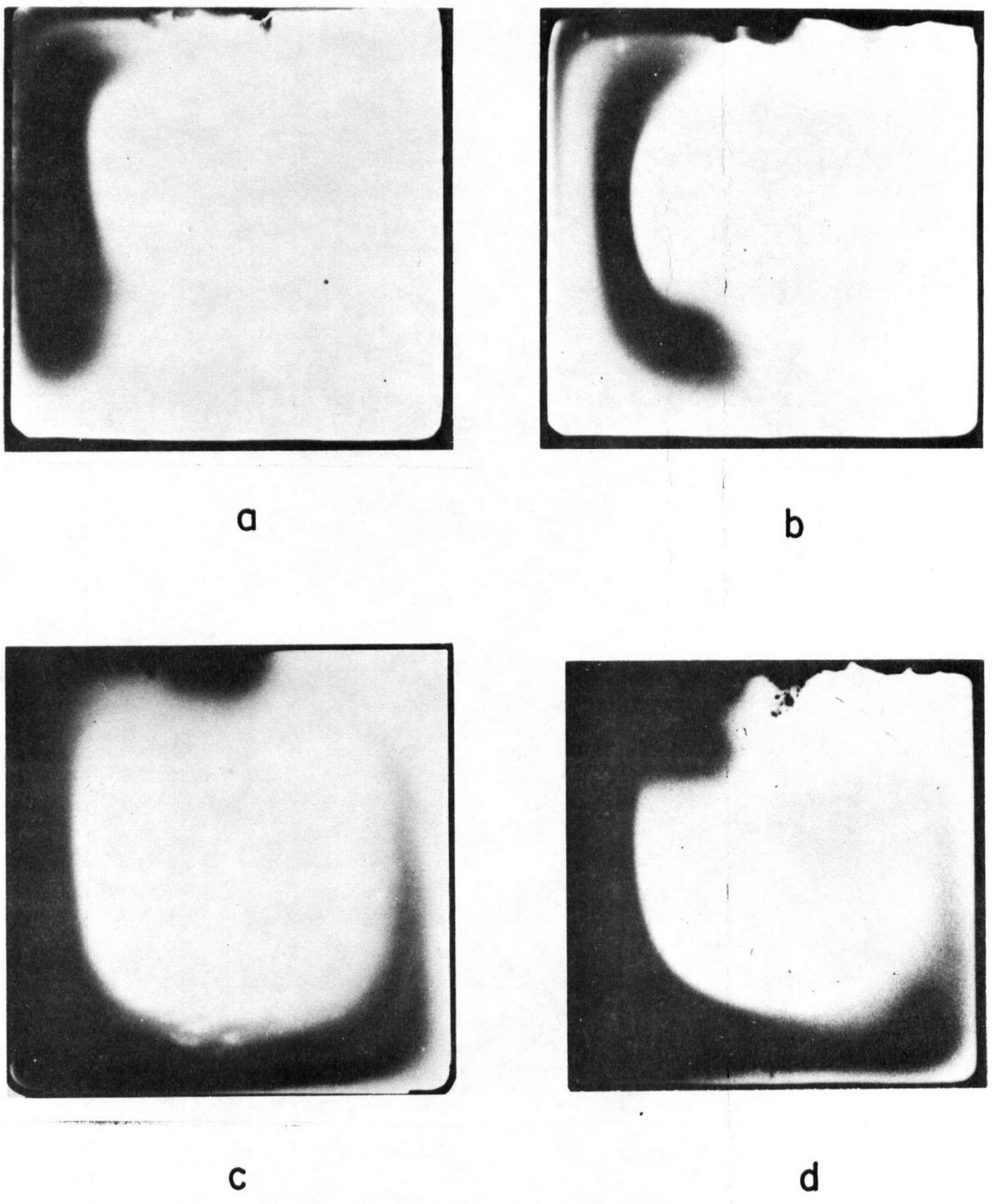

Figure 9. The tracer profile in tin melts (Sn^{113} tracer, 260°C average temperature, 0.32 cm. thick cell) with a temperature difference and a time before quenching of (a) 0.23°C, 300 seconds, (b) 0.67°C, 90 seconds, (c) 1.11°C, 120 seconds, (d) 1.96°C, 60 seconds.

(continued)

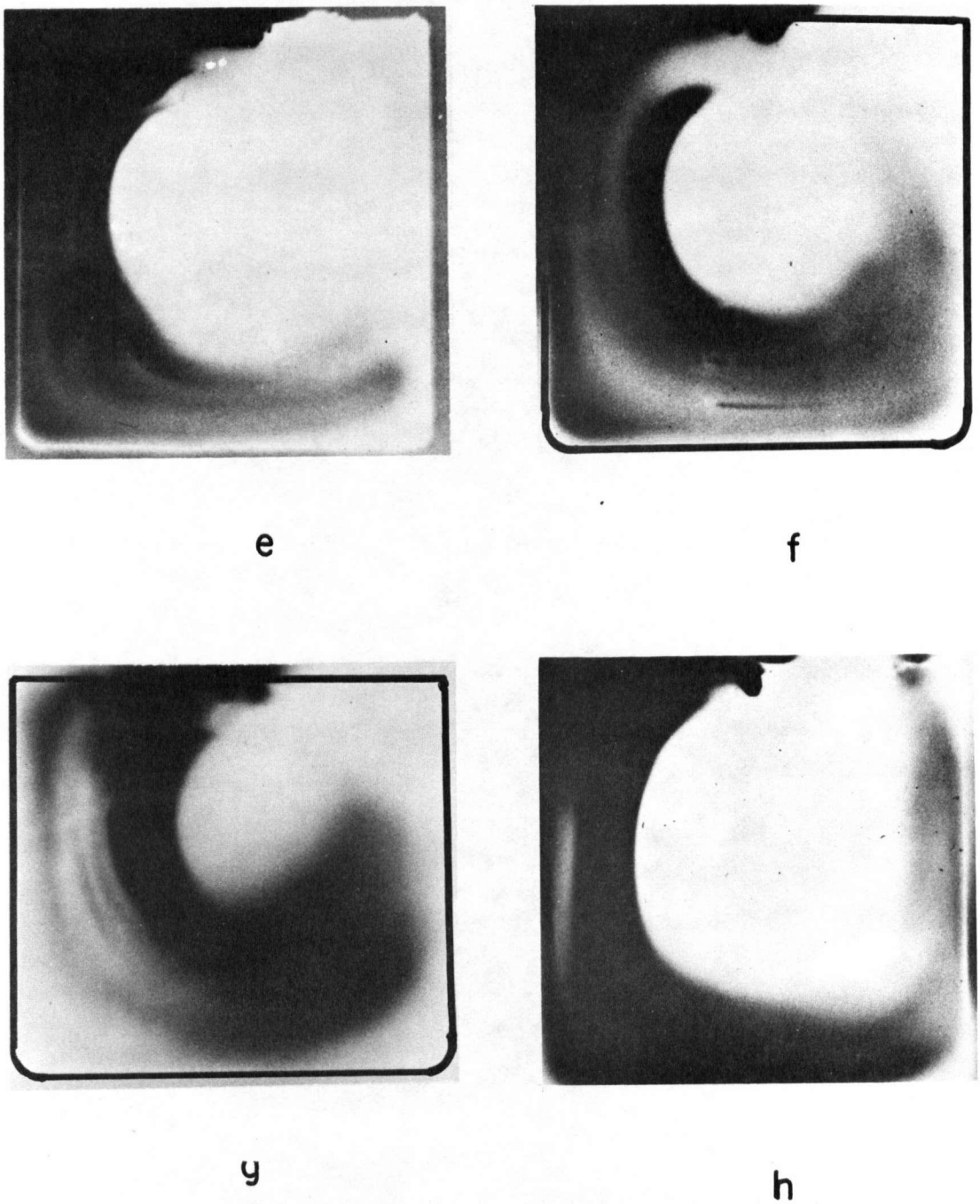

Figure 9 continued. The tracer profile in tin melts (Sn^{113} tracer, 260°C average temperature, 0.32 cm. thick cell) with a temperature difference and time before quenching of (e) 3.04°C, 30 seconds, (f) 4.00°C, 30 seconds, (g) 5.05°C, 15 seconds, and (h) 9.1°C, 15 seconds.

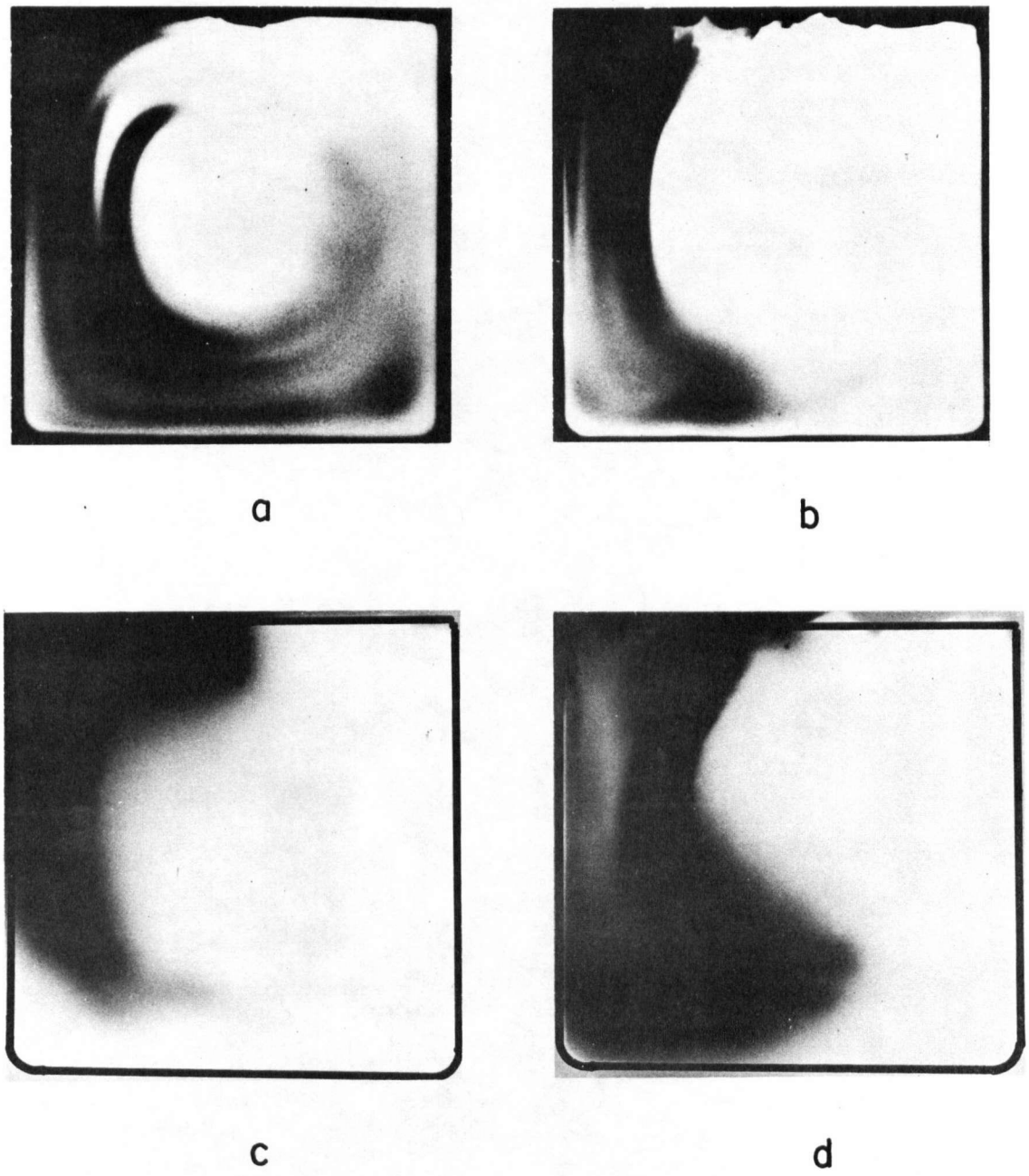

Figure 10. The tracer profile in tin melts (Sn^{113} tracer) with an average temperature, temperature difference, and time before quenching of (a) 236°C, 2.00°C, 60 seconds, (b) 305°C, 2.02°C, 30 seconds, (c) 237°C, 3.00°C, 30 seconds, and (d) 305°C, 3.02°C, 15 seconds.

lower superheat flows were left twice as long as the higher superheat flows for the same temperature difference prior to the quench. From the autoradiographs it is evident that an increase in the average temperature causes an increase in the flow rate for an equal temperature difference.

For quantitative analysis of the flow rates the time for the flow to complete one cycle around the cell has been chosen as the relevant parameter. Usually two to four experiments with differences in the times before quenching are done for a particular temperature difference and average temperature to obtain the time per cycle. The time per cycle for a particular casting is obtained by measuring the angular movement of the tracer front around the cell and then using the time to quench to calculate the period the tracer would take for a complete cycle of 360°. The sample must, therefore, be quenched before the tracer has completed one full cycle. This parameter has been chosen since it will allow a single value to describe the overall flow rate. The actual autoradiographs can be used for noting any changes in the shape of the flow pattern. The time per cycle for pure tin versus the temperature difference across the cell for three different degrees of superheat is plotted in Figure 11. It is seen from this graph, as with the autoradiographs, that the flow rates increase with increasing temperature difference across the cell and that they also increase with increasing melt superheat.

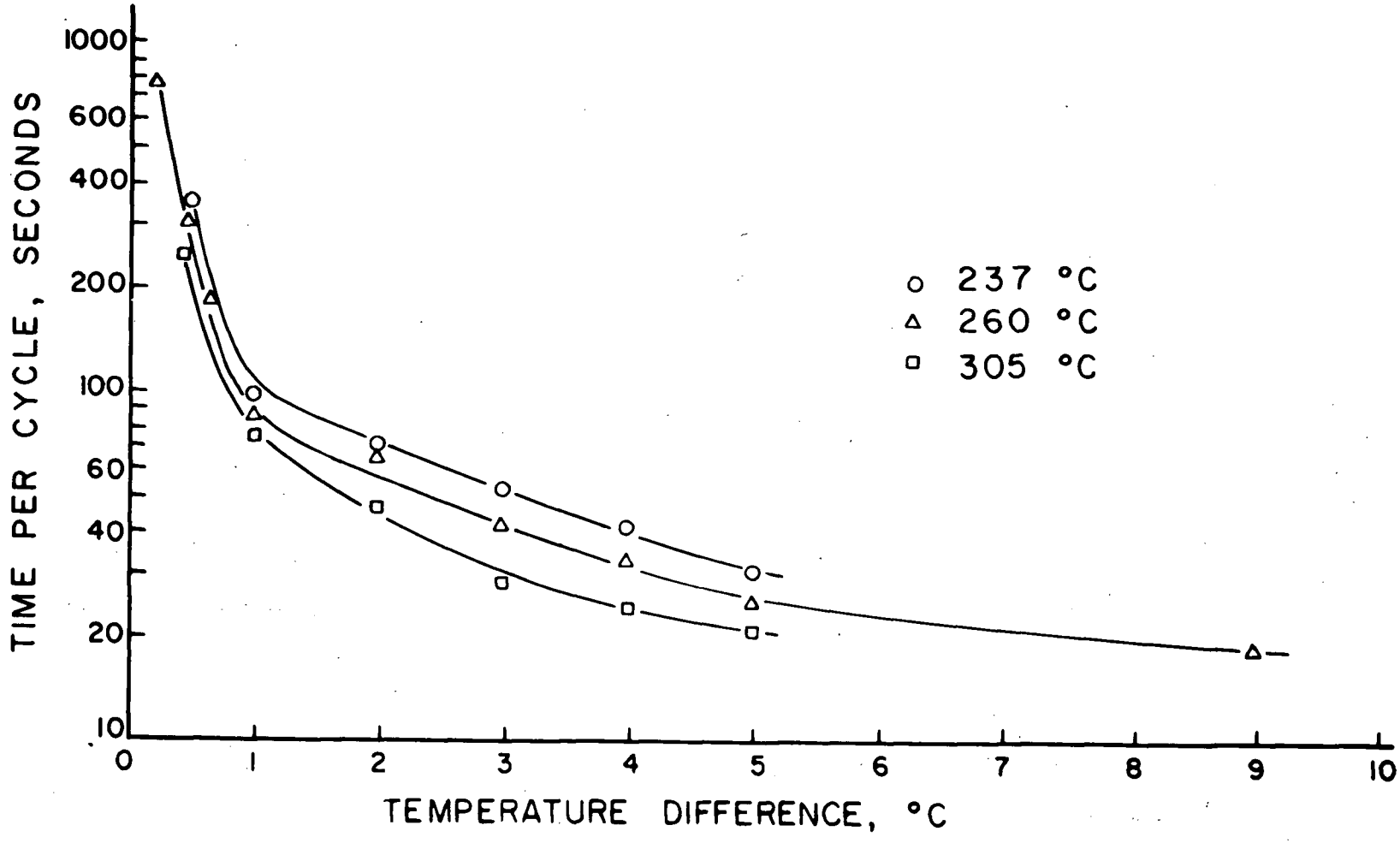

Figure 11. The time for the flow in tin melts to complete one cycle around the cell versus the temperature difference across the cell for average temperatures of 237°C, 260°C, and 305°C.

3.1.2. Variable liquid metal thickness

Three different molten zone thicknesses were investigated: 0.32 cm. (1/8 in.), 0.48 cm. (3/16 in.) and 0.95 cm. (3/8 in.). All the liquid cells had a molten zonelength of 6.4 cm. and a height of 6.4 cm. These experiments were done to determine if any significant change in the flow behaviour occurred with a thicker cell size possibly due to constraints by the large flat cell faces on the flow. The change in the flow pattern and flow rates were both investigated.

It was found that for increasing cell thicknesses and increasing temperature differences a completely different stable mode of thermal convection can develop in the liquid metal. The two different modes can be referred to as two-dimensional and three-dimensional flow. Figure 12 shows typical autoradiographs of as cast surfaces for two-dimensional and three-dimensional flows in liquid tin. Figure 12a is for the 0.32 cm. cell and a 5.60°C temperature difference which shows the two-dimensional type of flow like all the flow patterns shown in Figure 9. This flow is characterized by the single laminar flow cell with the tracer forming a continuous circular path around the liquid cell. By increasing the temperature difference across the 0.32 cm. cell to 19°C, Figure 12b, or by increasing the cell thickness to 0.48 cm., Figure 12c, or 0.95 cm., Figure 12d, the flow changes to the three-dimensional mode. The three-

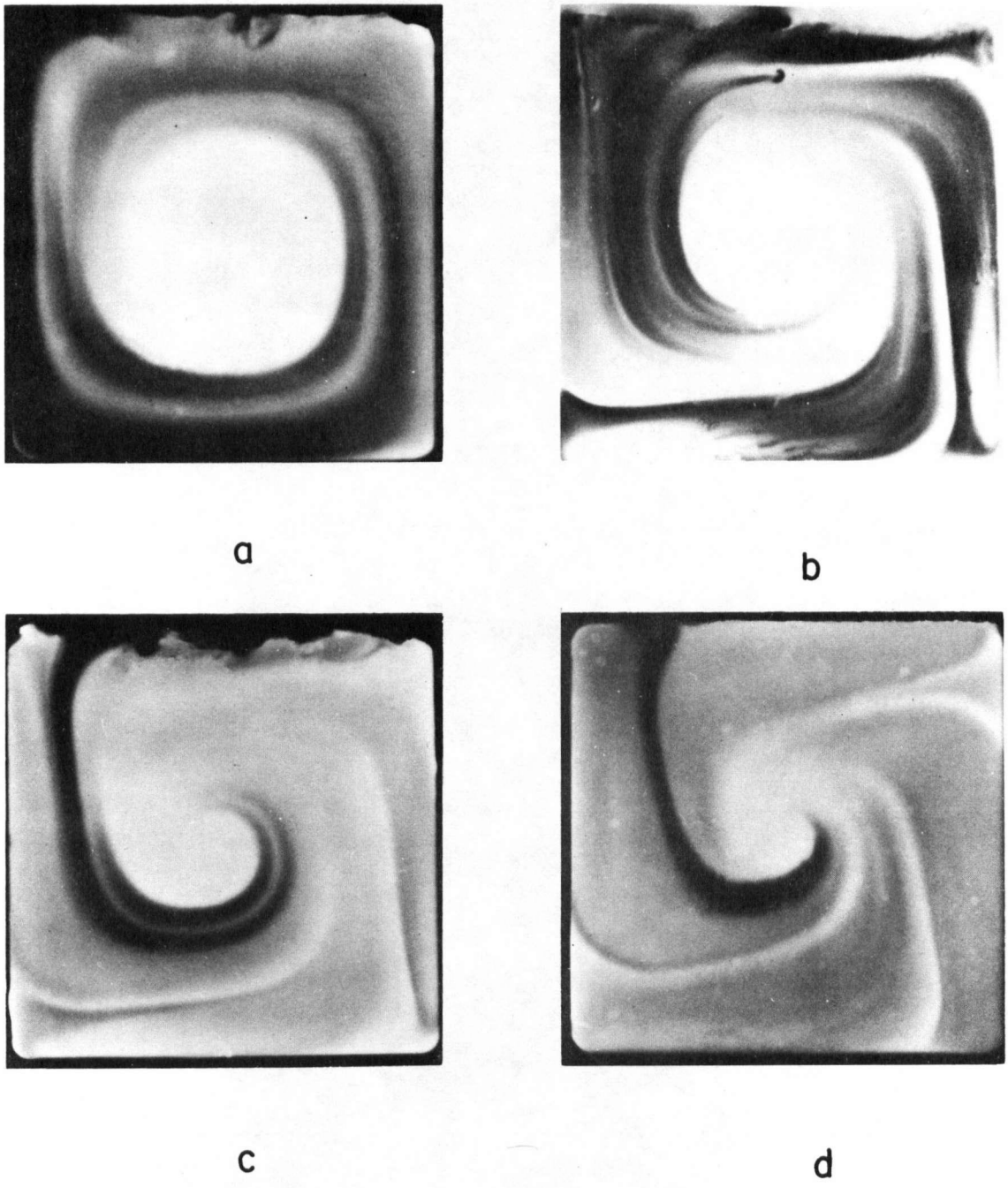

Figure 12. The tracer profile in tin melts (Sn^{113} tracer, 260°C average temperature) with a temperature difference, liquid cell thickness, and time before quenching of (a) 5.60°C, 0.32 cm, 60 seconds, (b) 19.0°C, 0.32 cm., 15 seconds, (c) 5.0°C, 0.48 cm., 60 seconds, and (d) 5.0°C, 0.95 cm., 90 seconds.

dimensional mode is characterized by a spiral pattern, with tracer depleted bands coming from three corners of the liquid zone and a tracer rich band from the top left-hand corner. The spiral pattern observed does not change with time, the bands remaining fixed in position with time. The pattern was found to be identical on both sides of the casting. There are no continuous flow lines connecting the areas where the tracer is present due to these depleted bands. Thus for the tracer to move throughout the cell, as seen in the autoradiographs, there must be an internal flow in the molten zone. This complex three-dimensional flow pattern is developed for higher gradients and thicker cells. Figure 13 shows quantitatively the dividing line between the two flow modes for a variable cell thickness and temperature gradient. A band is shown separating the two modes of flow at lower temperature differences since at very low gradients the autoradiograph interpretation becomes more difficult. The theoretical analysis of thermal convection is very complex and is usually only attempted for two-dimensional flow. Thus to enable theoretical and experimental comparisons to be made, most of the present observations of thermal convection have been made for the two-dimensional mode.

The variation in the actual flow rates for the various liquid cell thicknesses was also observed. For the three cell thicknesses used in Figure 12 experiments

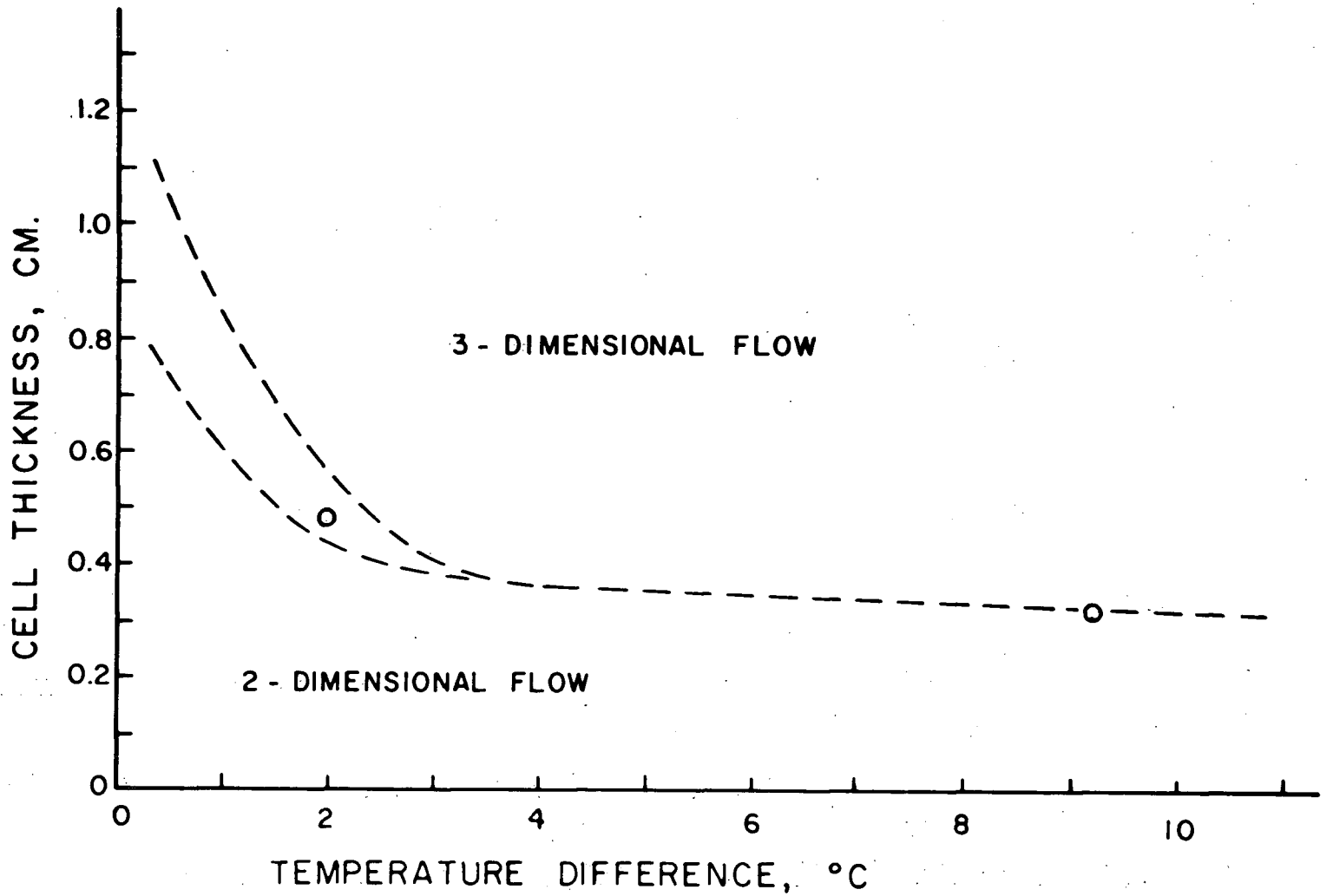

Figure 13. The liquid cell thickness versus the temperature difference across the cell showing the conditions for two dimensional and three dimensional flow in liquid tin at 260°C.

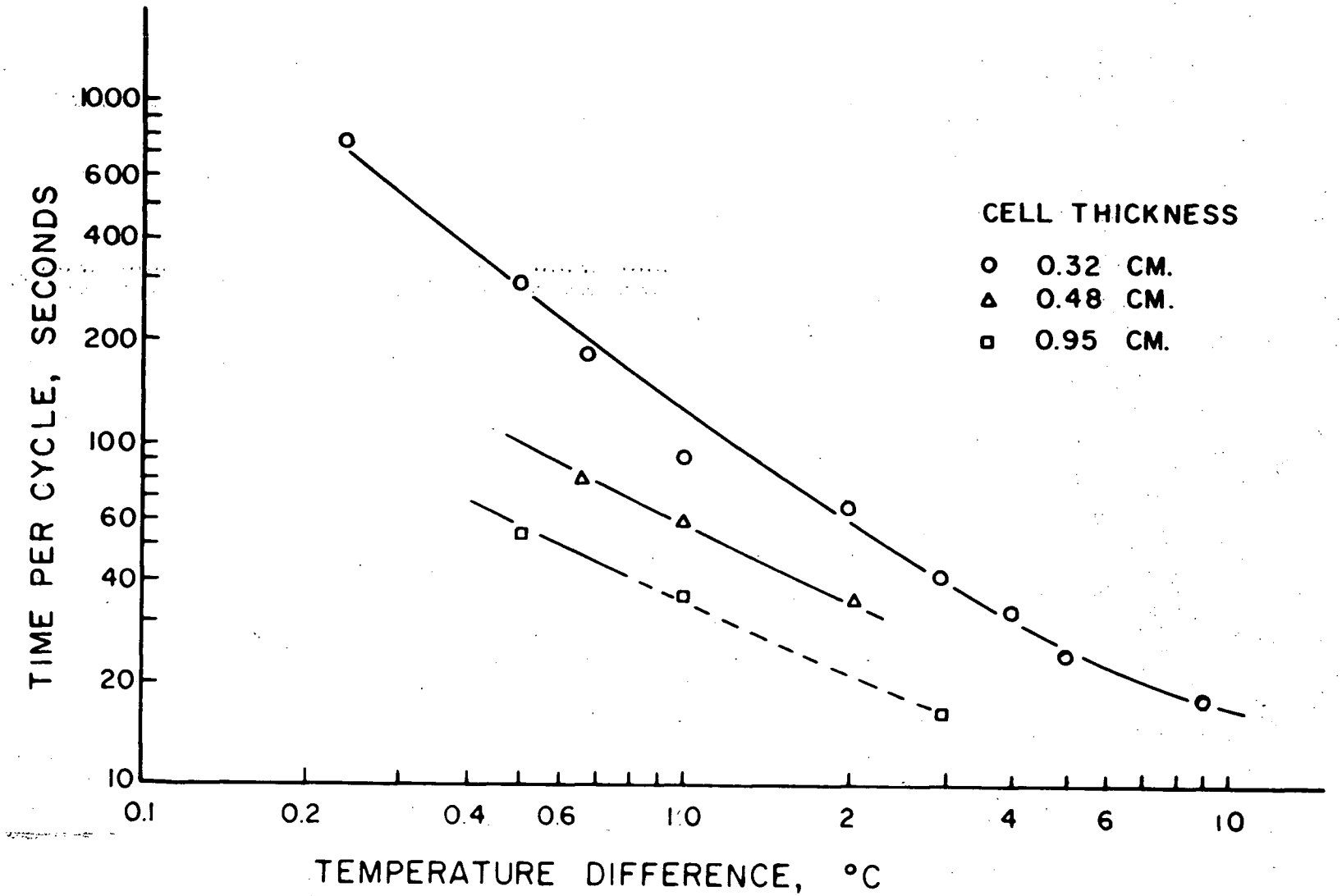

Figure 14. The time for the flow in tin melts to complete one cycle versus the temperature difference across the cell for liquid cell thicknesses of 0.32cm., 0.48 cm., and 0.95 cm.

were conducted with pure tin, at 260°C average temperature, to arrive at a time per cycle versus temperature difference curve for each cell. For a time per cycle value to be calculated, only two-dimensional flows or the very early stages of three-dimensional flows can be used. This is due to the three-dimensional flow resulting in the tracer "short circuiting" through the internal parts of the cell to give a false time per cycle reading for comparison purposes. A cycle time cannot really be defined for fully developed three dimensional flow. The flow rates versus the temperature difference across the cell for the three different cells is shown in Figure 14. It is evident that the thicker cells have more rapid flow rates. This shall be discussed when these results are compared with various theoretical solutions in section 3.4.

3.1.3. Temperature distribution in the liquid

The temperature distribution in the liquid tin prior to the quench is a function of the temperature difference across the molten zone and also the liquid thickness. To determine the temperature isotherms for a given set of conditions, temperatures are determined at eight points on each of five vertical traverses of the melt to give a total of forty temperature readings. The results in °C are plotted in Figure 15a - 15e normalized to a zero point at the geometric centre of the molten zone. The thermal

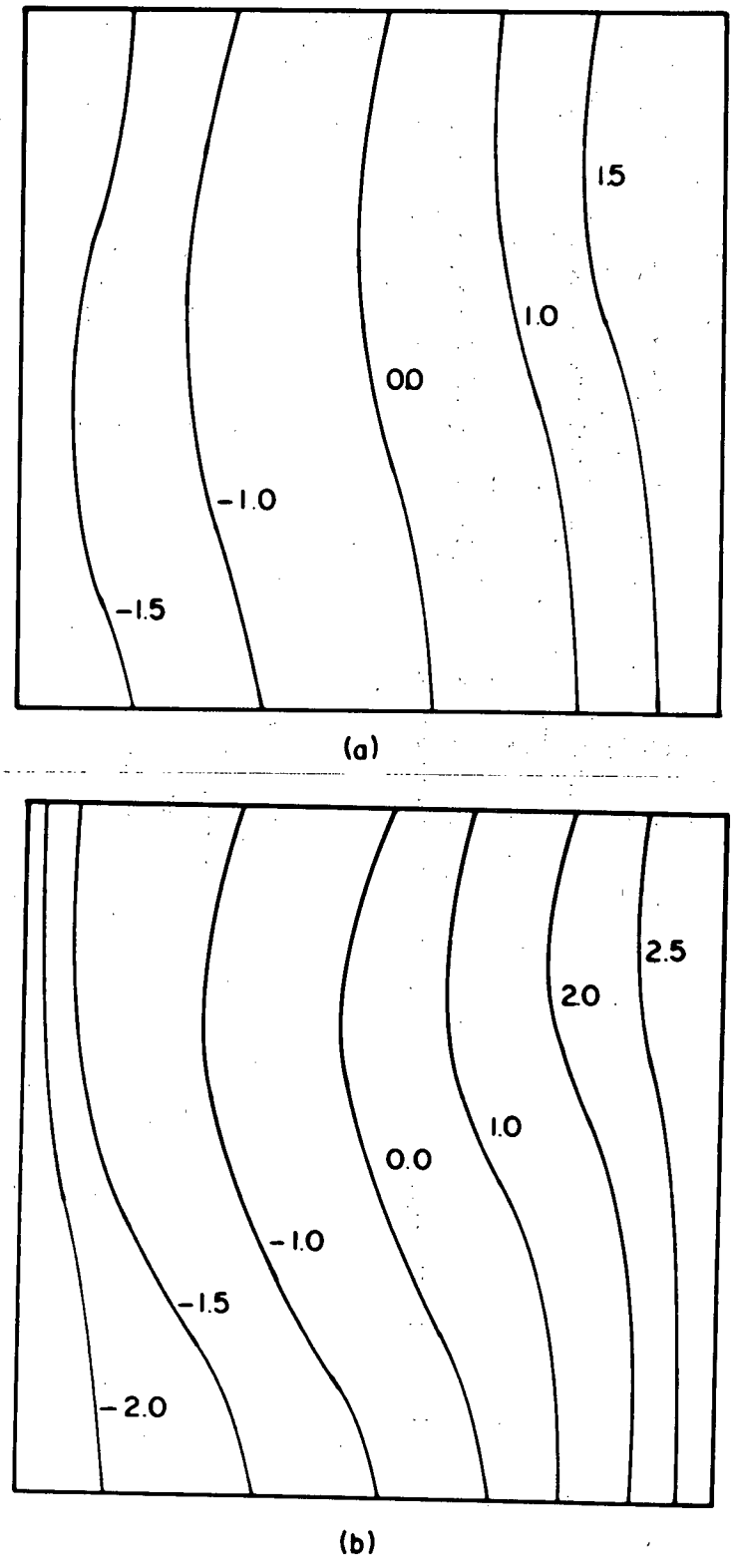

Figure 15. The experimental isothermal plots for liquid tin at 260°C for an approximate Rayleigh number and cell thickness of (a) 1.4×10^5, 0.32 cm., and (b) 2.4×10^5, 0.32 cm.

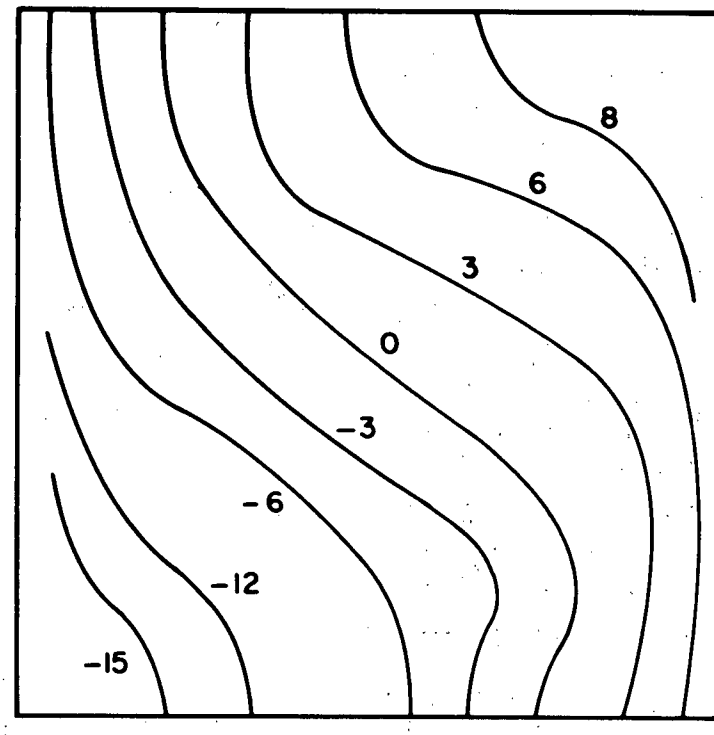

(c)

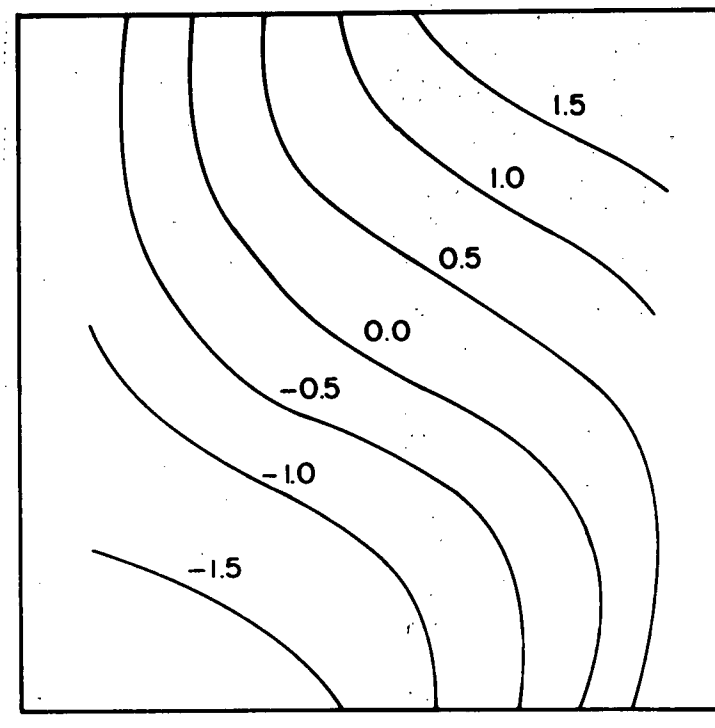

(d)

Figure 15 continued. The experimental isothermal plots for liquid tin at 260°C for an approximate Rayleigh number and cell thickness of (c) 8.0×10^5, 0.32 cm., (d) 1.4×10^5, 0.95 cm.

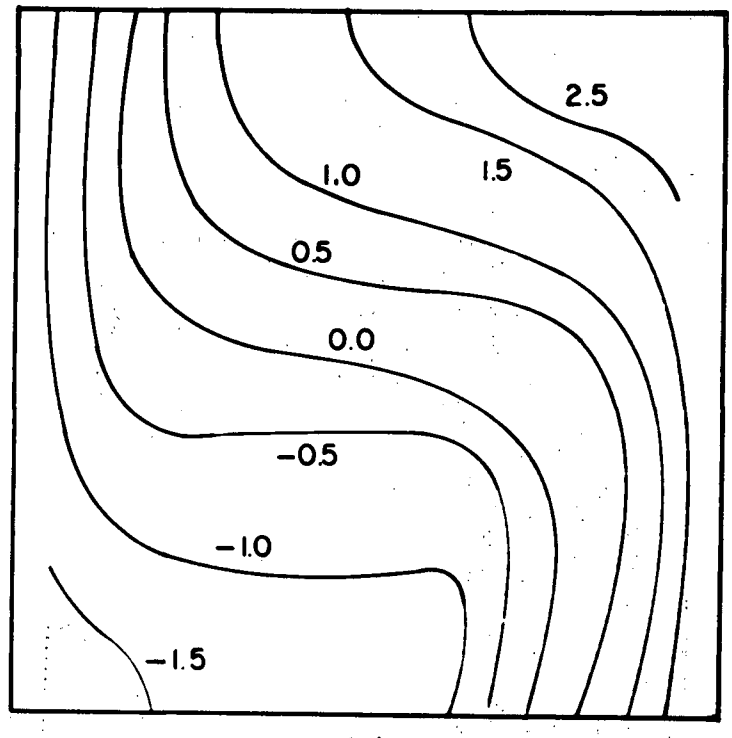

(e)

Figure 15 continued. The experimental isothermal plots for liquid tin at 260°C for an approximate Rayleigh number and cell thickness of (e) 2×10^5 and 0.95 cm.

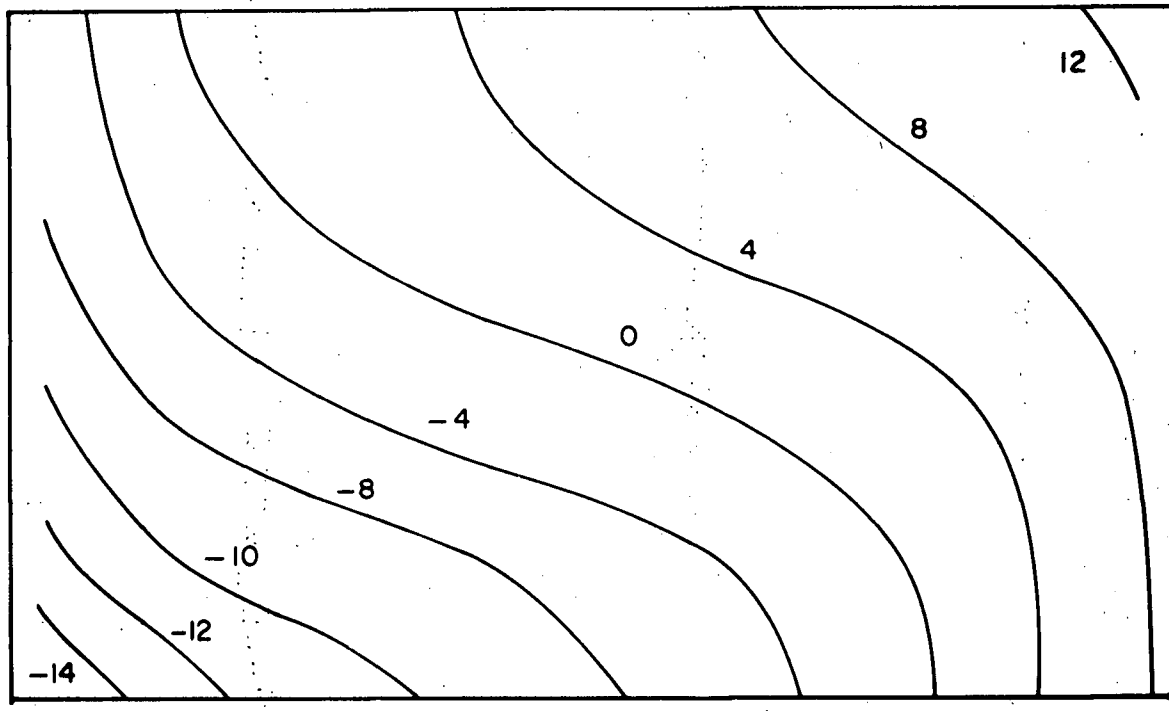

Figure 16. The experimental isothermal plot for liquid tin at 260°C in a 10.8 by 6.4 by 0.32 cm. liquid cell.

profiles for various temperature differences for the 0.32 cm. and 0.95 cm. thick cell are shown. It should again be noted that vertical, equally spaced isotherms would represent conductive heat transfer. The results clearly indicate that the isotherms in the liquid are bent in a manner indicative of convective flow. The isotherm shapes indicate a one cell flow pattern with the cool fluid moving to the right across the cell bottom while the hotter less dense fluid moves to the left across the top of the cell. Quantitatively, for a given liquid at a constant average temperature, the greater the bending of the isotherms, the greater the rate of fluid flow. Comparing Figures 15a, 15b and 15c, increasing the temperature difference increases the isotherm bending; comparing Figures 15a and 15d or 15b and 15e, increasing the cell thickness also increases the isotherm bending. The isothermal shape for the 0.32 cm. thick cell with a 19°C temperature difference is very similar to the 0.95 cm. thick cell with a 3°C temperature difference as seen by comparing Figures 15c and 15d. This is in agreement with the flow rate results presented previously.

For comparison, a thermal profile in a 10.8 cm. by 6.4 cm. by 0.32 cm. molten zone cell is shown in Figure 16. The material is tin and the plot is normalized in the same manner as the square cell profiles. The shape of the profile is very similar to the square cell profiles, again indicating a one cell flow pattern.

3.1.4. Variable height of the molten zone

The effect of the height of the molten zone on the flow pattern was investigated in a 10.8cm. long by 0.32 cm. thick liquid cell. The mould was filled to different levels to obtain the variable height required. The runs were done with a 9 - 10°C temperature difference across the cell, an average temperature of 260°C and were quenched 120 seconds after the tracer introduction. Figure 17 (a, b, c, d) shows the resultant flows for length to height ratios of 1.6 : 1, 3.5 : 1, 4.9 : 1 and 8.3 : 1 respectively. The tracer was added to the left-hand corner in each case, the cold side being on the left. In the 1.6 : 1, 3.5 : 1 and 4.9 : 1 length to height ratios the flow is of a one flow cell nature as was observed in the square mould. However, in the 8.3 : 1 ratio liquid cell the flow is starting to break into more than one cell. This is indicated by the secondary flow cell forming at the left-hand end of the sample. Due to experimental limitations the length to height ratio could not be increased further.

3.1.5. Double cell flow

Castings normally solidify in a three-dimensional configuration, such as illustrated in Figure 18a. The heat is extracted from the liquid in many directions at once and therefore the resulting flow in the liquid pool may

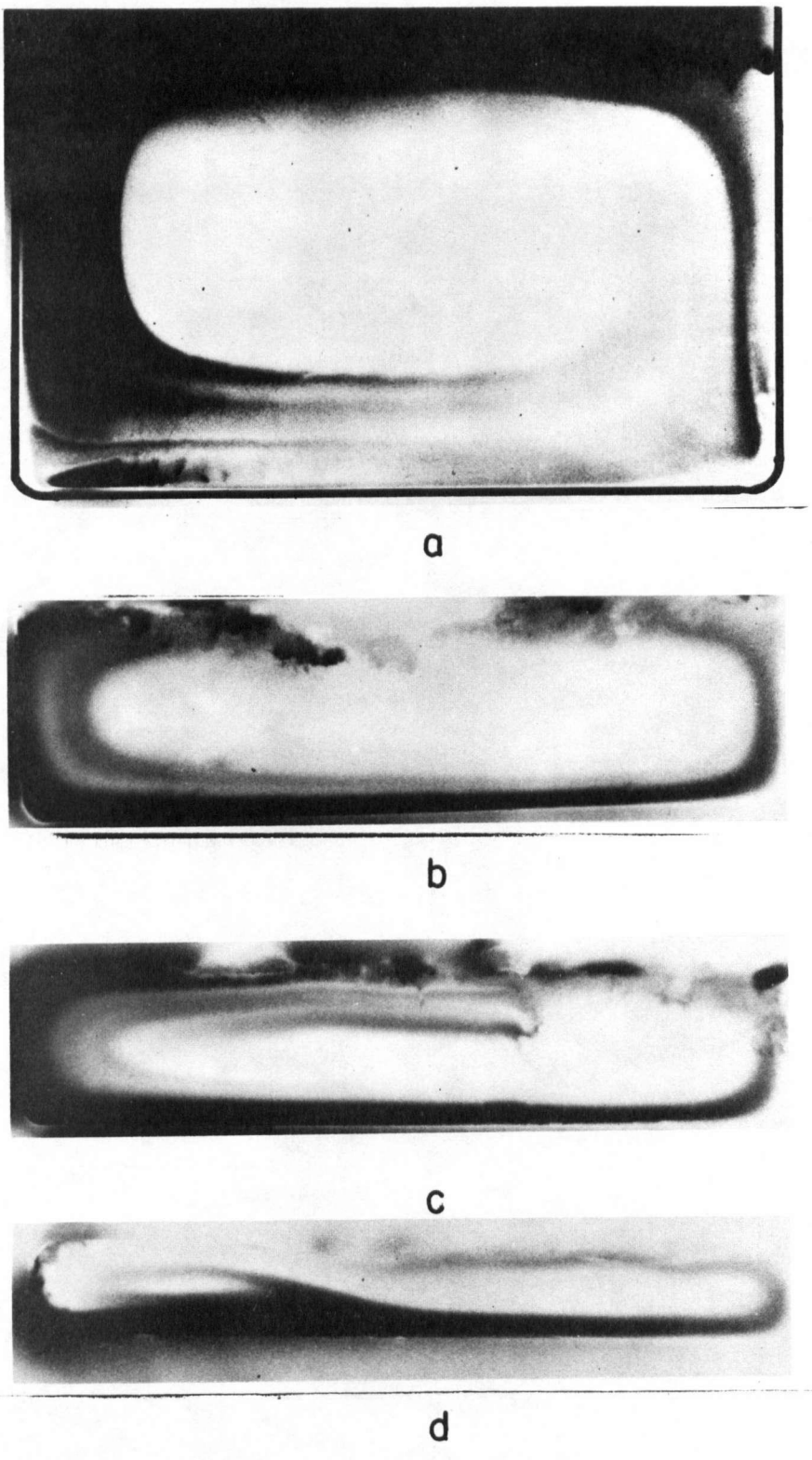

Figure 17. The tracer profile in tin melts (Sn^{113} tracer, 260°C average temperature, 10°C temperature difference, 0.32 cm. thick cell, time before quench of 120 seconds) with a length to height ratio of (a) 1.6 : 1. (b) 3.5 : 1, (c) 4.9 : 1, and 8.3 : 1.

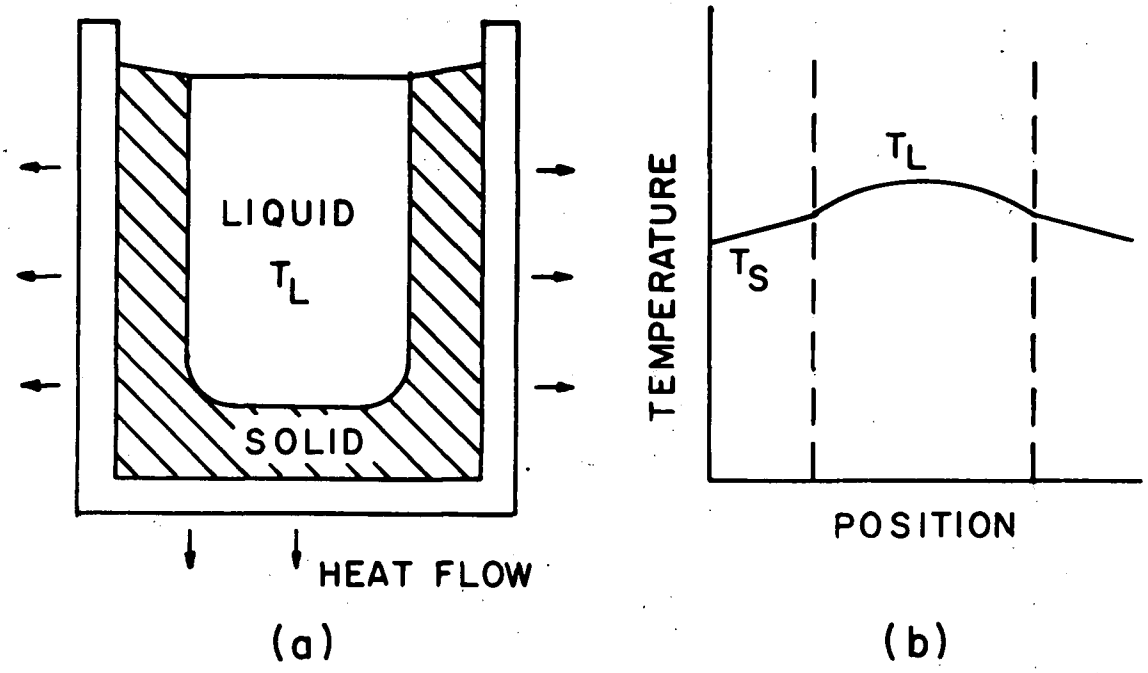

Figure 18. A schematic of the heat flow in a standard casting, (a), and the temperature profile, (b), in the residual liquid pool.

change from simple one cell flow patterns to very complex forms.

Figure 18a shows a partially solidified casting with solid-liquid interface moving towards the centre from each side leaving a central liquid pool. The temperature gradient across this pool will be of the form as shown in Figure 18b such that each side is at the liquidus temperature of the metal and the central region is at a somewhat higher temperature. The actual profile will depend on the vertical position in the melt and the time elapsed since the casting was poured. An experiment was carried out

which would approximate this more general casting configuration.

In this experiment cooling blocks were used at both ends of the rectangular cell (10.8 cm. by 6.4 cm. by 0.32 cm.). The average temperature of the liquid tin was maintained by raising the overall furnace temperature sufficiently to enable the heat lost through the cool ends to be balanced by heat gained through the flat faces of the mould. This could be done if the heat lost through the cooling blocks was kept small. Figure 19a shows a typical flow pattern with two flow cells. To show both cells the tracer was added at two points simultaneously, one in each half of the mould. This casting was quenched 120 seconds after the tracer introduction, had an average temperature of 267°C and a temperature difference from the mould walls to the central region of 1 - 2°C. The flow pattern that results has two cells of approximately the same size. The individual flow cells that result are very similar in form to the one cell flows discussed in an earlier section. Figure 19b shows a single cell pattern for liquid tin at 260°C with a temperature difference of 1.11°C and a time before the quench of 120 seconds. These conditions are similar to the double cell casting of Figure 19a. It can be seen that individual flow cells are the same for both experimental configurations. Although the temperature differences cannot really be compared, the flow rates are

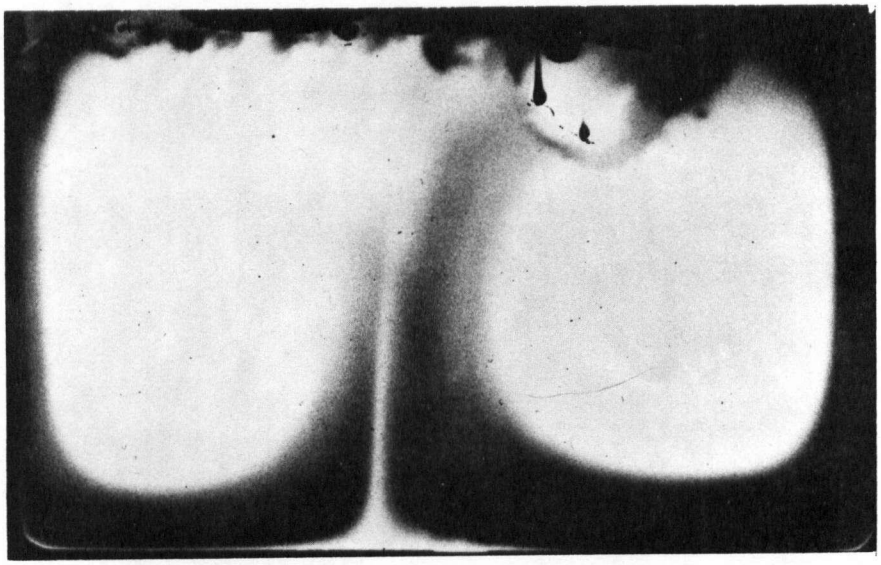

a

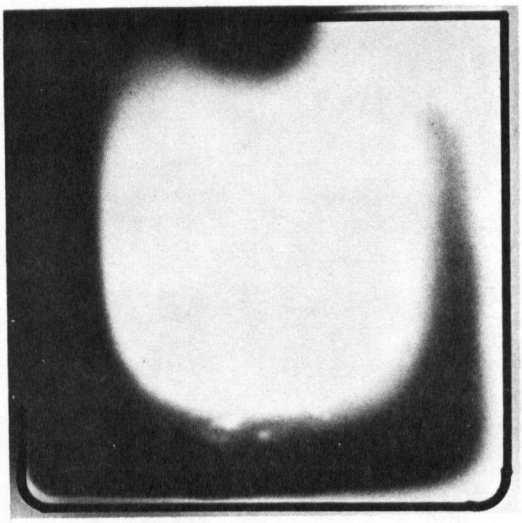

b

Figure 19. (a) The tracer profile in a tin melt cooled from both ends and left 120 seconds before quenching with a temperature difference across one-half of the cell of 1.5°C.
(b) The tracer profile in a tin melt cooled from one side with a temperature difference of 1.11°C and left 120 seconds before quenching.

quite similar indicating that the single cell flow results can be applied to more complex types of flow.

The relative sizes of the two flow cells can be manipulated by having the two cooling blocks at slightly different temperatures. In the sample of Figure 20a the two wall temperatures were held at the same temperatures while in Figure 20b the left-hand wall was maintained at 0.8°C lower than the right-hand side wall. The tracer was only added to the left-hand side of the molten zone in each case. For the equal temperature end walls the flow cell is one-half the width of the molten zone which is the case if a metal is solidifying from two sides since the liquidus temperature will be the same for both interfaces. In the sample with non-equal wall temperatures the flow cell on the coldest side is much larger than the opposite cell.

If the temperature gradient along a long liquid metal system is such that the gradient is increasing from both directions there will be a region in the melt where the thermal gradient is zero where the two gradients come together. This point of zero gradient will be the point of the maximum temperature in the melt. Davis and Fryzuk (32) have observed a lack of thermal convective mixing in this region of a maximum in the thermal profile. They observed the effect in 2 mm. diameter rods. This phenomenon can be referred to as a "thermal Valve" in the liquid since convection occurs on each side of the region but not

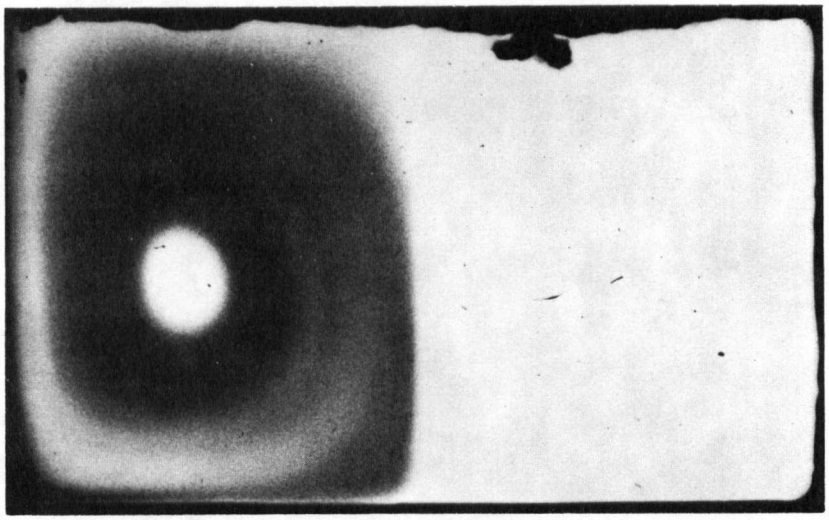

a

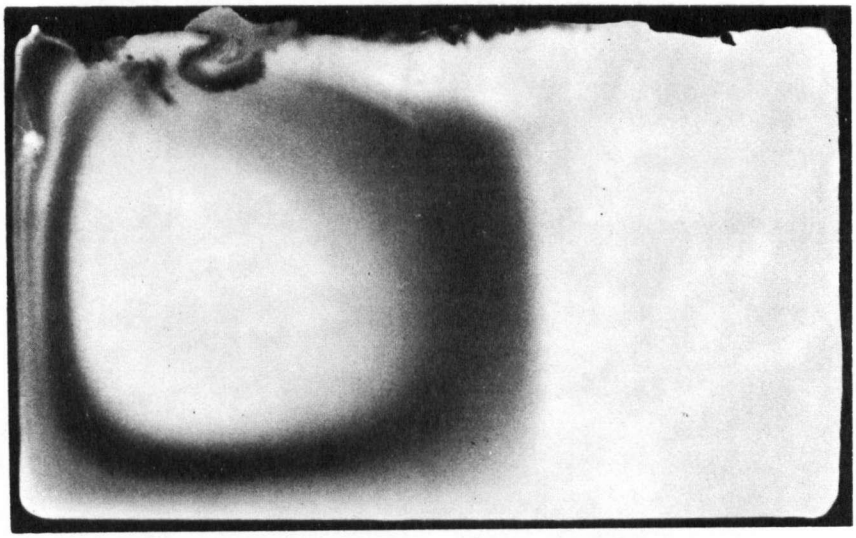

b

Figure 20. The tracer profile in a tin melt (a) cooled from both ends with equal end wall temperatures and left for 300 seconds before quenching and (b) cooled from both ends with the left hand wall cooler than the right hand wall, and left 120 seconds before quenching.

in the region itself. This condition may also occur naturally in the casting configuration described by Figure 18 as the thermal profile has a maximum. The double cell flow conditions observed in Figures 19 and 20 also have this maximum in the thermal gradient, thus it is possible they will also exhibit the "thermal valve" phenomenon. Figure 20a shows a double cell flow that had the tracer introduced into only the left cell and it was left five minutes before the quench. It is observed that there appears to be little if any transport of material between the two flow cells. This implies there must be some sort of quiescent buffer zone between the two cells. Such a zone is evident in Figure 19a as the light region between the two cells. It can be concluded from this result that the "thermal valve" also exists in much larger systems than those investigated by Davis and Fryzuk.

3.1.6. Liquid metal investigated

Several experiments were conducted with liquid lead melts for comparison with the liquid tin results. These experiments were intended to determine whether the results for one liquid metal can be applied to other liquid metals. The differences in fluid properties for lead when compared to tin are not great (TableI) although the Prandtl number for lead is almost double that of pure tin. Figures 21a and 21b show the flow patterns obtained for liquid

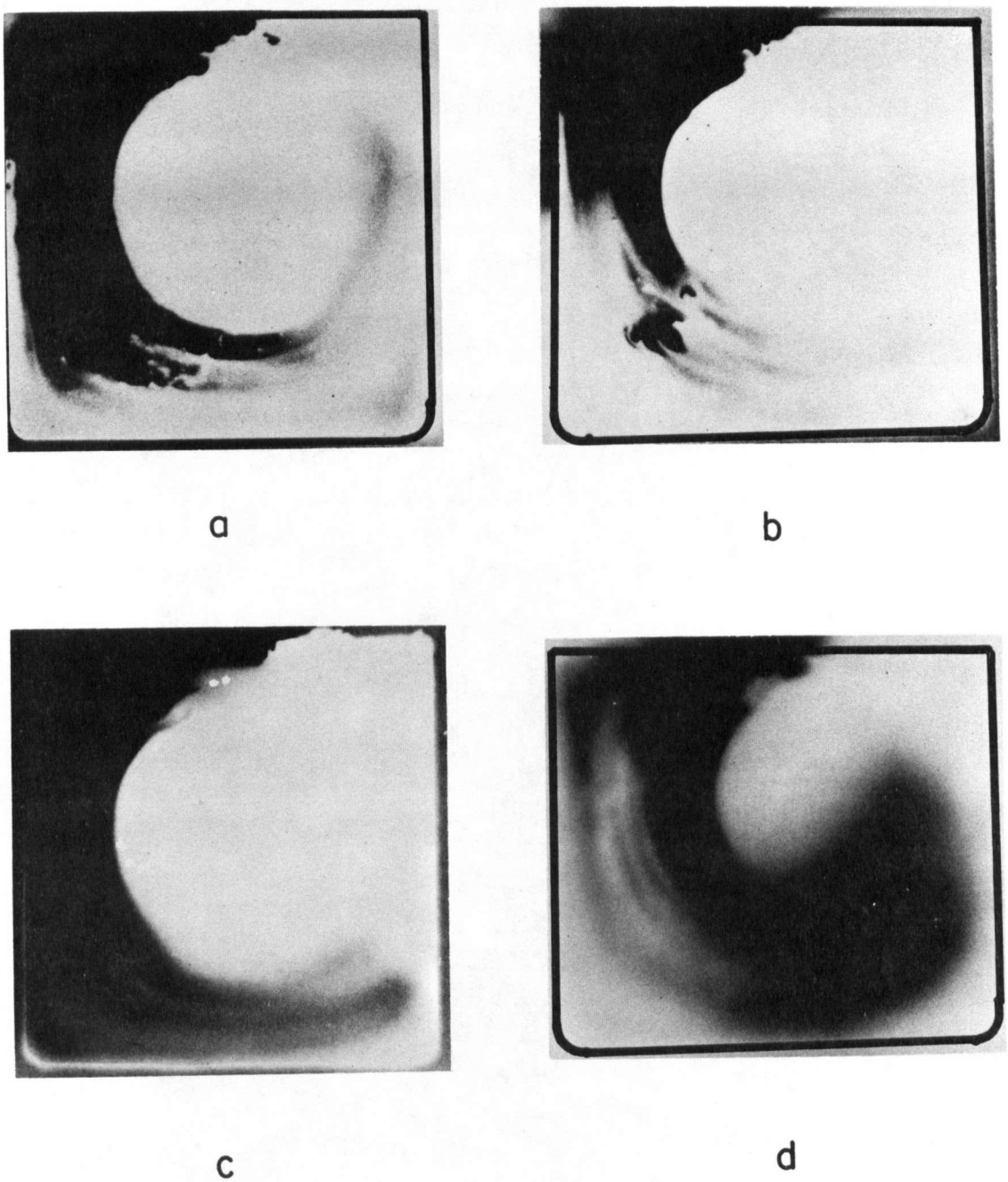

Figure 21. The tracer profile in liquid lead (Tl^{204} tracer, 357°C average temperature) with a temperature difference and time to quench of (a) 2.96°C, 30 seconds and (b) 4.98°C, 15 seconds, and in liquid tin (Sn^{113} tracer, average temperature of 260°C) with a temperature difference and time to quench of (c) 3.04°C, 30 seconds and (d) 5.05°C, 15 seconds.

lead at 357°C with a 2.96°C and a 4.98°C temperature difference respectively. Again a simple one cell flow pattern is developed. The tracer used with lead is Thallium^{204}, with 1.2% thallium in lead making up the addition dropped into the liquid lead. The density difference between lead and thallium is small (0.7%) which when combined with the low alloy content of thallium in the addition made to the lead, would justify the assumption that the difference between the melt and the addition is negligible. Thus only thermal convection is observed. For comparison, Figures 21c and 21d show the flow patterns for liquid tin under the same thermal conditions as the lead i.e. with the temperature difference and the superheat being the same. The flow patterns are quite similar with a small difference in the flow rate. The flow rates at a 3°C temperature difference across the cell are slightly faster for the liquid lead while at a 5°C difference the flow rate for the liquid tin is slightly higher.

3.1.7. Thermal fluctuations

Many researchers have based experiments on liquid metal convection on the observation of thermal oscillations in the melt (13, 22, 26). For thermal fluctuations to occur there must be some degree of periodicity or turbulence in the melt. Steady laminar flow by its very nature cannot produce any thermal fluctuations. Cole and

Winegard (22) derived an experimental equation which predicts when temperature fluctuations should occur. They found that fluctuations would start when

$$H^3 G_L \geq 3.1 \qquad (3.1)$$

where: H = height of the liquid zone, cm.

G_L = the temperature gradient, °C / cm.

For the apparatus in the present investigation the molten zone height is 6.4 cm. so that the critical temperature gradient for turbulent flow from equation (3.1) predicts thermal oscillations at a temperature difference of 0.076°C. A great deal of thermal probing has been done in the 6.4 cm. by 6.4 cm. cell for various temperature differences and various cell positions using both the sheathed 0.5 mm. diameter thermocouple and the 0.5 mm. diameter bare bead thermocouple. The maximum temperature difference observed was 19°C across the melt which is close to the limit of the apparatus using cold water cooling. This gives a nominal temperature gradient across the melt of about 3°C / cm. At no time were any temperature fluctuations observed at any position in the melt or at any temperature difference that could be attributed to fluid flow in the melt. Referring to Figure 12b for liquid tin with a 19°C temperature difference, although the flow is of a three dimensional mode, it is still evident that the flow is not composed of any turbulence. The flow still appears laminar and does not produce thermal fluctuations.

Fluctuations were observed in the upper centimeter of the liquid zone resulting from thermal fluctuations in the argon atmosphere above the melt. The fluctuations were greatest near the surface of the liquid and disappeared at depths greater than one centimeter as observed on a full scale deflection of 0.1 millivolts over the ten inch wide temperature recorder chart which is equivalent to 0.18°C / inch of chart. Covering the open surface of the melt resulted in the fluctuations disappearing even at the melt surface.

3.2. The theoretical problem of thermal convection

3.2.1. Problem statement

The theoretical fluid system under consideration is shown in Figure 22. This system is similar to the experimental conditions for observing thermal convection in the previous sections. The left-hand vertical wall is maintained at θ_1 and the right-hand vertical wall is maintained at θ_2, such that θ_1 is less than θ_2. Both the upper and lower surfaces are assumed to be perfectly insulated. At time $t = 0$, the fluid is at temperature θ_0 such that

$$\theta_0 = \frac{\theta_2 + \theta_1}{2} \qquad (3.2)$$

The cell width is d, and the cell height is 1, and it is

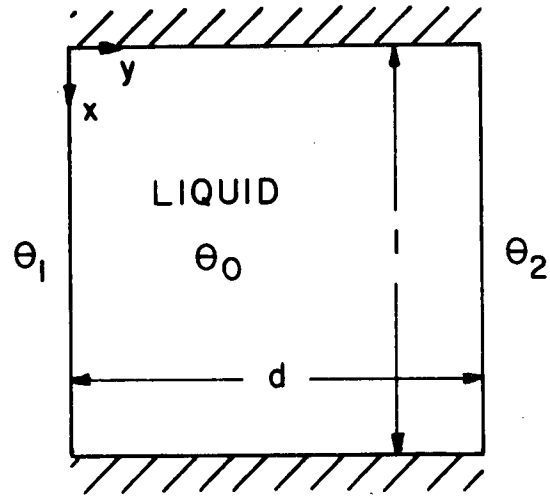

Figure 22. The theoretical fluid system to be used in the analysis of thermal convection.

assumed for theoretical considerations that the fluid is infinite in the z direction. The coordinate system is selected such that the origin is in the upper left-hand corner of the cell.

The theoretical system of Figure 22 is to be solved for liquid tin at 237°C, 260°C and 305°C for comparison with the experimental results. Table II lists the fluid properties of liquid tin at these temperatures. Also listed is the parameter Gr / ΔT for the 6.4 cm. wide cell. This parameter is only a function of the fluid properties and cell size. From the table it is seen that if temperature differences up to approximately 5°C across the cell are to be theoretically considered, the solution must hold for Prandtl numbers of the order of 10^{-2} and Grashof numbers of the order of 10^{7}. Previous analyses and solutions of the

TABLE II.

Properties of Liquid Lead and Tin

Metal	Temperature °C	Viscosity centipoise	Specific Heat cal/gm-°C	Thermal Conductivity cal/cm-sec-°C	Density gm/cm^3	Coefficient of Volume Expansion 1/°C	Kinematic Viscosity cm^2/sec	Prandtl Number	$\frac{Grashof}{\Delta T}$ 1/°C
Tin	237	2.022	0.05411	0.0798	6.9698	1.0215×10^{-4}	0.002901	0.01365	3.115×10^{6}
	260	1.880	0.05431	0.0806	6.9538	1.0239×10^{-4}	0.002704	0.01270	3.601×10^{6}
	305	1.680	0.05463	0.0809	6.9217	1.0287×10^{-4}	0.002427	0.01135	4.489×10^{6}
Lead	357	2.39	0.0384	0.0386	10.6231	1.1503×10^{-4}	0.00225	0.02378	5.842×10^{6}

present problem are not applicable to systems with such a low Prandtl and high Grashof number. Table II also lists the fluid properties of liquid lead at 357°C for comparison purposes. This theoretical system of Figure 22 will also be solved for other types of fluids such as gases and water. These results will be compared with the liquid metal results so that the difference in the flow behaviour can be analysed.

The governing equations of thermal convection to be analysed in order to obtain the flow rates and thermal profiles in the cell are as follows:

Momentum equation in the x direction:

$$\frac{\partial u}{\partial t} + u\frac{\partial u}{\partial x} + v\frac{\partial u}{\partial y} = -g\beta(\theta - \theta_0) - \frac{1}{\rho}\frac{\partial p'}{\partial x} + \nu\left(\frac{\partial^2 u}{\partial x^2} + \frac{\partial^2 u}{\partial y^2}\right) \tag{3.3}$$

Momentum equation in the y direction:

$$\frac{\partial v}{\partial t} + u\frac{\partial v}{\partial x} + v\frac{\partial v}{\partial y} = -\frac{1}{\rho}\frac{\partial p'}{\partial y} + \nu\left(\frac{\partial^2 v}{\partial x^2} + \frac{\partial^2 v}{\partial y^2}\right) \tag{3.4}$$

Energy equation:

$$\frac{\partial \theta}{\partial t} + u\frac{\partial \theta}{\partial x} + v\frac{\partial \theta}{\partial y} = \frac{k}{\rho C_p}\left(\frac{\partial^2 \theta}{\partial x^2} + \frac{\partial^2 \theta}{\partial y^2}\right) \tag{3.5}$$

Continuity equation:

$$\frac{\partial u}{\partial x} + \frac{\partial v}{\partial y} = 0 \tag{3.6}$$

All the notation is fully tabulated in Appendix I. The most important assumptions used in the derivation of the above equations are:

(a) All the fluid properties are constant, except density, ρ, which is a function of temperature.

(b) The temperature difference across the melt is small compared with $1 / \beta$.

(c) The viscous dissipation is neglected.

(d) Compressibility effects are neglected.

The boundary conditions to be used as shown in Figure 22 are as follows:

$$\begin{aligned}
&t = 0: && 0 \leq x \leq 1,\ 0 \leq y \leq d && u = v = 0,\ \theta = \theta_0 \\
&t > 0: && x = 1,\ x = 0; && u = v = 0,\ \frac{\partial \theta}{\partial x} = 0 \\
& && y = 0; && u = v = 0,\ \theta = \theta_1 \\
& && y = d; && u = v = 0,\ \theta = \theta_2
\end{aligned} \tag{3.7}$$

Three types of solutions will be presented for this problem of thermal convection in a closed system.

(a) An infinite series solution which is limited by the maximum values of the Grashof number.

(b) An integral method based on the boundary layer theory which is limited by a minimum length to height ratio of the cell.

(c) A finite difference numerical technique.

The Nusselt dimensionless parameter is also of interest in the problem of natural convection and will also be calculated. The Nusselt number is the ratio of the heat rate transferred by convection in a system to the heat rate that would be transferred by conduction in the system if no convection was allowed to occur for the same temperature difference. Therefore, a Nusselt number of unity is equivalent to conduction alone. The Nusselt is defined as:

$$Nu = \frac{hd}{k} \tag{3.8}$$

where Nu is the Nusselt number and h is the local heat transfer coefficient defined by:

$$h = \frac{-q}{\theta_2 - \theta_1} \tag{3.9}$$

where the heat transfer rate is

$$q = -k\left(\frac{\partial\theta}{\partial y}\right)_{y = 0} \tag{3.10}$$

3.2.2. Previous theoretical solutions

3.2.2.1. Solution of Batchelor (33)

The solution developed by Batchelor takes the general equations described in the previous section and by

the use of power series, obtains a solution for the flow rates. The solution uses non-dimensional forms of the governing equations by using the following dimensionless parameters:

$$X = \frac{x}{d}, \qquad Y = \frac{y}{d}$$

$$u = \frac{k}{\rho C_p d}\frac{\partial \psi}{\partial Y}, \qquad v = \frac{-k}{\rho C_p d}\frac{\partial \psi}{\partial X} \tag{3.11}$$

$$\theta' = \frac{\theta - \theta_1}{\theta_2 - \theta_1}, \qquad \alpha = \frac{k}{\rho C_p}$$

$$Ra = \frac{\left(\theta_2 - \theta_1\right) g d^3}{\theta_1 \alpha \nu}, \qquad \zeta = -\nabla^2 \psi$$

where Ψ is defined as the stream function and ζ is defined as the vorticity. Substituting the relations in (3.11) into equations (3.3), (3.4), (3.5) and (3.6) and eliminating the pressure terms in the momentum equation by differentiating (3.3) with respect to Y and (3.4) with respect to X results in:

$$\frac{1}{Pr}\left(\frac{\partial \zeta}{\partial X}\frac{\partial \psi}{\partial Y} - \frac{\partial \psi}{\partial X}\frac{\partial \zeta}{\partial Y}\right) = Ra\frac{\partial \theta'}{\partial Y} + \nabla^2 \zeta \tag{3.12}$$

$$\frac{\partial\theta'}{\partial X}\frac{\partial\psi}{\partial Y} - \frac{\partial\theta'}{\partial X}\frac{\partial\psi}{\partial Y} = \nabla^2\theta' \qquad (3.13)$$

All the time derivatives ($\partial/\partial t$) have been equated to zero since only the steady state solution is of interest. The boundary conditions in dimensionless form are:

$$\begin{aligned} &X = 0,\ X = \frac{1}{d}: && \psi = \frac{\partial\psi}{\partial Y} = 0 \\ & && \frac{\partial\theta'}{\partial X} = 0 \\ &Y = 0: && \psi = \frac{\partial\psi}{\partial Y} = 0, \quad \theta' = 0 \\ &Y = 1: && \psi = \frac{\partial\psi}{\partial Y} = 0, \quad \theta' = 0 \end{aligned} \qquad (3.14)$$

The series solution for θ' and ψ is obtained by expanding these terms in power series of the Rayleigh number as follows:

$$\theta'(X,Y) = Y + Ra\theta'_1(X,Y) + Ra^2\theta'_2(X,Y) + \cdots \qquad (3.15)$$

$$\psi(X,Y) = Ra\psi_1(X,Y) + Ra^2\psi_2(X,Y) + \cdots \qquad (3.16)$$

Substituting equations (3.15) and (3.16) into equations (3.12) and (3.14) and equating like powers of Rayleigh the

equations describing θ'_1, θ'_2, ψ_1, and ψ_2 can be obtained. For values of Rayleigh less than 10^3 and for a l / d ratio of close to unity the value of ψ_1 can be given by:

$$\psi_1 = \frac{2}{3}\left(1 + \frac{l^4}{d^4}\right)^{-1} X^2 \left(\frac{l}{d} - X\right)^2 Y^2 (1 - Y)^2 \qquad (3.17)$$

For the geometry under consideration experimentally, l / d = 1. Therefore the solution for the stream function can be written as:

$$\psi = \frac{1}{3} Ra\ X^2 (1 - X)^2 Y^2 (1 - Y)^2 \qquad (3.18)$$

The flow velocities may be obtained directly from equation (3.18) with the use of the velocity relationships in equation (3.11). The streamlines around the cell for this analysis are plotted in Figure 23a. The shape of the streamline field is independent of Rayleigh and therefore the function plotted is $\psi / Ra \times 10^4$. The streamlines represent the paths of the particles moving in a laminar fashion in the cell. Figure 23b shows the shape of the velocity profile in the X direction at a position half way down the cell (X = 0.5). Again the shape of the profile is independent of the Rayleigh number. The parameter $\frac{ud}{\alpha Ra}$ is plotted since this is only a function of the position in the cell and is given by:

$$\frac{ud}{\alpha Ra} = X^2 (1 - X)^2 [\ 2Y (1 - Y)^2 - 2Y^2 (1 - Y)\ ] \qquad (3.19)$$

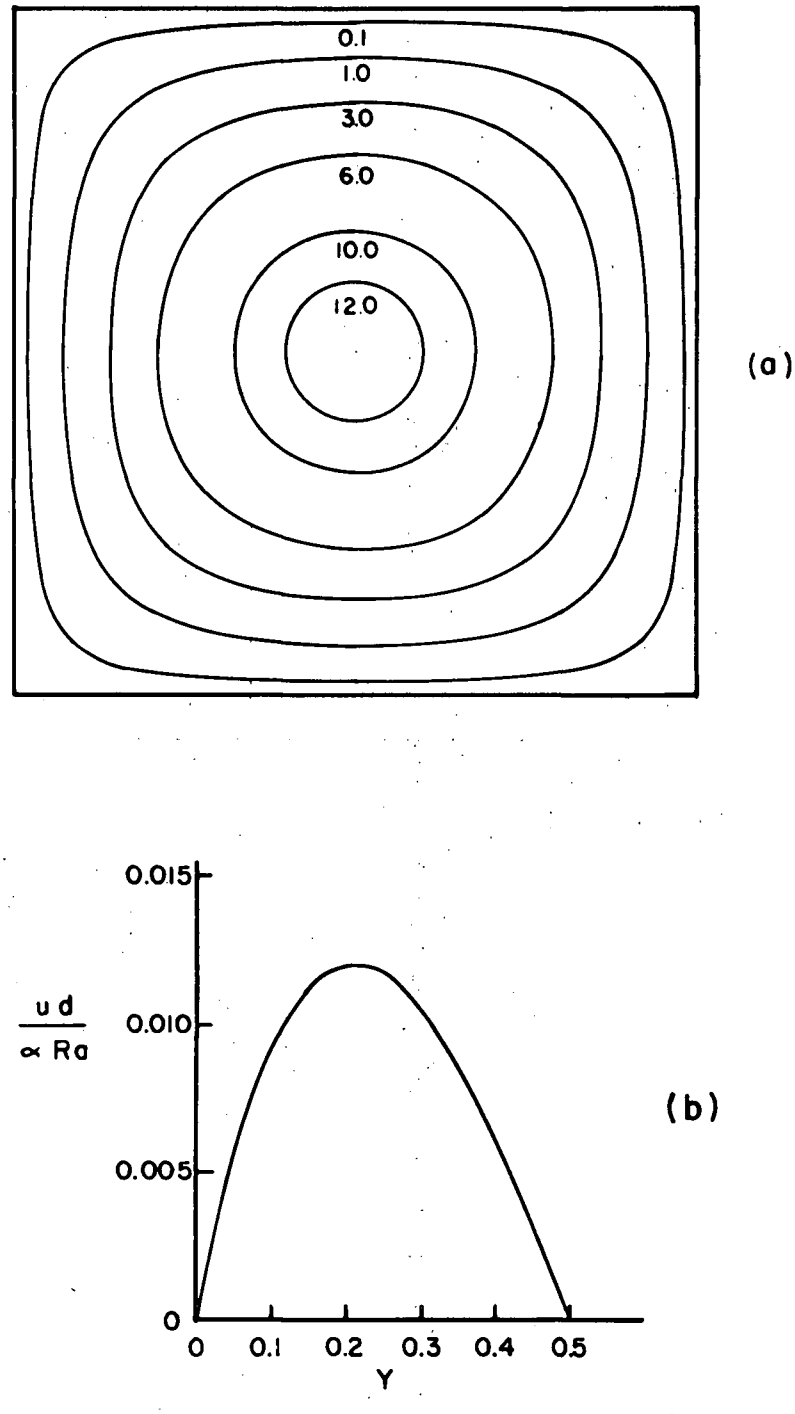

Figure 23. The solution of Batchelor for the problem of natural convection showing (a) a normalized streamfunction (ψ/ Ra) plot and (b) a normalized velocity in the X direction (ud / αRa) at a position one-half way down the liquid zone.

Figure 23b of the velocity profile shows that the maximum velocity is almost half way between the outer vertical wall and the cell centre.

The results of this analysis will be compared with other results in a following section. These results cannot be compared with the experimental results for liquid tin since the minimum temperature difference observed experimentally was 0.23°C. This temperature difference from the value of Prandtl and Gr / ΔT from Table II corresponds to a Rayleigh number of 1.1×10^4 which is an order of magnitude greater than the maximum value of Rayleigh the solution of Batchelor is valid for.

3.2.2.2. Solution of Emery and Chu (34)

The solution developed by Emery and Chu is based on a boundary layer development along each of the vertical walls as shown in Figure 24. The geometry is similar to the previous analysis and it is now assumed that there is a boundary layer of thickness, δ, for the thermal and velocity profiles along each cell side. The analysis will only apply when the boundary layers are relatively thin and they do not meet along the centre of the liquid cell. The liquid between the boundary layers is isothermal at temperature θ_∞ and the liquid velocity is zero in this region. The general boundary layer equations are developed from equations (3.3), (3.4), (3.5) and (3.6) by putting all the

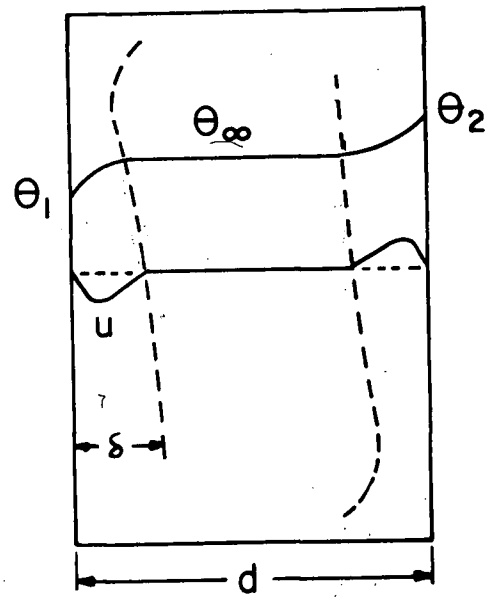

Figure 24. The boundary layer development along the vertical walls in the solution of Emery and Chu for thermal convection.

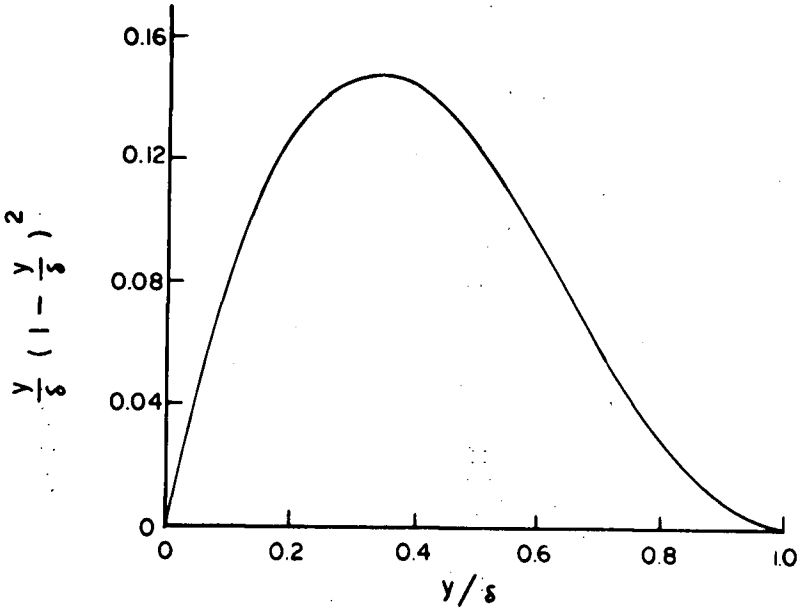

Figure 25. A normalized velocity [$y/\delta\ (1 - y/\delta)^2$] versus the position within the boundary layer from the solution of Emery and Chu.

time derivatives equal to zero and assuming v is negligible compared with u. The thermal and velocity boundary layers are assumed to be equal which is valid for a liquid metal (22). Integrating the boundary layer equations results in:

$$\frac{\partial}{\partial x}\int_0^{\delta} u^2\,dy = g\beta\int_0^{\delta}(\theta-\theta_\infty)\,dy - \nu\left.\frac{\partial u}{\partial y}\right|_{wall} \tag{3.20}$$

$$\frac{\partial}{\partial x}\int_0^{\delta} u(\theta-\theta_\infty)\,dy = -\alpha\left.\frac{\partial \theta}{\partial y}\right|_{wall} \tag{3.21}$$

The velocity and thermal profile shape in the boundary layer is assumed to be similar to those formed for a single vertical flat plate in an infinite fluid. Therefore:

$$u = u_a(x)\,\frac{y}{\delta}\left(1-\frac{y}{\delta}\right)^2 \tag{3.22}$$

$$\theta-\theta_\infty = (\theta_1-\theta_\infty)\left(1-\frac{y}{\delta}\right)^2 \tag{3.23}$$

Equations (3.22) and (3.23) are substituted in equations (3.20) and (3.21) assuming u_a, $(\theta_1-\theta_\infty)$ and δ to be exponential functions of x such that:

$$u_a(x) = C_1 x^n \tag{3.24}$$

$$\delta = C_2 x^m \tag{3.25}$$

$$\theta_1-\theta_\infty = C_3 x^\gamma \tag{3.26}$$

For the boundary conditions under consideration, θ_1 is a

constant such that $\gamma = 0$. Equating like powers of x results in values for C_1, C_2, n and m being calculated such that:

$$C_1 = \frac{240\alpha}{3C_2^2}$$

$$C_2^4 = \frac{720\alpha}{3g\beta(\theta_1 - \theta_\infty)}\left(\nu + \frac{20}{21}\alpha\right) \qquad (3.27)$$

$$n = 1/2 , \quad m = 1/4$$

Using the fluid properties of liquid tin at 260°C taken from Table II and for the 6.4 cm. wide cell this results in a velocity profile one half way up the cell of:

$$u = 0.7\,(\theta_1 - \theta_2)^{1/2}\,\frac{y}{\delta}\left(1 - \frac{y}{\delta}\right)^2 \quad \frac{cm.}{sec.} \qquad (3.28)$$

where: $$\delta = \frac{0.24}{(\theta_1 - \theta_2)^{1/4}} \text{ cm.} \qquad (3.29)$$

For example, with a 1°C temperature difference the boundary layer is 0.24 cm. thick at a point half way up the cell. The shape of the velocity profile is shown in Figure 25. The plot is of $\frac{y}{\delta}\left(1-\frac{y}{\delta}\right)^2$ versus y / δ since all temperature differences will give the same shaped profile in the boundary layer according to this analysis.

3.3. Numerical analysis of thermal convection

3.3.1. Technique of solution

The numerical analysis to be developed in this section will show the thermal profile and the flow pattern and flow rates for thermal convection in liquid metals. This analysis is based on the recent works of Wilkes (35) and Samuels and Churchill (36). The solution is based on a finite difference analysis of natural convection in the closed system described in Figure 22. The results obtained by Wilkes are not applicable to the present work since his analysis becomes unstable and breaks down at large values of the Grashof number, and his results were confined mainly to fluids with a Prandtl number of 0.733. The results of Samuels and Churchill do not apply since their solution is for a system with a vertically applied temperature difference and not a horizontal difference as in the present work.

A condensed version of the analysis will be presented in this section so that an understanding of the techniques may be obtained without the need to present all the equations required in the solution. The equations used in the computer program are all presented in Appendix II.

Equations (3.3), (3.4), (3.5), and (3.6) are put into a dimensionless form by the use of the following

dimensionless parameters.

$$X = \frac{x}{d}, \qquad Y = \frac{y}{d}, \qquad \tau = \frac{t\nu}{d^2}$$

$$U = \frac{ud}{\nu}, \qquad V = \frac{vd}{\nu}$$

$$T = \frac{\theta - \theta_0}{\theta_2 - \theta_0}, \qquad P = \frac{p'd^2}{\rho\nu^2} \tag{3.30}$$

$$\Delta\theta' = \theta_2 - \theta_0, \qquad L = \frac{l}{d}$$

$$Pr = \frac{\mu C_p}{k}, \qquad Gr' = \frac{g\beta\Delta\theta' d^3}{\nu^2}$$

Also, as in the solution of Batchelor a stream function and a vorticity function are introduced. A slightly modified Grashof is used in this calculation based on one half the temperature difference across the cell. Substituting the relationships of (3.30) into the governing equations, again eliminating the pressure terms, results in the following equations:

Vorticity equation:

$$\frac{\partial \zeta}{\partial \tau} + U\frac{\partial \zeta}{\partial X} + V\frac{\partial \zeta}{\partial Y} = Gr'\frac{\partial T}{\partial Y} + \nabla^2 \zeta \qquad (3.31)$$

Energy equation:

$$\nabla^2 \psi = -\zeta \qquad (3.33)$$

Stream function equation:

$$\frac{\partial T}{\partial \tau} + U\frac{\partial T}{\partial X} + V\frac{\partial T}{\partial Y} = \frac{1}{Pr}\nabla^2 T \qquad (3.32)$$

Velocity equation:

$$U = \frac{\partial \psi}{\partial Y}, \qquad V = -\frac{\partial \psi}{\partial X} \qquad (3.34)$$

These equations are to be solved with the following dimensionless boundary conditions:

$$\left.\begin{array}{l} \tau = 0: \quad 0 \leq X \leq L \\ \qquad\qquad 0 \leq Y \leq 1 \end{array}\right\} \quad T = 0, \ \zeta = 0 \qquad (3.35)$$

$$\tau > 0: \quad X = 0, \ X = L; \quad \psi = \frac{\partial \psi}{\partial X} = 0$$

$$\frac{\partial T}{\partial X} = 0$$

$$\tau > 0 : \quad Y = 0; \quad \psi = \frac{\partial \psi}{\partial Y} = 0, \quad T = -1$$

$$Y = 1; \quad \psi = \frac{\partial \psi}{\partial Y} = 0, \quad T = +1 \qquad (3.35)$$

The finite difference numerical technique used for the solution of the above equations is called the implicit alternating direction technique. In this method, the time step, $\Delta\tau$, over which the iteration is carried out, is split into two parts of duration $\Delta\tau$ / 2. For the first half time step, all the X direction derivatives are implicit and all the Y direction derivatives are explicit. For the second half time step the X direction derivatives are explicit and the Y direction derivatives are implicit. Explicit derivatives for any time step from τ_1 to τ_2 mean that the derivatives are calculated with the values of the parameters at the time equal to τ_1. Implicit derivatives for this time step means the values of the parameters are taken at the time equal to τ_2. Thus, for an iterative technique in which the time is progressed in steps and the parameters are calculated from their derivatives for each new time step, the explicit derivatives are known, whereas the implicit derivatives are unknown.

The grid system used in this analysis is shown in Figure 26. There are m-1 grid divisions of length ΔX

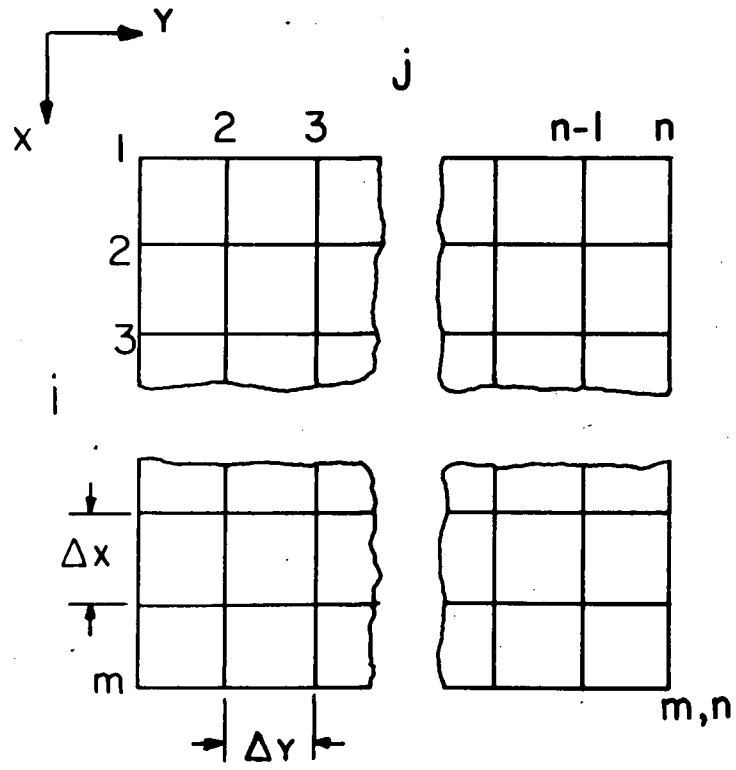

Figure 26. The finite difference grid system for the fluid cell used in the numerical analysis.

in the X direction and n-1 grid divisions of length ΔY in the Y direction. The subscripts i and j denote the position in the grid having the coordinates $X = i\Delta X$ and $Y = j\Delta Y$. In the following analysis the star superscript (*) denotes values of parameters after the end of the first half time step and the dash superscript (') denotes values of parameters after the end of the second half or total time step. The finite difference equations for the energy and vorticity equations are:

Vorticity equation for the first half time step:

$$\frac{\xi^*_{i,j} - \xi_{i,j}}{\Delta\tau/2} + U_{i,j}\,\frac{\xi^*_{i+1,j} - \xi^*_{i-1,j}}{2\Delta X} +$$

$$V_{i,j}\,\frac{\xi_{i,j+1} - \xi_{i,j-1}}{2\Delta X} = Gr'\,\frac{T'_{i,j+1} - T'_{i,j-1}}{2\Delta Y} +$$

$$\frac{\xi^*_{i-1,j} - 2\xi^*_{i,j} + \xi^*_{i+1,j}}{(\Delta X)^2} + \frac{\xi_{i,j-1} - 2\xi_{i,j} + \xi_{i,j+1}}{(\Delta Y)^2} \qquad (3.36)$$

Vorticity for the second half time step:

$$\frac{\xi'_{i,j} - \xi^*_{i,j}}{\Delta\tau/2} + U_{i,j}\,\frac{\xi^*_{i+1,j} - \xi^*_{i-1,j}}{2\Delta X} +$$

$$V_{i,j}\,\frac{\xi'_{i,j+1} - \xi'_{i,j-1}}{2\Delta Y} = Gr'\,\frac{T'_{i,j+1} - T'_{i,j-1}}{2\Delta Y} +$$

$$\frac{\xi^*_{i-1,j} - 2\xi^*_{i,j} + \xi^*_{i+1,j}}{(\Delta X)^2} + \frac{\xi'_{i,j-1} - 2\xi'_{i,j} + \xi'_{i,j+1}}{(\Delta Y)^2}$$

(3.37)

Energy equation for the first half time step:

$$\frac{T^*_{i,j} - T_{i,j}}{\Delta\tau/2} + U_{i,j}\,\frac{T^*_{i+1,j} - T^*_{i-1,j}}{2\Delta X} + V_{i,j}\,\frac{T_{i,j+1} - T_{i,j-1}}{2\Delta Y} =$$

$$\frac{1}{Pr}\,\frac{T^*_{i-1,j} - 2T^*_{i,j} + T^*_{i+1,j}}{(\Delta X)^2} + \frac{1}{Pr}\,\frac{T_{i,j-1} - 2T_{i,j} + T_{i,j+1}}{(\Delta Y)^2}$$

(3.38)

Energy equation for the second half time step:

$$\frac{T'_{i,j} - T^*_{i,j}}{\Delta\tau/2} + U_{i,j}\frac{T^*_{i+1,j} - T^*_{i-1,j}}{2\Delta X} + V_{i,j}\frac{T'_{i,j+1} - T'_{i,j-1}}{2\Delta Y}$$

$$= \frac{1}{Pr}\frac{T^*_{i-1,j} - 2T^*_{i,j} + T^*_{i+1,j}}{(\Delta X)^2} + \frac{1}{Pr}\frac{T'_{i,j-1} - 2T'_{i,j} + T'_{i,j+1}}{(\Delta Y)^2} \qquad (3.39)$$

The velocities at points not adjacent to the walls are calculated by equations of the form:

$$U_{i,j} = \left(\frac{\partial\psi}{\partial Y}\right)_{i,j} = \frac{\psi_{i,j-2} - 8\psi_{i,j-1} + 8\psi_{i,j+1} - \psi_{i,j+2}}{12\Delta Y} \qquad (3.40)$$

A slightly different approximation is used for the points adjacent to the boundary, such as for the points just beside the cold wall:

$$U_{i,2} = \frac{-3\psi_{i,2} + 6\psi_{i,3} - \psi_{i,4}}{6\Delta Y} \qquad (3.41)$$

To solve for the stream function equation (3.33) is converted from a steady state to an unsteady state problem and the implicit alternating direction technique is applied. This is the method used by Samuels and Churchill. Equation (3.33) then becomes:

$$\zeta^{n+1} + \nabla^2\psi^{n+1} = \frac{\partial\psi^{n+1}}{\partial\tau'} \qquad (3.42)$$

where n+1 refers to the n+1 iteration in τ'. The numerical integration is continued until the stream function is

negligible. The finite difference forms are for the first half time step

$$\frac{\psi^*_{i,j} - \psi_{i,j}}{\Delta\tau'/2} = \zeta_{i,j} + \frac{\psi^*_{i-1,j} - 2\psi^*_{i,j} + \psi^*_{i+1,j}}{(\Delta X)^2}$$

$$+ \frac{\psi_{i,j-1} - 2\psi_{i,j} + \psi_{i,j+1}}{(\Delta Y)^2} \qquad (3.43)$$

and for the second half time step

$$\frac{\psi'_{i,j} - \psi^*_{i,j}}{\Delta\tau'/2} = \zeta_{i,j} + \frac{\psi^*_{i-1,j} - 2\psi^*_{i,j} + \psi^*_{i+1,j}}{(\Delta X)^2}$$

$$+ \frac{\psi'_{i,j-1} - 2\psi'_{i,j} + \psi'_{i,j+1}}{(\Delta Y)^2} \qquad (3.44)$$

The equations of vorticity only apply to interior grid points since if equation (3.36) is applied to the cold wall, for example, parameters such as $\zeta_{i,0}$ are indeterminate since they are outside the cell. Thus, equations of the form

$$\zeta_{i,1} = -\frac{2\psi_{i,2}}{(\Delta Y)^2} \qquad (3.45)$$

are used. Wilkes uses a higher order approximation of the form

$$\zeta_{i,1} = -\left[\frac{8\psi_{i,2} - \psi_{i,3}}{2(\Delta Y)^2}\right] \qquad (3.46)$$

but serious problems arise with the use of it for large Grashof numbers. This is due to the rapid increase in stream function values causing a sign change in the vorticity with equation (3.46).

It is advantageous to also solve for the local Nusselt number. Non-dimensionalizing equation (3.10) gives:

$$q = -\frac{k}{d}(\theta_2 - \theta_0)\left(\frac{\partial T}{\partial Y}\right)_{Y=0} \qquad (3.47)$$

Substituting equation (3.9) and (3.47) into equation (3.8) results in

$$Nu = \frac{1}{2}\left(\frac{\partial T}{\partial Y}\right)_{Y=0} \qquad (3.48)$$

which is readily solved for after the temperature profile is known.

The procedure for the solution of the overall problem can be summarized as follows:

(a) The new temperatures are computed for the n+1 time step.

(b) The new interior vorticities are computed for the n+1 time step from the new temperatures.

(c) The new stream function for the n+1 time step is calculated from the new interior vorticities.

(d) The new velocities are computed for the n+1 time step.

(e) The new boundary vorticities are computed for the n+1 time step.

(f) The new local Nusselt number and the average Nusselt number are calculated from the new temperatures. The above procedure is repeated until a steady state solution is obtained.

The method of actually solving for the temperature, vorticity and stream functions for the individual rows and columns is described fully in the appendix. The method essentially consists of writing an equation for each point in the column or row of immediate interest from the equations derived for the various parameters, T, ξ, and ψ. For each row or column a set of n-1 equations are obtained in the form:

$$\begin{aligned}
b_1 s_1 + c_1 s_2 &= d_1 \\
a_2 s_1 + b_2 s_2 + c_2 s_3 &= d_2 \\
a_3 s_2 + b_3 s_3 + c_3 s_4 &= d_3 \\
&\cdots\cdots\cdots\cdots \\
a_{n-2} s_{n-3} + b_{n-2} s_{n-2} + c_{n-2} s_{n-1} &= d_{n-2} \\
a_{n-1} s_{n-2} + b_{n-1} s_{n-1} &= d_{n-1}
\end{aligned} \tag{3.49}$$

for which a solution for s is available knowing all the values of the a, b, c and d coefficients. For each set of equations s will represent T, ξ, or ψ. The computer program used in this analysis is shown in Appendix III.

TABLE III.

Computer Runs Conducted

Run Number	Prandtl Number	Grashof Number Gr'	Grid Size	Temperature Difference	Average Temperature
1	0.0127	10^3	11 x 11	0.000555	260
2	0.0127	10^4	11 x 11	0.00555	260
3	0.0127	10^5	11 x 11	0.0555	260
4	0.0127	10^6	21 x 21	0.555	260
5	0.0127	10^7	31 x 31	5.55	260
6	0.01365	10^6	21 x 21	0.642	237
7	0.01365	0.865×10^6	21 x 21	0.555	237
8	0.01135	10^6	21 x 21	0.446	305
9	0.01135	1.247×10^6	21 x 21	0.555	305
10	0.733	10^4	11 x 11	-	-
11	0.1	10^3	21 x 21	-	-
12	0.1	10^4	21 x 21	-	-
13	0.1	10^5	21 x 21	-	-
14	0.1	10^6	21 x 21	-	-
15	1.0	10^3	21 x 21	-	-
16	1.0	10^4	21 x 21	-	-
17	1.0	10^5	21 x 21	-	-
18	10.0	10^3	21 x 21	-	-
19	10.0	10^4	21 x 21	-	-
20	10.0	10^5	21 x 21	-	-

The program is written in Fortran IV language and was run on an IBM/360 model 67 computer at the University of British Columbia. Twenty runs of the program were conducted for various values of the Grashof and Prandtl numbers. The various run parameters are listed in Table III. The runs for Prandtl equal to 0.0127, 0.01365 and 0.01135 correspond to liquid tin at the three different superheats and the corresponding temperature differences are also listed for each Grashof number. The printout of the computation results consists of five m by n matrices for each of T, ψ, U, V and ξ and also the local Nusselt number for each grid point along the cold wall plus the average Nusselt number.

3.3.2. Results of numerical analysis

The temperature matrix and the stream function matrix from the computer printout were converted into isothermal plots and streamline plots for visual interpretation. The thermal results will be presented first.

The thermal profile results were found to be dependent on the Rayleigh number only, and not on the Grashof and Prandtl numbers independently. The non-dimensional isothermal plots are shown in Figure 27a - 27f for Rayleigh numbers of 2×10, 2×10^2, 2×10^3, 2×10^4, 2×10^5 and 2×10^6 respectively. Each plot consists of seven isotherms within the liquid cell. The vertical left side is the

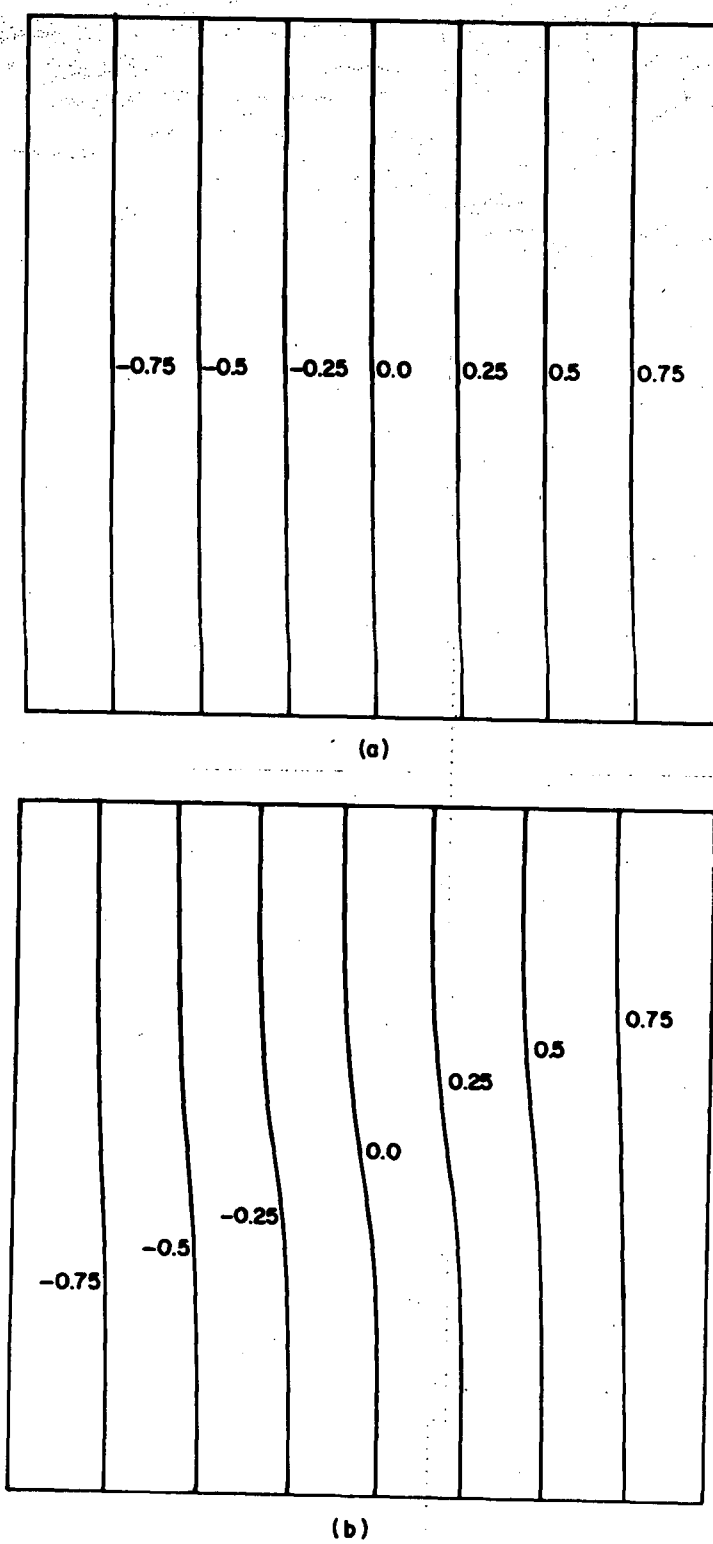

Figure 27. The theoretical plots of the nondimensional temperature, T, for a Rayleigh number of (a) 2 x 10, (b) 2 x 10^2.

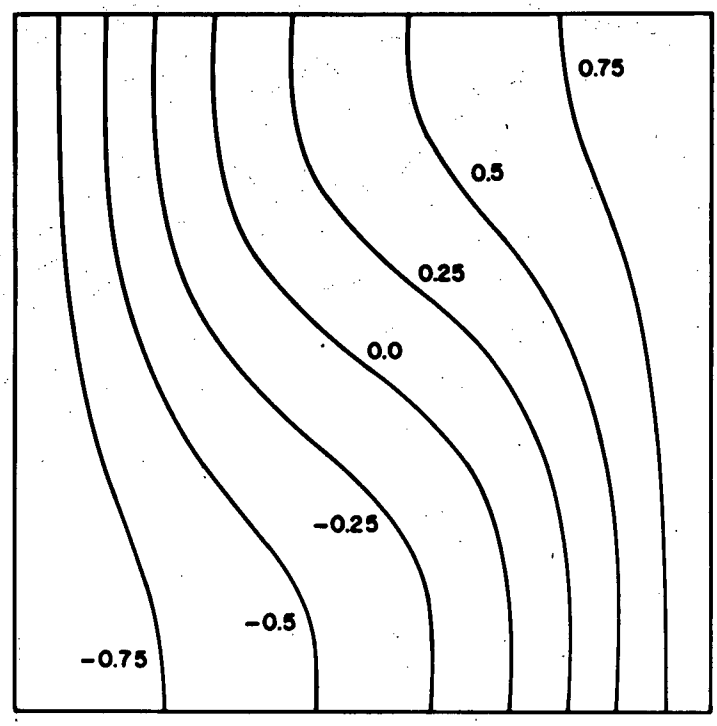

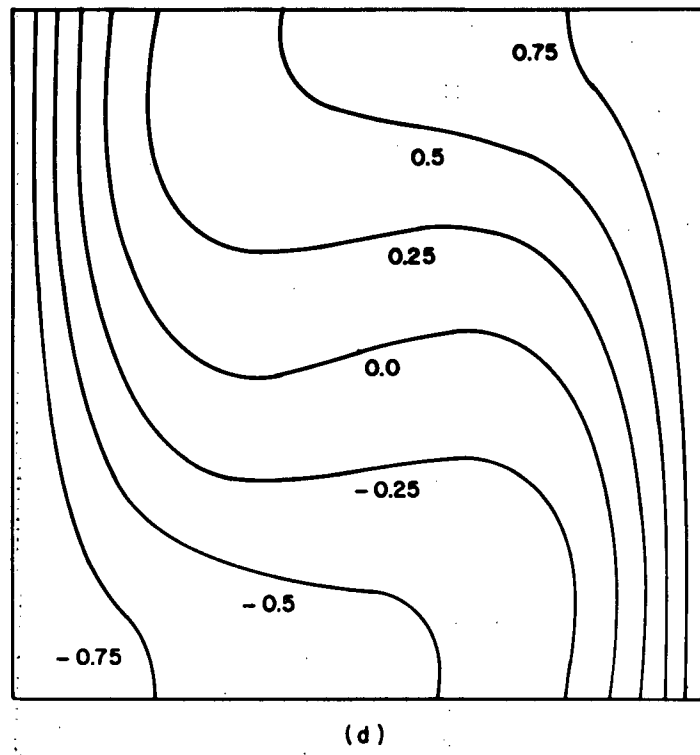

Figure 27 continued. The theoretical plots of the nondimensional temperature, T, for a Rayleigh number of (c) 2×10^3, (d) 2×10^4.

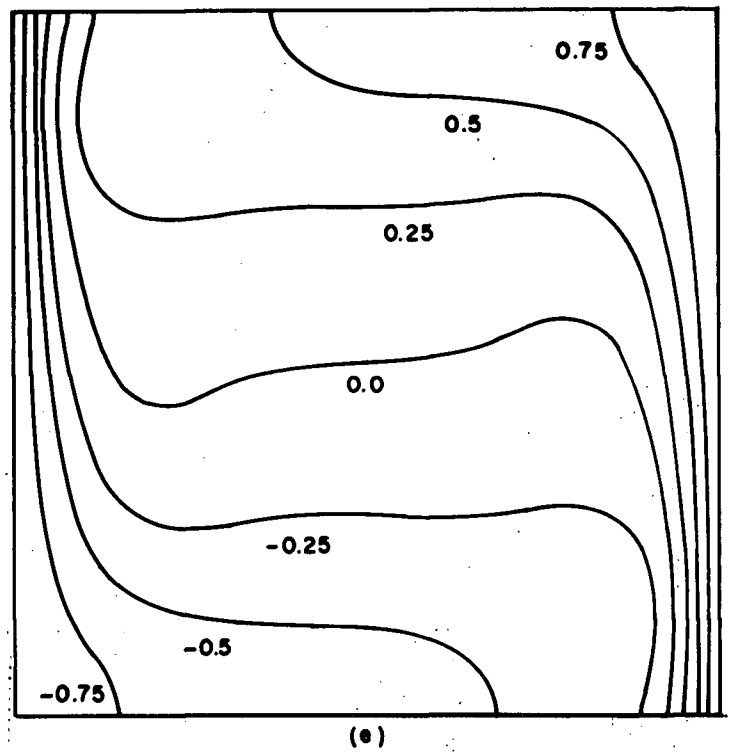

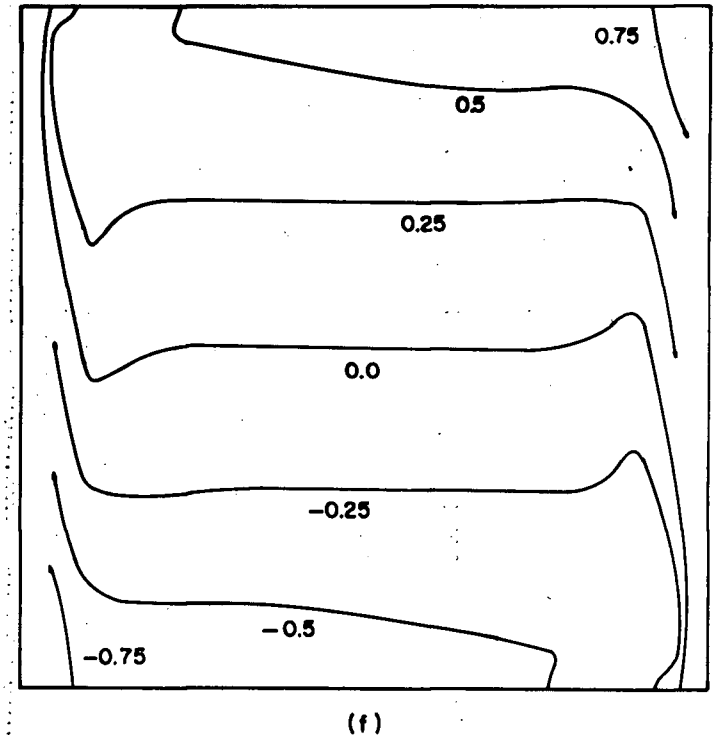

Figure 27 continued. The theoretical plots of the nondimensional temperature, T, for a Rayleigh number of (e) 2 x 10^5, (f) 2 x 10^6.

TABLE IV.

Equivalent Rayleigh and Grashof Numbers

Corresponding to Figure 27

Rayleigh Number	Profile in Figure 27	Prandtl Number	Grashof Number
2×10	27a	0.01	2×10^3
		0.1	2×10^2
		1.0	2×10
		10.0	2
2×10^2	27b	0.01	2×10^4
		0.1	2×10^3
		1.0	2×10^2
		10.0	2×10
2×10^3	27c	0.01	2×10^5
		0.1	2×10^4
		1.0	2×10^3
		10.0	2×10^2
2×10^4	27d	0.01	2×10^6
		0.1	2×10^5
		1.0	2×10^4
		10.0	2×10^3
2×10^5	27e	0.01	2×10^7
		0.1	2×10^6
		1.0	2×10^5
		10.0	2×10^4
2×10^6	27f	0.01	2×10^8
		0.1	2×10^7
		1.0	2×10^6
		10.0	2×10^5

- 1.0 isotherm and the vertical right side is the + 1.0 isotherm. Table IV tabulates the equivalent Rayleigh and Grashof numbers for the various Prandtl numbers and gives the corresponding plot in Figure 27. The progressive increase in the bending of the isotherms is obvious as the Rayleigh number increases. The average Nusselt number is plotted against the Rayleigh number in Figure 28. This plot shows that up to a value of the Rayleigh of approximately 10^3, the heat transfer is essentially all by conduction, with convection playing a very small role. This is also seen in Figure 27 where below a Rayleigh of about 10^3 the isotherms are vertical lines as in conduction heat transfer. For comparison of the various types of fluids, Figure 29 shows the average Nusselt number plotted against the Grashof number for the various Prandtl numbers. It is seen that the lower the Prandtl number, the higher the Grashof number required to cause convective heat transfer. The change in the local Nusselt number with changing Rayleigh number is seen in Figure 30. For low Rayleigh numbers the nusselt is fairly constant down the length of the wall, while at large Rayleigh numbers a peak occurs in the local Nusselt number towards the top of the cell.

The streamline plots corresponding to liquid tin at 260°C are shown in Figure 31. The plots correspond to Grashof numbers of 2×10^3, 2×10^4, 2×10^5, 2×10^6 and 2×10^7 and are drawn with the purpose of showing the

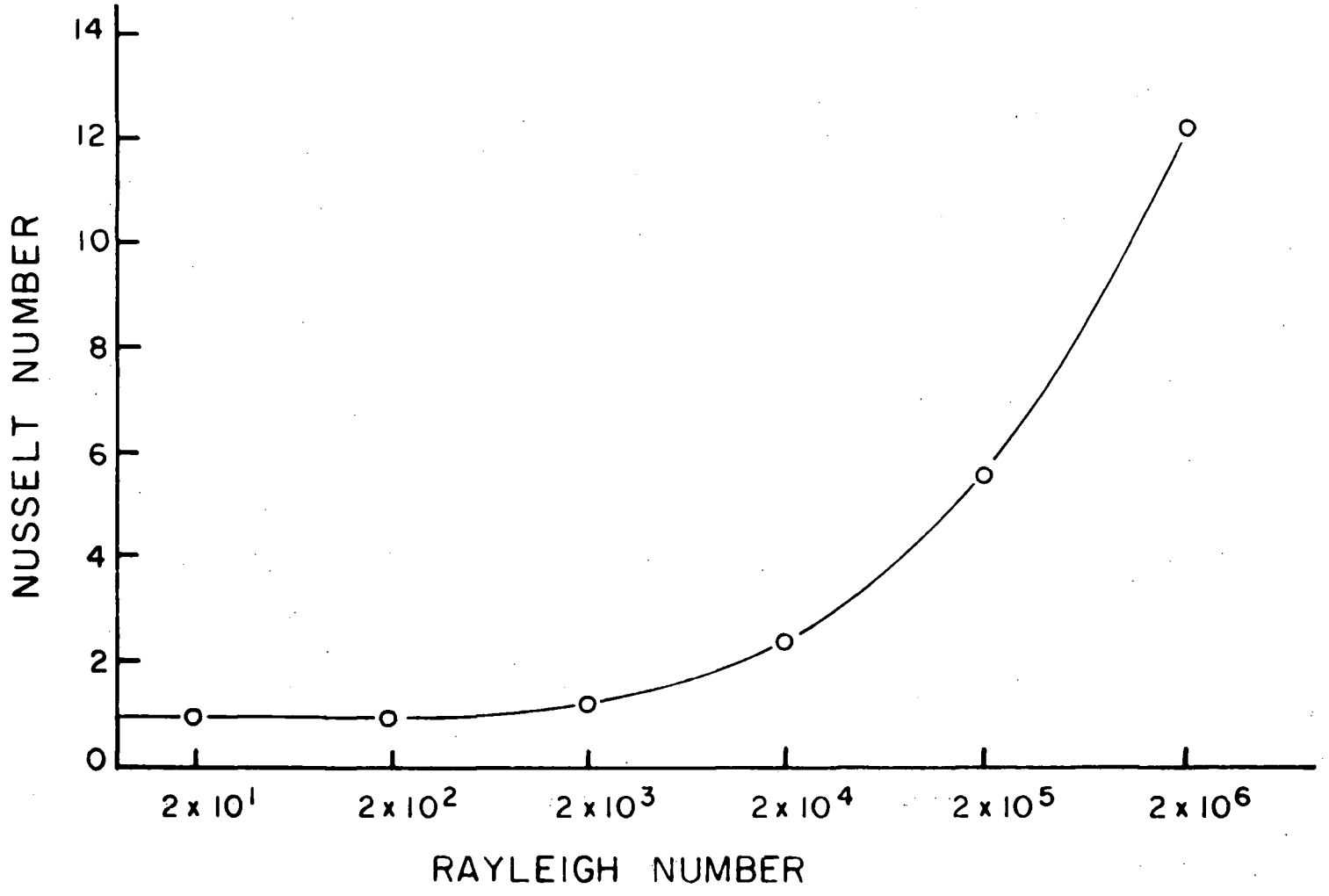

Figure 28. A plot of the theoretical average Nusselt number versus the Rayleigh number.

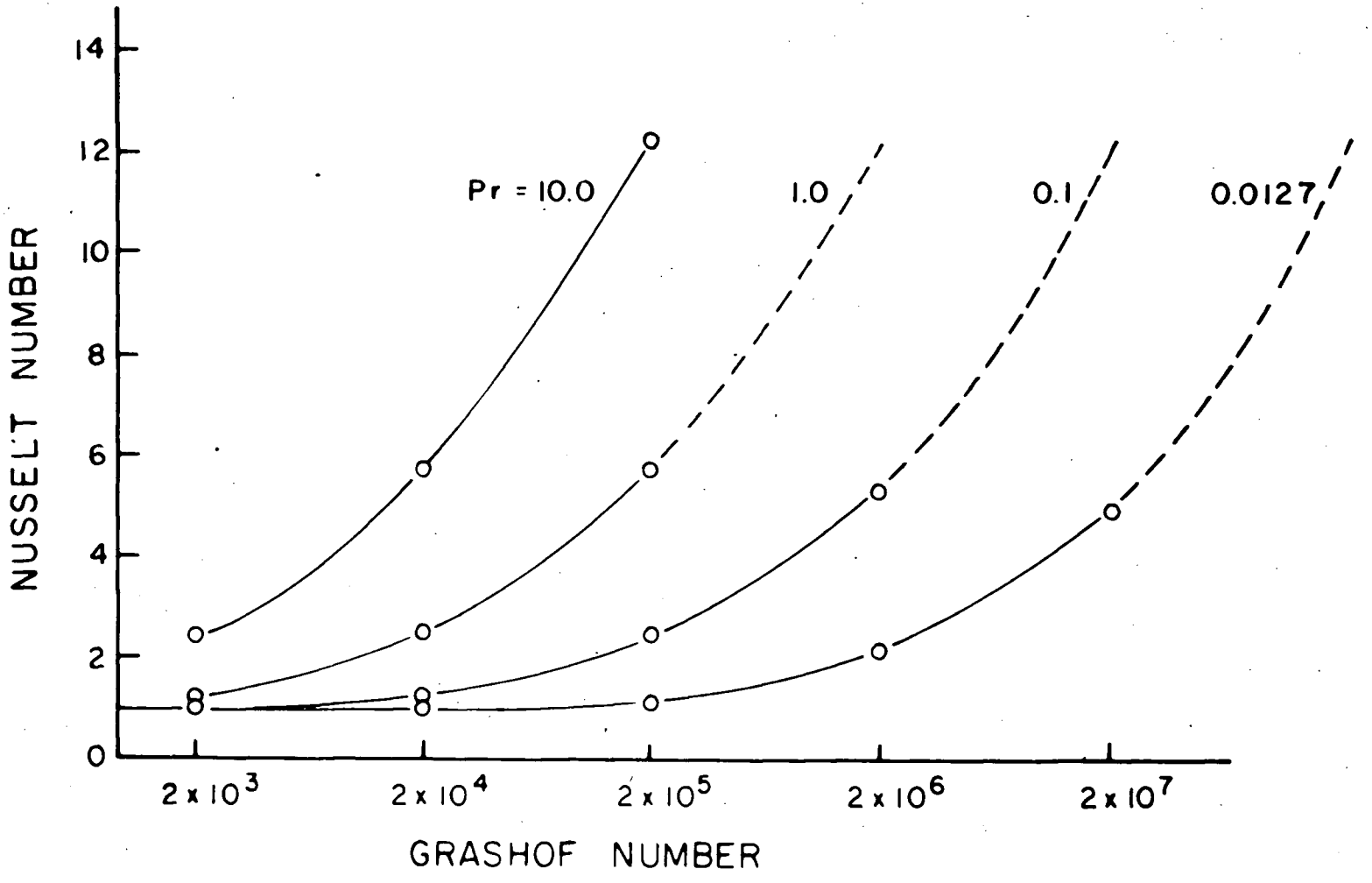

Figure 29. A plot of the theoretical average Nusselt number versus the Grashof number for Prandtl numbers of 10.0, 1.0, 0.1, and 0.0127.

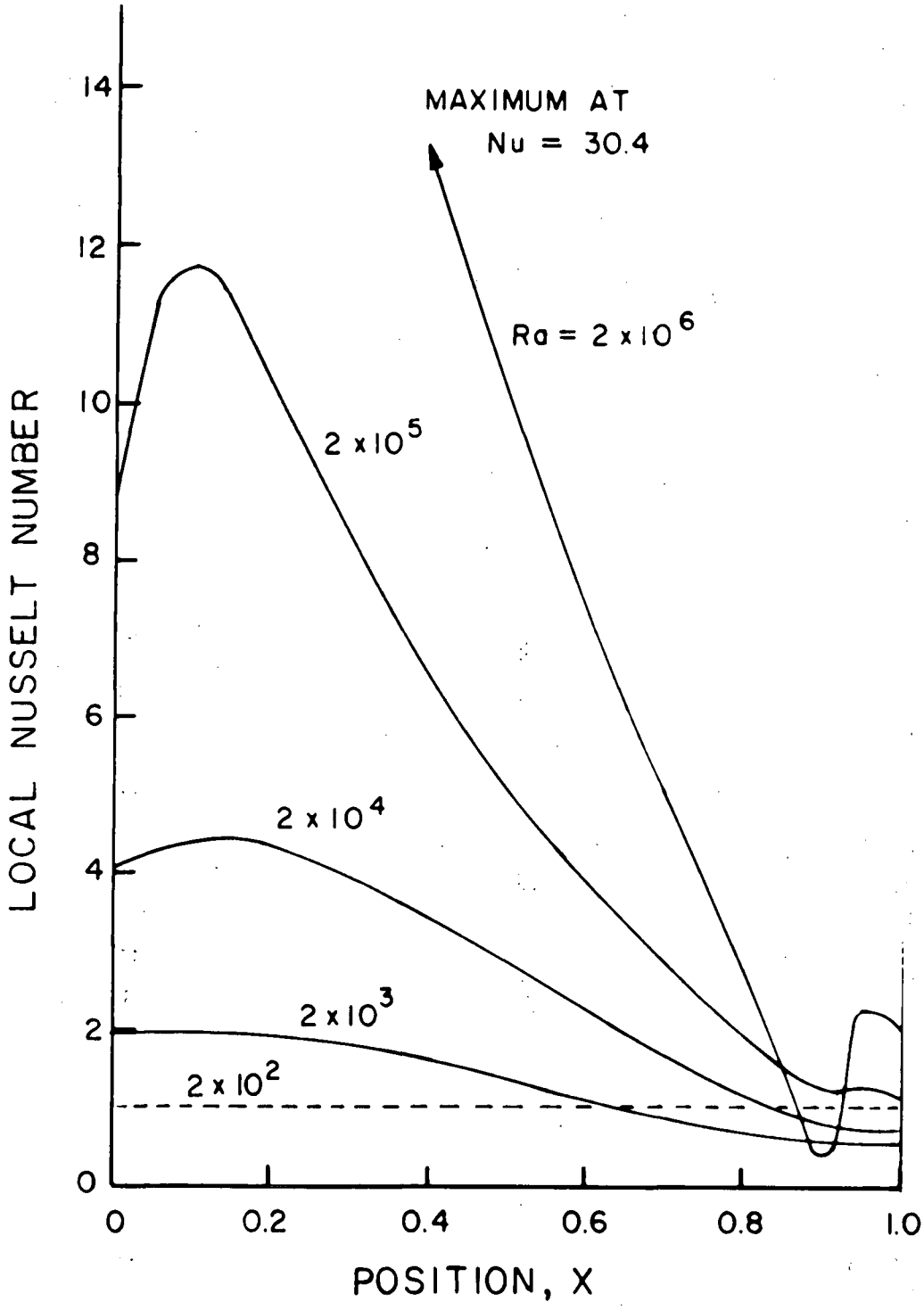

Figure 30. A plot of the local Nusselt number versus the position along the cold end wall, X, for Rayleigh numbers of 2×10^2, 2×10^3, 2×10^4, 2×10^5, and 2×10^6.

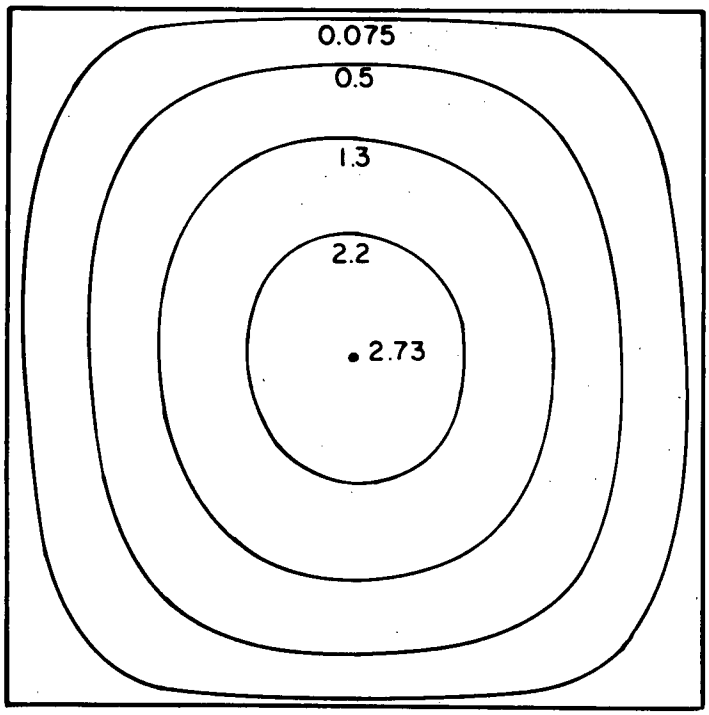

(a)

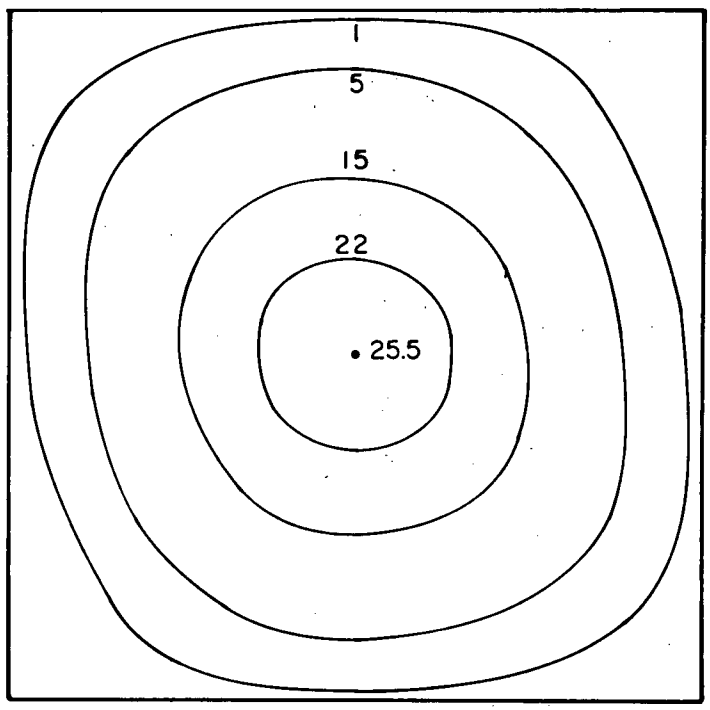

(b)

Figure 31. The theoretical stream function for liquid tin at 260°C (Prandtl = 0.0127) with a Grashof number of (a) 2×10^3, (b) 2×10^4.

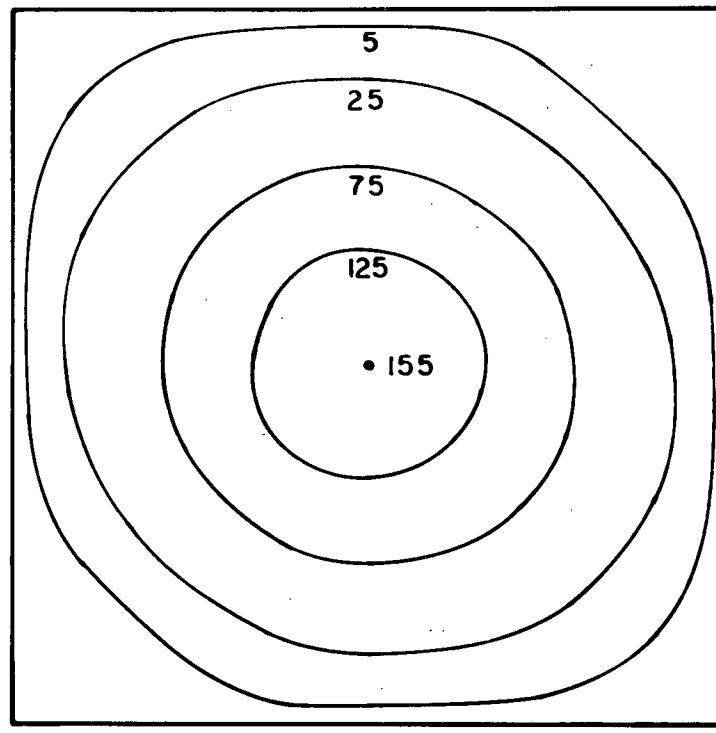

(c)

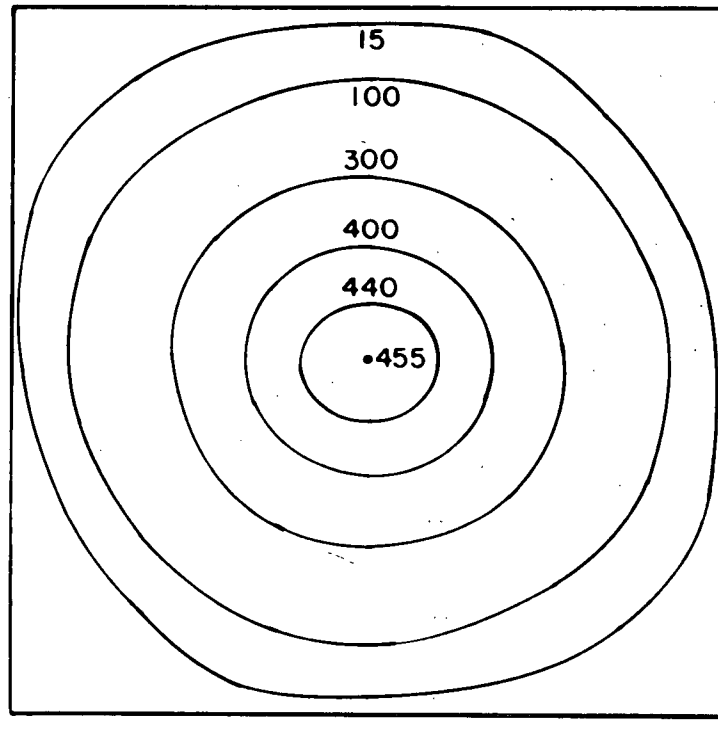

(d)

Figure 31 continued. The theoretical stream function for liquid tin at 260°C (Pr = 0.0127) with a Grashof number of (c) 2 x 10^5, (d) 2 x 10^6.

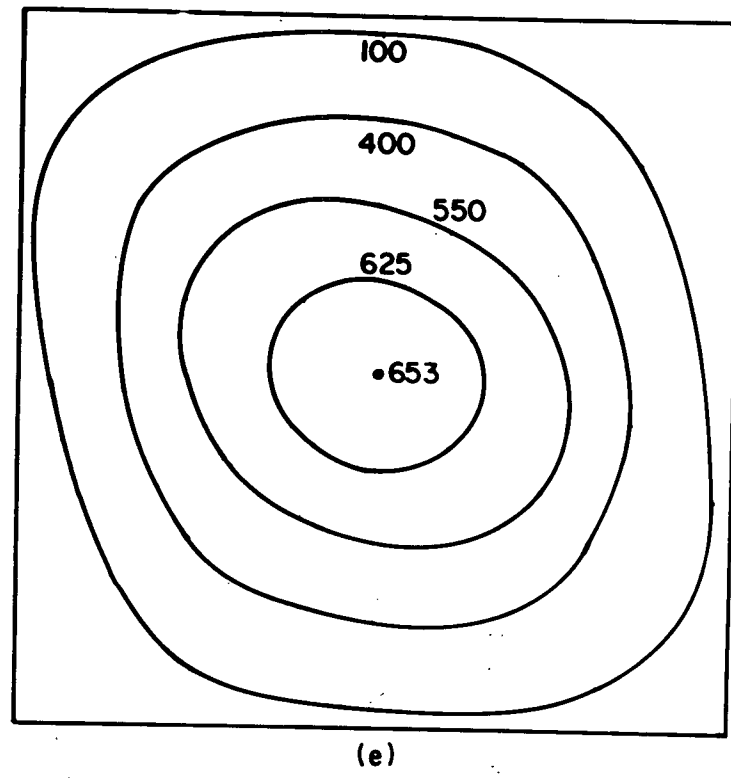

Figure 31 continued. The theoretical stream function for liquid tin at 260°C (Pr = 0.0127) with a Grashof number of (e) 2 x 10^7.

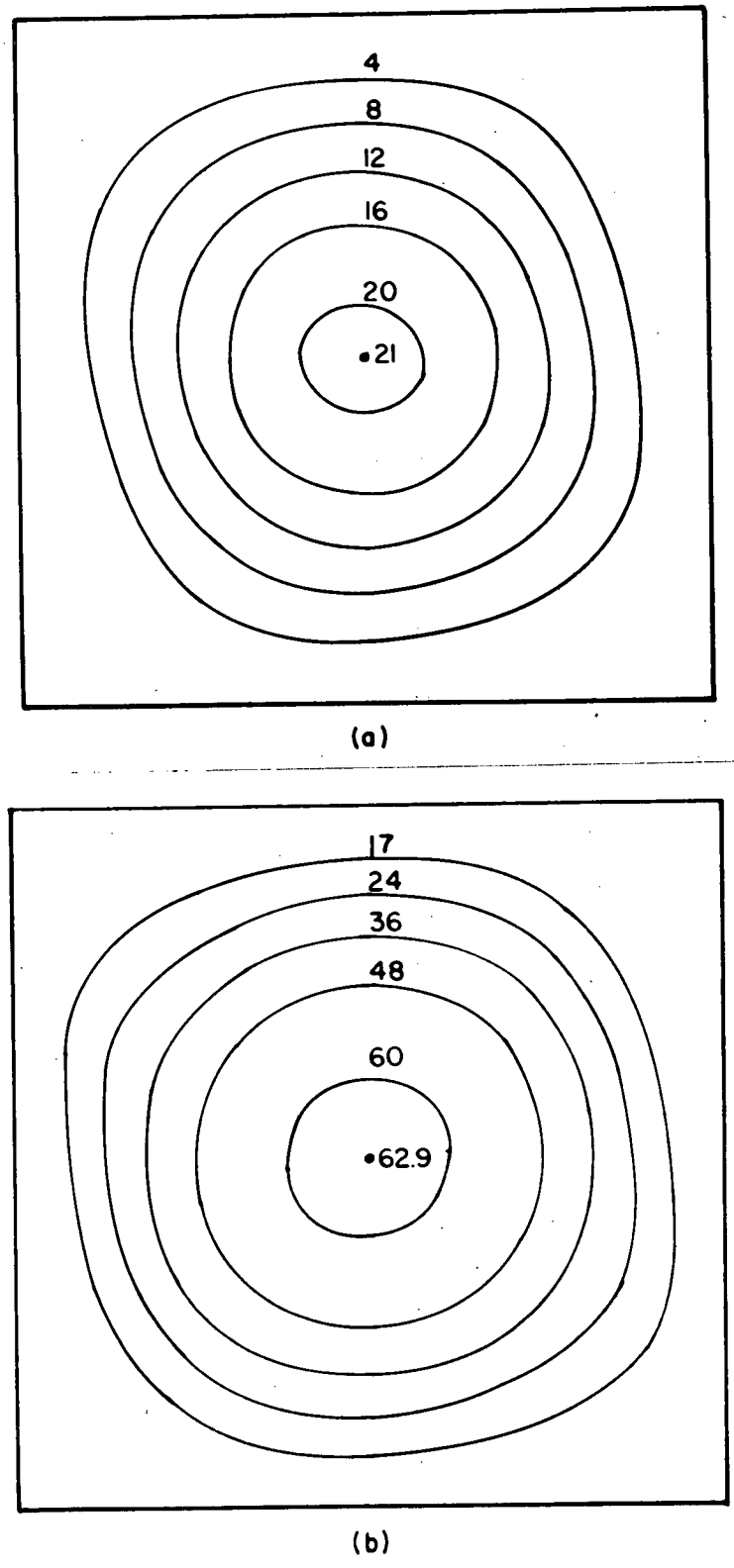

Figure 32. The theoretical stream function for a Prandtl number of 0.1 with a Grashof number of (a) 2×10^4 and (b) 2×10^5.

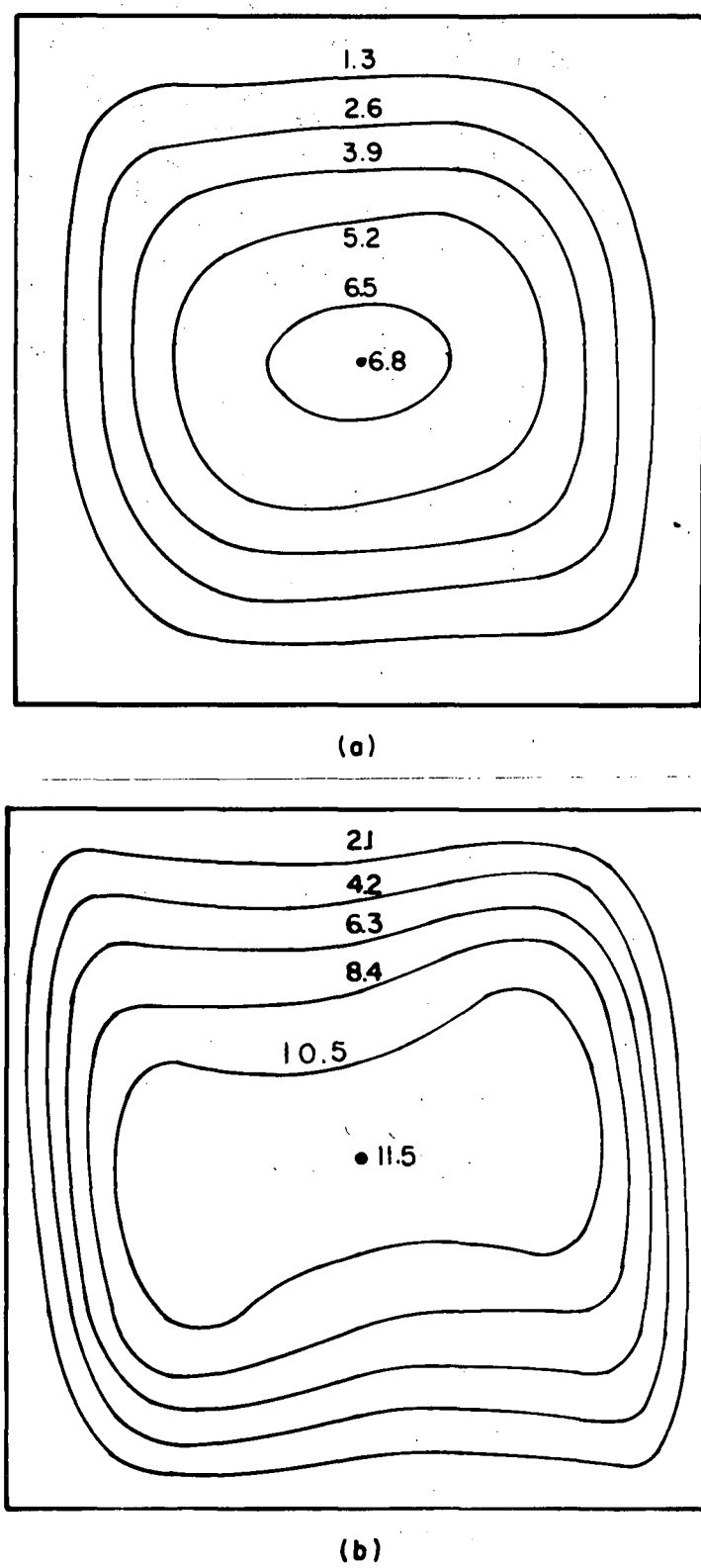

Figure 33. The theoretical stream function for a Prandtl number of 1.0 with a Grashof number of (a) 2×10^4 and (b) 2×10^5.

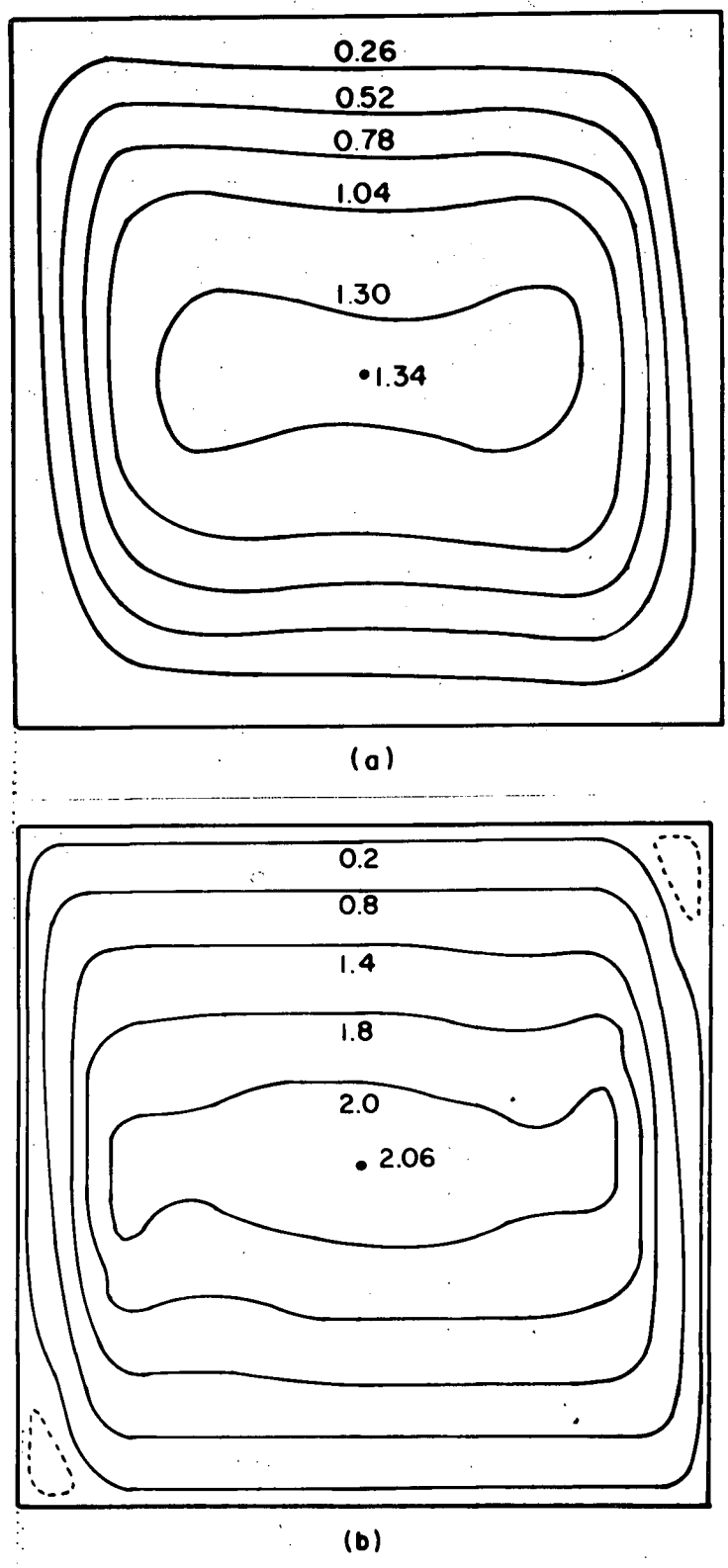

Figure 34. The theoretical stream function for a Prandtl number of 10.0 with a Grashof number of (a) 2×10^4 and (b) 2×10^5.

shape of the flow in the cell. Therefore, the increments between the streamlines are not equal and the spacing does not represent velocity as is normal in plots of this type. Figures 32, 33 and 34 show the streamlines for the Prandtl number equal to 0.1, 1.0 and 10.0 respectively for a Grashof number of 2×10^4 and 2×10^5. A comparison of Figures 31 through 34 shows the change in shape of the flow pattern by changing the Prandtl number. Figure 35 shows the shape of the velocity profile, U, at a position half way down the cell, X = 0.5, in the X direction. Each of the plots in Figure 35 are for a different Prandtl number and it should be noted that the vertical scale on each plot is very different. The smaller the Prandtl number, the greater is the dimensionless flow velocities for a given Grashof number. All the various types of fluids behave in the same general way as the Grashof number is increased. As the Grashof number increases the peak in the velocity profile shifts towards the cell wall.

A scale of actual velocities is also included on the plots in Figure 35. From equation (3.30) the actual velocity is given by:

$$u = \frac{U\nu}{d} \qquad (3.30)$$

If a value of the kinematic viscosity, ν, and cell size, d, is chosen then the dimensional velocity, u, may be computed. Values of the kinematic viscosity for each value

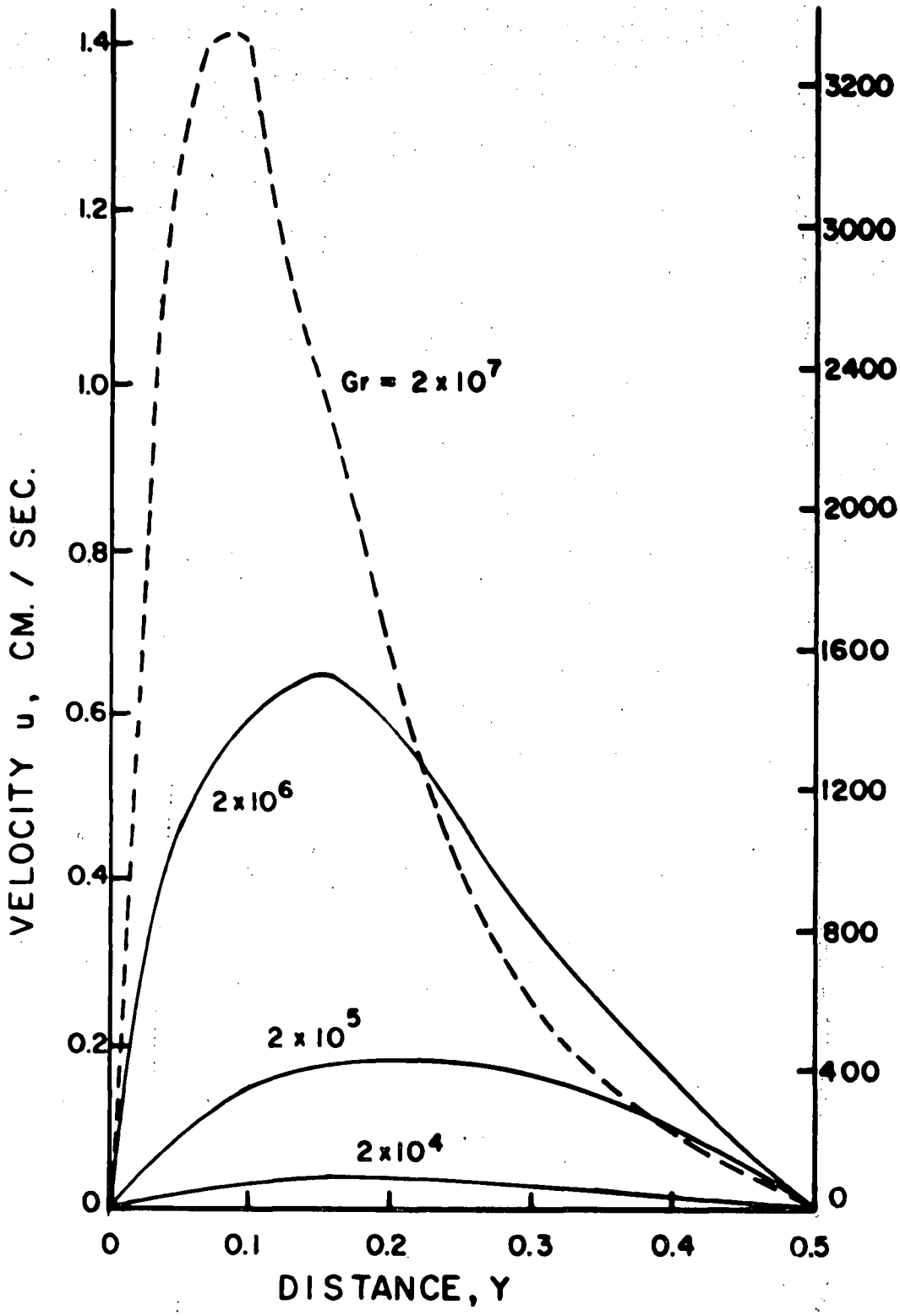

Figure 35a. The theoretical flow velocity (u and U) at a position X = 0.5 for various values of the Grashof number for liquid tin at 260°C (Pr = 0.0127).

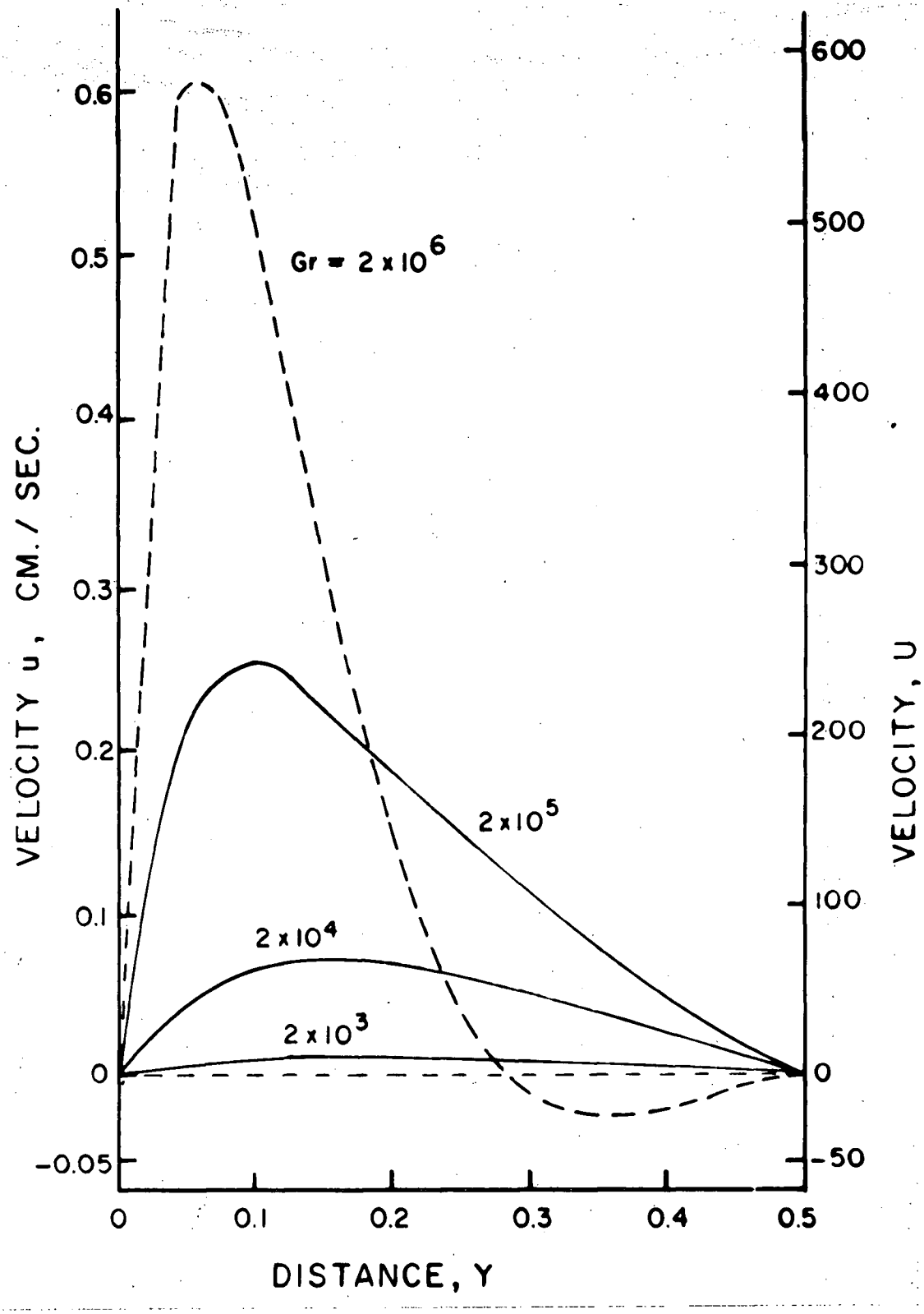

Figure 35b. The theoretical flow velocity (u and U) at a position X = 0.5 for various values of the Grashof number for Pr = 0.1 and assuming NaCl properties to calculate u.

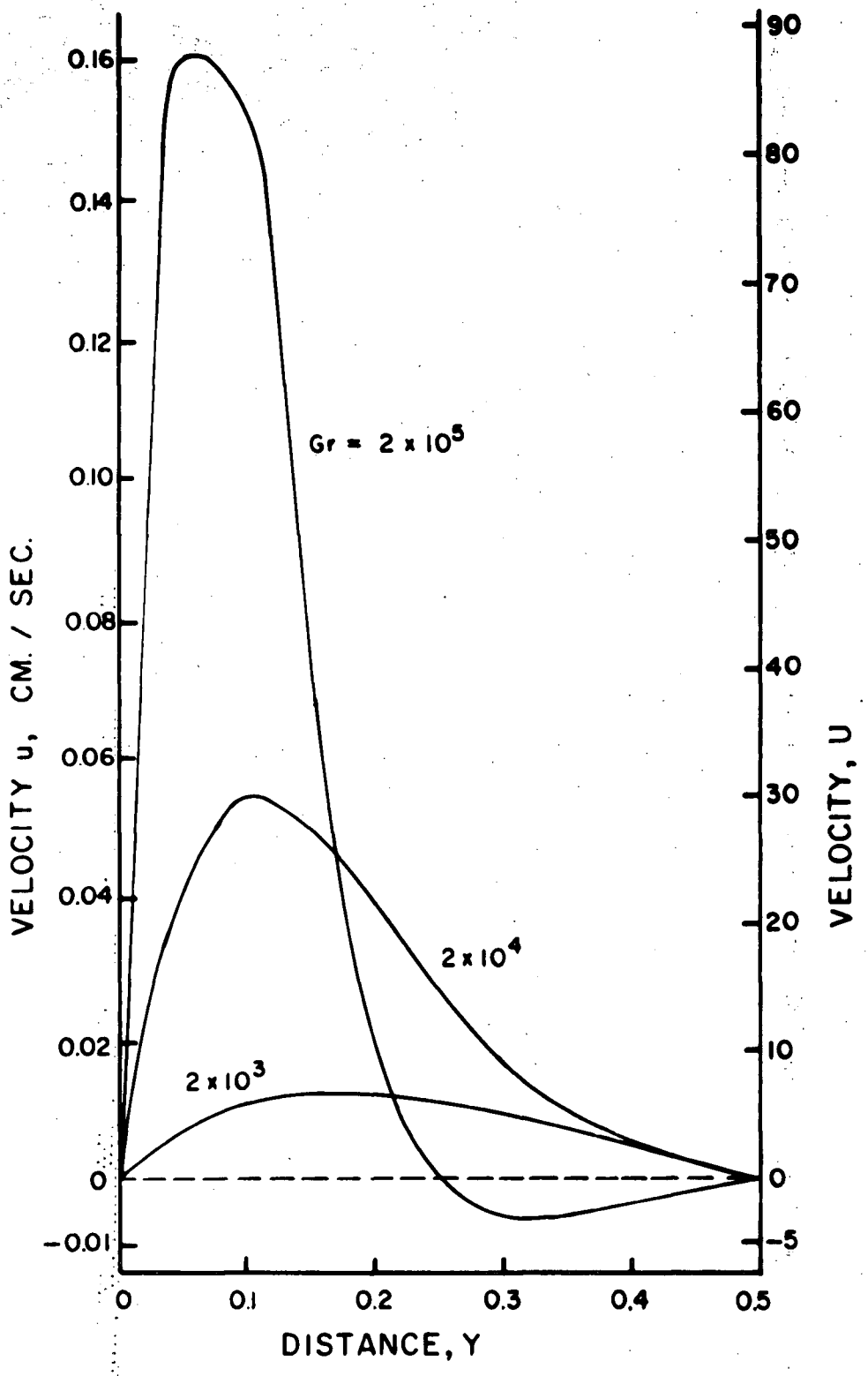

Figure 35c. The theoretical flow velocity (u and U) at a position X = 0.5 for various values of the Grashof number for Pr = 1.0 and assuming NH_3 properties to calculate u.

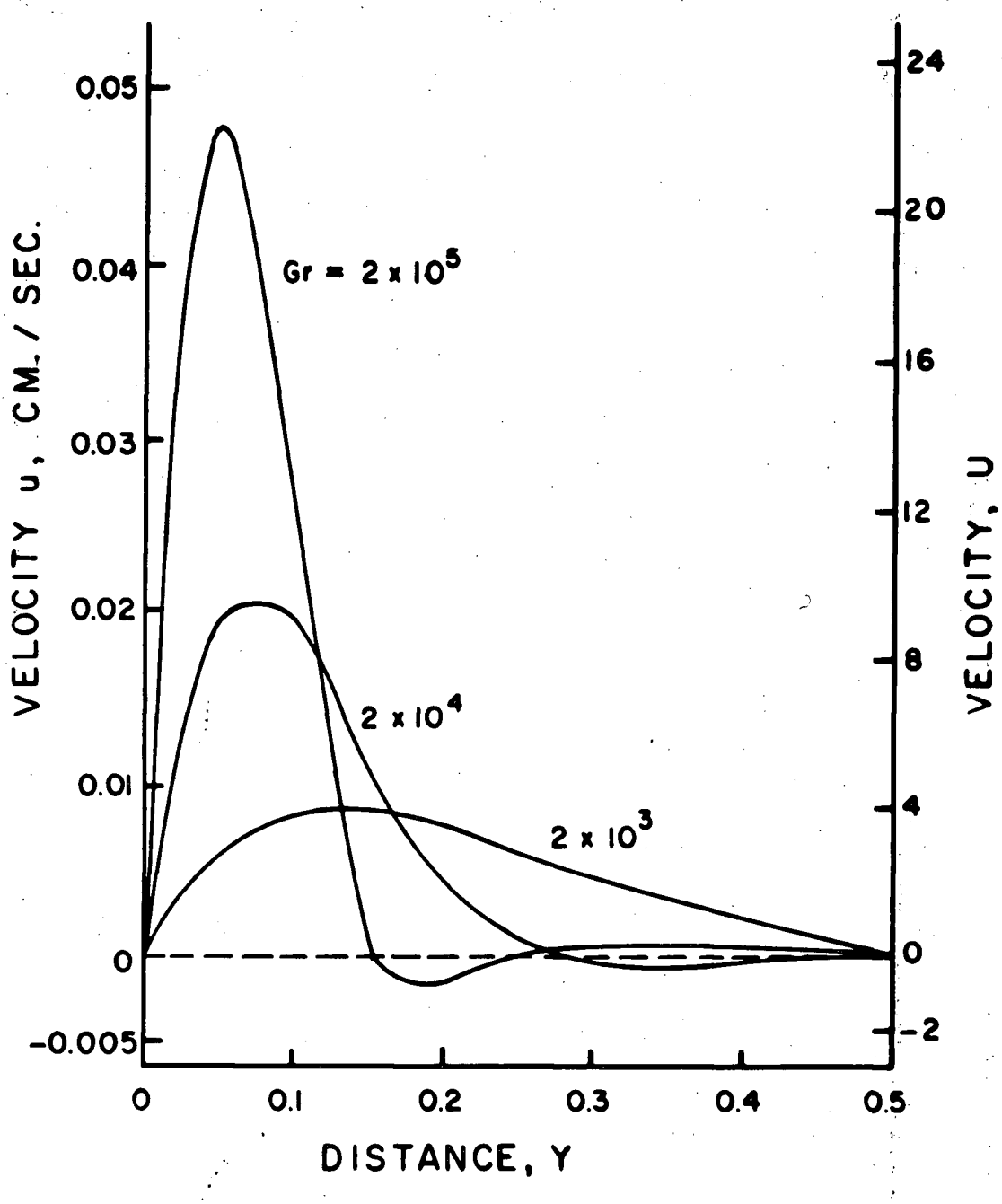

Figure 35d. The theoretical flow velocity (u and U) at a position X = 0.5 for various values of the Grashof number for Pr = 10.0 and assuming water properties to calculate u.

of the Prandtl number used in the computation can be estimated from Table I for the various types of fluids. Also a value of d equal to 6.4 centimeters has been chosen for the cell size for velocity comparisons.

A discussion of the various behaviors in flow for the various Prandtl numbers can be shown best by comparing two particular fluids. A comparison of Prandtl numbers of 0.0127 and 10 will be done to illustrate the important thermal convection differences. The Prandtl number of 0.0127 can represent liquid tin, and the Prandtl number of 10 can represent water. As was pointed out earlier, equal Rayleigh numbers produce equal thermal conditions in the melt. Comparing Figure 31e for liquid tin (Pr = 0.0127) with Rayleigh equal to 2.5×10^5 and Figure 34a for water (Pr = 10.0) with Rayleigh equal to 2×10^5 we see that the flow patterns are not similar. The liquid metal flow is still quite circular in nature, especially in the central regions of the cell. The water flow is quite rectangular in nature and appears to conform more to the shape of the square cell than the liquid metal flow. The actual velocities of the flows can be seen by comparing Figures 35a and 35d. For a Rayleigh number of near 2×10^5 the liquid metal flow has a maximum velocity at the X = 0.5 position of about 1.4 cm. / sec. while at the same position the maximum flow in the water cell is 0.02 cm. / sec. Thus there is a factor of two orders of magnitude difference

in the flow rates for the two materials with an equal thermal profile.

The comparisons between the liquid metal and water can be made in another way, comparing the thermal profiles for equal flow rates. For liquid tin at a Grashof of 2.5×10^4 the maximum flow rate is about 0.03 cm. / sec. and for the water at a Grashof of 2×10^4 the maximum flow rate is about 0.02 cm. / sec., which are similar. However, comparing the thermal profiles for these two flows, the liquid tin profile is still in a conductive nature ($Ra = 2.5 \times 10^2$, $Nu = 1.0$) while a great deal of bending occurs for the water isotherms ($Ra = 2 \times 10^5$, $Nu = 5.7$).

A comparison of the other various types of fluids can be accomplished in the same manner by comparing the various figures. The general flow behaviour and how it relates to the various parameters can be simply summarized. Using the maximum value of U at a position of X = 0.5 for comparing flow rates, and using the Nusselt number to compare the degree of isotherm warping Table V shows the behaviour in thermal convection.

Several important comments can be made in terms of the differences between liquid metal flow and other types of fluid flow. For equivalent thermal profiles in the liquid (Nu = constant) the flow velocities in liquid metals are much higher than in other types of fluids. For liquid metals, large flow rates may be developed in a melt

TABLE V.

The effect on the Natural Convection of Altering Dimensionless Parameters

Alteration	Affect on Nusselt Number	Affect on Flow Rate (U_{max} at X=0.5)
Gr → Constant Pr → Increasing	Increasing	Decreasing
Gr → Increasing Pr → Constant	Increasing	Increasing
Ra → Increasing	Increasing	Unknown

while the thermal profile is still unaltered from the pure conduction form. For example, with an average Nusselt number of only 1.25 ($Gr = 2 \times 10^5$) flow velocities of nearly 0.2 cm. / sec. were calculated for the liquid tin in the 6.4 cm. wide cell. For equal flow rates, the liquid metal flow is less dependent on the shape of the cell enclosure as was seen by the liquid flows in tin remaining circular while other liquids approach a rectangular shaped flow corresponding to the rectangular cell.

Phenomena of metallurgical interest that are affected by convective flow in the melt, as was mentioned in the introduction to this thesis, are dependent on both the liquid flow rates and flow pattern and also the thermal profile in the liquid pool. The nature of both the flow rates and heat flow combine to give the resultant effect that occurs. If one of the controlling effects is altered, either flow rate or thermal conditions, the

resulting effect will be different. By using fluids other than liquid metals to observe metallurgical phenomena, the effect is to alter the relative nature of the flow and thermal conditions such that the system will not be comparable to a liquid metal. The differences produced are unknown, and hence the results from non-metallic analogs are at best only qualitative indicators of metallurgical effects.

3.4. Comparison of theoretical and experimental results

3.4.1. Thermal profiles

The experimental profiles of liquid tin in Figure 15 can be compared to the profiles obtained in the numerical solution in Figure 27. Figure 15b and 15e with a Rayleigh number near 2×10^5 may be compared with Figure 27e. Although the experimental figures are not in the non-dimensional form the shapes will be comparable. For the thick liquid cell the profile is very similar in nature to the computer solution. The thin liquid cell profile, however, is indicative of a much lower Rayleigh number. The good agreement between the theory and the thicker liquid cell indicates the large flat faces of the experimental cell are not causing a large change in the thermal convection. The differences in the thin liquid cell can be caused either by the viscous drag of the large walls or the thermal conduction of the side walls. The flow could also

be influenced by the 0.5 mm. diameter thermocouple probe by a slowing of the flow. These effects would all tend to decrease the flow and hence the thermal profile bending.

A rigorous comparison of the thermal profiles has not been attempted due to the inherent limitations of the experimental techniques of putting a relatively large foreign body into the very sensitive thermal convective flow. In the thicker cell, where these effects are less important, the results seem to compare much more favourably.

3.4.2 Flow patterns and flow rates

The flow patterns that were observed for pure tin in Figures 9 and 10 all have the one flow cell pattern. This is in agreement with the analytical treatment presented which also generates a one cell flow pattern of a similar nature. The experimental results will be compared with the theoretical results in a quantitative way by comparing the time for the flow to complete one full cycle around the liquid cell. The experimental curves are shown in Figure 14 for the various cell thicknesses with pure tin at 260°C average temperature. For the comparison to be made, the computer results must be converted to a time per cycle for each value of the Grashof number for the Prandtl equal to 0.0127. This is done by a graphical integration of the velocity along the streamlines shown in Figure 31. A

number of increments are taken around each streamline and knowing the velocity in each increment from U and V computer printouts the total time for the flow to complete one cycle on each streamline is obtained. For comparison purposes the minimum time per cycle is taken. Thus, the computer solution times per cycle will be a minimum value which should be approached by the experimental results.

The numerical analysis results are shown in Figure 36, plotted on a log-log scale because of the orders of magnitude changes in both the time per cycle and Grashof numbers of interest. The three curves for the three cell thickness flow rates are also shown on the curve which are taken from Figure 14. It is evident that the agreement between the experiments and theory at low Grashof numbers is very poor. The exact reasons for this poor agreement are somewhat unclear, but are probably related to the sidewall restrictions in the experimental cell. At the low flow rates and low temperature gradients the hydrodynamic resistance and the heat flow through the side plates must have a greater effect on the flow. The agreement between the experiments and theory is quite good for higher temperature differences. Also, the thicker the cell, the better the agreement becomes at a particular temperature difference. For example, with the 0.95 cm. thick liquid cell the experimental point at a 3°C temperature difference is almost on the theoretical line, while for the

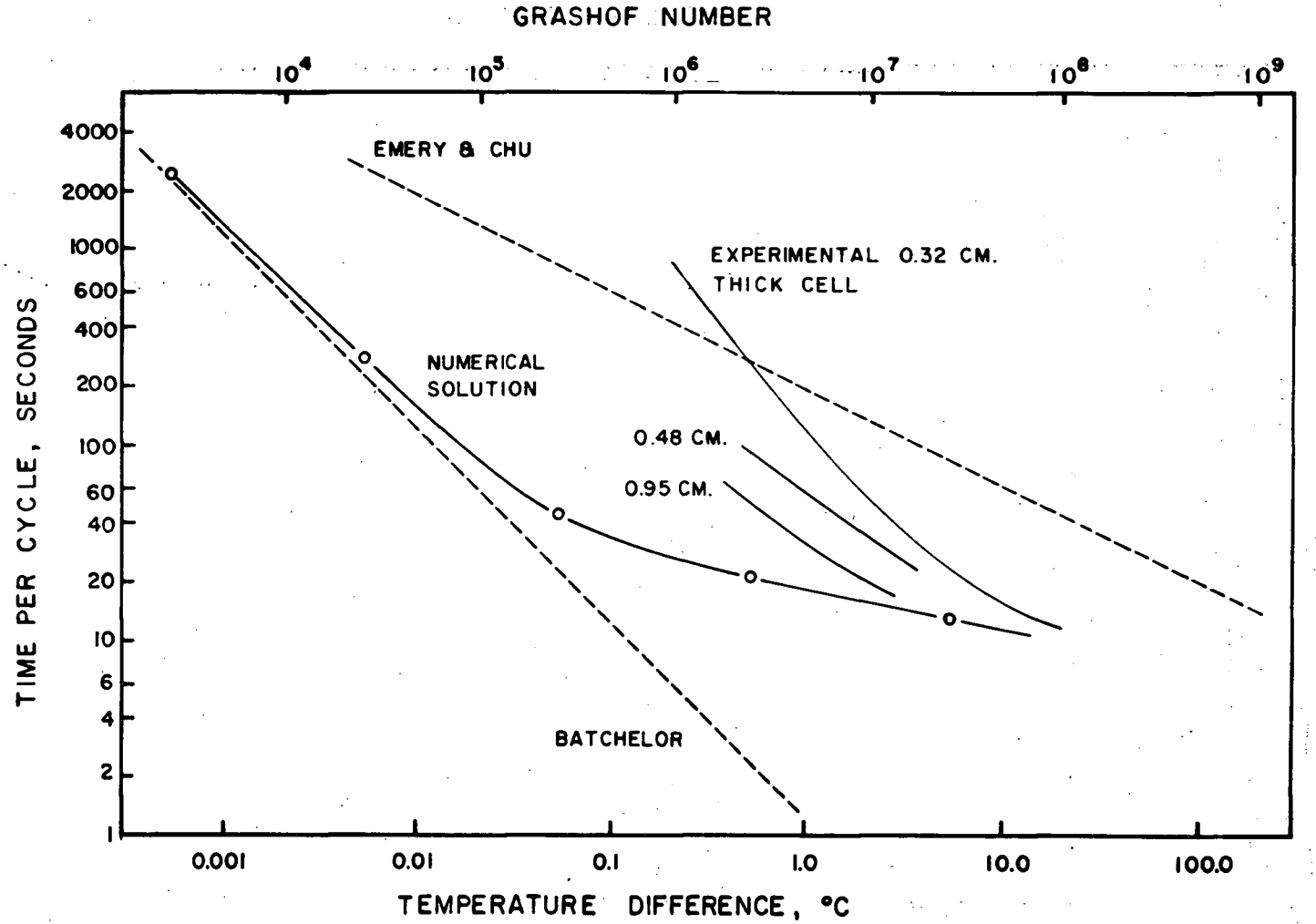

Figure 36. The flow time per cycle versus the Grashof number and temperature difference across the cell (tin at 260°C) for the solution of Batchelor, solution of Emery and Chu, numerical solution, and experimental results.

0.32 cm. cell, very good agreement is not reached until approximately 10°C temperature differences. The curve for the intermediate thickness cell lies between the other two as expected. It is evident by noting the progression of the experimental curves as the thickness increases, that they are approaching the computer solution in a systematic and expected manner. The theoretical line represents the infinitely thick cell and should be the asymptotic limit. This can be shown graphically by plotting the time per cycle for a particular temperature difference against the cell thickness. Figure 37 shows such a plot for a 1°C temperature difference. The horizontal dashed line represents the theoretical time per cycle for this temperature difference. This curve supports the proposal that the experimental results approach the theory and that for a very thick cell greater than approximately 1.5 cm. thick the theory and actual flows should be in complete agreement.

Computer runs were made corresponding to altering the average temperature in the liquid tin melt from 260°C to 305°C and 237°C. For 305°C the Prandtl number is 0.01135 and for 237°C the Prandtl number is 0.01365. The theoretical change in the time per cycle for a constant temperature difference of 0.55°C for the various degrees of superheat is shown in Figure 38. These results are in agreement with the results of Figure 11 which also shows that an increase

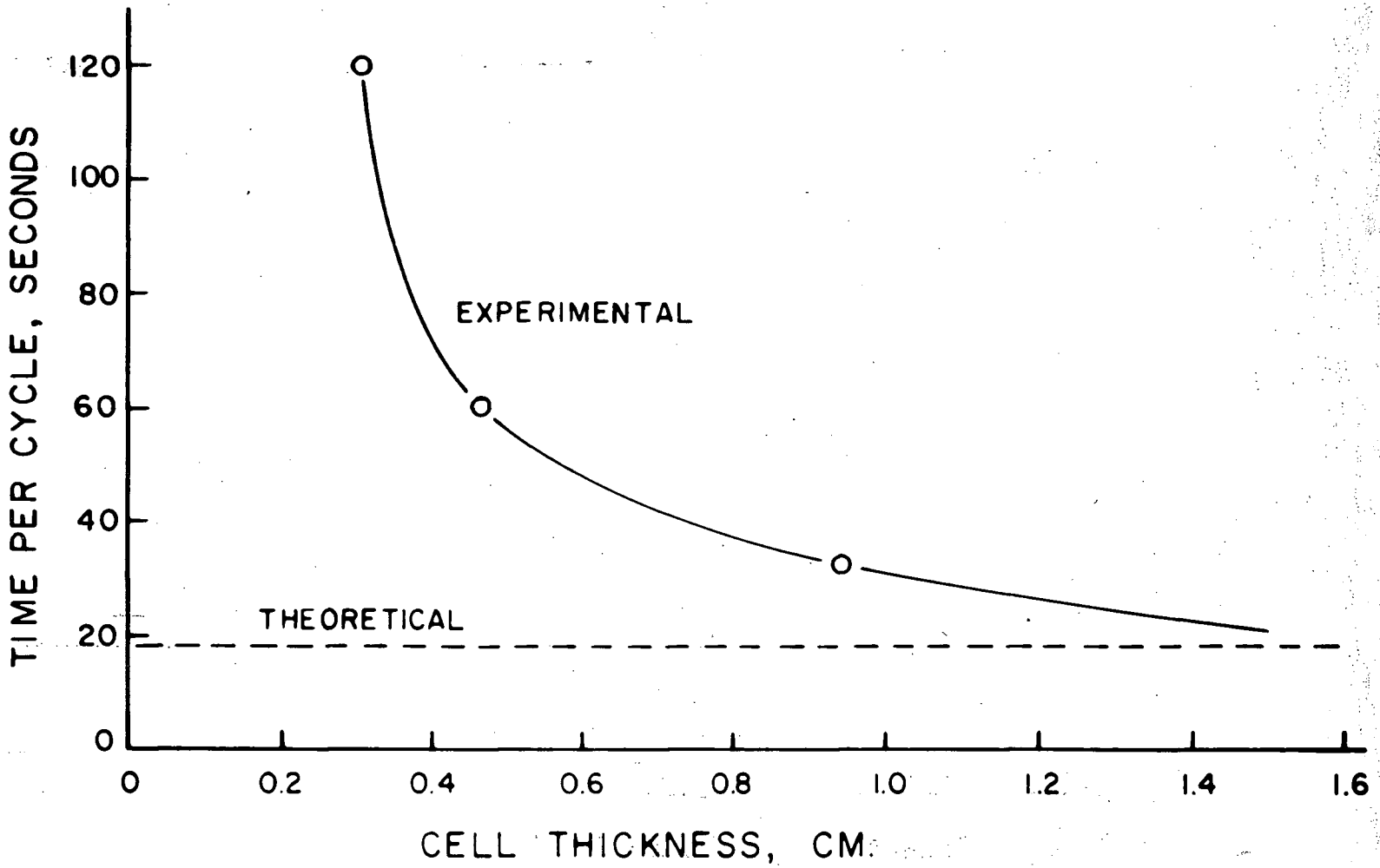

Figure 37. The flow time per cycle versus the liquid cell thickness for a temperature difference of 1°C showing the experimental and theoretical curves.

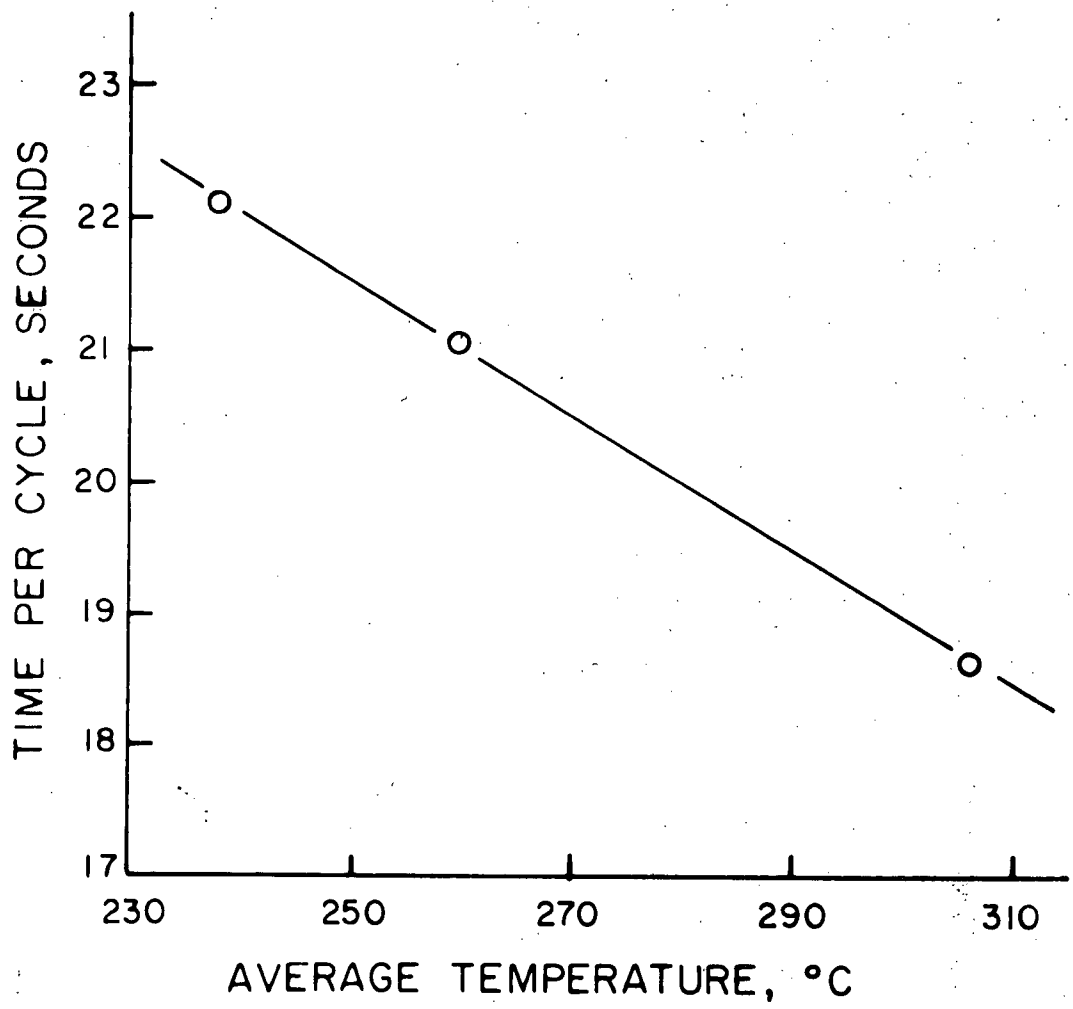

Figure 38. The theoretical flow time per cycle for liquid tin versus the average temperature in the cell for a temperature difference across the cell of 0.555°C.

in the average temperature causes a decrease in the time per cycle.

The numerical analysis presented here can be compared with the analytical solution of Batchelor. As stated earlier, the solution of Batchelor should be valid for Rayleigh numbers of less than 10^3. For liquid tin at 260°C this corresponds to a Grashof number of 7.9×10^4 or a temperature difference of 0.022°C. In a similar manner as for the numerical results, the results of Batchelor's solution can be converted into a time per cycle. Figure 36 shows the solution of Batchelor on the same plot as the numerical results. Batchelor's solution appears as a straight line of slope equal to unity since the stream function is directly proportional to the Rayleigh number, andhence Grashof for constant Prandtl number. The computer solution is asymptotic to Batchelor's solution at the lower Grashof numbers, and below the value of 7.9×10^4 mentioned above, the agreement becomes quite close. This is expected if the numerical solution is correct.

The theory of Emery and Chu is also shown on Figure 36. The time per cycle was taken assuming the velocity profile at X = 0.5 is taken around the cell in a circular manner at a radius equal to the distance from the cell centre to position of the maximum velocity in the boundary layer. This is very approximate but will be used in this qualitative discussion. The times are very much

longer due to the larger distances around the cell at the position of maximum flow. The time per cycle curve is again a straight line with a slope of one-half since u is proportional to $(\Delta\theta)^{1/2}$ in this theory. From the numerical results, the higher the Grashof number, the closer to the outside wall is the peak in the velocity curve. This means also that the analysis of Emery and Chu should become closer to the actual case at very large Grashof numbers where the flow is similar to a narrow boundary layer on each vertical wall. The solution of Emery and Chu will approach the numerical solution at very large Grashof numbers of the order of 10^9 to 10^{10}. This is out of the range of experimental interest, but does qualitatively support the numerical results.

In summary, several points can be made concerning the theoretical numerical solution developed:

(a) The solution agrees with the infinite series analytical solution at low values of the Grashof number.

(b) The solution approaches that of an integral boundary layer model for very large values of the Grashof number.

(c) The solution corresponds to the experimental results, when projected to a very thick cell.

Thus it is very reasonable to conclude that the numerical analysis presented here is a good and proper solution to the problem of thermal convection.

4. Solute Convection

The problem of separating solute convection from other types of fluid flow and observing the solute convection directly is very difficult. Solute gradients are set up during the solidification of any multicomponent system where the solute distribution coefficient is other than unity. If the components are of a different density the solute gradients will also be density gradients and a potential driving force for natural convection exists. Generally during freezing or melting thermal gradients of some sort exist and hence both thermal and solute convection will occur. The thermal convection can be reduced or eliminated by solidifying vertically with the warmer less dense liquid in the upper part of the system. If thermal gradients are stabilizing the system then in order for solute convection to be observed, there must first be a sufficient driving force from the solute to overcome the stability in the system due to the thermal gradients retarding liquid motion. Several experimental investigations were conducted to observe the effect of solute convection

alone, the combined effect of thermal and solute convection, and also to observe quantitatively the relative strengths of thermal and solute convection.

4.1. Independent solute convection

An experiment was conducted to observe the extent of mixing in a molten pool caused by an initial solute gradient. Schematically a system was set up as shown in Figure 39. A copper sheet divider was placed in slots on the large flat faces of the mould to separate the liquid into two distinct regions. The composition of the liquid in each of the two regions varied depending on the experiment. The experiment consisted of holding the

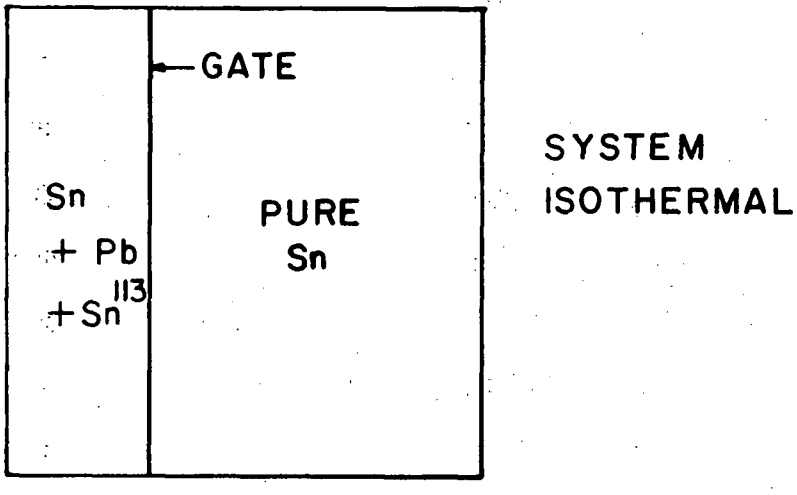

Figure 39. The experimental initial conditions for observing independent solute convection.

entire system isothermally, then removing the copper sheet gate by pulling it upwards out of the mould and observing the resulting flow. To establish that the observed fluid flow was due solely to solute convection it was necessary to establish that no premature leakage of material occurred past the gate and that the action of opening the gate did not itself produce significant fluid flow. To determine if leakage occurred across the gate pure tin was put in the right-hand liquid cell and tin plus 0.1 wt. % lead plus radioactive tin was put in the smaller left-hand liquid cell. If leakage occurred the denser liquid in the left-hand cell would flow past the gate. The system was left in the molten state for 50 minutes and quenched. Figure 40 shows the resultant casting. The very slight leakage observed is considered negligible considering the long period of time involved. To determine to what extent fluid flow was induced by removing the gate a test was carried out with pure tin on the large right-hand side liquid cell and pure tin plus radioactive tin on the left-hand side, i.e. no density difference across the gate. The gate was rapidly removed and the system quenched thirty seconds later. Figure 41 shows the resultant flow. The bulk of the active material has remained in its original position. A small flow is observed along the bottom of the cell and along the top of the cell. This small flow is thought to result from the motion of the gate as it is pulled upwards and also the movement of the liquid tin to fill the void

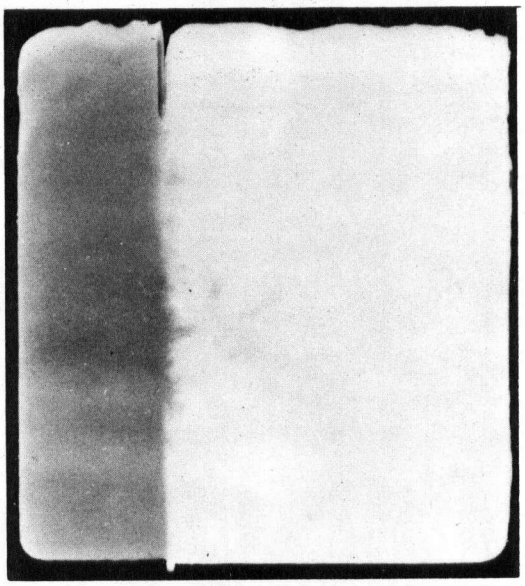

Figure 40. The tracer profile in the system described in Figure 39 left molten 50 minutes without opening the gate.

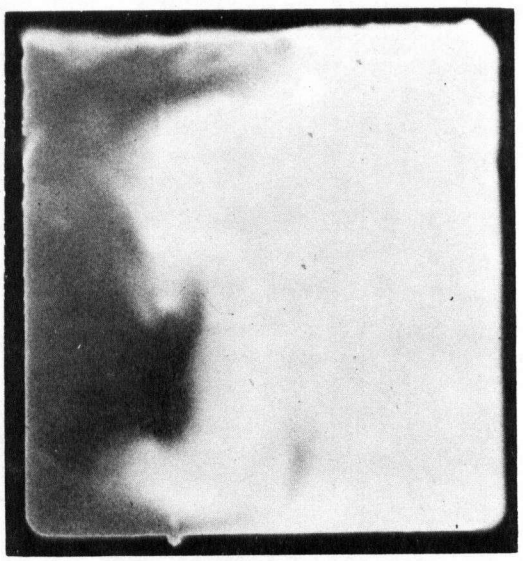

Figure 41. The tracer profile in the system of Figure 39 with only pure tin plus Sn^{113} in the left section and the system is quenched 30 seconds after the gate is opened.

a

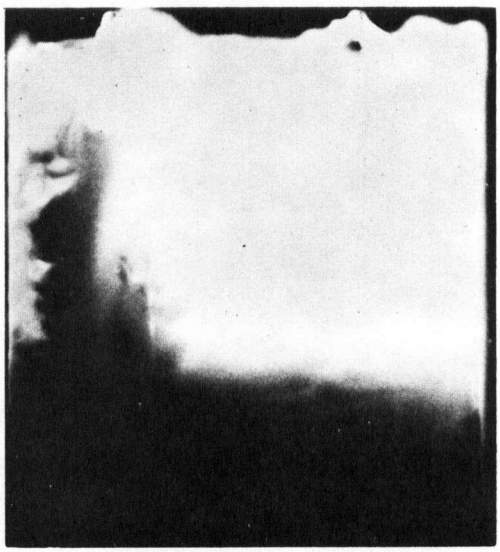

b

Figure 42. The tracer profile in the system of Figure 39 with tin plus 0.1 wt. % lead plus Sn^{113} in the left section, quenched (a) 15 seconds and (b) 30 seconds after the gate is opened.

left by the gate as it is removed. The flow, however, is not extensive.

Experiments to determine fluid flow resulting from a solute density effect were carried out with the right-hand section containing pure tin and the left-hand section containing tin plus 0.1 wt. % lead plus radioactive tin. The gate was opened and the system quenched at variable times. Figures 42a and 42b show two resultant castings quenched fifteen and thirty seconds respectively after removal of the gate. It is observed that the denser liquid falls rapidly to the lower region of the cell in both cases. There appears to be no tracer rising on the right-hand side of the liquid cell indicating that extensive mixing in the right-hand section is not occurring. The tin-lead alloy appears to displace the pure tin "en masse" with very little mixing occurring. The stability of such a dense layer of liquid below a less dense region will be discussed in a following section.

4.2. The influence of solute convection on thermal convection

A series of experiments was carried out in which small amounts of tin containing 0.1 wt. % Tl^{204} were added to pure tin melts subject to different degrees of thermal convection. Initially there is a small density difference between the added material and the melt which

progressively decreases as the addition spreads. Figure 43 shows the results of these experiments. The autoradiographs on the left-hand side are pure tin with tin tracer for a given temperature difference and those on the right-hand side are pure tin with thallium tracer for the same temperature difference across the cell. For the case of a zero temperature difference, Figures 43a and 43b, fluid flow results only from solute convection. The heavier tracer is observed to drop very rapidly to the lower regions of the cell and in doing so induces additional fluid motion in the cell. This is evidenced by the swirling action in the lower regions and the rapidly formed band of tracer at the bottom. With an increase in the temperature gradient to 1°C, Figures 43c and 43d, the two flow patterns are still very dissimilar. The thallium tracer drops down the cell much more quickly than the tracer under thermal convection only. There is still an accumulation of tracer in the lower regions of the cell. The pattern, however, shows a counterclockwise swirl similar to the thermal convective flow. This flow is in effect a composite of the flows of Figures 43b and 43c. For Figures 43e and 43f the temperature difference has been increased to 3°C and the two patterns are becoming similar. There is still an accumulation of thallium in the lower regions of the mould and a single cell flow pattern is now readily apparent. For a temperature difference of 5°C, Figures 43g and 43h, the flow patterns are very similar, apparently dominated by thermal convection.

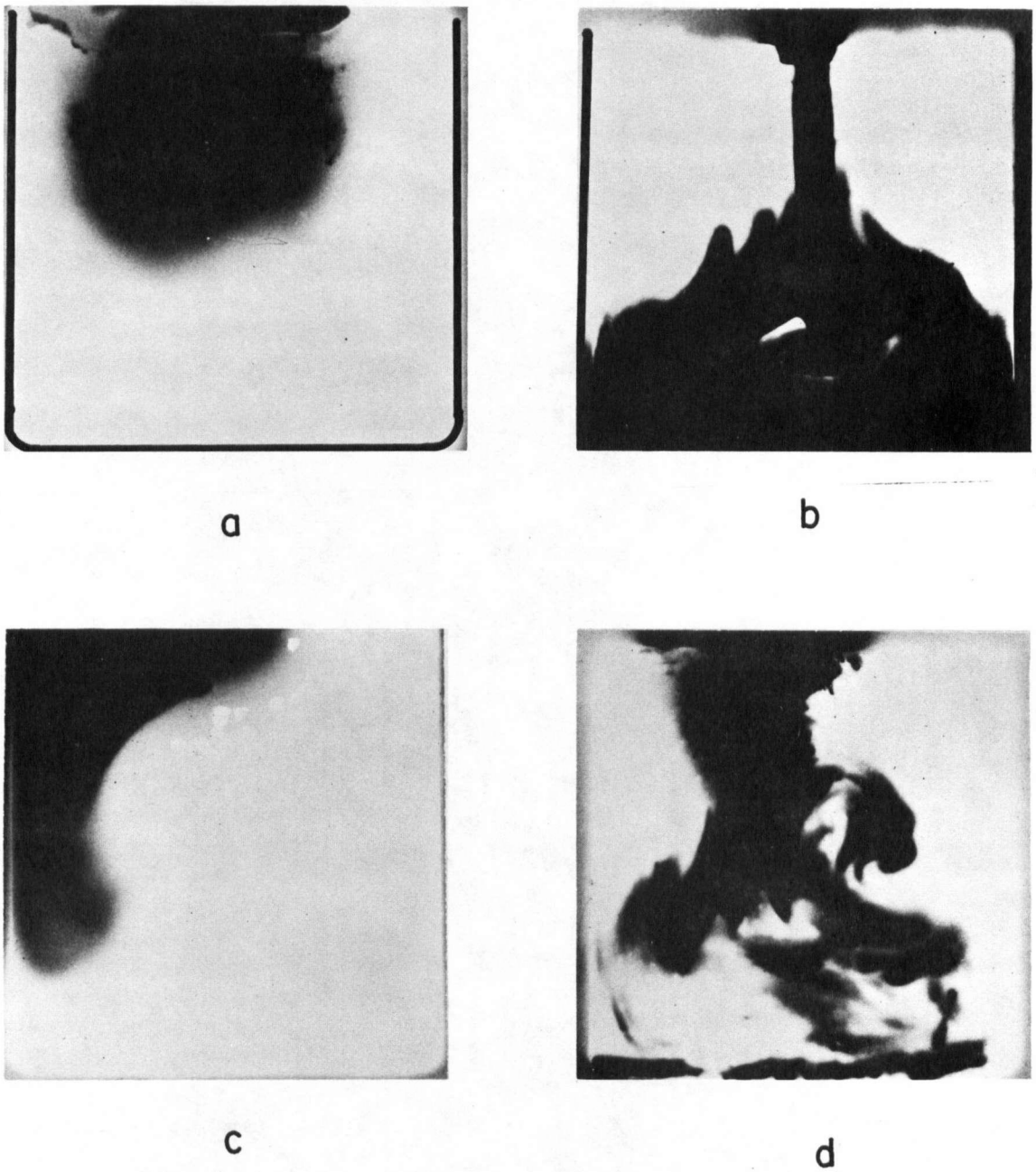

Figure 43. The effect of solute convection on thermal convection; the tracer distribution in samples with melt material, average temperature, temperature difference, and time to quench of (a) Sn - Sn^{113}, 260°C, 0°C, 60 seconds, (b) Pb - Tl^{204}, 357°C, 0°C, 60 seconds, (c) Sn - Sn^{113}, 260°C, 1.11°C, 30 seconds, (d) Pb - Tl^{204}, 357°C, 0.98°C, 30 seconds.

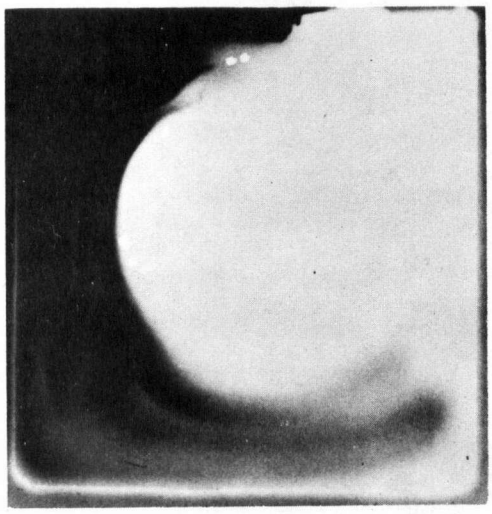

e

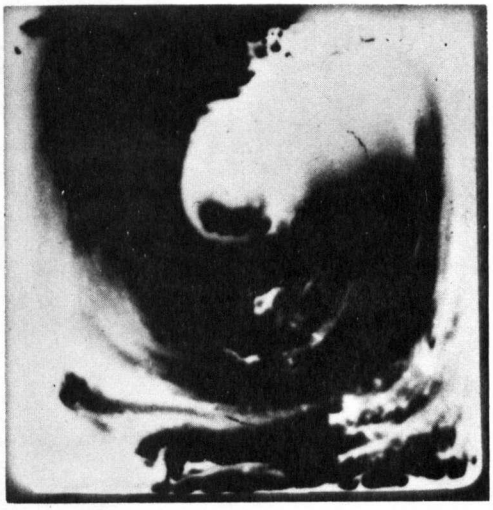

f

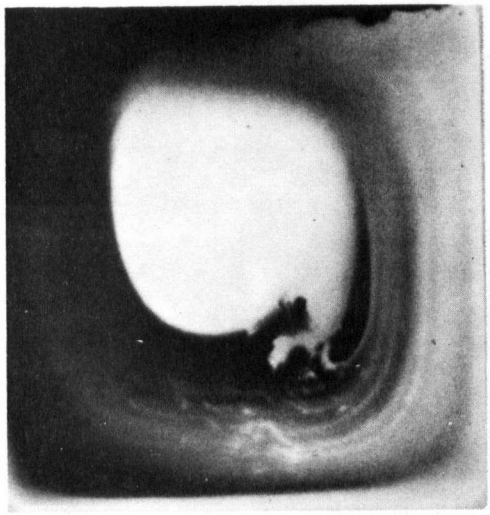

g

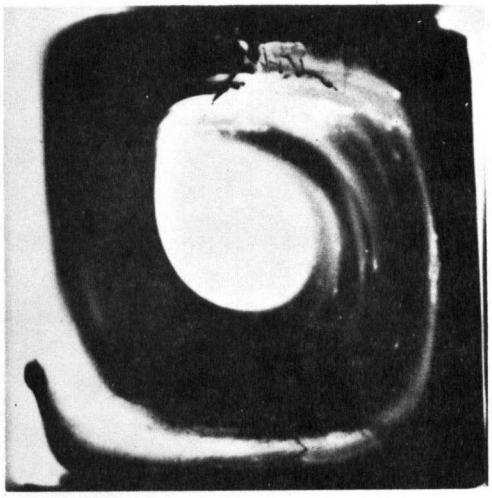

h

Figure 43 continued. The effect of solute convection on thermal convection; the tracer distribution in samples with melt material, average temperature, temperature difference, and time to quench of
(e) Sn - Sn^{113}, 260°C, 3.04°C, 30 seconds,
(f) Pb - Tl^{204}, 357°C, 3.00°C, 30 seconds,
(g) Sn - Sn^{113}, 260°C, 4.80°C, 30 seconds,
(h) Pb - Tl^{204}, 357°C, 5.00°C, 30 seconds.

Any accumulation in the lower regions appears to be swept up the right-hand side of the liquid cell.

In the previous experiments more dense material was added to the melt. Alternative experiments were carried out in which less dense material was added to a melt. This was done by using a pure lead melt and adding lead plus 19 wt. % radioactive tin in which case the addition should tend to float in the liquid lead melt. Figure 44 shows the results. For a temperature difference of 1°C and 3°C, (Figures 44a and 44b respectively), the tracer spreads across the top of the cell and does not significantly enter the bulk of the melt. With a larger temperature difference of 5°C (Figure 44c) the flow resulting from thermal convection completely overshadows solute convection producing a normal thermal convection flow pattern.

The results of the above two sets of experiments show that a certain temperature difference is required for the less dense solute to enter the bulk of the liquid melt or the more dense solute to be swept from the bottom of the liquid melt. The following section will investigate the conditions required for complete mixing with both solute and thermal gradients.

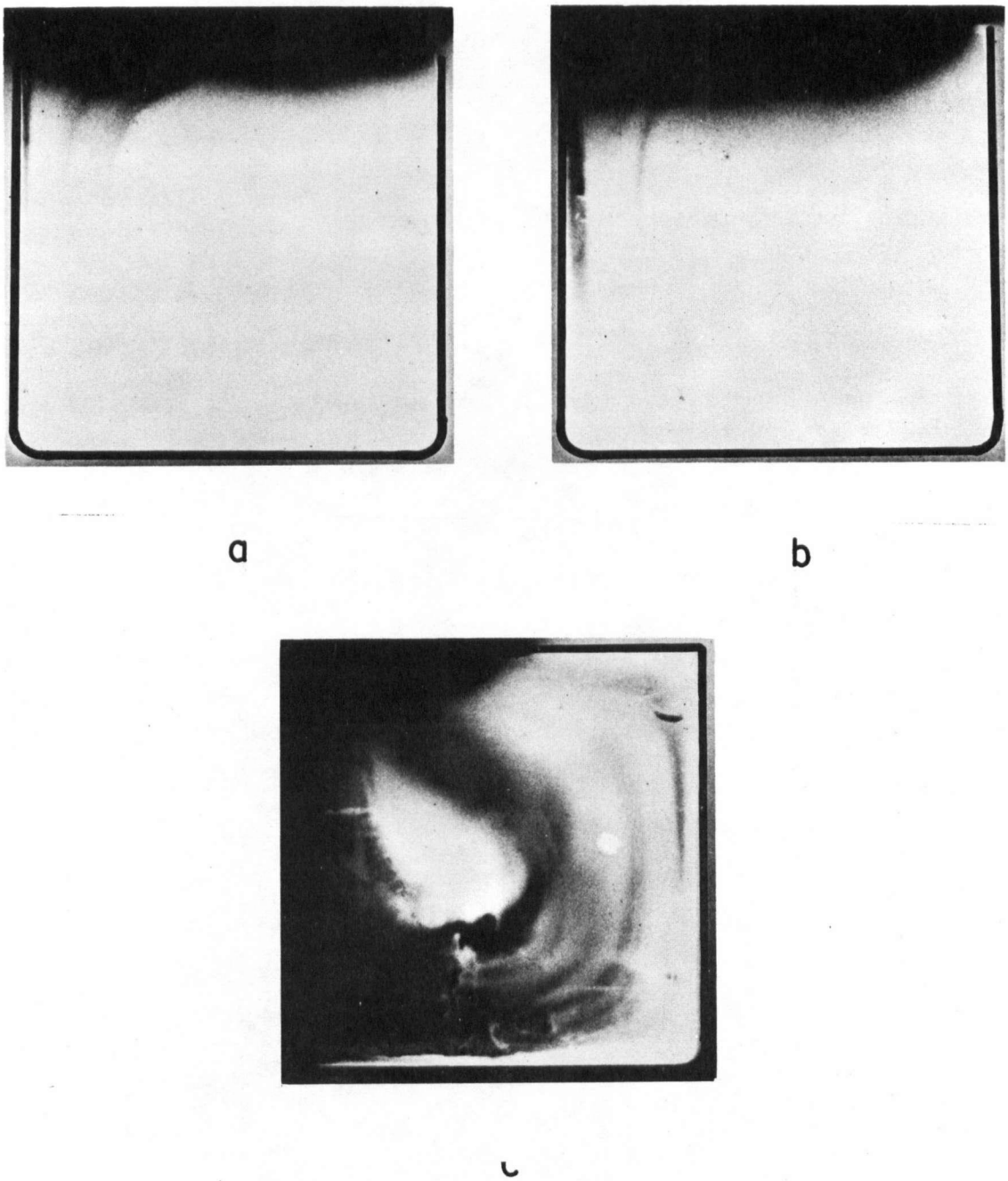

Figure 44. Tracer profile in lead melts (Sn^{113} tracer, 357°C average temperature) with a temperature difference and time to quench of (a) 1.07°C, 60 seconds, (b) 3.07°C, 30 seconds, and (c) 5.00°C, 15 seconds.

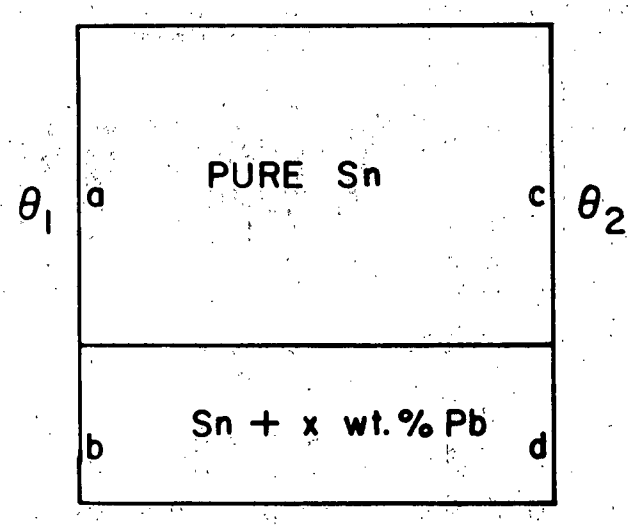

Figure 45. The experimental initial conditions for deriving the thermal and solute conditions for complete liquid mixing.

4.3. Thermal and solute conditions for complete liquid mixing

The thermal and solute conditions required for complete mixing in the cell can be observed using the initial conditions shown in Figure 45. The upper layer of the liquid zone is pure tin and the lower layer is composed of a lead-tin alloy of known composition. A temperature difference is applied across the cell and the flow pattern in the liquid cell is observed. A simple theory can be developed to determine when the temperature gradient will be sufficiently high to cause complete mixing in the cell. For the cell shown in Figure 45,

let $\theta_2 > \theta_1$ (4.1)

and let the density at position a be ρ_a, at b be ρ_b etc.

Since $\rho_c < \rho_a$

$\rho_d < \rho_b$ (4.2)

and since the alloy is of tin + x wt. % lead where $x \neq 0$ and the vertical walls are isothermal

$\rho_a < \rho_b$

$\rho_c < \rho_d$ (4.3)

The hypothesis of this analysis is that for complete mixing to occur for a certain temperature difference and solute difference, $\rho_a \geq \rho_d$. This will cause the pure tin to enter the lower region of the liquid cell on the left-hand side by displacing the alloy on the right-hand side. Once the mixing begins the system will become completely mixed since the temperatures are fixed and the solute difference is diminished. When there is a vertical solute difference stabilizing a liquid system by preventing fluid flow between adjacent liquid layers, even in the presence of a temperature gradient, then a condition exists which can be referred to as a "solute valve". This condition is similar to the thermal valve discussed earlier.
Figure 46 shows several experiments done to test the above hypothesis, with approximately the same thermal conditions and with a variable lead content in the lower regions of the mould. The samples with incomplete mixing show a small

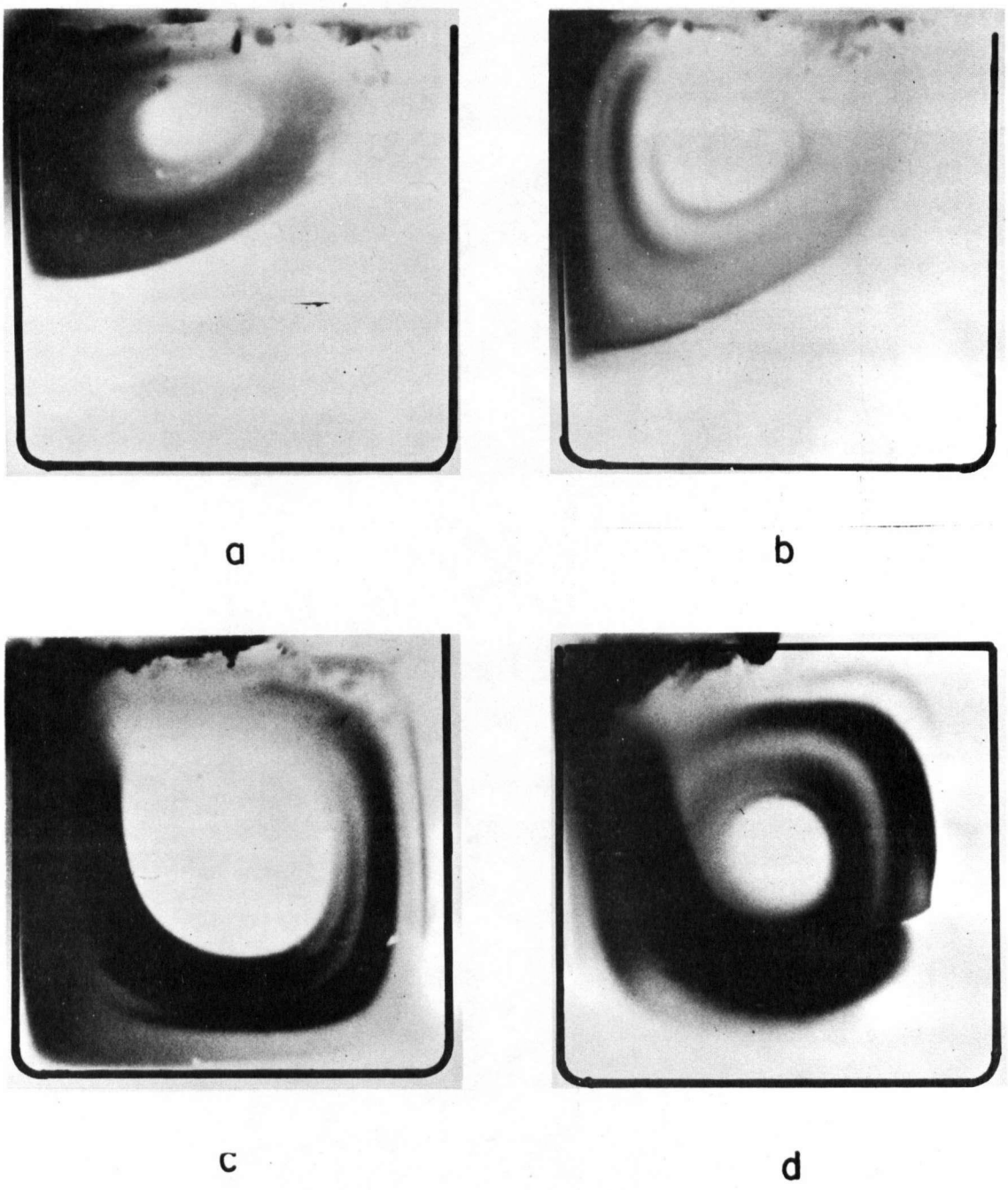

Figure 46. The tracer profile for steady-state flows for the initial conditions as shown in Figure 45 with lead content x, temperature difference, and time to quench of (a) 10 wt. %, 3.02°C, 60 seconds, (b) 0.2 wt. %, 2.64°C, 60 seconds, (c) 0.1 wt. %, 2.91°C, 60 seconds, and (d) 0.05 wt. %, 2.89°C, 60 seconds.

cell in the upper left-hand corner on the cold side of the cell, Figures 46a and 46b. The samples that have mixed completely show a single cell pattern throughout the liquid zone, Figures 46c and 46d. To help account for the odd shape of the incompletely mixed region another experiment was carried out in which pure tin was used in the upper layer and tin plus 1% lead plus radioactive thallium in the lower layer. The system was left molten for 60 minutes under a 2.82°C temperature gradient to allow the system to reach complete steady state. The resultant pattern is shown in Figure 47 and is very similar in nature to the incomplete mixing patterns. The same curved demarcation line between the upper and lower regions is evident. This could be due to the thermal convection in the lower cell forcing a small amount of solute up the hot side of the cell. Some sort of complex density gradient is set up which is stable as shown in the figure and allows no mixing between the two regions.

The results for the full set of experiments are listed in Table VI including the temperature difference and the initial solute difference for each experimental run. The calculated values of ρ_a and ρ_d are also included. The densities of pure tin and tin-lead alloys as a function of temperature were obtained in the form $\rho = a + bT$ from the work of Thresh (37). Table VII lists the values of a and b used. It is evident from Figure 46 and Table VI

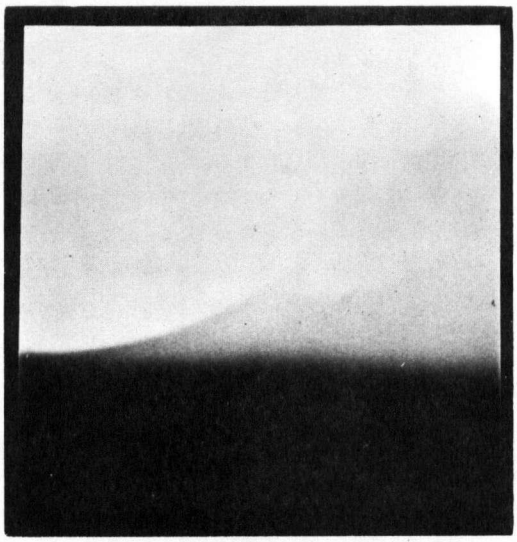

Figure 47. The steady-state tracer profile resulting from the lower section of the cell being composed of tin, 1.0 wt. % lead, and Tl^{204} and with a temperature difference of 2.82°C.

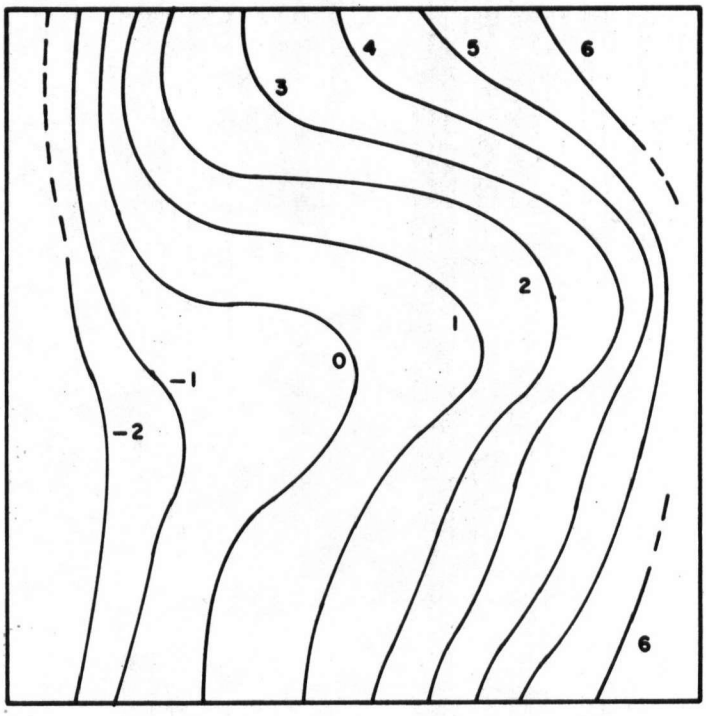

Figure 48. The experimental isothermal profile in a system initially as in Figure 45 with the lower section composed of tin plus 10 wt. % lead.

TABLE VI.

Experimental Results for Combined

Thermal and Solute Convection

Run Number	θ_1 °C	θ_2 °C	wt. % Pb	ρ_a gm/cm^3	ρ_d gm/cm^3	$\rho_a > \rho_d$	$\rho_d - \rho_a$	Complete Mixing
1	275.49	278.51	10	6.9427	7.1978	No	0.2551	No
2	282.43	285.58	10	6.9378	7.1925	No	0.2547	No
3	279.64	282.37	2	6.9398	6.9893	No	0.0495	No
4	273.37	276.64	0.5	6.9442	6.9548	No	0.0106	No
5	275.5	278.5	0.1	6.9427	6.9431	Equal	0.0004	Yes
6	276.56	279.45	0.05	6.9420	6.9411	Yes	-.0009	Yes
7	274.55	277.46	0.1	6.9434	6.9439	Equal	0.0005	Yes
8	276.96	274.32	0.2	6.9417	6.9513	No	0.0096	No
9	278.41	281.60	0.5	6.9406	6.9512	No	0.0106	No
10	277.59	280.41	1.0	6.9412	6.9650	No	0.0238	No

TABLE VII.

Density of Lead-Tin Alloys as a Function of Temperature (37)

$\rho = a + bT \quad (T°C)$

wt. % Pb	a	b x 10^4
10	7.4083	7.5583
2	7.1929	7.2117
1	7.1659	7.1683
0.5	7.1525	7.1467
0.2	7.1471	7.1380
0.1	7.1417	7.1293
0.05	7.1403	7.1272

that the change to complete mixing occurs when $\rho_a \geq \rho_d$ as predicted. The actual change occurs near 0.1 wt. % lead for the temperature difference of approximately 3°C. Corresponding to the incomplete mixing autoradiographs of Figures 46 and 47 is the temperature traverse shown in Figure 48. This casting had a 9°C temperature difference across the cell and a 10 wt. % lead content in the alloy region. These conditions will not allow complete mixing throughout the liquid cell. The temperature profile shows a single flow cell in the upper part of the mould as evidenced by the bending of the isotherms in the figure. The lower region appears to be relatively still as the isotherms are vertical and evenly spaced.

The results obtained in this section clearly show that complete mixing will not occur in a liquid containing a vertical density gradient. Complete mixing can be obtained by imposing a thermal gradient on the system of sufficient magnitude to develop a horizontal density inversion leading to fluid flow.

5. Volume Change on Freezing

The volume change on freezing in liquid metals may be a driving force leading to fluid flow during solidification. This volume change is small and may be an expansion or contraction depending on the liquid metal being considered. The small volume change would produce a corresponding small fluid flow which would be difficult to isolate from normal thermal convection. A comparative technique was attempted to determine if the volume change did result in fluid flow. This consisted of comparing flow in pure tin which contracts 2.6% on freezing and a 44.5 wt. % lead 55.5 wt. % bismuth eutectic alloy which has no volume change on freezing. Both systems were initially stabilized at about 2°C above the melting point (232°C for tin, 125°C for the lead-bismuth alloy) and a small amount of tracer introduced into each melt. The systems were then cooled until nucleation occurred and they solidified completely. The differences in the movement of the tracer between the pure tin sample and the alloy sample should be attributable to the volume change on freezing. The

pure tin sample had radioactive tin added and the lead-bismuth alloy had radioactive thallium added in order that solute effects should not contribute to fluid flow.

In order to assure that the tracer did not move prior to nucleation, the tracer addition was added in a molten state at the same temperature as the melt; thermal gradients were eliminated and no premature nucleation occurs. Figure 49 shows a tin casting and an eutectic casting which were left five minutes in the molten state after the tracer was introduced before quenching. The tracer has not moved significantly. Figure 50 shows the flow that has resulted when the two systems are allowed to nucleate and freeze. Both Figure 50a for pure tin, and Figure 50b for the lead-bismuth eutectic show extensive mixing in the liquid cell. The two flow patterns are very dissimilar but the degree of mixing appears to be equivalent. It is evident from the eutectic flow pattern that the flow must be a result of something other than the volume change on freezing as the volume change is zero for this system. Since the system is isothermal before nucleation, the flow must occur after nucleation has occurred. The feathery nature of the tracer profile edges indicate that some solid was present in the form of dendrites before the tracer moved around the liquid cell. The only reasonable explanation is that large thermal gradients are set up in the melt during the recalescence of the liquid just after the

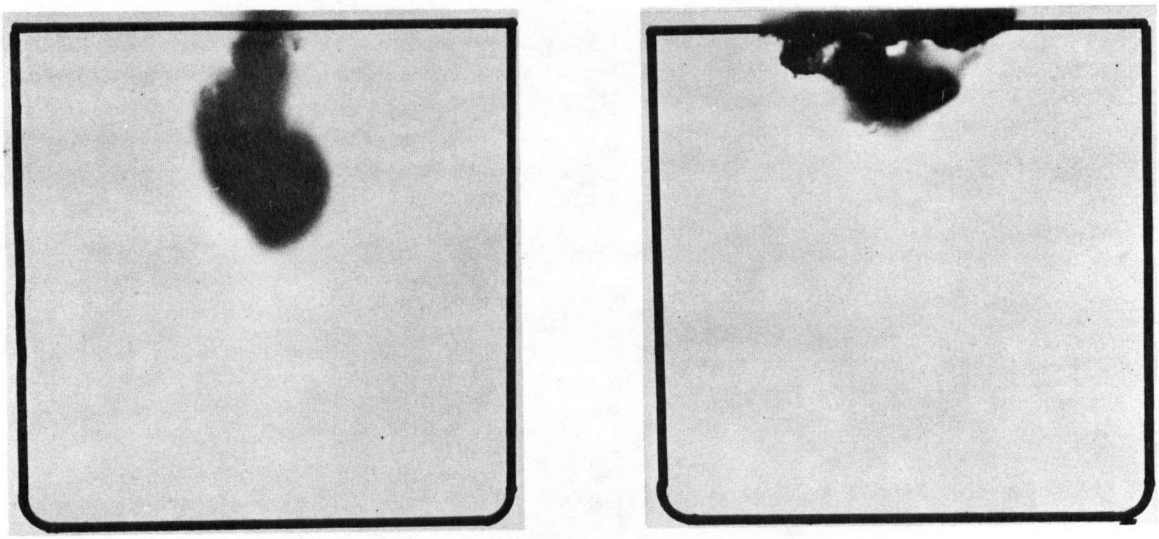

Figure 49. The tracer profile in an isothermal melt of (a) pure tin at 235°C (Sn^{113} tracer) and (b) 44.5 wt. % Pb - 55.5 wt. % Bi at 127°C (Tl^{204} tracer), both left 300 seconds before quenching.

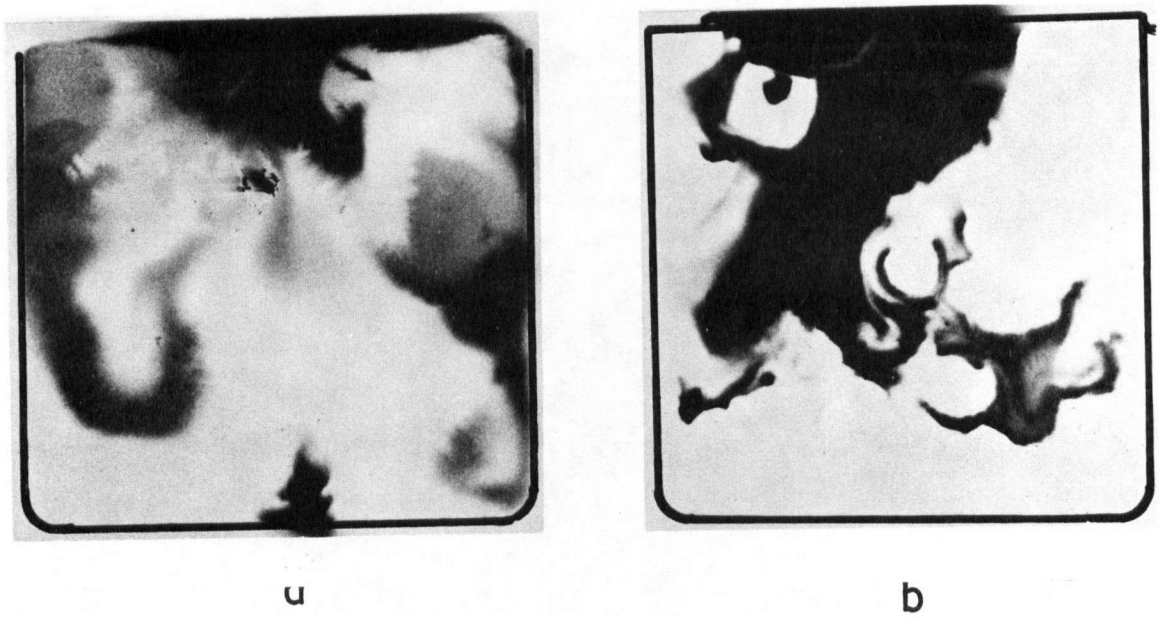

Figure 50. The tracer profile in a melt of (a) pure tin (Sn^{113} tracer) and (b) 44.5 wt. % Pb - 55.5 wt. % Bi (Tl^{204} tracer) allowed to cool, nucleate, and freeze completely without quenching.

initial nucleation.

Two temperature recorders were used to monitor the system during the nucleation process. Two bare thermocouples were placed one-half centimeter apart, one centimeter below the liquid surface at the middle of the cell. One recorder monitored the temperature of the melt from one of the thermocouples and the other recorded the temperature difference between the two thermocouples. The eutectic system was allowed to cool at approximately 1/2°C per minute and nucleate. Figure 51 shows the resulting temperature

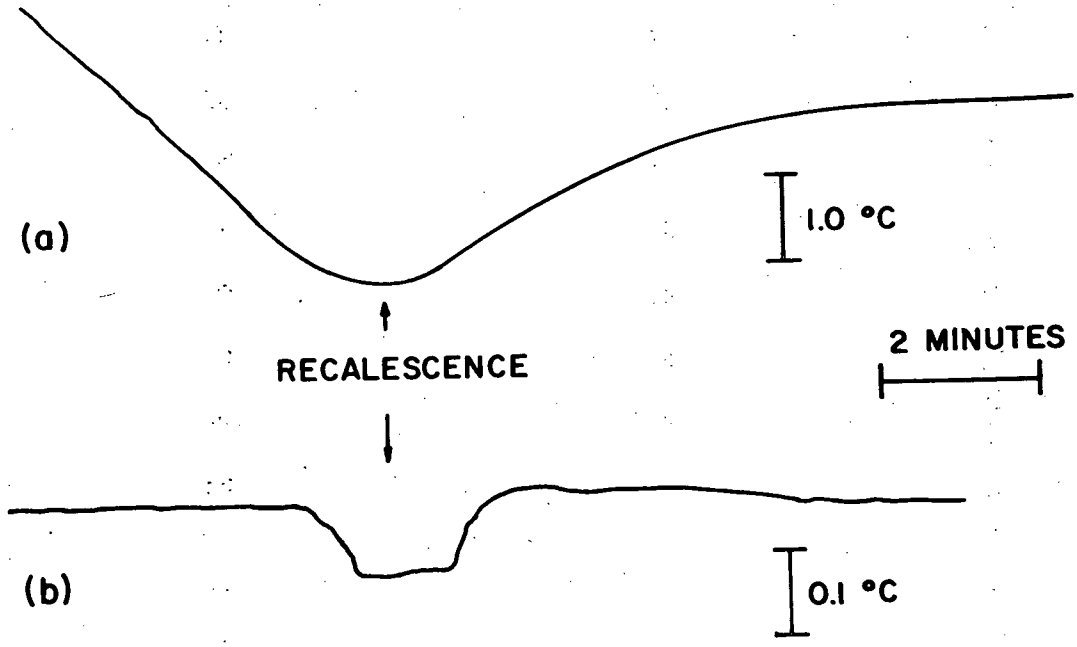

Figure 51. (a) The temperature versus time plot for the melt temperature during nucleation and freezing of the lead-bismuth eutectic melt and (b) the differential temperature versus time plot between two 0.5 cm. apart points in the lead-bismuth eutectic during nucleation and freezing.

time curves. Figure 51a shows the overall temperature cooling rate with the supercooling and recalescence readily evident. The differential thermal curve, Figure 51b, on the same time scale as the overall temperature curve but a ten times expansion on the temperature scale, shows the perturbation caused by a local temperature fluctuation between the two thermocouples. The magnitude of the temperature perturbation is about one-tenth of a degree over the small distance and persists for almost two minutes. It is not unreasonable to assume that temperature gradients are set up throughout the melt during the recalescence period, and that these cause thermal convection which results in the flow observed in Figure 50. This also accounts for some solid being present prior to the tracer movement.

The results obtained in an attempt to isolate the flow due to volume change on freezing have proven inconclusive. The flow observed is dependent more on the degree of supercooling before the nucleation than the volume change. However, it should be noted, that significant fluid movement resulted from very shallow temperature gradients over relatively short time periods, when there was also solid particles present in the melt.

6. Interdendritic Fluid Flow

There has been a great deal of interest recently in the importance of the interdendritic flow in metals during solidification (9, 10, 30, 31). Direct observation of this flow has been made in ammonium chloride cells (10) but not in liquid metals. The driving forces for interdendritic flow are the volume change on freezing pulling the liquid into the mushy zone, the thermal contraction in the mushy zone pulling liquid back, thermal convection, solute convection and the fluid motion in the residual liquid pool. The problem of interdendritic flow is basically a problem of flow through a very complex network of channels. The network is a function of the growth conditions at the interface such as growth rate, temperature gradient, composition and position in the mushy zone. An investigation was conducted to observe the interdendritic flow directly. Due to the complexity of the problem several experimental models were constructed with the aim of simplifying the complex geometry. This allows the various parameters to be controlled and analyzed individually.

A two dimensional model and two three dimensional models were used. Also lead-tin alloys were directionally cast for direct observation of an actual growing interface.

6.1. Two dimensional model

The two dimensional model is as shown in Figure 52. This consists of a 0.31 cm. thick block inserted into the cold end of the 0.31 cm. thick mould. The copper block has large slots cut back into it to represent the interdendritic spaces, and the metal remaining represents the dendrites. This is a very crude approximation as there is no continuous vertical channels and hence the flow into each of the interdendritic regions will be independent,

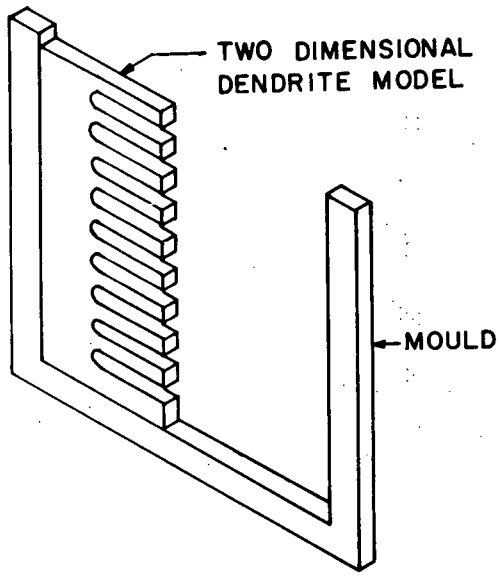

Figure 52. The two dimensional experimental model for observing interdendritic flow.

to a large degree, of the regions above and below it. Figure 53 shows three runs with this model. Figure 53a was quenched 60 seconds after the tracer was introduced and had a temperature difference of 3.68°C across the molten pool. Figure 53b was also quenched 60 seconds after the tracer was introduced but had a 5.02°C temperature difference. Figure 53c shows a casting quenched ten minutes after the tracer introduction and had a 5.18°C temperature difference. All the castings are pure tin with radioactive tin tracer. The autoradiograph film was exposed to a light with the casting on the film and the dendrite block removed. This causes the interdendritic regions to appear light since they were shielded and the areas where the dendrite block was, now appear dark in the autoradiograph. It is evident that there is very little penetration into the interdendritic region. There is a slight increase in the penetration by increasing the gradient from 3.68°C to 5.02°C but very little increase in penetration is shown by leaving the system for an additional nine minutes. From this simple model, if the assumptions for its use are correct, it must be concluded that there is no significant interdendritic flow resulting from the residual liquid pool convection.

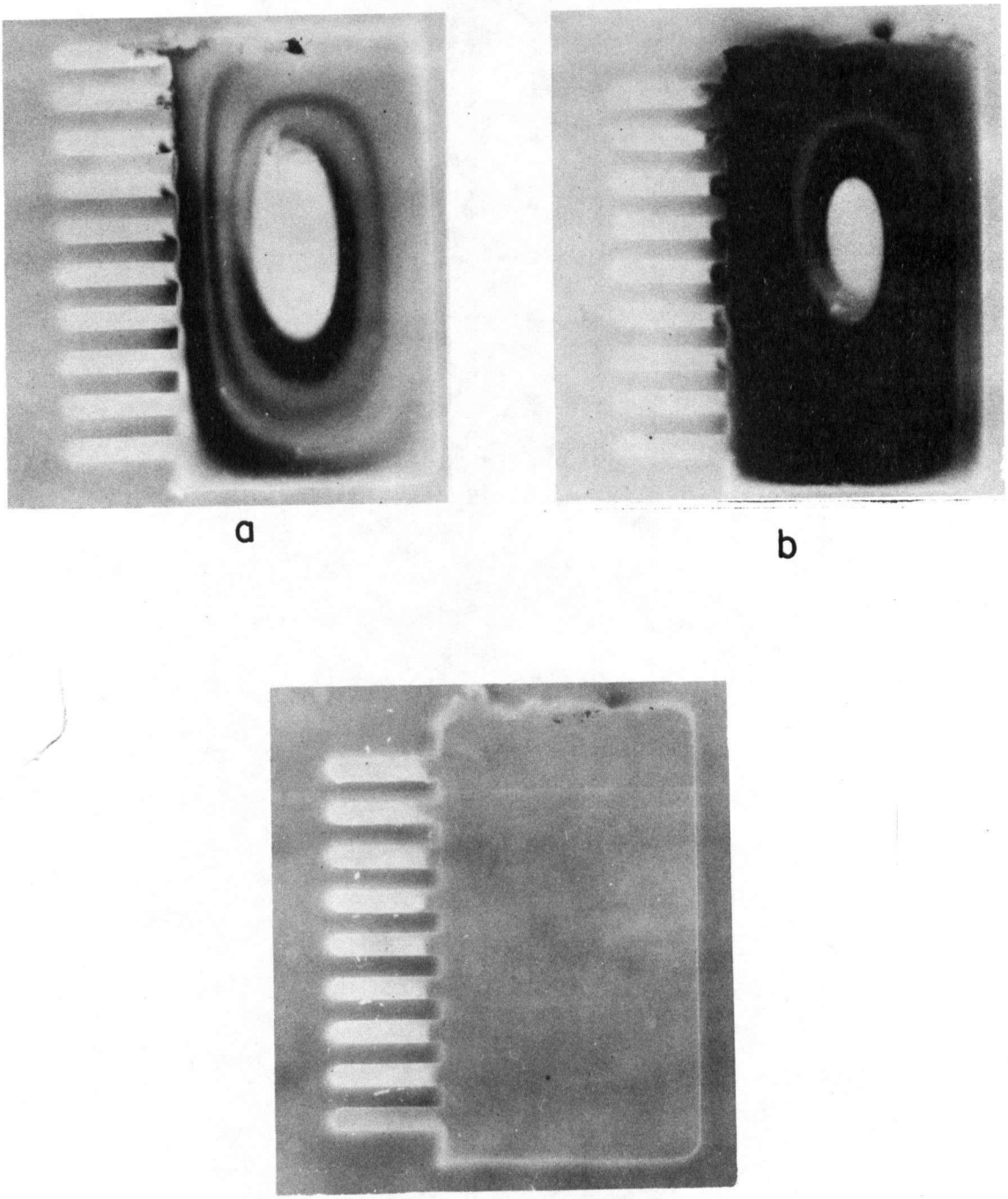

Figure 53. The experimental results of the model of Figure 52 with a pure tin melt (Sn^{113} tracer) with a temperature difference across the pool and a time before quenching of (a) 3.68°C, 60 seconds, (b) 5.02°C, 60 seconds, and (c) 5.18°C, 600 seconds.

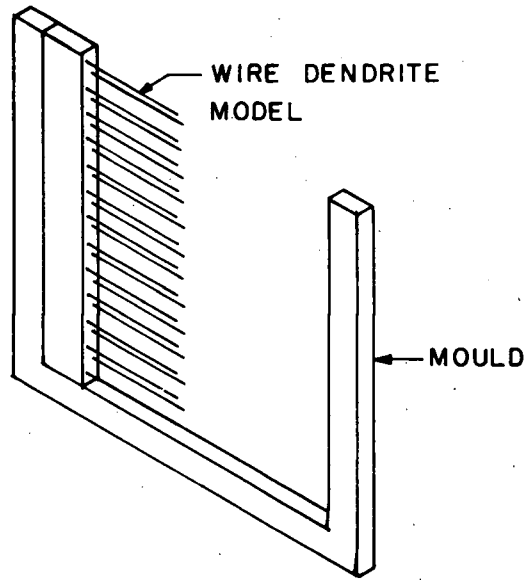

Figure 54. The three dimensional wire rod model for observing interdendritic flow.

6.2. Three dimensional wire model

The experimental configuration for the three dimensional model is shown in Figure 54. A copper block, the same thickness as the cell, with twenty-six stainless steel wires of 0.035 inch (0.89mm.) diameter protruding approximately two centimeters from the block, is placed in the cold end of the cell. The evenly spaced steel wires represent the dendrite interface in this experimental model. This model is more realistic than the two dimensional one as this allows vertical flow channels for the liquid metal flow. The main approximations in this system are that there is no decrease in the liquid to solid ratio back from the molten pool into the mushy zone and that the number of wires that could be equally spaced in the block

was limited. The wires tend to bend and several wires could come into contact which would change the geometry significantly. For the case studied here the mushy zone was 17% solid with a 1.9 mm. dendrite spacing. This dendrite model does not take into account dendrite side branching which may possibly affect the resulting flow.

The interdendritic flow through this model with a pure tin melt and a 5.73°C temperature difference in the molten pool is shown in Figure 55. The wires are in the cooler left-hand side of the cell as for actual growing interfaces. Figure 55a shows the flow pattern on the sample surface and Figure 55b shows the flow pattern 0.45 mm. below the surface of the 3.1 mm. thick sample. The end of the wire dendrite zone is marked by the arrows on the figure. The flow is seen to penetrate the mushy zone all the way to the copper base block with a one cell flow pattern in the bulk fluid. The interior view, Figure 55b, shows a very similar flow penetration through the mushy zone and the pool flow is also similar to the surface pattern. It is evident from the interior view that the flow rate through the wire dendrite zone is slower than in the fluid bulk. The bulk flow has completed over one cycle while the main part of the interdendritic flow has only progressed three-quarters of the way down the mushy zone, as seen by the tracer front in the mushy zone in Figure 55b. Figure 56a shows another run that is experimentally similar

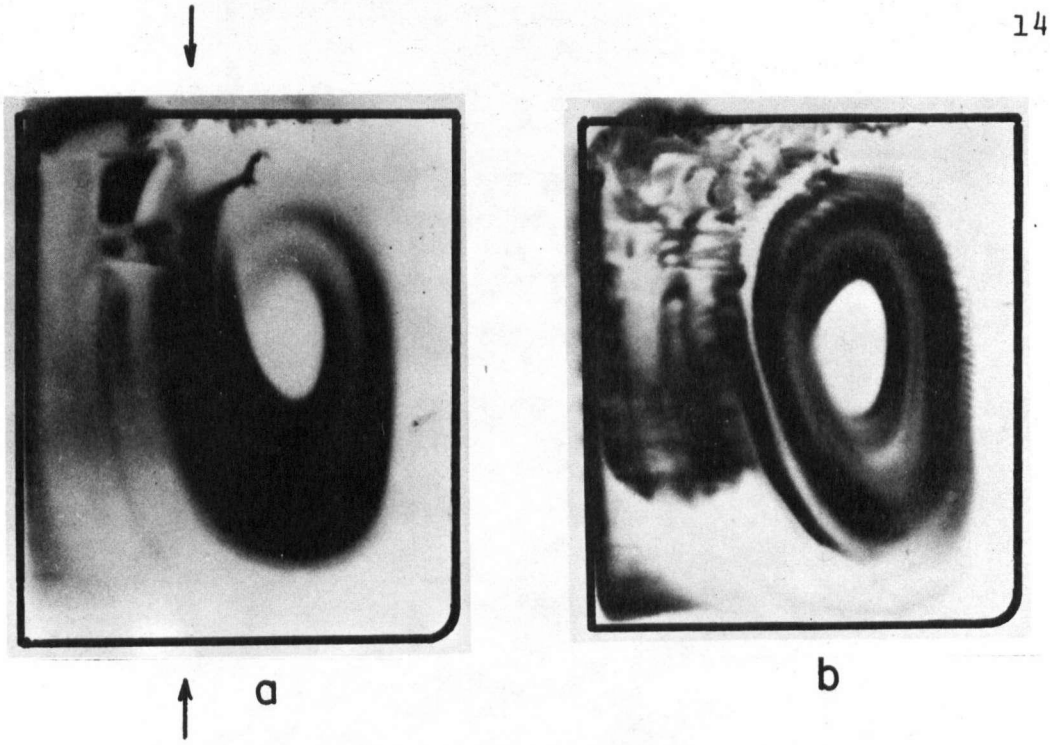

Figure 55. The tracer distribution in the system of Figure 54 (tin melt, Sn^{113} tracer) with a temperature difference of 5.73°C across the pool showing (a) the as cast surface and (b) the profile 0.45 mm. below the surface.

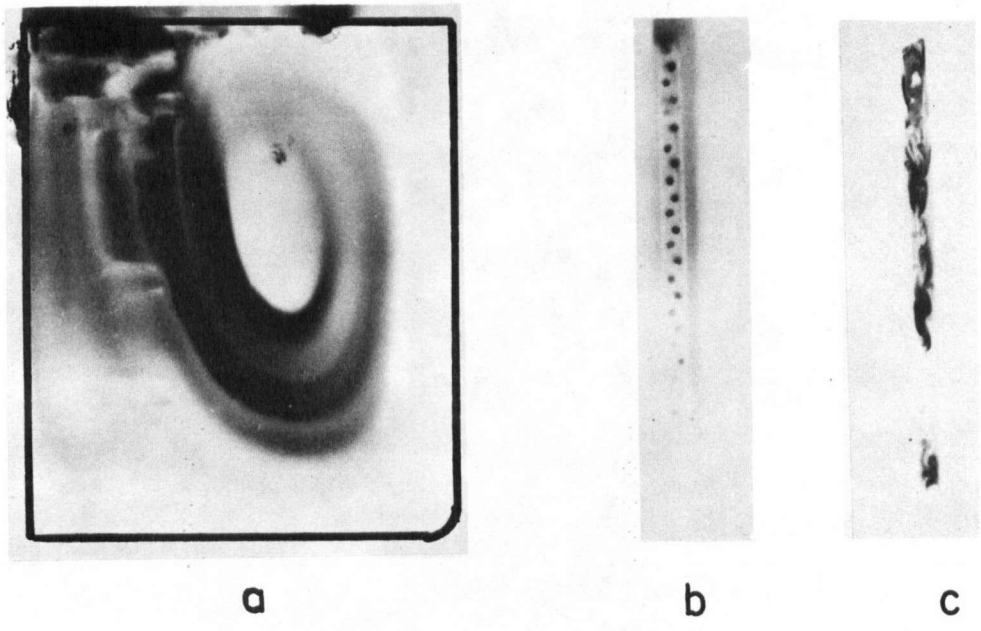

Figure 56. The tracer distribution in the system of Figure 54 (tin melt, Sn^{113} tracer) with a temperature difference of 5.1°C across the pool showing (a) the as cast surface, (b) the left hand end of the block with the wires removed, and (c) the left hand end with 3/8 inches of the block end removed.

to the sample of Figure 55. The outer flow and the inter-dendritic flow are very similar to the flow of Figure 55. Figure 56b and Figure 56c show the end view of the sample looking at the dendrite end and the end view with 3/8 inch machined off the sample, respectively. The wire dendrites have been removed from the sample for Figures 56b and 56c by simply mechanically pulling them out of the soft tin block. No distortion results from removing the wires. The as cast end view shows little tracer in the casting except for small trails of tracer down from the wire dendrite positions in the upper regions. The holes where the wires were pulled out appear dark due to the radiation coming from the more active interior of the casting down the hole left by the wire. The wire distribution can be readily seen in this picture. Figure 56c further into the end of the casting shows that the flow is quite complex around the wires.

The retarding force due to these artificial dendrites seems significantly large considering the low percent solid and the large dendrite spacing of 1.9 mm. Also the very smooth nature of the wires and their regular spacing should allow greater flow than an actual interface of equal average spacing and percent solid since side branching will undoubtedly retard flow. This model indicates that an actual dendritic interface will very greatly retard fluid motion as even this model with its many less restrictive properties reduces the flow substantially.

6.3. Wire mesh model

All the conditions of an actual dendrite interface are impossible to meet with an experimental model. From the two preceeding models it is evident that a three dimensional model must be used to get any correlation. Other desirable features are a change in the solid-liquid percentage and the dendrite spacing. Also the liquid metal should wet the artificial dendrites as in a real interface but not dissolve the artificial dendrites significantly during a test. After considering all these conditions the model shown in Figure 57 was chosen for extensive experimental analysis. A wire mesh is placed vertically in the 0.31 cm. wide mould. The mesh slides into slots on the two large wall faces and into a slot in the U shaped piece of the mould to prevent any leakage around the edges of the mesh. A temperature gradient is then placed across the cell as shown schematically in Figure 58 and a flow develops as shown in this figure. Due to the flow coming across the bottom of the liquid cell towards the mesh there will be a flow through the mesh from the large flow cell to the small flow cell. Similarly there will be a flow out of the small flow cell into the large flow cell at the top of the cell. The vertical mesh represents a position in a dendritic interface of an equal solid-liquid ratio and dendrite spacing.

A series of meshes are used with a range of wire size and wire spacing. Table VIII lists the properties

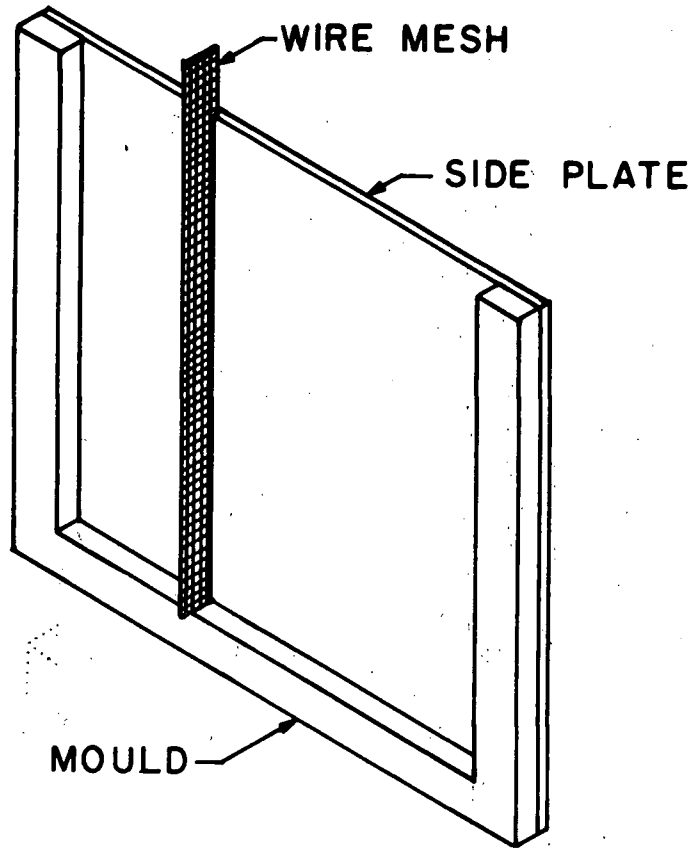

Figure 57. The three dimensional wire mesh model for observing interdendritic flow.

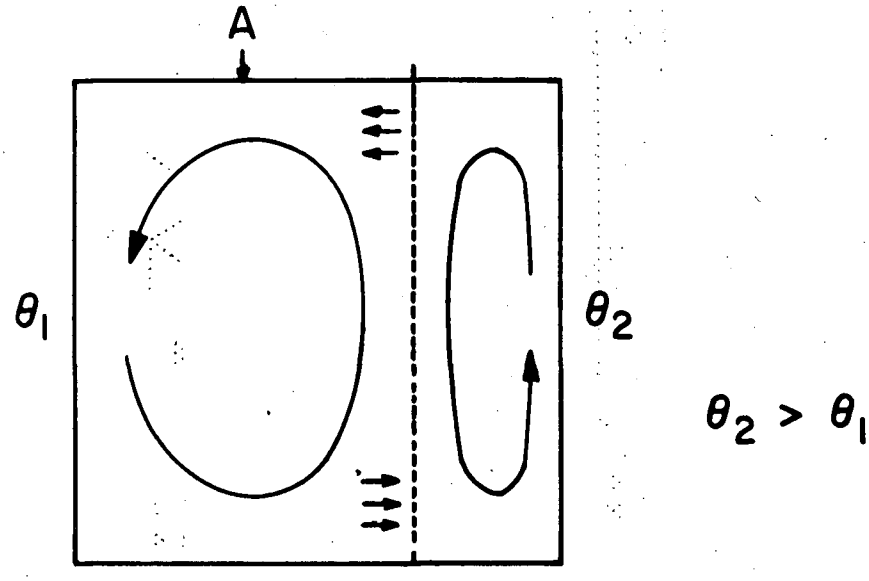

Figure 58. The qualitative flow lines in the system of Figure 57 showing the two flow cells and intermesh flow directions.

TABLE VIII.

Data on Wire Meshes Used in Flow Experiments

and Fraction Flowed Results

Mesh Properties					Experimental Results		
Sample Number	Mesh Number wires/inch	Wire Diameter d_w, mm.	Wire Spacing S_a, mm.	Hole Size h_a, mm.	Counts, large cell	Counts, small cell	Fraction Flowed
1	100	0.114	0.254	0.140	9559	1692	0.1073
2	100	0.102	0.254	0.152	7368	662	0.0824
3	80	0.165	0.317	0.152	11374	266	0.0229
4	80	0.127	0.317	0.191	8445	409	0.0462
5	60	0.241	0.424	0.183	7384	259	0.0339
6	60	0.178	0.424	0.246	7348	720	0.0892
7	40	0.279	0.635	0.356	6934	311	0.0429
8	40	0.216	0.635	0.419	10330	1149	0.1001
9	30	0.330	0.846	0.516	6569	279	0.0407
10	30	0.254	0.846	0.592	7121	2410	0.2529

of the specific wire meshes used. All the meshes studied were square woven and were either of copper or phosphor bronze. For the experiments pure liquid lead was used with radioactive thallium tracer. The mesh was coated with a soldering type flux and then dipped in a bath of molten lead before being inserted into the slots in the mould. This gave a thin layer of lead on the wire mesh so that there was a good wetted surface for the experiment. All the experiments were conducted with a temperature difference across the cell of 6.05 ± 0.05°C so the driving forces present for the intermesh flow was constant for all tests.

Figure 59 shows a section view of the casting

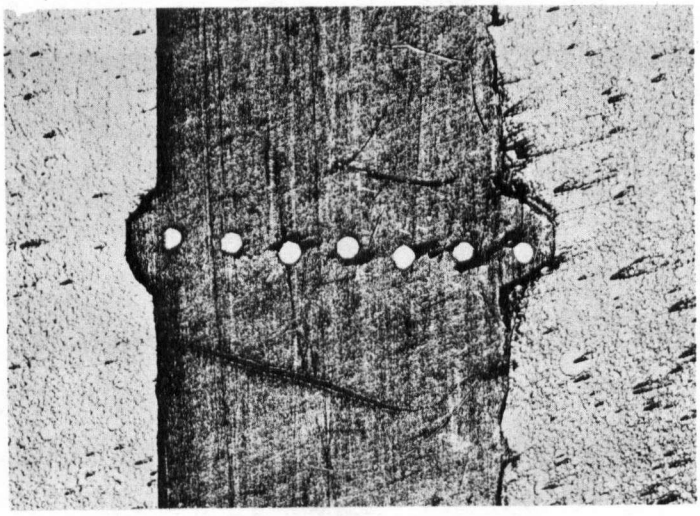

Figure 59. A micrograph of a cross section of a wire mesh in an actual lead sample that has been mounted and polished.

showing the view of a number 40 mesh embedded in the casting. The mesh is seen to be perpendicular across the mould so that the lead has no path around the mesh. By the regular nature of the wires it would appear that there is little dissolution of the mesh by the molten lead.

Figure 60 shows the flow patterns that result for the various mesh sizes. The tracer is introduced at point A on Figure 58. At least two runs were done with each particular mesh and the sample that showed the least flow from the large to the small flow cell was used in the analysis to follow. This method was used as any deviation such as flow past the side of the mesh, a large degree of dissolution of the mesh by the molten lead or an irregularly woven mesh would all cause an increase in the observed flow. Thus if the minimum flow is used it would better correspond to the original dimensions of the mesh. The four castings of Figure 60 correspond to samples 2, 4, 5 and 10 of Table VIII. For quantitative analysis of the flow through the wire mesh in these samples a radioactive counting technique was used. The counting apparatus used is shown in Figure 61. A two inch scintillation tube was used, connected to a Hamner modular amplifier, timer and scaler. The activity of the large flow cell and of the small flow cell of the solid block were counted separately as shown in Figure 61. The block was counted still intact by sheilding one part of the sample with a lead shield. All

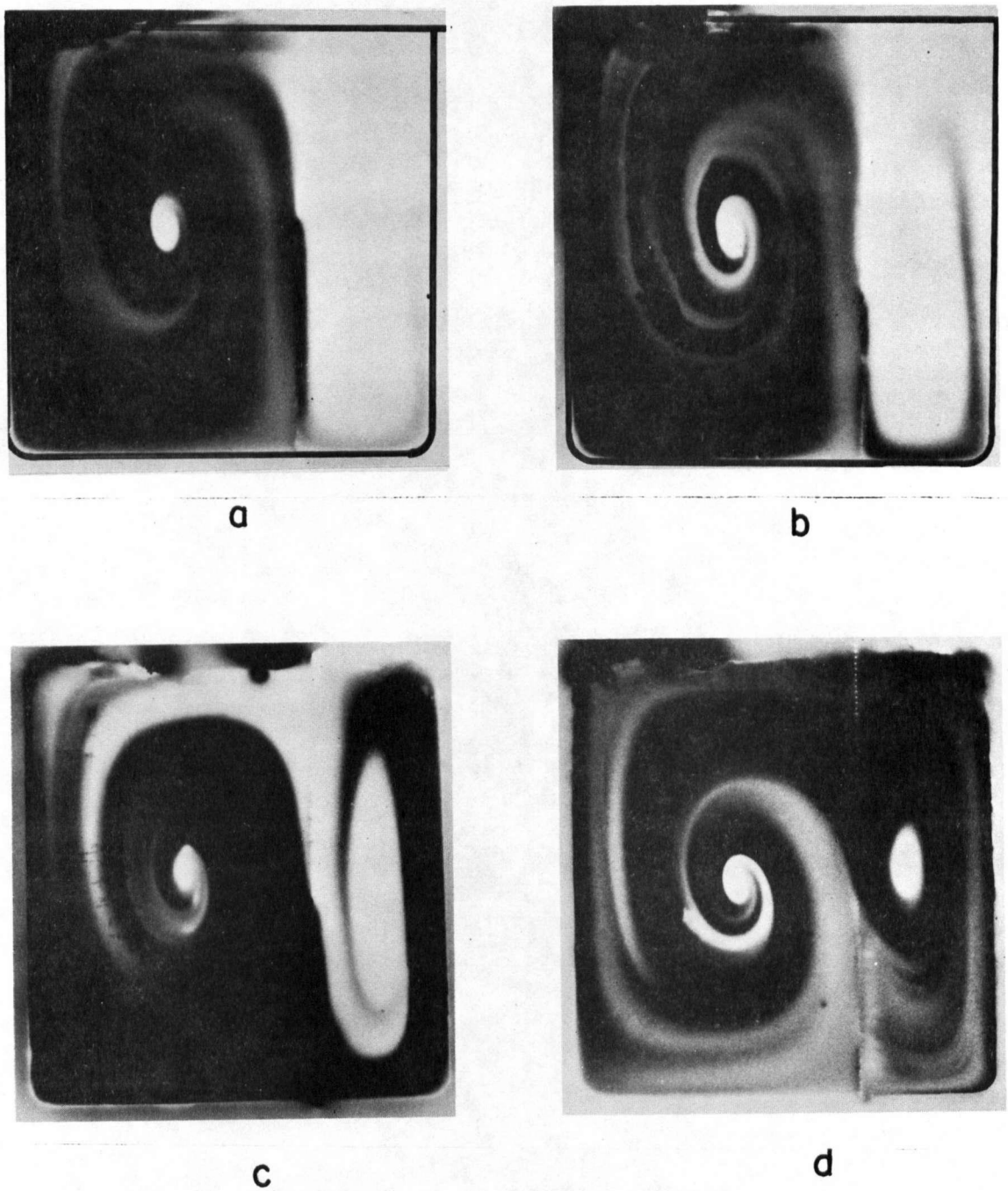

Figure 60. The tracer profile of the intermesh flow that occurs in 120 seconds after the tracer introduction with a 6.05°C temperature difference for samples corresponding to number (a) 5, (b) 4, (c) 2, and (d) 10 sample of Table VIII.

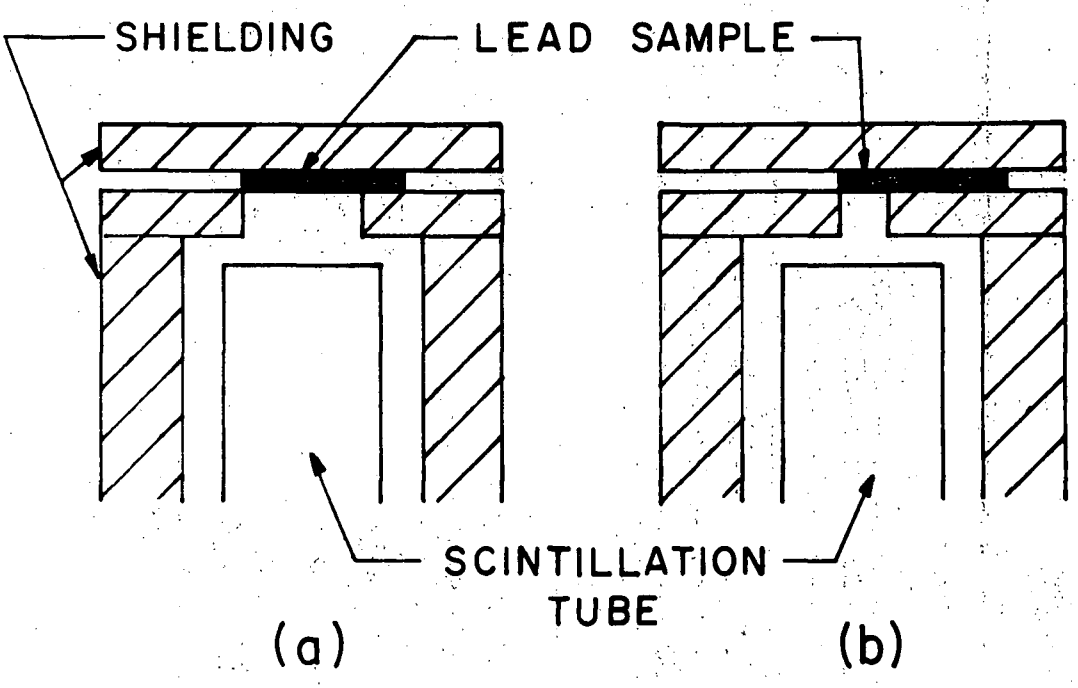

Figure 61. The counting arrangement for monitoring the activity in the (a) large flow cell and (b) small flow cell in the intermesh flow samples.

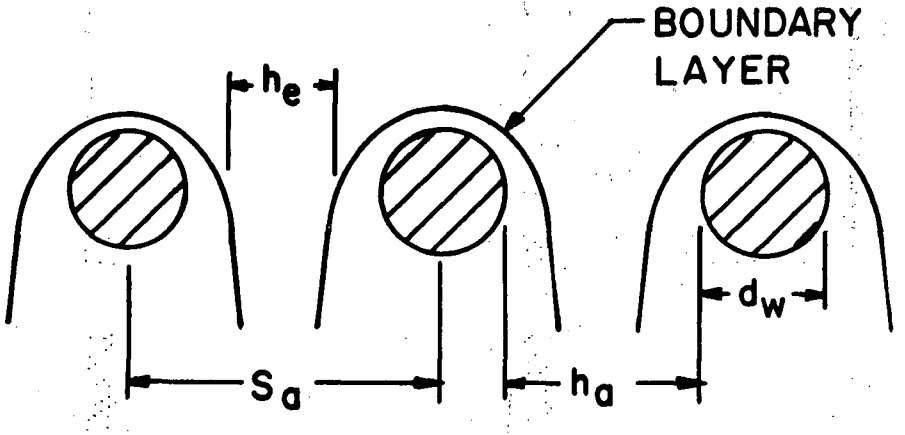

Figure 62. The boundary layers around the mesh wires showing the notation used in the analysis.

counts were corrected for background. The degree of intermesh flow is taken as a ratio of the number of counts from the small flow cell over the sum of the counts from the large flow cell plus the small flow cell. This is essentially the fraction of the tracer that has gone through the mesh. Table VIII lists this information for each sample as fraction flowed, f.

The interpretation of these results has proven quite complex. Various plots of flow versus some of the relevant variables such as wire size, wire spacing, percent solid or ratios of wire diameter to wire spacing give scattered arrays of individual points without any indication of a simple functional relationship between the variables.

The flow through the mesh can be taken as equivalent to flow past a series of cylinders placed horizontally and vertically. Figure 62 shows a sketch of the boundary layer type of flow around a portion of such a system. S_a is the wire spacing, d_w the wire diameter and h_a the distance between the wires. Due to a boundary layer building up around the wires resulting from the intermesh flow, the flow itself will be reduced. A parameter, h_e, the effective flow width between the wires can be taken as the distance between the boundary layers of two adjacent wires. For this analysis it will be assumed that the effective hole size and hence the flow, is a function of the geometric shape of the mesh and also the actual physical size of the

mesh. Figure 63 is a plot of the fraction of tracer that flowed through the mesh, f, versus the ratio of the inter-wire spacing to the wire diameter, h_a/d_w, a geometric non-dimensional factor. The number on each point is the normal mesh size in numbers of wires per inch. It should be noted that a single line through all the points is impossible. This shows that the flow is not related to this geometric factor alone. The relevant information that is desired from this analysis is the conditions for no flow through the mesh. Therefore, for each wire spacing (i.e. mesh size) a line is drawn back to the abscissa for the value of h_a/d_w for no flow. The results are not completely consistant, especially the 80 mesh results, but are reproducible. The zero flow values from Figure 63 are now plotted against the actual wire spacing in Figure 64. This plot gives the experimental conditions for no flow through a mesh. The straight line produced is:

$$S_a = 0.061(h_a / d_w) + 0.0102 \qquad (6.1)$$

where S_a is in centimeters. With a suitable interpretation of equation (6.1) it is possible to predict for an actual interface the function between the fraction solid and the dendrite spacing for no interdendritic flow to occur. Figure 65 shows a model of a dendritic interface perpendicular to the primary stalks. Only a very simple model is chosen, as the results from the mesh experiments are at best very limited. For this model:

$$\text{Fraction solid} = F_s = (\pi d_w^2) / (4S_a^2) \qquad (6.2)$$

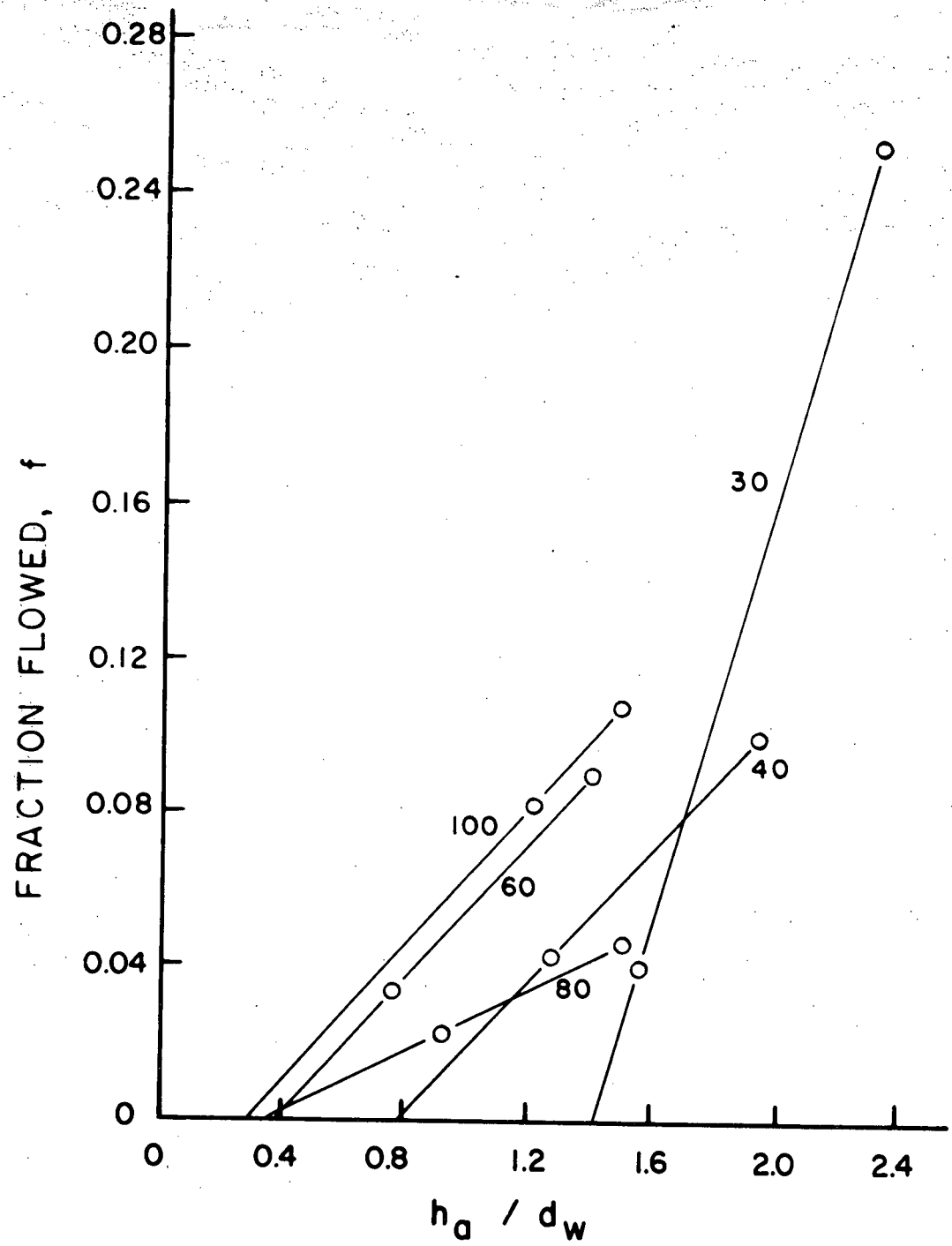

Figure 63. A plot of the fraction flowed, f, versus the ratio of the hole size to the wire diameter, h_a / d_w, for the various mesh sizes investigated.

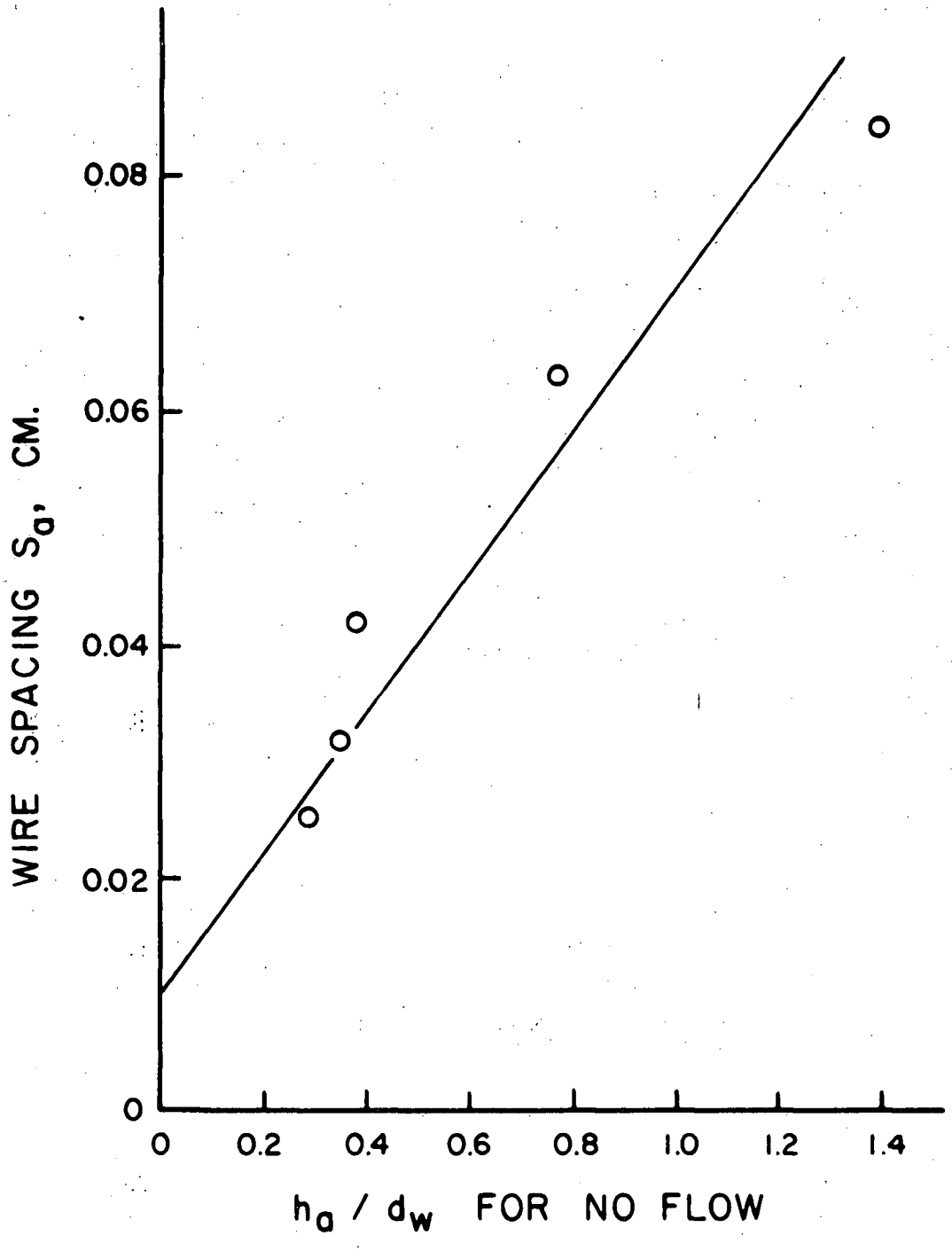

Figure 64. A plot of the wire spacing, S_a, versus the ratio of the hole size to the wire diameter, h_a / d_w, for the no flow condition (f = 0) from Figure 63.

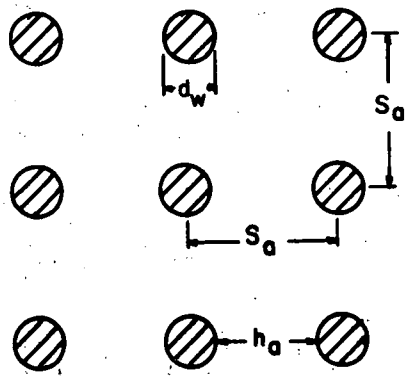

Figure 65. A perpendicular view of the primary dendrite model used in the interpretation of the intermesh flow results.

Also from the geometry:

$$\frac{S_a}{d_w} = 1 + \frac{h_a}{d_w} \tag{6.3}$$

Combining equations (6.1), (6.2) and (6.3):

$$F_s = \left(\frac{0.054}{S_a + 0.051}\right)^2 \tag{6.4}$$

where S_a is in centimeters. Therefore, there should be no flow through the mushy zone when

$$F_s \geq \left(\frac{540}{S_a + 510}\right)^2 \tag{6.5}$$

where S_a is in microns. Figure 66 shows equation (6.5) plotted out. The region above the curve represents conditions for no interdendrite flow and the area below the curve represents conditions for interdendritic flow. From the plot it is seen that for decreasing dendrite spacings the flow will penetrate deeper into a mushy zone since the

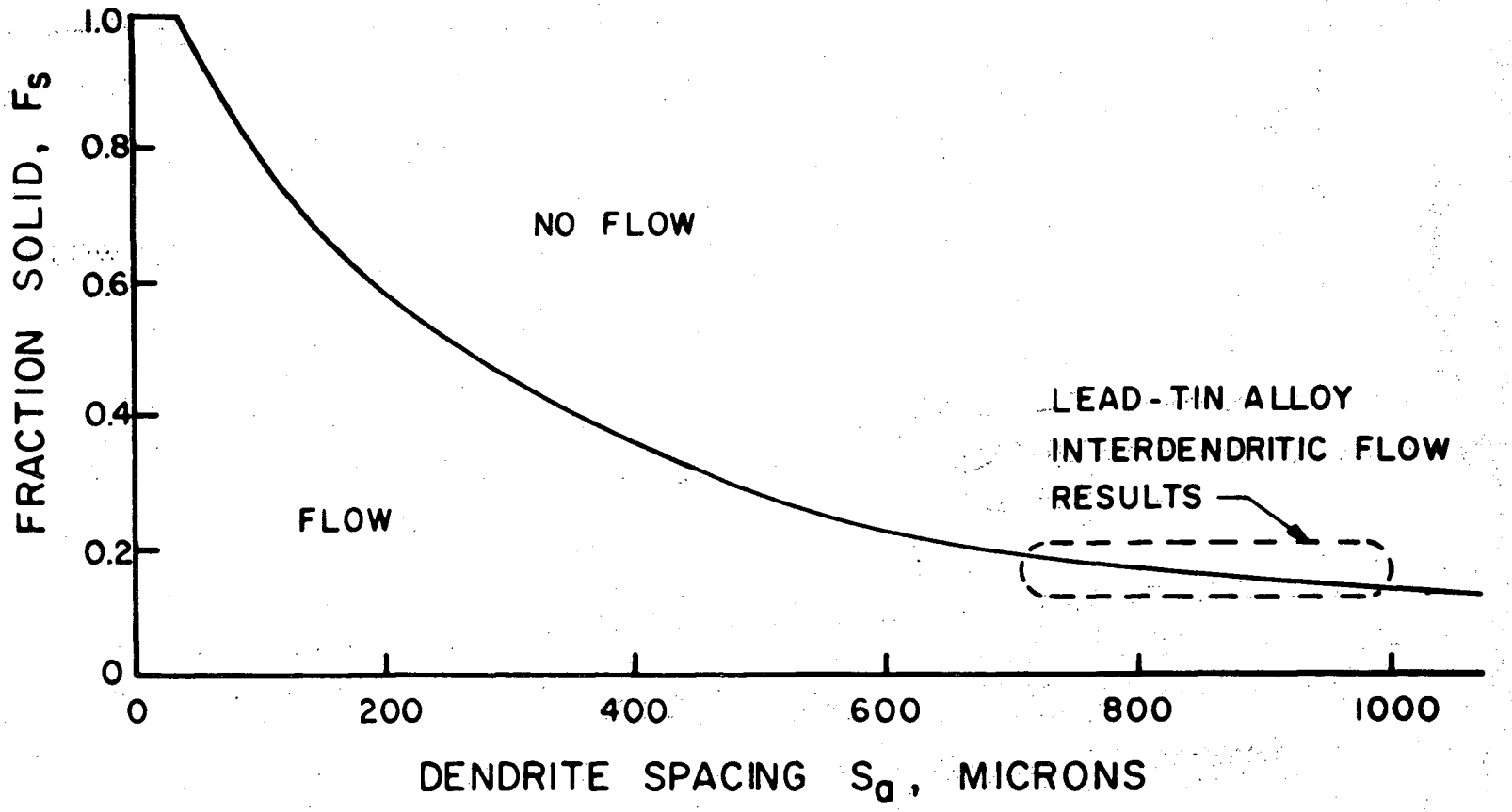

Figure 66. A plot of the fraction solid in the solid-liquid interface, F_s, versus the primary dendrite spacing showing the flow and no flow conditions obtained from the intermesh flow results. Also shown is the lead-tin alloy interdendritic flow results.

fraction solid for no flow conditions is higher. From equation (6.5) and Figure 66 it is seen that for a dendrite spacing of less than 30 microns the flow will completely penetrate the mushy zone, that is until $F_s = 1$. From these results it is reasonable to assume that the effects of interdendritic flow, such as dendrite remelting, channel formation and solute movement, will be more pronounced the finer the dendritic structure, due to the depth of penetration of the flow. It should be noted that this theory does not include any dependence on the temperature gradient and hence the depth of the mushy zone, but is only a function of the fraction solid and dendrite spacing.

6.4. Interdendritic flow in lead-tin alloys

To observe interdendritic flow directly and to test the hypothesis presented based on a theoretical mesh model several experiments were conducted to observe the interdendritic flow in lead-tin alloys. The experimental conditions are shown in Figure 67. The 10.8 cm. by 6.4 cm. by 0.31 cm. mould was used in the experiments. Solid was nucleated at the cold end and solidification was allowed to progress across the mould. Three thermocouples were placed in the upper regions of the cell for measuring the temperature gradients and monitoring the solidification process. When the solid had progressed to approximately the half way point, a radioactive master alloy of an

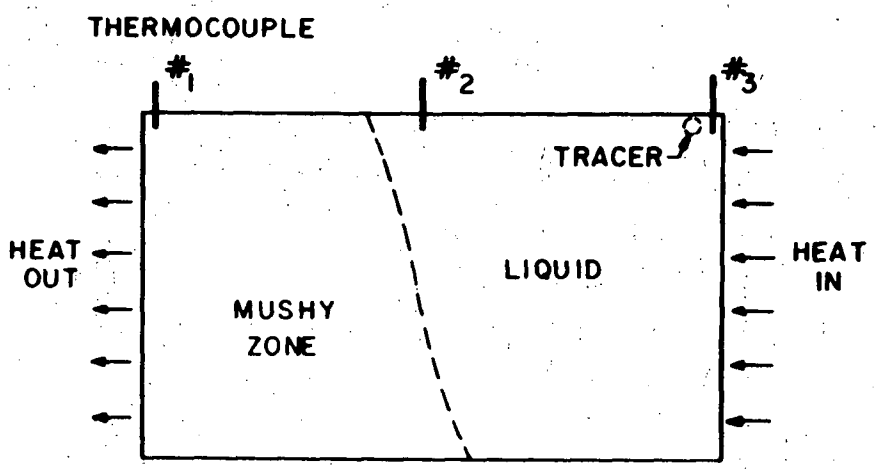

Figure 67. The experimental conditions used for observing interdendritic flow in lead-tin alloys showing the thermocouple and tracer addition positions.

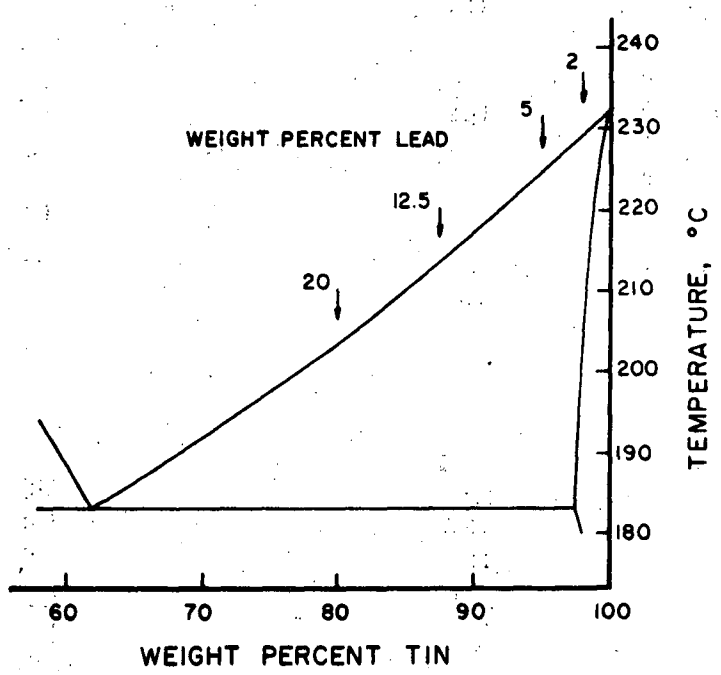

Figure 68. The relevant portion of the lead-tin phase diagram showing the four alloys used to observe interdendritic fluid flow.

equivalent density as the bulk fluid was introduced and allowed to flow for a short period before being quenched. Four different alloys of lead-tin were used, 2, 5, 12.5 and 20 wt. % lead in tin and also pure tin. The phase diagram for the lead-tin system for the relevant alloys is shown in Figure 68 with the various alloys shown on the diagram.

The casting produced by using a pure tin melt is shown in Figure 69. The solidification front is easily seen and appears to be planar. The solid region is on the left and the flow in the remaining liquid is readily seen. The shape of the interface is in agreement with the shape described in the Introduction and is caused by the thermal convection altering the heat flow conditions. In this run as in all others in this section the solidification rate is of the order of 2 - 5 cm./hour and the tracer is left 30 seconds before quenching so that very little interface movement occurs while the tracer is in the melt. Thus the tracer represents the interface at an instant in time due to the relatively large differences in the rate of the tracer and interfacial movements.

For all the alloy castings a dendritic type growth mode was observed. A casting of tin plus 2 wt. % lead plus radioactive thallium was directionally solidified the complete width of the mould. The thallium segregates with the lead to show the dendritic structure in

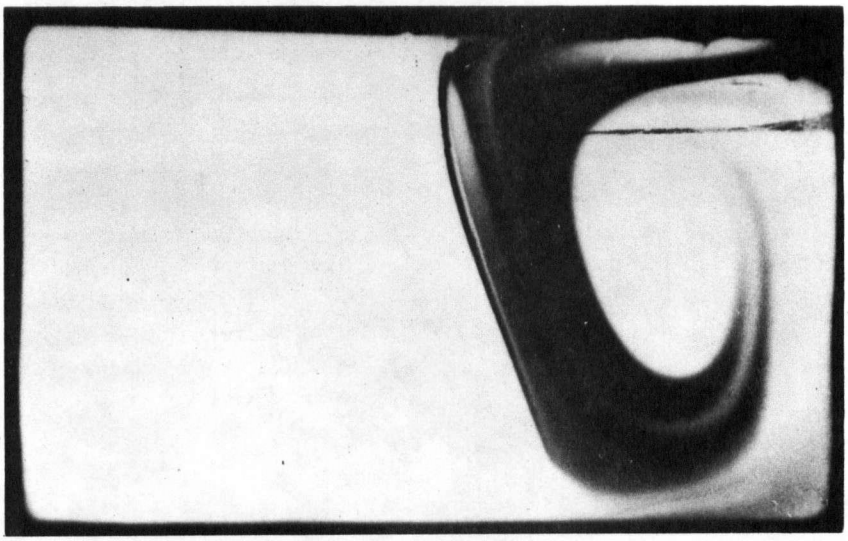

Figure 69. The tracer distribution in the residual liquid pool of a pure tin casting (Sn^{113} tracer) with the experimental conditions of Figure 67.

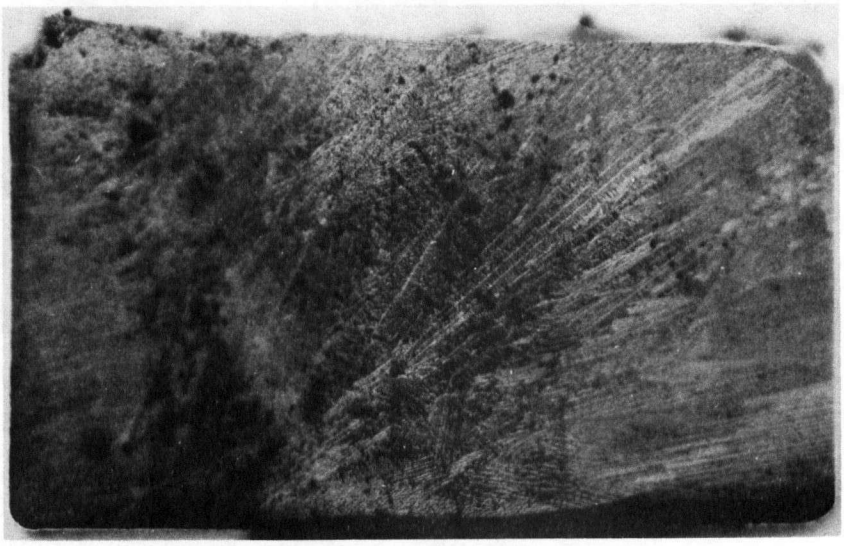

Figure 70. An autoradiograph showing the cast structure of a tin - 2 wt. % lead alloy directionally cast with Tl^{204} tracer.

the autoradiograph. Figure 70 shows a typical cast structure. The left-hand side is very irregular as this area is where the nucleation occurs at the start of the run and it requires a certain distance for the directional dendritic growth to stabilize. The growth direction is seen to be towards the upper right and this is controlled by the fluid motion in the liquid pool.

The resultant directional castings showing the interdendritic flow for the lead-tin alloys are shown in Figure 71. Table IX lists all the various casting conditions and results for the castings. The temperature gradient in the solid is obtained by assuming a linear gradient between the temperature at thermocouple #1 in Figure 67 and the temperature at the front of the mushy zone taken to be the liquidus temperature of the alloy in question. The flow penetration distance into the mushy zone is taken as an average penetration distance along the entire interface length from the original autoradiographs. To correct this distance to a fraction solid, the temperature difference between the outer edge of the mushy zone and the point of penetration is calculated. With the use of Figure 72 this temperature difference is converted to a weight percent solid. Figure 72, of weight percent solid versus the temperature below the liquidus temperature, is derived from the phase diagram in Figure 68. A plot of fraction solid at the penetration distance versus

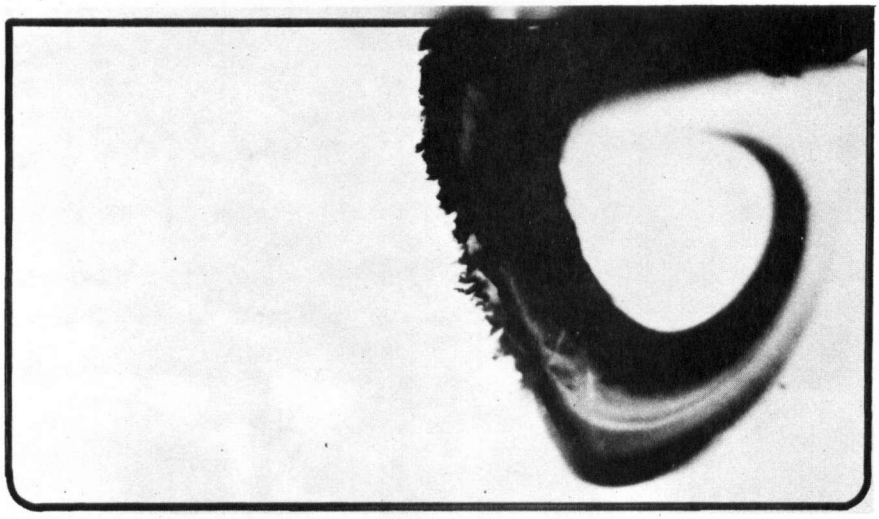

a

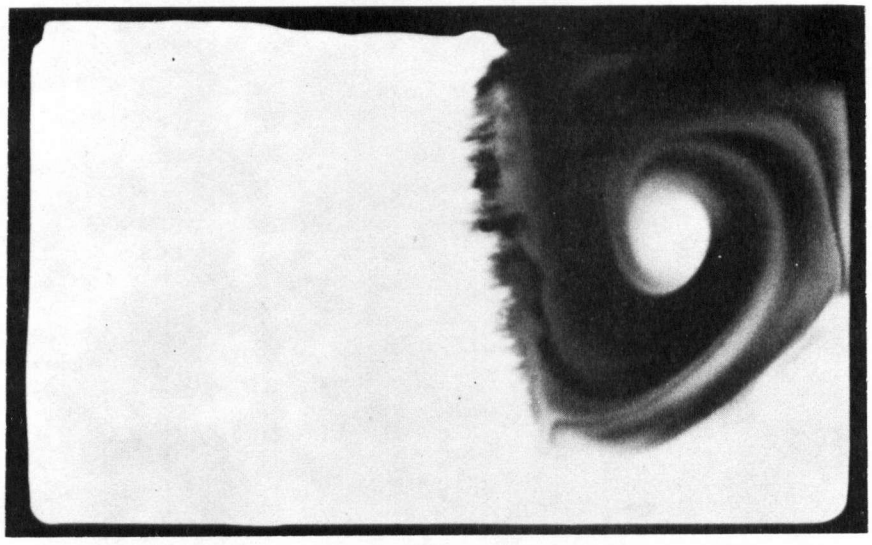

b

Figure 71. The tracer distribution showing interdendritic flow in castings of (a) tin - 2 wt. % lead and (b) tin - 5 wt. % lead with the casting conditions of Figure 67.

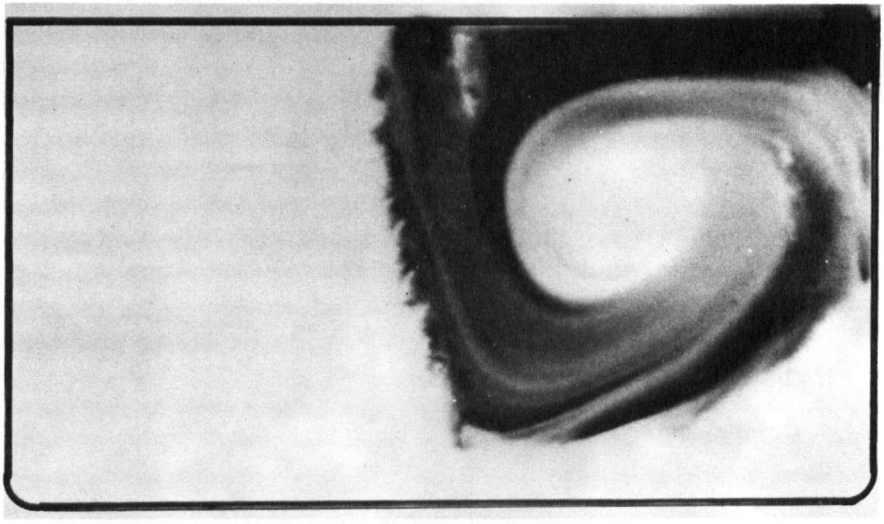

c

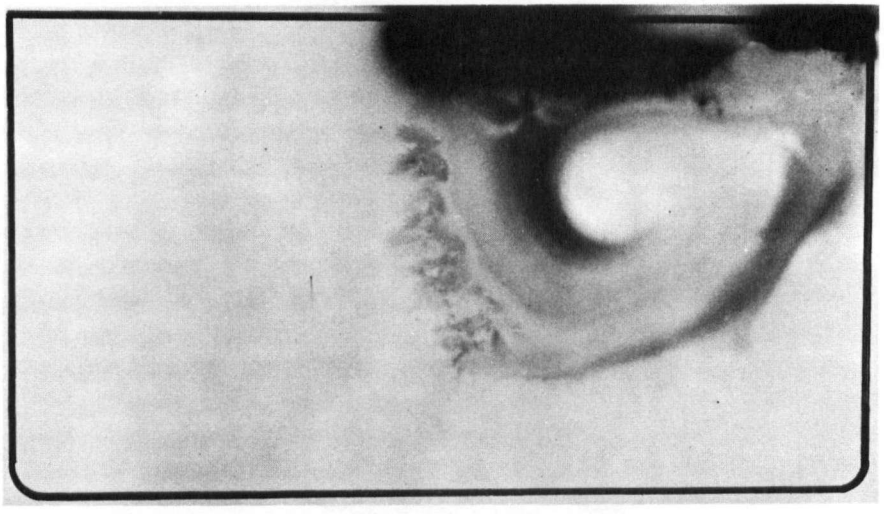

d

Figure 71 continued. The tracer distribution showing interdendritic flow in castings of (c) tin - 12.5 wt. % lead and (d) tin - 20 wt. % lead with the casting conditions of Figure 67.

TABLE IX.

Lead-Tin Alloy Interdendritic Flow Results

wt. % Pb	Temperature at T/C #1 °C	Liquidus Temperature °C	Temperature Gradient °C/cm	Flow Penetration mm. (Average)	Percent Solid for No Flow
2	212.5	229	3.69	2.0	22.5
5	206	224.5	3.08	3.7	16.0
12.5	192	213.5	5.20	4.0	11.8
20	186	203.5	3.50	8.9	12.5 } 11.3
20	186.5	203.5	4.07	6.1	10.0 }

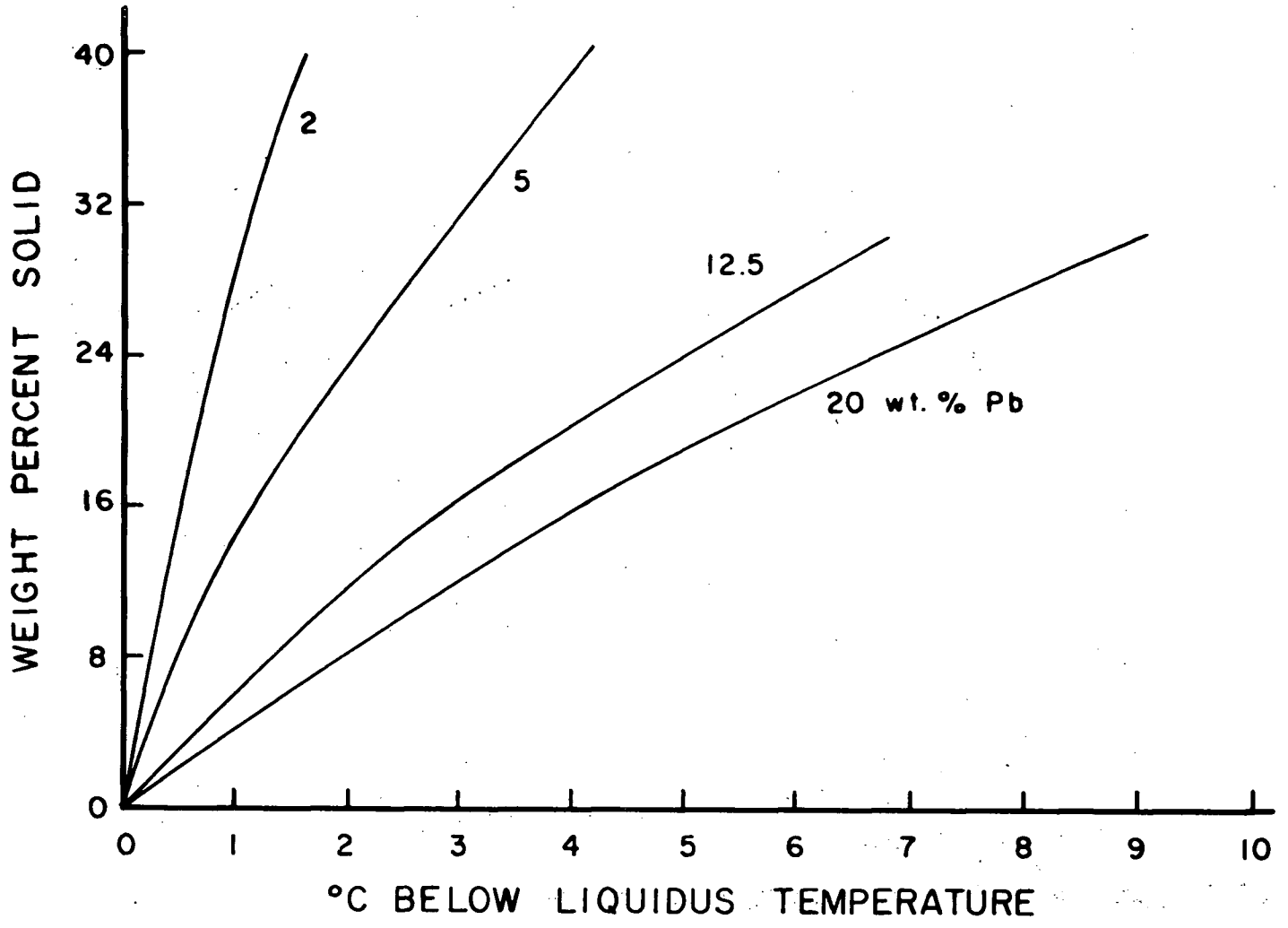

Figure 72. A plot of weight percent solid versus °C below the liquidus temperature obtained from the phase diagram of Figure 68 for the four alloys considered.

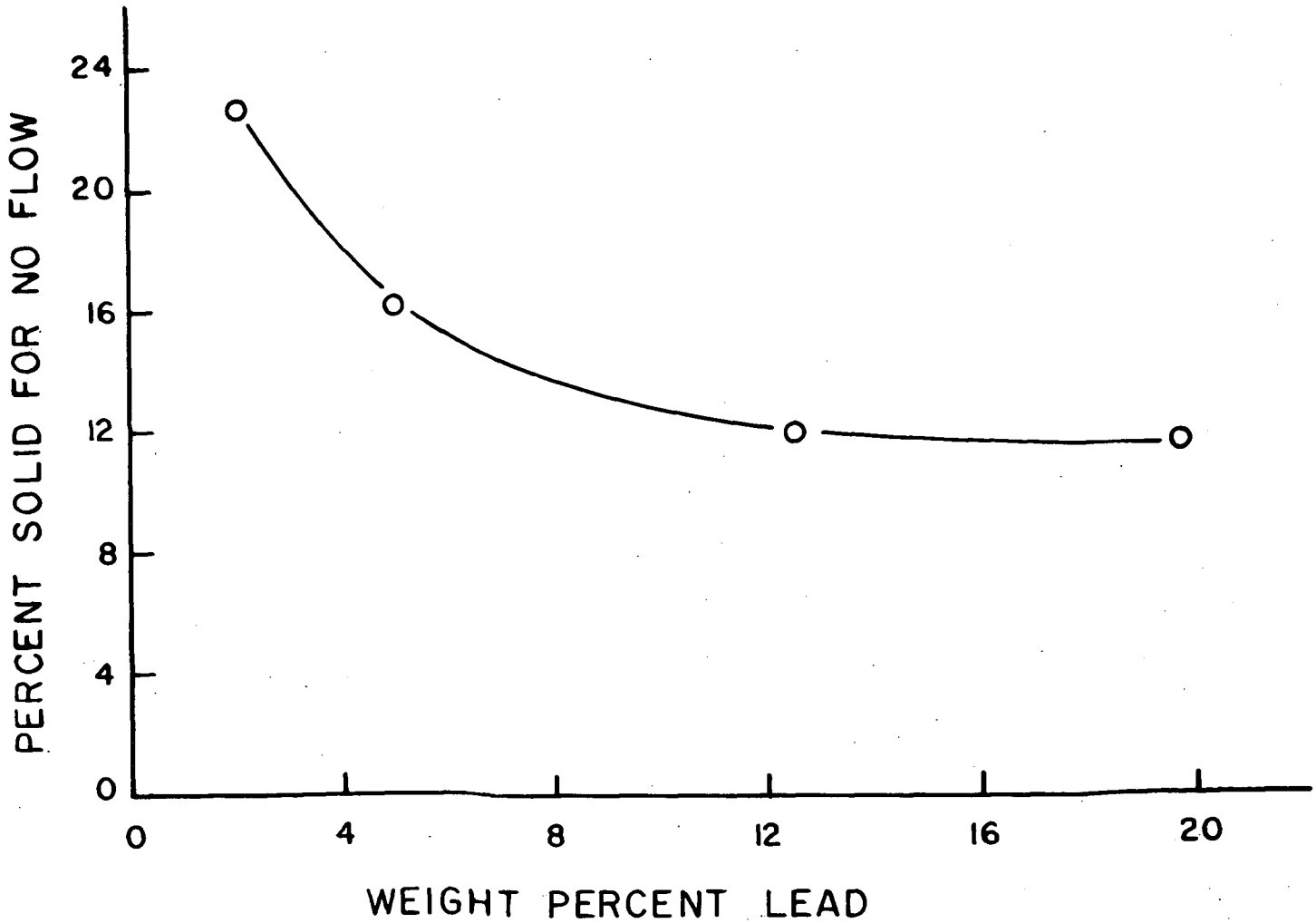

Figure 73. A plot of percent solid for no flow versus the weight percent lead for the lead-tin alloy interdendritic flow experiments.

the percent lead in the alloy is shown in Figure 73. The penetration distance appears quite insensitive to the lead content.

All castings had a very similar dendrite spacing. Exact measurements were quite difficult to accomplish but they were all in the range of 700 to 1000 microns. The lead-tin alloy interdendritic flow results are plotted on Figure 66. Due to the many limitations and approximations the results are remarkably consistent with the mesh model theory. Unfortunately, finer dendrites were not grown due to experimental limitations so that the whole range of Figure 66 could not be compared with actual interdendritic flow results.

A direct experiment can be conducted in which it is experimentally shown that the mushy zone is still very open and the fraction solid is still low past the depth of the tracer penetration. To do this an interdendritic flow experiment is done exactly as described above except that immediately prior to the quench a stainless steel wire, 0.6 mm. in diameter, is plunged into the liquid and pushed into the mushy zone. The diameter of the wire is about the same as the dendrite spacing so it should have no difficulty in penetrating the mushy zone to a considerable depth. This experimental casting is shown in Figure 74a. The casting is of 2 wt. % lead in tin and

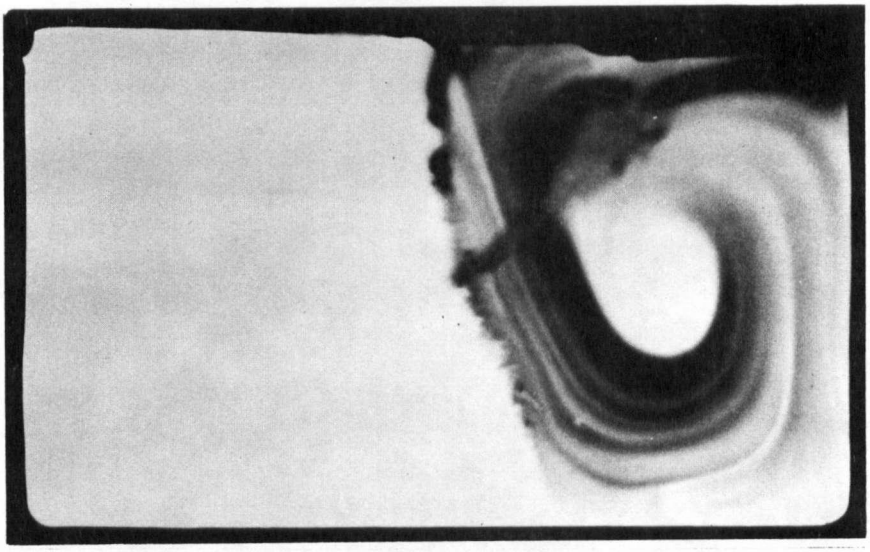

a

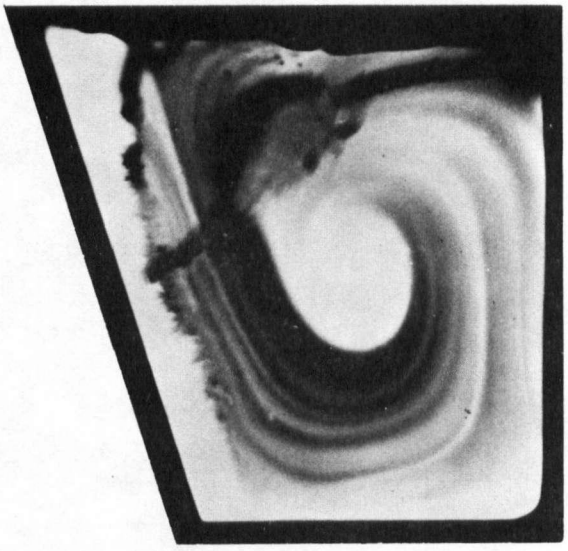

b

Figure 74. The tracer profile in a tin - 2 wt. % lead casting residual liquid pool showing the (a) interdendritic flow and the overall casting size and (b) the maximum position reached by the 0.6 mm. diameter wire into the interface.

is very similar to the casting of Figure 71a of the same alloy composition. The casting was machined down from the left-hand side at an angle the same as the observed interface until the top of the stainless steel wire was met. Figure 74b shows the outline of the casting remaining with the observed interdendritic flow stopping well before the penetration distance of the wire. This qualitatively shows that the mushy zone is still quite open and the fraction solid is low past the penetration distances observed for interdendritic flow.

Much has been said in the literature recently concerning the interdendritic flow caused by the pulling of liquid into the mushy zone by volume contraction. This should result in the pulling of liquid into the upper regions of the mushy zone and the rejection of liquid out of the lower regions of the mushy zone.

The case considered here is when the rejected solute is denser than the solvent as in the tin rich lead-tin alloys. In the experiments done to show the interdendritic flow in Figure 71 the mushy zone extended back to the left-hand end of the cell from thermal considerations so the whole left-hand region is a mushy zone. It is possible that the backflow from the shrinkage requires a longer time to occur than the 30 seconds before the quench of the previous experiments presented, such that the backflow will not be observed. If this is so by leaving

the tracer a longer period of time before quenching, the tracer will be allowed to flow into the upper regions of the mushy zone and the non-tracer material will be pushed out of the lower regions. Figure 75 shows a comparison between two identical runs of lead-tin alloy except the casting in Figure 75a was quenched after 30 seconds and the casting in Figure 75b was not quenched at all but was left to solidify completely. Radioactive tin was used so that there would not be any observed segregation of the tracer on solidification. No flow pattern is visible in Figure 75b since the tracer has a long period of time in which to be evenly mixed throughout the melt. It is easily seen that the shapes of the interfaces are almost identical. This shows that if there was any flow into the mushy zone as solidification progressed due to volume change on freezing or density difference in the inner regions of the mushy zone it does not cause any long range movement of liquid and the flow rates in the mushy zone must be extremely small.

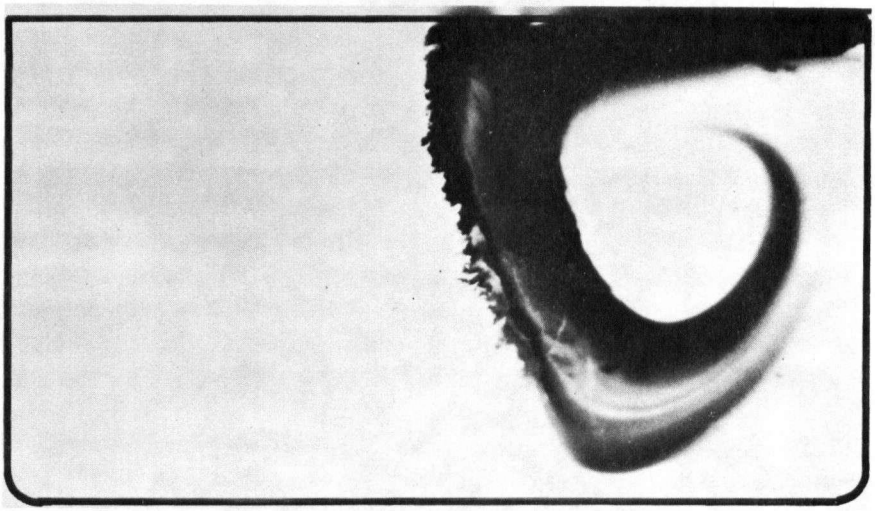

a

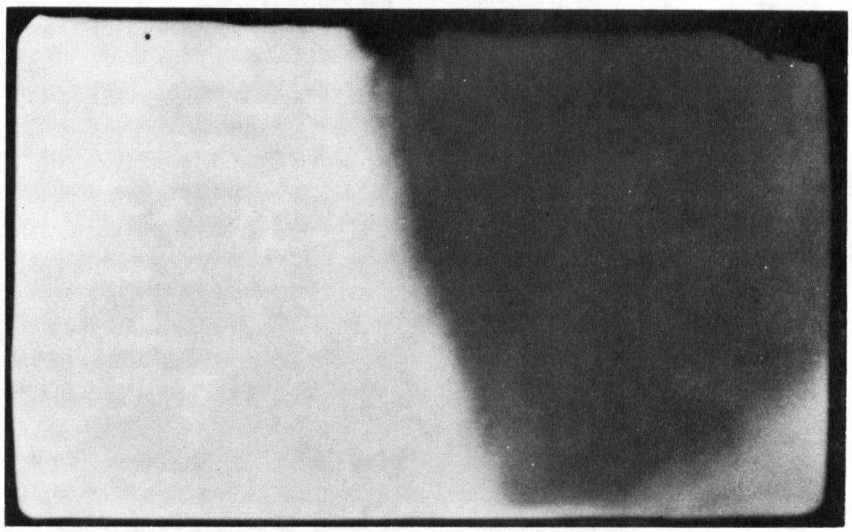

b

Figure 75. The tracer profile in a tin - 2 wt. % lead casting residual liquid pool with (a) quenching 30 seconds after the tracer introduction and (b) complete directional solidification of the casting without quenching.

7. Macrosegregation in Castings Rotated and Oscillated During Solidification

7.1. Introduction

Castings which have a small equiaxed grain structure are considered to be more homogeneous and to have better mechanical properties than equivalent castings with a partially columnar structure. One way of controlling the grain structure is by mechanically mixing the residual liquid during solidification. This can be done by moving the mould. Constant rotation of a cylindrical mould, radically cooled, will suppress the columnar to equiaxed transition (CET); oscillation of the mould will promote an earlier CET; and a stationary mould will have a structure between the rotation and oscillation cases (16, 42). The control of grain structure by mechanical mixing of the liquid during casting may cause macrosegregation -- (a function of the kind and extent of liquid mixing). In addition, rotational forces might influence solute transport in the liquid if there is a large density difference between solute and solvent. If macrosegregation

is enhanced by liquid mixing this could be detrimental to casting quality.

The purpose of the present investigation is to determine the extent of macrosegregation in stationary, rotated, and oscillated castings, and relate the results to the cast structure.

7.2. Experiment

The macrosegregation in the castings was determined by a radioactive tracer technique. The alloy used was Al-3 wt. % Ag made up of 99.99% Al and 99.8% Ag. The ingots were cylindrical, 3 1/4 inches in diameter and approximately 6 inches high. The casting apparatus used, Figure [76], enabled the casting of Al-Ag alloys to be made in stationary, rotating, or oscillating moulds. Melting was done in a graphite crucible in a resistance furnace. The alloy was superheated to approximately 800°C and immediately prior to casting, a small amount of radioactive Ag^{110} was added into the melt. The castings were all poured at 750°C (90°C superheat) into stainless steel moulds, water cooled before and during casting. A graphite hot top was used to keep the heat transfer from the upper surface to a minimum. Three casting conditions were used: stationary mould, rotated mould at 126 rpm, and an oscillated mould. The oscillation was a rotation of 126 rpm with the direction of rotation being reversed every five seconds.

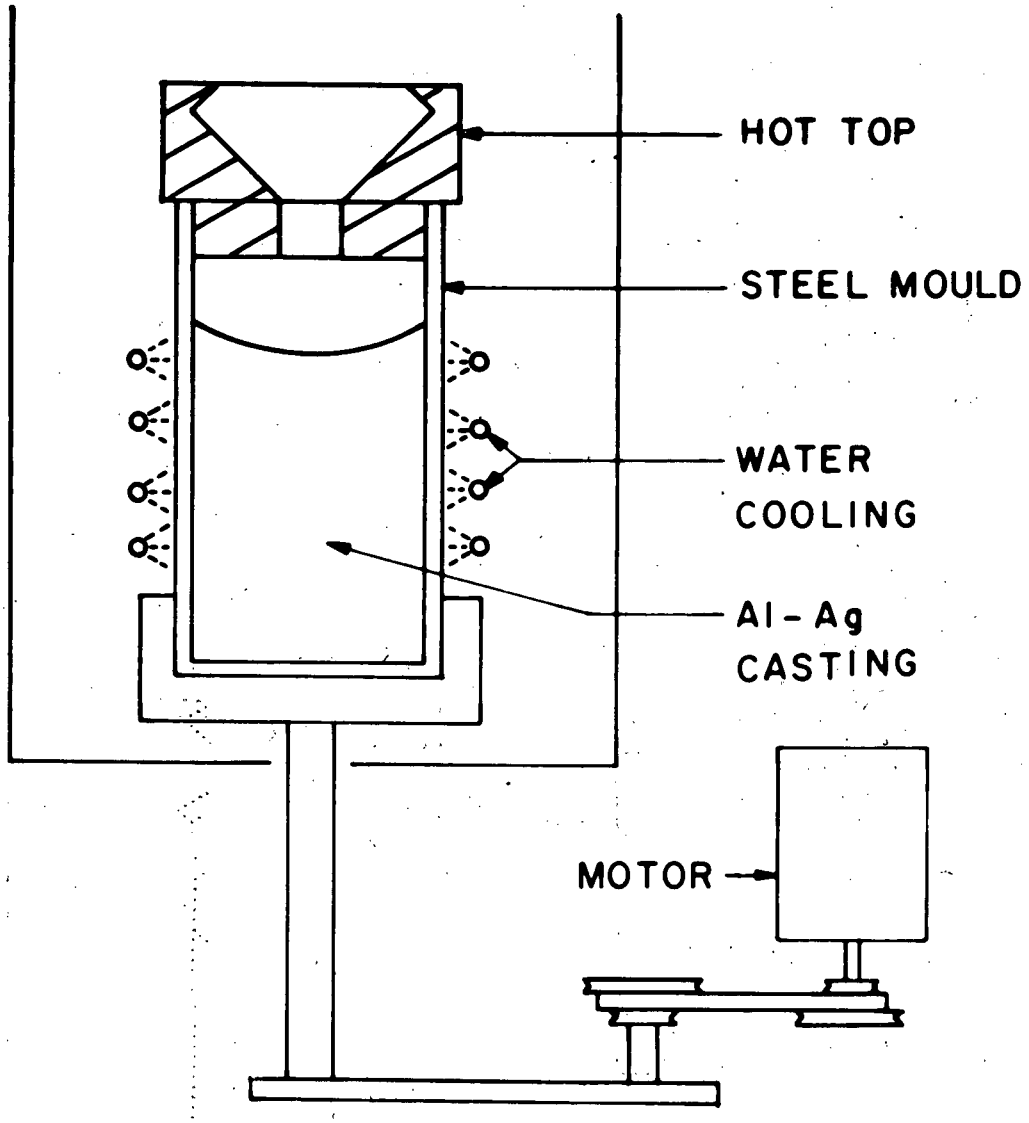

Figure 76. The experimental apparatus used for producing the stationary, rotated, and oscillated castings of Al - 3 wt. % Ag.

The casting microstructure was determined by sectioning and etching of the castings parallel and perpendicular to the cylindrical axis. Etching was done in a Modified Tucker etch (HCl, HNO_3, HF, and H_2O in a 2:2:1:15 ratio) and the etching products were washed off immediately with concentrated nitric acid.

To measure the macrosegregation in the ingot, the most expedient procedure, as commonly used, is to measure the solute concentration of cuttings taken at various points in the ingot by drilling. This is satisfactory if there is no microsegregation and no short range variations in the macrosegregation, which is rarely the case. To improve the averaging process, more drillings and analyses could be made, or alternatively a layer of the casting can be machined off and samples taken from this. Finally, the entire casting can be machined and the concentration of all the casting by sections can be measured. The time and effort involved increases very greatly from the first to final process listed above. Accordingly, all four procedures were used initially to determine their accuracy and reproducibility for the present castings. Four methods of sampling were employed to determine the degree of radial macrosegregation.

(a) Holes of 1/4 inch diameter were drilled through the casting in 1/4 inch steps in the radial direction. A fixed weight of solid turnings was packed into a standard

container. The activity of the radioactive silver present in each sample was then measured with a scintillation well counter.

(b) Holes of 1/4 inch diameter were drilled as in method (a) except 1/8 inch steps were used. The analysis was the same as method (a).

(c) The castings were mounted in a lathe and 0.030 inch thick concentric cylinders one inch long were progressively removed. From each cut a random five gram sample was taken and the activity of the sample measured in a scintillation well counter under conditions of fixed geometry.

(d) The castings were machined as in (c) except the cut was 0.050 inches thick. All the material removed in each cut was dissolved in a concentrated solution of nitric acid containing a small amount of mercury in solution. The solutions were then made up to either 250 or 500 ml. by adding water. A 10 ml. sample was taken from each solution and the activity of each sample measured.

In evaluating the results the concentration of silver is taken to be proportional to the measured activity. Ag^{110} is a strong gamma emitter and aluminum a weak absorber. As a result, small geometrical differences in samples counted in (a), (b) and (c) techniques should be negligible.

Autoradiography was used to show qualitatively the macrosegregation in the ingots. Since the energy of

the radiation is high and the sample absorption is low the autoradiograph will represent the activity of a large distance into the ingot. Therefore to obtain reasonable resolution thin sections are required. Thin discs perpendicular to the cylindrical axis were prepared by machining and polishing the discs to a thickness of 0.020 inches.

7.3 Results

Vertical sections of castings which were stationary, rotating, and oscillating during solidification are shown in Figures 77a, 77b, and 77c respectively. The stationary casting has a small equiaxed region in the centre, the rotated casting has a columnar zone to the centre of the casting, and the oscillated casting has a large equiaxed region, in agreement with previous observations. The equiaxed grains in the oscillated ingot are clearly shown to have grown dendritically in Figure 78, taken at higher magnification.

The structures obtained on etched cross sections of the ingots (Figures 79a, 79b, 79c) show the effect of the applied fluid motion on the columnar zone. In Figure 79a of the stationary cast ingot the columnar region is in a radial direction with all the grains growing perpendicular to the mould wall. The columnar region for the rotated ingot (Figure 79b) shows a spiral shape with the initial columnar grains growing non-perpendicular to the mould walls.

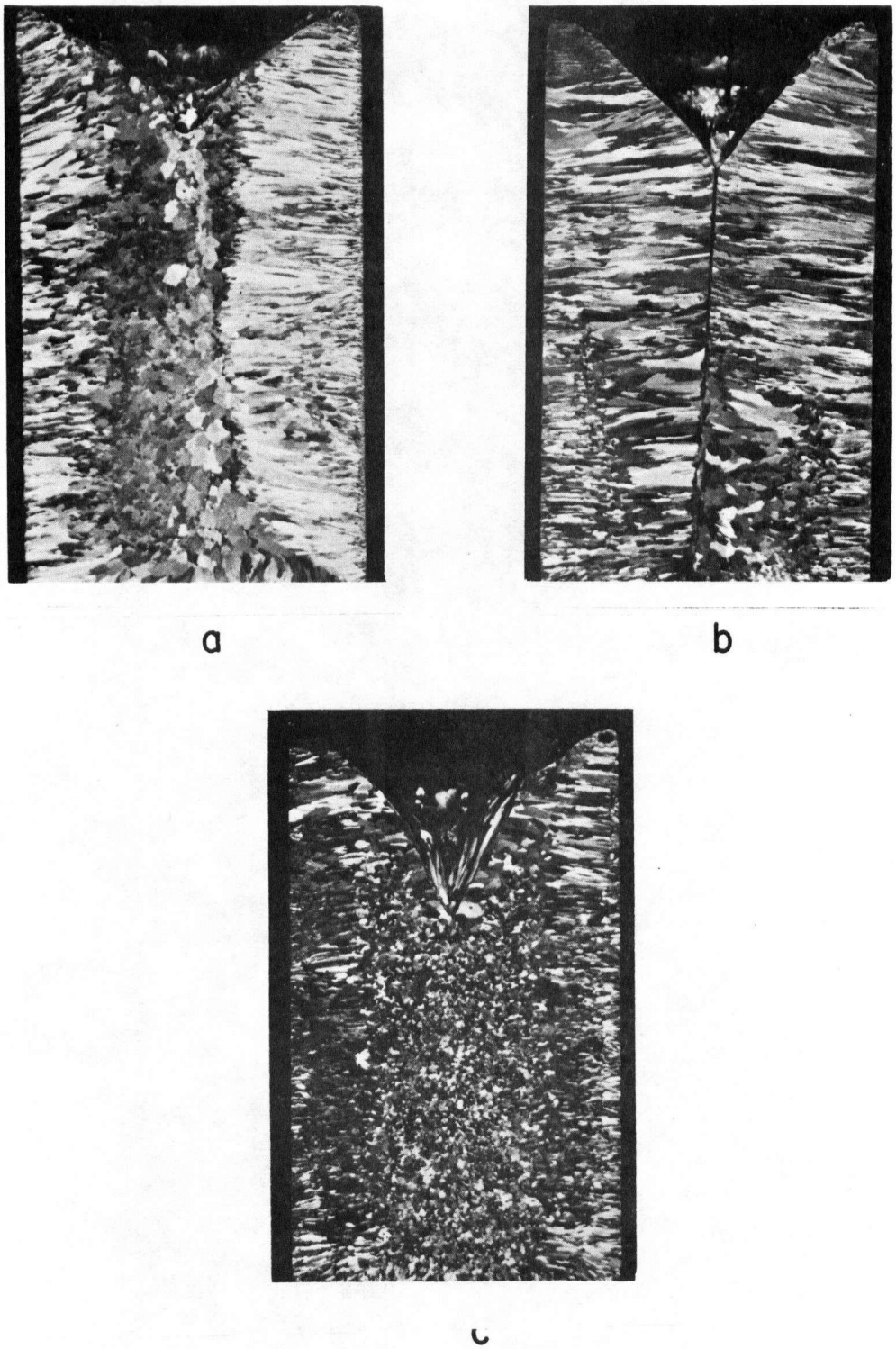

Figure 77. Representative ingots cast in (a) stationary, (b) rotating, and (c) oscillating moulds. Approximately 2/3 magnification.

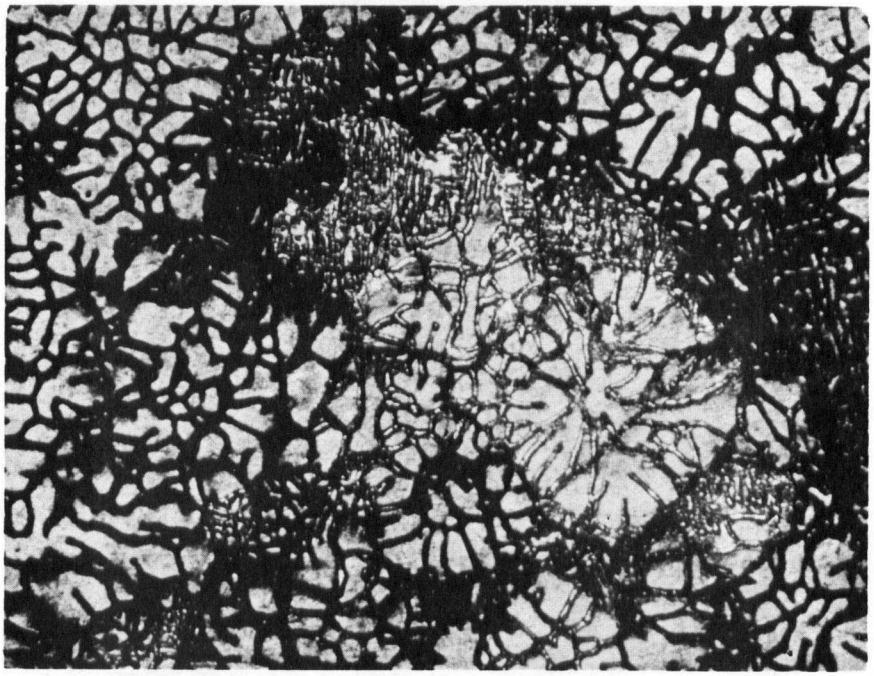

Figure 78. Equiaxed grains in the central region of the oscillated casting, magnification 40 times.

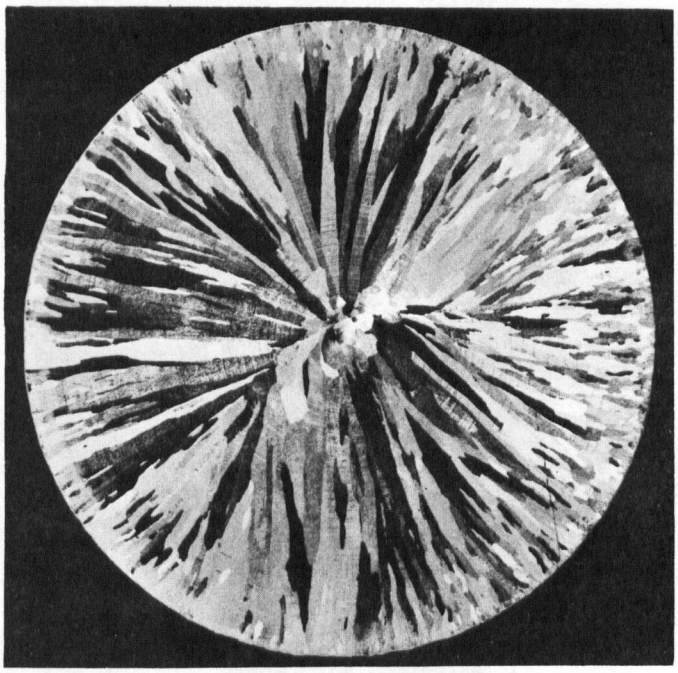

Figure 79. Representative ingot cast in a (a) stationary mould, actual size.

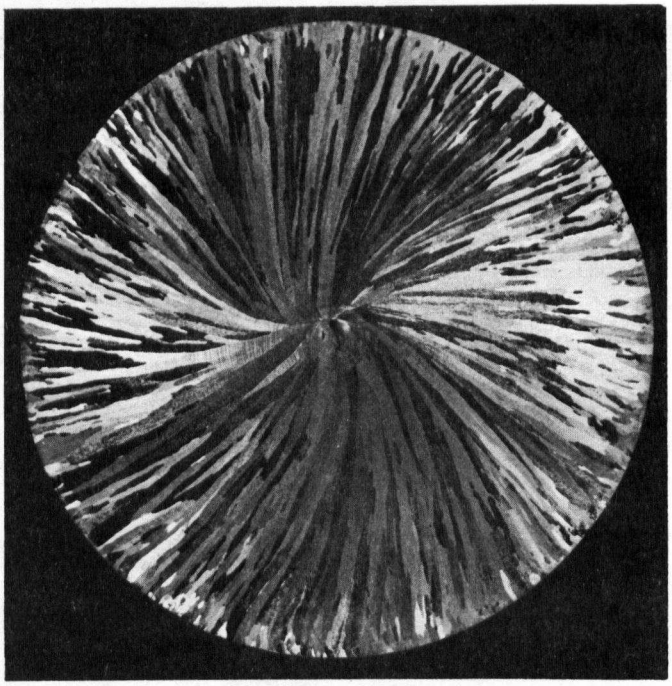

b

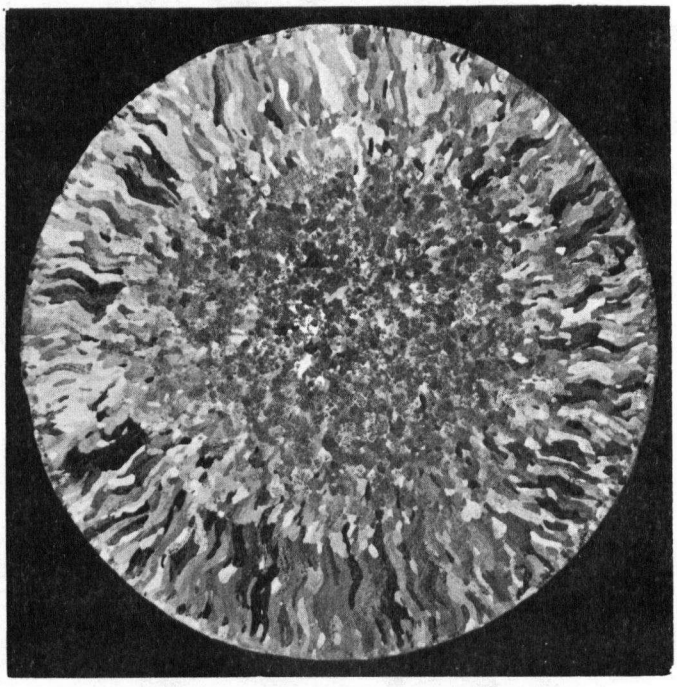

c

Figure 79 continued. Representative ingots cast in (b) rotating and (c) oscillating moulds, actual size.

These grains are growing towards the oncoming fluid in the liquid pool. In the oscillated ingot (Figure 79c) the direction of the columnar zone changes when the mould rotation is reversed so that they always grow into the flow. A similar observation has been made by Roth and Schippen (43). In both the rotated and oscillated ingot there is a renucleation of the columnar grains to achieve the curved effects. There were no grains observed which curved or had a kink, indicating that the crystallographic growth orientation was always maintained.

The solute concentration of Ag in a stationary casting using the four sampling techniques described is shown in Figure 80. Comparing the four sets of points it is evident that the different techniques have various degrees of scatter associated with them. For the drilled holes with 1/4 inch steps (Figure 80a) the macrosegregation appears cyclic from the outer mould wall to the centreline. The experimental accuracy of the points plotted is such that they are a true representation of the concentration of the sample measured in the scintillation counter. Thus the scatter must be due to a change in the concentration along the drill hole. To test if this cyclic behavior is genuine the 1/8 inch step hole method is shown in Figure 80b. Again the points show a cyclic behaviour, but the cycle period is different for the two cases. Thus microsegregation along the drill hole must be the cause of the cycling. The

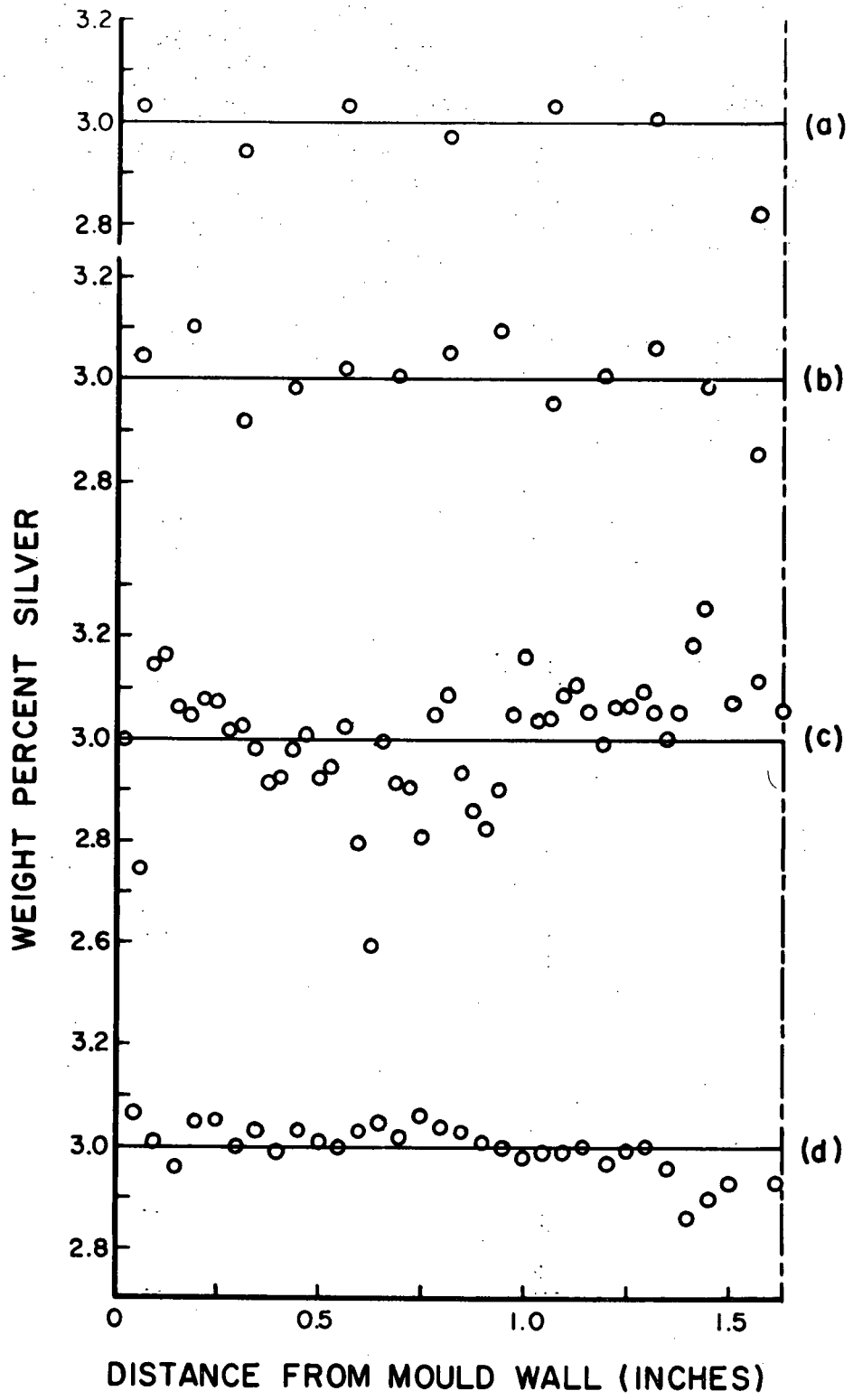

Figure 80. The radial silver distribution in a stationary casting; (a) 1/4 inch drill holes in 1/4 inch steps, (b) 1/4 inch drill holes in 1/8 inch steps, (c) 0.030 inch lathe turnings, and (d) 0.050 inch lathe turnings dissolved in acid.

plot for the solid lathe turnings (Figure 80c) shows an extensive scatter between points. This large scatter could be caused by the microsegregation, by the selection of the material taken from the whole sample, or by not having a sufficiently constant sample geometry due to the nature of the lathe turnings. The final method of dissolving the turnings of the entire sample gave the results of Figure 80d, which shows much less scatter than the other methods. In this case the counting geometry is not a problem as the liquid is contained in a standard tube and the liquid counted is a true average of the sample composition. This method gave reproducible results and was used for all the subsequent macrosegregation measurements.

The radial macrosegregation in the three types of ingots is shown in Figure 81. Three sets of data were obtained for the radial macrosegregation, one from the central region of one group of castings, and the other two from near the top and bottom of a second similar group of castings. All the results for a particular type of casting were very similar.

The silver concentration in the stationary and rotated ingots, shown in Figures 81a and 81b, is essentially constant indicating little macrosegregation, except for a small drop in concentration at the centreline of the casting. There is no effect on the macrosegregation due to the difference in density of the silver and aluminum in the

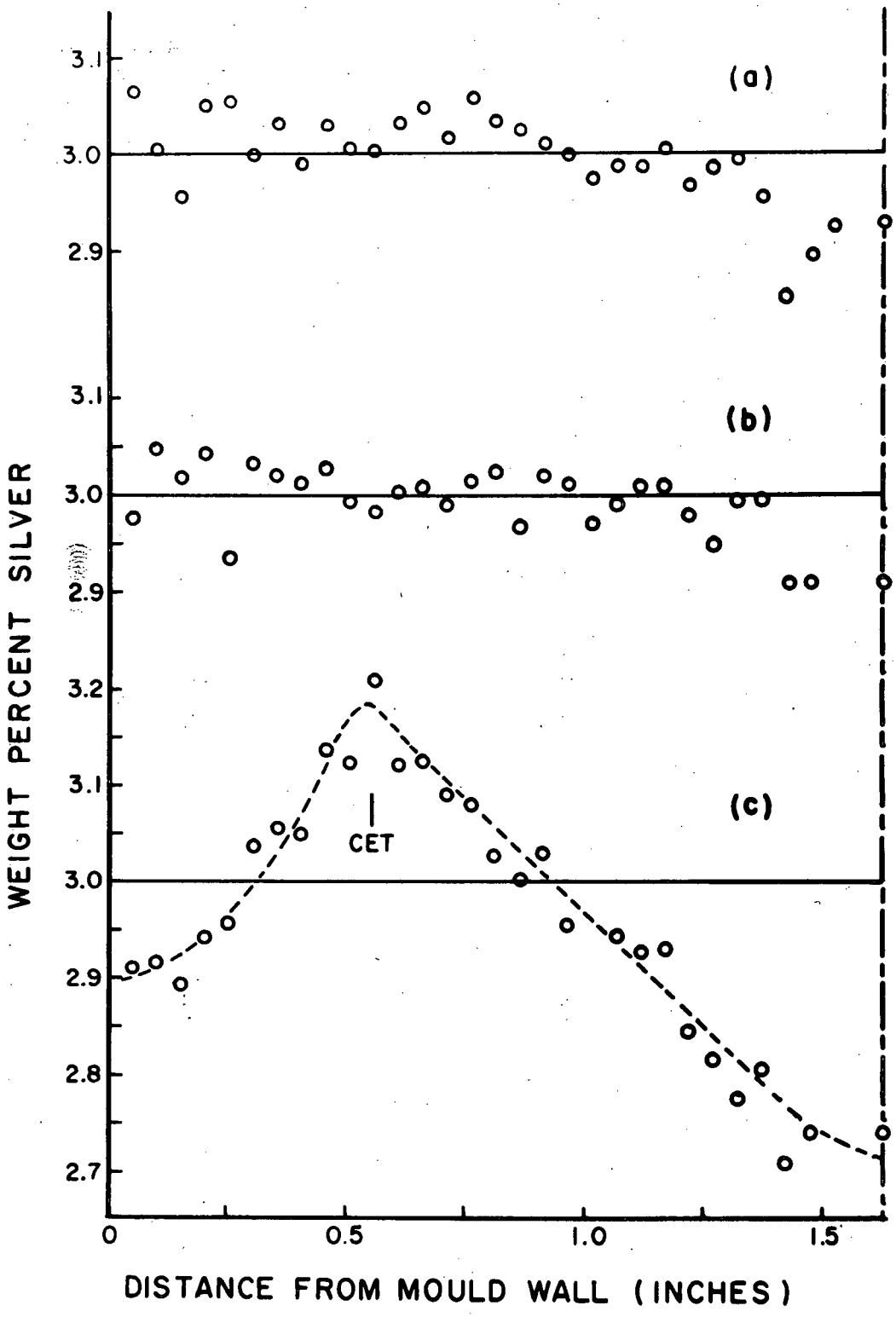

Figure 81. The radial silver distribution in (a) stationary, (b) rotated, and (c) oscillated ingots using method (d) of Figure 80.

rotated casting. In the oscillated case macrosegregation is present, with an initial rise in the silver concentration up to a peak. The concentration then decreases to the centreline of the casting to a value over 0.25% Ag below the Co value. The position of the CET is shown on the curve; this position corresponds to the CET in Figure 77c. The results show that the CET corresponds to the maximum silver concentration.

An autoradiograph of the oscillated ingot (Figure 82) shows the macrosegregation qualitatively. The lighter areas towards the centre of the ingot represent silver depleted areas which correspond to the quantitative measurements (Figure 81c). Due to this mottled effect in the silver distribution it can easily be seen that the drill hole methods of analysis could give spurious results, as can any analysis that does not include the total radial sample.

7.4. Discussion

The cast structure associated with stationary, rotated, and oscillated castings are similar to those reported by Cole and Bolling (16) and others and will not be discussed here. Two points will be considered.

(1) The relation of the observed macrosegregation with the cast structure.

(2) The shape of the solute curves.

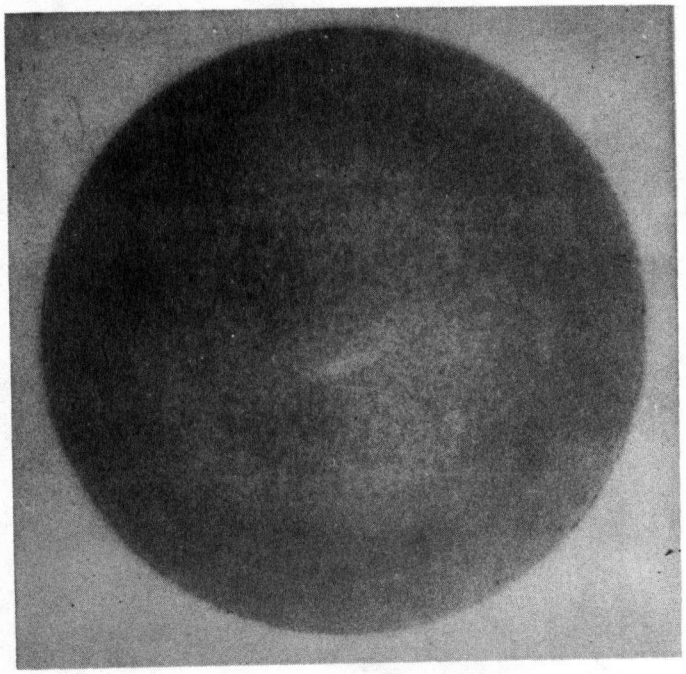

Figure 82. An autoradiograph of the cross-section of the oscillated ingot showing the silver distribution in the casting, actual size.

Conditions for the CET are met much earlier in the oscillated casting than in either the rotated or stationary casting. This is believed due to the lowering of the temperature gradient in the molten region (oscillation causes extensive mixing) thus allowing "nuclei", produced by large shear forces at the interface, to survive and grow. During rotation reversal these large shear forces will cause remelting and/or breaking off of dendrite fragments (14, 15) which can act as "nuclei". These can easily be swept into the central region of the liquid pool by the violent turbulent flow occurring as a result of oscillation. Observation of this flow in a rheoscopic liquid shows the existence of a turbulent wave generated at the interface and rapidly moving to the centre. If the mould is rotated at a constant speed the temperature gradient will remain high (16) and no shear forces will be present at the interface. Therefore, no nuclei will be produced and the CET will be suppressed, as observed. For the stationary ingot natural convection will yield low shear forces at the interface and the temperature gradient will be of some intermediate value.

The lack of macrosegregation in the rotated and stationary ingots can be attributed to the lack of significant fluid flow in the interdendritic region. Without fluid flow there will be no net solute flux from the interface region, and therefore, no macrosegregation.

For the oscillated casting high shear forces in the vicinity of the solid-liquid interface will produce more extensive interdendritic flow. This flow will sweep solute rich liquid out of the mushy zone. The solute distribution near the mould wall will then tend to conform to the equation for complete mixing:

$$C_s = kCo(1-g)^{k-1}$$

where C_s is the solid solute composition, k the distribution coefficient, Co the average initial solute composition and g the fraction solidified. When the rotation is reversed a turbulent wave is produced which will transport this solute towards the centre of the solidifying ingot.

During columnar growth the solute distribution will therefore be as shown in Figure 83a. When the CET is immenent the distribution will be that shown in Figure 83b. The initial part of the curve corresponds to a complete mixing situation up to the peak. Beyond the peak the composition gradually decreases towards the centre due to the incomplete mixing of the solute rich liquid generated at the interface. Concurrent with this solute movement is the reduction of the temperature gradient which, until the CET occurs, does not allow survival of nuclei. (At every rotation reversal high shear forces and temperature fluctuations, due to turbulence, will produce a large number of dendrite fragments.) When the temperature gradient is

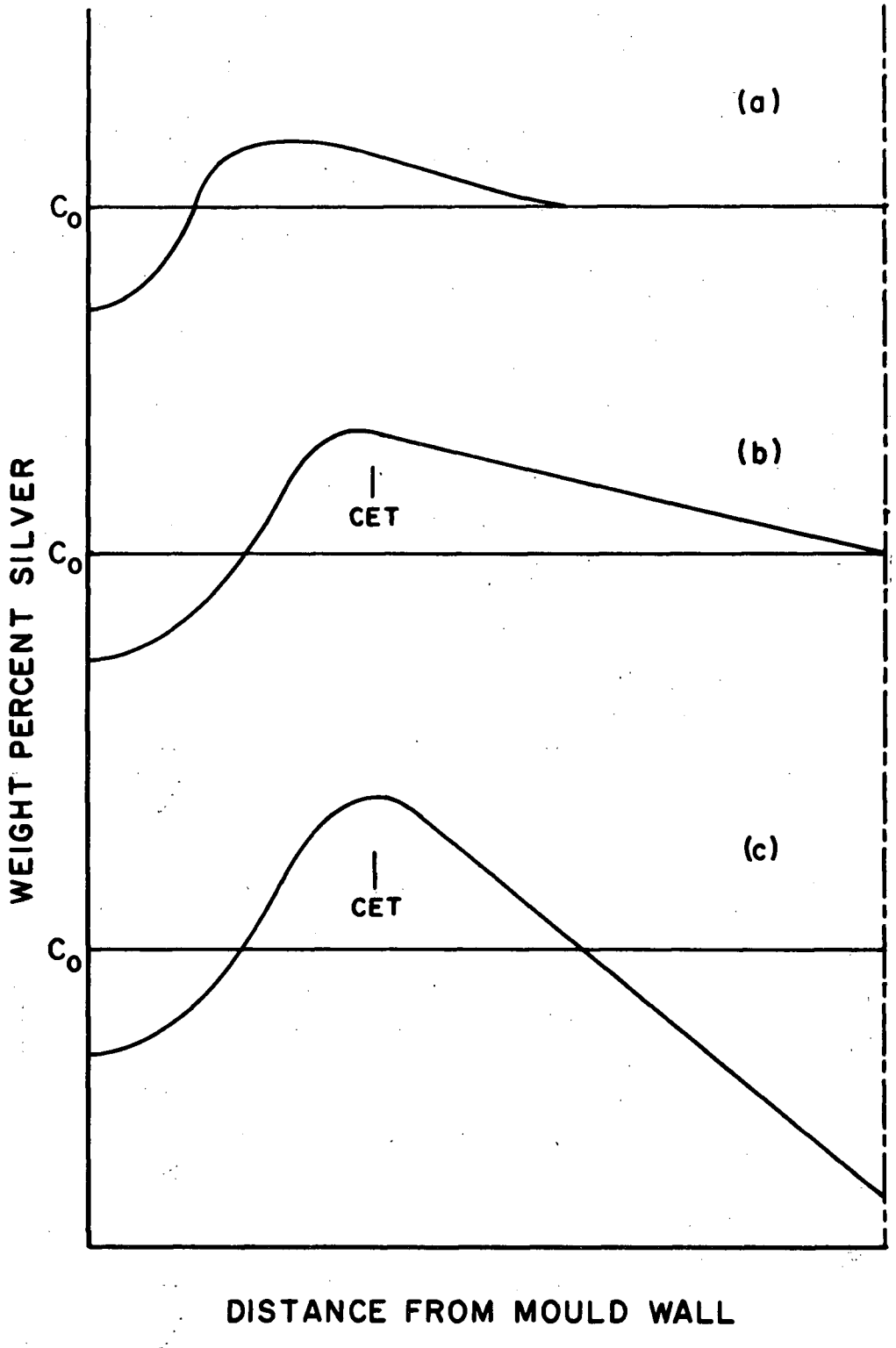

Figure 83. The development of the radial macrosegregation in an oscillated ingot, (a) prior to the time of the CET, (b) at the time of the CET, and (c) the final silver distribution in the casting.

sufficiently low these fragments will be able to survive and grow and be swept by the turbulent wave throughout the remaining liquid. Since these fragments are of composition less than Co the overall composition in this region will be reduced as shown in Figure 83c. Also, due to the lowering of the temperature gradient the mushy zone will be increased in length. The mass and composition of dendrite fragments necessary to cause this reduction in composition (Figure 83b - Figure 83c) is calculated in the Appendix, Section 7.6. The solute distribution profile of Figure 83c will be that of an ingot oscillated during solidification. The macrosegregation predicted above was observed in the oscillated ingot, Figure 81c.

7.5 Conclusion

The present investigation has shown that no significant macrosegregation accompanies solidification in stationary or rotated moulds for the system examined. This implies that the large density difference between the solvent (Al) and solute (Ag) has no effect on the radial solute distribution. However, appreciable macrosegregation is associated with the oscillation mode of solidification. The initial rise is attributed to solute mixing in the liquid interfacial region due to the turbulent flow. The maximum concentration is associated with the columnar to equiaxed transition. The solute depletion in the centre

of the casting is caused by small grains of low solute concentration being swept, by the turbulent waves, from the mushy zone to the ingot centre.

7.6. Appendix to section 7.

The model proposed for macrosegregation in the oscillated ingot assumes sufficient dendrite fragments are swept into the central liquid zone, to give the change in the distribution between Figure 83b and 83c. The following analysis is an approximate calculation for the mass of fragments which is required.

Assume V_E is the volume of the central liquid region just prior to the CET. The average composition in this volume after total solidification assuming a linear distribution profile in this region and Co = 3.0 wt.% Ag, is given by:

$$\overline{C} = \frac{\int_o^R 2\pi\ r\ C(r)dr}{\int_o^R 2\pi\ rdr}$$

where C(r) is composition as a function of radius and R is radius of CET. From Figure 81c, $C(r) = \frac{.48}{R}\ r + 2.70$, therefore $\overline{C}$ = 3.02 wt. % Ag. Comparing Figures 83b and 83c an estimate of the average composition in V_E just prior to the CET can be made ($C(r) = \frac{.15}{R}\ r + 3.00$) and is equal to 3.10 wt. % Ag.

Assuming the composition of dendrite fragments swept into the central region is $\alpha K_o C_o$, where α is a factor to account for the increase in solute concentration in the dendrite branches as solidification progresses, assumed to be 1.5. K_o is 0.25 for the alloy under consideration.

Therefore: $\alpha K_o C_o = (1.5)(0.25)(3.0)$

$= 1.12$ wt. % Ag.

Let v be the volume of dendrite fragments swept into the central molten region (V_E) at the time of the CET. The resulting change in the average concentration in V_E can then be used to solve for v.

Therefore: $3.10\ V_E + 1.12\ v = 3.02\ (V_E + v)$

Therefore: $v = 0.04\ V_E$

This calculation shows that a small amount of solid fragments is required relative to the total liquid volume to cause the decrease in concentration observed. The large mushy zone, due to the low thermal gradient, and the large interdendritic flow, due to the turbulence produced during the rotation reversal, should result in this small volume of fragments being made available to cause the observed effect.

8. Summary and Conclusions

Natural convection in liquid tin and liquid lead has been observed in a small closed system by a radioactive tracer technique. It has been demonstrated that the distribution of radioactive material in the quenched metal corresponds to the distribution in the liquid prior to quenching.

To examine thermal convection, experiments were carried out in pure liquid tin and lead under a variety of conditions. It was observed that the flow rates in the liquid increase with

(a) increasing temperature difference across the cell

(b) increasing average temperature

and (c) increasing thickness of the liquid zone.

For a temperature difference across the cell ranging from 0.23°C to 19°C (corresponding to Grashof numbers from 10^6 to 10^8 for a 6.4 cm. wide cell) the time for a complete cycle around the cell varied between 780 and 12 seconds. When either the temperature difference or the cell thickness was increased beyond a certain point the flow rate increased

and the mode of flow changed from a simple cell to a more complex three dimensional flow pattern. No thermal oscillations were detected in the liquid for the entire range of temperature differences and cell thicknesses examined.

The flow pattern in the thin cell was found to be a function of the length to height ratio. For ratios of 4.9 : 1 or less the flow pattern is a single cell, while for a ratio of 8.3 : 1 the flow becomes multicellular in nature. The pattern also changes if the temperature distribution is changed. If both sides of the cell are cooled with respect to the centre, a double flow cell pattern is obtained, each cell corresponding to the simple cell described previously. The width of the cells are determined by the position of the maximum temperature in the liquid. A buffer zone exists between the two cells inhibiting mass transfer from one cell to the other. In larger castings with many solidification directions and complex thermal conditions, the present results would suggest that many cells are set in motion with no interaction, or at least very little interaction between these cells. Thus long range transport of solute or solid particles in the liquid may be severly restricted by the multicellular behavior.

An analysis of the thermal convection problem

has been made for this system using a finite difference numerical procedure. The analysis has been solved for Prandtl numbers of 10.0, 1.0, 0.1 and 0.0127 with Grashof numbers of 2×10^3 to 2×10^7. The thermal profile has been found to be a function of only the Rayleigh number while the flow velocities are a function of both the Prandtl and Grashof numbers independently. The numerical solution agrees with an analytical series solution for low values of the Grashof number.

In an attempt to determine fluid flow in metals, observations have been reported in the literature of flow in transparent liquid systems which have been extended to liquid metals. The present results show that there are serious limitations in extrapolating non-metallic fluid flow behaviour to liquid metals. The thermal and flow profiles in different types of fluids cannot be matched simultaneously and hence phenomena depending on both parameters must be altered for various types of fluids.

Measurements of temperature gradients in castings have been used to estimate fluid flow during solidification. Often no temperature differences are observed in the centre of the casting from which it is concluded that there is no thermal convection. This can be entirely erroneous, as shown by the theoretical solution in Figure 27f where the central region has essentially a zero horizontal temperature

gradient. However, there is extensive flow associated with significant temperature gradients near the cell walls. Accordingly to predict thermal convection a complete thermal profile in the liquid pool is required. The relevant parameter in thermal convection is the temperature difference between the flow cell boundaries and not the temperature gradients in the cell.

The experimental thermal convection results in liquid tin tend towards the theoretical solution for large temperature differences and large cell thicknesses. It is seen that for a liquid cell thickness of 1.5 cm., or greater, the experimental and theoretical results should correspond. The thermal profiles in the 0.95 cm. thick cell are in close agreement with the theoretical results.

Solute convection is observed by three different series of experiments:

(a) independent solute convection

(b) the influence of solute convection on thermal convection, and

(c) the thermal and solute conditions for complete mixing. It is shown that if a vertical stable solute difference is imposed on a system, the horizontal thermal condition required to cause complete mixing in the liquid zone must be sufficient to cause a horizontal density inversion. If the temperature difference is not great enough, a multicell flow pattern will result with a buffer

zone between the flow cells.

The interdendritic fluid flow in lead-tin alloys due to the residual liquid pool convection has been examined. The flow penetrates to a distance of from 12 to 22% solid in the solid-liquid zone. The alloy castings have a primary dendrite spacing of approximately 700 to 1000 microns.

Three experimental models to analyse interdendritic flow are presented,

(a) a two dimensional channel model

(b) a three dimensional wire rod model, and

(c) a wire mesh model.

The wire mesh model predicts that as the primary dendrite spacing decreases, the extent of interdendritic liquid flow will increase. Although lead-tin alloy growth experiments were not conducted over a wide range of dendrite spacings, the experiments conducted did agree with the results predicted by the wire mesh model.

As an extension of the fluid flow considerations, an investigation was carried out to determine the macrosegregation in castings which have imposed fluid flow patterns. The macrosegregation in Al-3%Ag alloys subjected to oscillation and rotation during solidification shows that extensive macrosegregation occurs in oscillated castings, but little segregation occurs in stationary and rotated

castings. A concentration peak occurs at the columnar to equiaxed transition and a general depletion occurs in the central equiaxed zone. The segregation in the oscillated casting is accounted for by long range movement of dendrite fragments which break and/or melt off in the solid-liquid interface region.

9. Suggestions for Future Work

(a) Using the tracer techniques developed in this work, observations on natural and forced convection could be made on much more complex systems, considering both thermal and solute driving forces. Also the effects of an advancing solid-liquid interface on the natural convection could be investigated. This could be applied to specific geometric configurations such as obtained in continuous casting.

(b) The interdendritic flow experiments could be continued for large ranges of dendrite spacings and different alloy systems. Systems which have the rejected solute less dense than the bulk liquid could be analysed to observe flow differences between this and more dense solutes.

(c) The theoretical numerical solution could be applied to a great variety of geometric shapes and thermal conditions which occur in casting situations. This analysis could be used in a more exact solution to a growing interface rate analysis.

(d) More extensive experiments are required in order to establish the theory that a mass of dendrite fragments are swept out of the interface in oscillated castings to produce the observed macrosegregation.

Bibliography

1. J. P. Holman: Heat Transfer, McGraw-Hill Book Co., New York, 1963.

2. J. O. Wilkes and S. W. Churchill: A.I.Ch.E. J., 1966, vol. 12, p. 161.

3. J. Szekely and P. S. Chhabra: Metallurgical Transactions, 1970, vol. 1, p. 1195.

4. F. Weinberg: Crystal Growth, Proceedings of an International Conference on Crystal Growth, Boston, 20-24 June 1966, p. 639.

5. J. S. Kirkaldy and W. V. Youdelis: trans TMS-AIME, 1958, vol.212, p. 833.

6. M. C. Flemings and G. E. Nereo: trans TMS-AIME, 1967, vol. 239, p. 1449.

7. M. C. Flemings, R. Mehrabian, and G. E. Nereo: trans TMS-AIME, 1968, vol. 242, p. 41.

8. M. C. Flemings and G. E. Nereo: trans TMS-AIME, 1968, vol. 242, p. 50.

9. R. Mehrabian, M. Keane, and M. C. Flemings: Metallurgical Transactions, 1970, vol. 1, p. 1209.

10. R. J. McDonald and J. D. Hunt: trans TMS-AIME, 1969, vol. 245, p. 1993.

11. A. Muller and M. Wiehelm: Z. Naturforsch, 1964, vol. 19a(2), p. 254.

12. D. T. J. Hurle: Crystal Growth, Proceedings of an International Conference on Crystal Growth, Boston, 20-24 June, 1966, p. 659.

13. H. P. Utech and M. C. Flemings: ibid., p. 651.

14. K. A Jackson, J. D. Hunt, D. R. Uhlmann,and T. P. Seward, III: trans TMS-AIME, 1966, vol. 236, p. 149.

15. S. Wajciechowski and B. Chalmers: trans TMS-AIME, 1968, vol. 242, p. 690.

16. G. S. Cole and G. F. Bolling: Ford Motor Company report "Enforced Fluid Motion and the Control of Grain Structures in Metal Castings," March 15, 1967.

17. B. Chalmers: J. Aust. Inst., 1963, vol. 8, p. 255.

18. R. T. Southin: trans TMS-AIME, 1967, vol. 239, p. 220.

19. W. A. Tiller and S. O'Hara: The Solidification of Metals, ISI Publication 110, December 1967, p. 27.

20. M. J. Stewart and F. Weinberg: trans TMS-AIME, 1969, vol. 245, p. 2108.

21. L. MacAulay and F. Weinberg: trans TMS-AIME, 1969, vol. 245, p. 1831.

22. G. S. Cole and W. C. Winegard: J. Inst. of Metals, 1964-65, vol. 93, p. 153.

23. G. F. Bolling: Ford Motor Company report "Manipulation of Structure and Properties," October 30, 1969.

24. W. C. Johnston and W. A. Tiller: Westinghouse Research Report, "Fluid Flow Control During Solidification," December 15, 1959.

25. G. S. Cole and G. F. Bolling: trans TMS-AIME, 1966, vol. 236, p. 1366.

26. H. P. Utech, W. S. Bower, and J. G. Early: Crystal Growth, Proceedings of an International Conference on Crystal Growth, Boston, 20-24 June, 1966, p.201.

27. D. R. Uhlmann, T. P. Seward, III, and B. Chalmers: trans TMS-AIME, 1966, vol. 236, p. 527.

28. A. Ohno: The Solidification of Metals, ISI Publication 110, December 1967, p. 349.

29. R. J. McDonald and J. D. Hunt: Metallurgical Transactions, 1970, vol. 1, p. 1787.

30. G. S. Cole and G. F. Bolling: "Visual Observations of Crystallization from Aqueous Solutions Under Enforced Fluid Motion," unpublished.

31. N. Standish and G. Lang: J. Aust. Inst., 1970, vol. 15, p. 120.

32. K. G. Davis and P. Fryzuk: trans TMS-AIME, 1965, vol. 233, p. 1796.

33. G. K. Batchelor: Quart. of Applied Math, 1954, vol. 12, p. 209.

34. A. Emery and N. C. Chu: Trans. of ASME, Feb. 1965, p. 110.

35. J. O. Wilkes: Ph.D. thesis, University of Michigan, Ann Arbor, Michigan, 1963.

36. M. R. Samuels and W. Churchill: A.I.Ch.E. J., 1967, vol. 13, p. 77.

37. H. R. Thresh, A. F. Crawley, and D. W. G. White: trans TMS-AIME, 1968, vol. 242, p. 819.

38. H. Thresh: "The Viscosity of Liquid Tin, Lead and Lead-Tin Alloys," to be published.

39. R. N. Lyon: Liquid Metals Handbook, The Committee on the Basic Properties of Liquid Metals, Office of Naval Research, Department of the Navy, 1954.

40. H. E. McGannon, ed.: The Making, Shaping and Treating of Steel, United States Steel, 1964.

41. Molten Salts: Volume 1, Electrical Conductance, Density, and Viscosity Data, National Bureau of Standards 15, October 1968.

42. G. S. Cole and G. F. Bolling: trans. TMS-AIME, 1969, vol. 245, p. 725.

43. W. Roth and M. Schippen: Z. Metallk, 1956, vol. 47, p. 78.

44. M. Hansen: Constitution of Binary Alloys, 2nd. ed., McGraw-Hill Book Co., New York, 1958.

Appendix I

Notation Used

Cp	=	Specific heat
d	=	Width of liquid zone
d_w	=	Diameter of the wire mesh wires
f	=	Fraction of the tracer that has flowed through the mesh
F_s	=	Fraction solid in the solid-liquid interface region
g	=	Acceleration due to gravity
G_L	=	Temperature gradient
Gr	=	Grashof number, based on total temperature difference
Gr'	=	Grashof number, based on one-half the temperature difference
h	=	Convective heat transfer coefficient
H	=	Height of a molten metal pool
h_a	=	Actual hole size in the wire mesh
h_e	=	The effective hole size in the wire mesh
k	=	Thermal conductivity
L	=	Height to length ratio of the liquid zone
l	=	Height of the liquid cell
Nu	=	Nusselt number
P	=	Dimensionless pressure
p'	=	Pressure deviation from initial static value
Pr	=	Prandtl number

q	=	Heat flux at the cold wall
Ra	=	Rayleigh number
S_a	=	Spacing distance of the wire mesh wires
T	=	Dimensionless temperature
t	=	Time
u	=	Velocity in the x direction
U	=	Dimensionless velocity in the X direction
v	=	Velocity in the y direction
V	=	Dimensionless velocity in the Y direction
x	=	Vertical coordinate
X	=	Vertical dimensionless coordinate
y	=	Horizontal coordinate
Y	=	Horizontal dimensionless coordinate
*	=	Superscript denoting values of the parameters after a one-half time step
'	=	Superscript denoting values of the parameters after a full time step
α	=	Thermal diffusivity
β	=	Coefficient of volume expansion
δ	=	Boundary layer thickness
ζ	=	Vorticity function
θ	=	Temperature
θ_1	=	Temperature of the cold wall
θ_2	=	Temperature of the hot wall

μ = Absolute viscosity

ν = Kinematic viscosity

ρ = Density

τ = Dimensionless time

τ' = Dimensionless time for the stream function iteration

ψ = Stream function

Appendix II

The Theoretical Solution to the Problem of Natural Convection in Liquid Metals

The governing equations and the boundary conditions to be solved are given by equations (3.31), (3.32), (3.33), (3.34), and (3.35). Also equations (3.36), (3.37), (3.38), and (3.39) give the vorticity and energy finite difference equations for the governing equations for the first and second half time step. The general finite difference approximations used are the central difference forms such as

$$\frac{\partial U}{\partial X} = \frac{U_{i+1,j} - U_{i-1,j}}{2\Delta X} \tag{1}$$

for the first derivatives and

$$\delta^2_x U_{i,j} = \frac{\partial^2 U}{\partial X^2} = \frac{U_{i-1,j} - 2U_{i,j} + U_{i+1,j}}{\Delta X^2} \tag{2}$$

for the second derivatives. The forward difference approximation is used for the time derivatives such as

$$\frac{\partial U}{\partial \tau} = \frac{U'_{i,j} - U_{i,j}}{\Delta \tau} \tag{3}$$

The general procedure of the solution is given in Section 3 of the thesis, and this appendix will state all the equations used in the computer program.

1. Computation of the new temperature

For the boundary values of the second derivative a series expansion is used such as:

$$T_{2,j} = T_{1,j} + \Delta X\left(\frac{\partial T}{\partial X}\right)_{1,j} + \frac{\Delta X^2}{2}\left(\frac{\partial^2 T}{\partial X^2}\right)_{1,j} \tag{4}$$

From the boundary condition of no heat transfer through the upper and lower wall the finite difference becomes:

$$\left(\frac{\partial^2 T}{\partial X^2}\right)_{1,j} = \frac{2}{\Delta X^2}\,(T_{2,j} - T_{1,j}) \tag{5}$$

For the first half time step the following simultaneous equations are solved for columns $j = 2, 3, \ldots n-1$ in turn with

$i = 1$:

$$\left(\frac{2}{\Delta\tau} + \frac{2}{Pr(\Delta X)^2}\right)T^*_{1,j} - \frac{2}{Pr(\Delta X)}T^*_{2,j} = \frac{2}{\Delta\tau}T_{1,j} + \frac{1}{Pr}\,\delta^2_y T_{1,j} \tag{6}$$

$i = 2,3, \ldots m-1$:

$$\left(-\frac{U_{i,j}}{2\Delta X} - \frac{1}{Pr(\Delta X)^2}\right)T^*_{i-1,j} + \left(\frac{2}{\Delta\tau} + \frac{2}{Pr(\Delta X)^2}\right)T^*_{i,j} +$$

$$\left(\frac{U_{i,j}}{2\Delta X} - \frac{1}{Pr(\Delta X)^2}\right)T^*_{i+1,j} = \frac{2}{\Delta\tau}T_{i,j} - V_{i,j}\frac{T_{i,j+1} - T_{i,j-1}}{2\Delta Y}$$

$$+ \frac{1}{Pr}\,\delta^2_y T_{i,j} \tag{7}$$

i = m:

$$\frac{-2}{Pr(\Delta X)^2} T^*_{m-1,j} + \left(\frac{2}{\Delta\tau} + \frac{2}{Pr(\Delta X)^2}\right) T^*_{m,j} = \frac{2}{\Delta\tau} T_{m,j} + \frac{1}{Pr}\delta^2_y T_{m,j} \tag{8}$$

For the second half time step the following simultaneous equations are solved for row i = 1 with

j = 2:

$$\left(\frac{2}{\Delta\tau} + \frac{2}{Pr(\Delta Y)^2}\right) T'_{1,2} - \frac{1}{Pr(\Delta Y)^2} T'_{1,3} = \frac{2}{\Delta\tau} T^*_{1,2} +$$

$$\frac{2}{Pr(\Delta X)^2} (T^*_{2,2} - T^*_{1,2}) + \frac{1}{Pr(\Delta X)^2} T_{1,1} \tag{9}$$

j = 3,4, ... n-2:

$$- \frac{1}{Pr(\Delta Y)^2} T'_{1,j-1} + \left(\frac{2}{\Delta\tau} + \frac{2}{Pr(\Delta Y)^2}\right) T'_{1,j} - \frac{1}{Pr(\Delta Y)^2} T'_{1,j+1}$$

$$= \frac{2}{\Delta\tau} T^*_{1,j} + \frac{2}{Pr(\Delta X)^2} (T^*_{2,j} - T^*_{1,j}) \tag{10}$$

j = n-1:

$$- \frac{1}{Pr(\Delta Y)^2} T'_{1,n-2} + \left(\frac{2}{\Delta\tau} + \frac{2}{Pr(\Delta Y)^2}\right) T'_{1,n-1} = \frac{2}{\Delta\tau} T^*_{1,n-1} +$$

$$\frac{2}{Pr(\Delta X)^2} (T^*_{2,n-1} - T_{1,n-1}) + \frac{1}{Pr(\Delta Y)^2} T_{1,n} \tag{11}$$

Solve for rows i = 2,3, ... n-1 with

$j = 2$:

$$\left(\frac{2}{\Delta\tau} + \frac{2}{Pr(\Delta Y)^2}\right)T'_{1,2} + \left(\frac{V_{i,2}}{2\Delta Y} - \frac{1}{Pr(\Delta Y)^2}\right)T'_{i,3} = \frac{2}{\Delta\tau}T^*_{i,2} +$$

$$\left(\frac{V_{i,2}}{2\Delta Y} + \frac{1}{Pr(\Delta Y)^2}\right)T_{i,1} - U_{i,2}\frac{T^*_{i+1,2} - T^*_{i-1,2}}{2\Delta X} + \frac{1}{Pr}\delta^2_x T^*_{i,2} \qquad (12)$$

$j = 3,4, \ldots n-2$:

$$\left(-\frac{V_{i,j}}{2\Delta Y} - \frac{1}{Pr(\Delta Y)^2}\right)T'_{i,j-1} + \left(\frac{2}{\Delta\tau} + \frac{2}{Pr(\Delta Y)^2}\right)T'_{i,j} + \left(\frac{V_{i,j}}{2\Delta Y} -\right.$$

$$\left.\frac{1}{Pr(\Delta Y)^2}\right)T'_{i,j+1} = \frac{2}{\Delta\tau}T^*_{i,j} - U_{i,j}\frac{T^*_{i+1,j} - T^*_{i-1,j}}{2\Delta X}$$

$$+ \frac{1}{Pr}\delta^2_x T^*_{i,j} \qquad (13)$$

$j = n-1$:

$$\left(-\frac{V_{i,n-1}}{2\Delta Y} - \frac{1}{Pr(\Delta Y)^2}\right)T'_{i,n-2} + \left(\frac{2}{\Delta\tau} + \frac{2}{Pr(\Delta Y)^2}\right)T'_{i,n-1} =$$

$$\frac{2}{\Delta\tau}T^*_{i,n-1} + \left(-\frac{V_{i,n-1}}{2\Delta Y} + \frac{1}{Pr(\Delta Y)^2}\right)T_{i,n} - U_{i,n-1}\frac{T^*_{i+1,n-1} - T^*_{i-1,n-1}}{2\Delta X}$$

$$+ \frac{1}{Pr}\delta^2_x T^*_{i,n-1} \qquad (14)$$

Solve for row $i = m$ with

$j = 2$:

$$\left(\frac{2}{\Delta\tau} + \frac{2}{Pr(\Delta Y)^2}\right)T'_{m,2} - \frac{1}{Pr(\Delta Y)^2}\,T'_{m,3} = \frac{2}{\Delta\tau}\,T^*_{m,2} +$$

$$\frac{2}{Pr(\Delta X)^2}\,(T^*_{m-1,2} - T^*_{m,2}) + \frac{1}{Pr(\Delta Y)^2}\,T_{m,1} \qquad (15)$$

$j = 3, 4, \ldots n-2$:

$$-\frac{1}{Pr(\Delta Y)^2}T'_{m,j-1} + \left(\frac{2}{\Delta\tau} + \frac{2}{Pr(\Delta Y)^2}\right)T'_{m,j} - \frac{1}{Pr(\Delta Y)^2}\,T'_{m,j+1}$$

$$= \frac{2}{\Delta\tau}\,T^*_{m,j} + \frac{2}{Pr(\Delta X)^2}\,(T^*_{m-1,j} - T^*_{m,j}) \qquad (16)$$

$j = n-1$:

$$-\frac{1}{Pr(\Delta Y)^2}T'_{m,n-2} + \left(\frac{2}{\Delta\tau} + \frac{2}{Pr(\Delta Y)^2}\right)T'_{m,n-1} = \frac{2}{\Delta\tau}T^*_{m,n-1}$$

$$+ \frac{2}{Pr(\Delta X)^2}\,(T^*_{m-1,n-1} - T^*_{m,n-1}) + \frac{1}{Pr(\Delta Y)^2}\,T_{m,n} \qquad (17)$$

2. Computation of the new interior vorticity

For the first half time step the following simultaneous equations are solved for columns $j = 2,3, \ldots n-1$ in turn with

$i = 2$:

$$\left(\frac{2}{\Delta\tau} + \frac{2}{\Delta X^2}\right)\zeta^*_{2,j} + \left(\frac{U_{2,j}}{2\,X} - \frac{1}{\Delta X^2}\right)\zeta^*_{3,j} = Gr\,\frac{T'_{2,j+1} - T'_{2,j-1}}{2\Delta Y}$$

(over)

$$+\left(\frac{V_{2,j}}{2\Delta Y}+\frac{1}{\Delta Y^2}\right)\zeta_{2,j-1}+\left(\frac{2}{\Delta\tau}-\frac{2}{\Delta Y^2}\right)\zeta_{2,j}+\left(-\frac{V_{2,j}}{2\Delta Y}+\frac{1}{\Delta Y^2}\right)\zeta_{2,j+1}$$

$$-\left(-\frac{U_{2,j}}{2\Delta X}-\frac{1}{\Delta X^2}\right)\zeta_{i,j} \qquad (18)$$

$i = 3,4, \ldots m-2$

$$\left(-\frac{U_{i,j}}{2\Delta X}-\frac{1}{\Delta X^2}\right)\zeta^*_{i-1,j}+\left(\frac{2}{\Delta\tau}+\frac{2}{\Delta X^2}\right)\zeta^*_{i,j}+\left(\frac{U_{i,j}}{2\Delta X}-\frac{1}{\Delta X^2}\right)\zeta^*_{i+1,j}$$

$$=\ Gr\ \frac{T'_{i,j+1}-T'_{i,j-1}}{2\Delta Y}+\left(\frac{V_{i,j}}{2\Delta Y}+\frac{1}{\Delta Y^2}\right)\zeta_{i,j-1}+\left(\frac{2}{\Delta\tau}-\frac{2}{\Delta Y^2}\right)\zeta_{i,j}$$

$$+\left(-\frac{V_{i,j}}{2\Delta Y}+\frac{1}{\Delta Y^2}\right)\zeta_{i,j+1} \qquad (19)$$

$i = m-1$:

$$\left(-\frac{U_{n-1,j}}{2\Delta X}-\frac{1}{\Delta X^2}\right)\zeta^*_{n-2,j}+\left(\frac{2}{\Delta\tau}+\frac{2}{\Delta X^2}\right)\zeta^*_{n-1,j}\ =$$

$$Gr\frac{T'_{n-1,j+1}-T'_{n-1,j-1}}{2\Delta Y}+\left(\frac{V_{n-1,j}}{2\Delta Y}+\frac{1}{\Delta Y^2}\right)\zeta_{n-1,j-1}+\left(\frac{2}{\Delta\tau}-\right.$$

$$\left.\frac{2}{\Delta Y^2}\right)\zeta_{n-1,j}+\left(-\frac{V_{n-1,j}}{2\Delta Y}+\frac{1}{\Delta Y^2}\right)\zeta_{n-1,j+1}-\left(\frac{U_{n-1,j}}{2\Delta X}-\frac{1}{\Delta X^2}\right)\zeta_{n,j} \qquad (20)$$

For the second half time step the following simultaneous equations are solved for rows $i = 2,3, \ldots n-1$ in turn with $j = 2$:

$$\left(\frac{2}{\Delta\tau}+\frac{2}{\Delta Y^2}\right)\zeta'_{i,2}+\left(\frac{V_{i,2}}{2\Delta Y}-\frac{1}{\Delta Y^2}\right)\zeta'_{i,3}\ =\ Gr\ \frac{T'_{i,3}-T'_{i,1}}{2\Delta Y}$$

(continued over)

$$+\left(\frac{U_{i,2}}{2\Delta X}+\frac{1}{\Delta X^2}\right)\zeta^*_{i-1,2}+\left(\frac{2}{\Delta\tau}-\frac{2}{\Delta X^2}\right)\zeta^*_{i,2}+$$

$$\left(-\frac{U_{i,2}}{2\Delta X}+\frac{1}{\Delta X^2}\right)\zeta^*_{i+1,2}-\left(-\frac{V_{i,2}}{2\Delta Y}-\frac{1}{\Delta Y^2}\right)\zeta_{i,1} \qquad (21)$$

$j = 3,4,\ldots\ n-2$:

$$\left(-\frac{V_{i,j}}{2\Delta Y}-\frac{1}{\Delta Y^2}\right)\zeta'_{i,j-1}+\left(\frac{2}{\Delta\tau}+\frac{2}{\Delta Y^2}\right)\zeta'_{i,j}+\left(\frac{V_{i,j}}{2\Delta Y}-\frac{1}{\Delta Y^2}\right)\zeta'_{i,j+1}$$

$$=\ Gr\ \frac{T'_{i,j+1}-T'_{i,j-1}}{2\Delta Y}+\left(\frac{U_{i,j}}{2\Delta X}+\frac{1}{\Delta X^2}\right)\zeta^*_{i-1,j}+$$

$$\left(\frac{2}{\Delta\tau}-\frac{2}{\Delta X^2}\right)\zeta^*_{i,j}+\left(-\frac{U_{i,j}}{2\Delta X}+\frac{1}{\Delta X^2}\right)\zeta^*_{i+1,j} \qquad (22)$$

$j = n-1$:

$$\left(-\frac{V_{i,n-1}}{2\Delta Y}-\frac{1}{\Delta Y^2}\right)\zeta'_{i,n-2}+\left(\frac{2}{\Delta\tau}+\frac{2}{\Delta Y^2}\right)\zeta'_{i,n-1}\ =$$

$$Gr\frac{T'_{i,n}-T'_{i,n-2}}{2\Delta Y}+\left(\frac{U_{i,n-1}}{2\Delta X}+\frac{1}{\Delta X^2}\right)\zeta^*_{i-1,n-1}+\left(\frac{2}{\Delta\tau}-\right.$$

$$\left.\frac{2}{\Delta X^2}\right)\zeta^*_{i,n-1}+\left(-\frac{U_{i,n-1}}{2\Delta X}+\frac{1}{\Delta X^2}\right)\zeta^*_{i+1,n-1}-\left(\frac{V_{i,n-1}}{2\Delta Y}-\frac{1}{\Delta Y^2}\right)\zeta_{i,n}$$

(23)

3. Computation of the new stream function

For the first half time step the following simultaneous equations are solved for columns $j = 2,3,\ldots\ n-1$ in turn with

$i = 2$:

$$\left(\frac{2}{\Delta\tau'} + \frac{2}{\Delta X^2}\right)\psi^*_{2,j} - \frac{1}{\Delta X^2}\psi^*_{3,j} = \zeta_{2,j} + \left(\frac{2}{\Delta\tau'} - \frac{2}{\Delta Y^2}\right)\psi_{2,j}$$

$$+ \frac{1}{\Delta Y^2}\left(\psi_{2,j-1} + \psi_{2,j+1}\right) \qquad (24)$$

$i = 3,4, \ldots m-2$:

$$-\frac{1}{\Delta X^2}\psi^*_{i-1,j} + \left(\frac{2}{\Delta\tau'} + \frac{2}{\Delta X^2}\right)\psi^*_{i,j} - \frac{1}{\Delta X^2}\psi^*_{i+1,j} = \zeta_{i,j} +$$

$$\left(\frac{2}{\Delta\tau'} - \frac{2}{\Delta Y^2}\right)\psi_{i,j} + \frac{1}{\Delta Y^2}\left(\psi_{i,j+1} + \psi_{i,j-1}\right) \qquad (25)$$

$i = m-1$:

$$-\frac{1}{\Delta X^2}\psi^*_{m-2,j} + \left(\frac{2}{\Delta\tau'} + \frac{2}{\Delta X^2}\right)\psi^*_{m-1,j} = \zeta_{m-1,j} +$$

$$\left(\frac{2}{\Delta\tau'} - \frac{2}{\Delta Y^2}\right)\psi_{m-1,j} + \frac{1}{\Delta Y^2}\left(\psi_{m-1,j-1} + \psi_{m-1,j+1}\right) \qquad (26)$$

For the second half time step the following simultaneous equations are solved for rows $i = 2,3, \ldots m-1$ in turn with $j = 2$:

$$\left(\frac{2}{\Delta\tau'} + \frac{2}{\Delta Y^2}\right)\psi'_{i,2} - \frac{1}{\Delta Y^2}\psi'_{i,3} = \zeta_{i,2} + \left(\frac{2}{\Delta\tau'} - \frac{2}{\Delta X^2}\right)\psi^*_{i,2}$$

$$+ \frac{1}{\Delta X^2}\left(\psi^*_{i-1,2} + \psi^*_{i+1,2}\right) \qquad (27)$$

$j = 3,4, \ldots n-2$:

$$-\frac{1}{\Delta Y^2}\psi'_{i,j-1} + \left(\frac{2}{\Delta\tau'} + \frac{2}{\Delta Y^2}\right)\psi'_{i,j} - \frac{1}{\Delta Y^2}\psi'_{i,j+1} = \zeta_{i,j} + \left(\frac{2}{\Delta\tau'} - \frac{2}{\Delta X^2}\right)\psi^*_{i,j} + \frac{1}{\Delta X^2}\left(\psi^*_{i-1,j} + \psi^*_{i+1,j}\right) \quad (28)$$

$j = n-1$:

$$-\frac{1}{\Delta Y^2}\psi'_{i,n-2} + \left(\frac{2}{\Delta\tau'} + \frac{2}{\Delta Y^2}\right)\psi'_{i,n-1} = \zeta_{i,n-1} + \left(\frac{2}{\Delta\tau'} - \frac{2}{\Delta X^2}\right)\psi^*_{i,n-1} + \frac{1}{\Delta X^2}\left(\psi^*_{i-1,n-1} + \psi^*_{i+1,n-1}\right) \quad (29)$$

4. Computation of the velocities

For column $j = 2$, row $i = 2,3, \ldots m-1$:

$$U_{i,2} = \frac{-3\psi_{i,2} + 6\psi_{i,3} - \psi_{i,4}}{6\Delta Y} \quad (30)$$

For column $j = n-1$, row $i = 2,3, \ldots m-1$:

$$U_{i,n-1} = \frac{-3\psi_{i,m-1} + 6\psi_{i,m-2} - \psi_{i,m-3}}{6\Delta Y} \quad (31)$$

For row $i = 2,3, \ldots m-1$, column $j = 3,4, \ldots m-2$:

$$U_{i,j} = \frac{\psi_{i,j-2} - 8\psi_{i,j-1} + 8\psi_{i,j+1} - \psi_{i,j+2}}{12\Delta Y} \quad (32)$$

For row i = 2, column j = 2,3, ... n-1:

$$V_{2,j} = \frac{3\psi_{2,j} - 6\psi_{3,j} + \psi_{4,j}}{6\Delta X} \tag{33}$$

For row i = m-1, column j = 2,3, ... n-1:

$$V_{m-1,j} = \frac{3\psi_{m-1,j} - 6\psi_{m-2,j} + \psi_{m-3,j}}{6\Delta X} \tag{34}$$

For row i = 3,4, ... m-2, column j = 2,3, ... n-1:

$$V_{i,j} = \frac{-\psi_{i-2,j} + 8\psi_{i-1,j} - 8\psi_{i+1,j} + \psi_{i+2,j}}{12\Delta X} \tag{35}$$

5. Computation of the new boundary vorticities

Expanding the stream function into a Taylor series results in:

$$\psi_{2,j} = \psi_{1,j} + \Delta X \frac{\partial \psi_{1,j}}{\partial X} + \frac{\Delta X^2}{2} \frac{\partial^2 \psi_{1,j}}{\partial X^2} \tag{36}$$

From the boundary conditions of:

$$\psi_{i,j} = \frac{\partial \psi_{1,j}}{\partial X} = 0 \quad \text{and} \quad \frac{\partial^2 \psi_{1,j}}{\partial Y^2} = 0$$

equation (36) can be reduced to:

$$\nabla^2 \psi_{1,j} = \frac{\partial^2 \psi_{1,j}}{\partial X^2} = \frac{2\psi_{2,j}}{(\Delta X)^2} = -\zeta_{1,j} \tag{37}$$

Thus the equation used to solve for the wall vorticity are as follows for

i = 1:

$$\zeta_{1,j} = -\frac{2\psi_{2,j}}{\Delta X^2} \qquad (38)$$

j = 1:

$$\zeta_{i,1} = -\frac{2\psi_{i,2}}{\Delta Y^2} \qquad (39)$$

i = m:

$$\zeta_{m,j} = -\frac{2\psi_{m-1,j}}{\Delta X^2} \qquad (40)$$

j = n:

$$\zeta_{i,n} = -\frac{2\psi_{i,n-1}}{\Delta Y^2} \qquad (41)$$

6. Computation of the Nusselt number

$$\left(\frac{\partial T}{\partial Y}\right)_{i,1} = \frac{-11T_{i,1} + 18T_{i,2} - 9T_{i,3} + 2T_{i,4}}{6\Delta Y} \qquad (42)$$

7. The solution of the tridiagonal coefficient matrix of the set of linear equations given by equation (3.49)

$$\begin{aligned} s_{n-1} &= \gamma_{n-1} \\ s_i &= \gamma_i - \frac{c_i\, s_{i+1}}{\beta_i}, \quad i = n-2, n-3, \ldots 1 \end{aligned} \qquad (43)$$

where:

$$\begin{aligned} \beta_1 &= b_1, \qquad \gamma_1 = \frac{d_1}{\beta_1} \\ \beta_i &= b_i - \frac{a_i\, c_{i-1}}{\beta_{i-1}}, \quad i = 2,3, \ldots n-1 \\ \gamma_i &= \frac{d_i - a_i\, \gamma_{i-1}}{\beta_i}, \quad i = 2,3, \ldots n-1 \end{aligned} \qquad (44)$$

Appendix III

Computer Program

1. Flow chart of the computer program

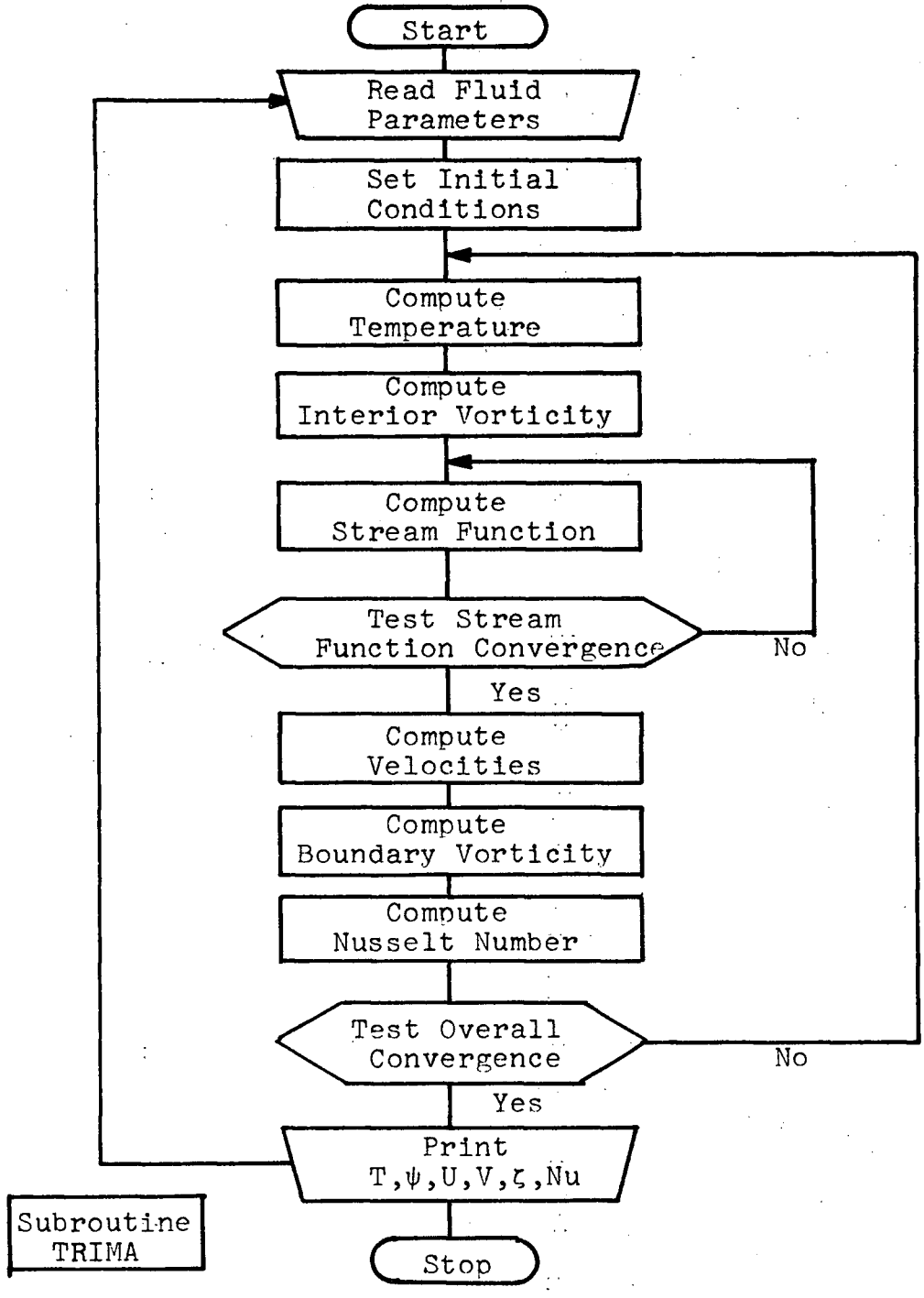

2. Notation used in the computer program

A,B,C,D	Arrays used in the tridiagonal coefficient matrix
AN	Local Nusselt number
AVNU	Average Nusselt number
DT	Time increment, $\Delta\tau$
DT1	Time increment, $\Delta\tau'$
DX, DY	Grid spacing, ΔX, ΔY
GR	Grashof number, Gr'
I,J	Grid positions, i,j
K	Number of iterations the program is to complete
M,N	Maximum value of I and J respectively
PR	Prandtle number, Pr
S	Stream function, ψ
SS	Stream function, ψ^*
SFC	Convergence limit on stream function
T	Temperature, T
TS	Temperature, T*
TD	Temperature, T'
TRIMA	Tridiagonal matrix solution subroutine
U,V	Velocities, u,v
V1	Solution of tridiagonal matrix
Z	Vorticity, ζ
ZS	Vorticity, ζ^*
ZD	Vorticity, ζ'

```
FORTRAN IV G COMPILER        MAIN          08-12-70        12:56:05       PAGE 0001

0001                 DIMENSION T(21,21),TS(21,21),TD(21,21),Z(21,21),ZS(21,21),
                    1 ZD(21,21),S(21,21),SS(21,21),U(21,21),V(21,21),AN(21),B(21),
                    2 A(21),C(21),D(21),V1(21)
0002                 M = 21
0003                 N = 21
0004                 NUM = 500
0005                 DX = 0.05
0006                 DY = 0.05
0007                 DO 50 I = 1,21
0008                 DO 50 J = 1,21
0009                 T(I,J) = 0.0
0010                 S(I,J) = 0.0
0011                 Z(I,J) = 0.0
0012                 U(I,J) = 0.0
0013                 V(I,J) = 0.0
0014                 SS(I,J) = 0.0
0015           50    V1(I) = 0.0
0016                 DO 51 I = 1,21
0017                 T(I,1) = -1.0
0018           51    T(I,N) = 1.0
0019                 DT1 = 0.04
0020                 SEC = 0.02
0021                 S1 = 2.0 / DT1 + 2.0 / ( DX**2 )
0022                 S2 = 2.0 / DT1 - 2.0 / ( DX**2 )
0023                 S3 = 1.0 / ( DX**2 )
0024                 N1 = N - 1
0025                 N2 = N - 2
0026                 M1 = M - 1
0027                 M2 = M - 2
0028                 K5 = 0
0029          170    CONTINUE
0030                 K5 = K5 + 1
0031                 READ (5,200) GR, PR, DT
0032          200    FORMAT ( F20.6 / F20.6 / F20.6 )
0033                 IF ( GR .LT. 10.0 ) GO TO 603
0034                 E1 = 2.0 / DT + 2.0 / ( PR * DX**2 )
0035                 E2 = 2.0 / ( PR*DX**2 )
0036                 E3 = 2.0 / DT
0037                 E4 = E2 / 2.0
0038                 E6 = 2.0 / DT + 2.0 / DX**2
0039                 E7 = 1.0 / ( DX**2 )
0040                 E8 = 1.0 / (2.0*DX )
0041                 E9 = 2.0 / DT - 2.0 / DX**2
0042                 E10 = DX**2
0043                 E11 = 1.0 / ( 6.0*DY )
0044                 E12 = 1.0 / ( 12.0 * DY )
0045                 E13 = 2.0 / DY**2
0046                 E5 = GR / (2.0*DY )
0047                 WRITE (6,700) M,N,NUM,GR,PR,DX,DY,DT
0048          700    FORMAT (1HO,' M = ',I5,' N = ',I5,' NUM = ',I5,' GR = ',1PE12.3,
                    1 ' PR = ',1PE12.3,' DX = ',1PE12.3,' DY = ',1PE12.3,
                    2 ' DT = ',1PE12.3)
0049                 K = 0.0
0050          401    K = K + 1
                     C CALCULATE NEW TEMPERATURES FOR FIRST HALF TIME STEP
```

```
0051              DO 100 J = 2,N1
0052              B(1) = E1
0053              C(1) = -E2
0054              A(M) = -E2
0055              B(M) = E1
0056              D(1) = E3*T(1,J) + E4*(T(1,J-1)-2.0*T(1,J) + T(1,J+1))
0057              D(M) = E3*T(M,J) + E4*(T(M,J-1)-2.0*T(M,J) + T(M,J+1))
0058              DO 101 I = 2,M1
0059              A(I) = -U(I,J)*E8 - E4
0060              B(I) = E1
0061              C(I) = U(I,J)*E8 - E4
0062              D(I) = E3*T(I,J)-V(I,J)*E8*(T(I,J+1)-T(I,J-1))+E4*(T(I,J-1) -
                 12.0*T(I,J) + T(I,J+1))
0063        101   CONTINUE
0064              CALL TRIMA (A,B,C,D,V1,M,1)
0065              DO 102 I = 1,M
0066              TS(I,J) = V1(I)
0067        102   CONTINUE
0068        100   CONTINUE
              C CALCULATE NEW TEMPERATURES FOR SECOND HALF TIME STEP
              C FOR ROW I = 1
0069              B(2) = E1
0070              C(2) = -E4
0071              D(2) = E3*TS(1,2) +E2*(TS(2,2)-TS(1,2)) + E4*T(1,1)
0072              A(N-1) = -E4
0073              B(N-1) = E1
0074              D(N-1) = E3*TS(1,N-1)+E2*(TS(2,N-1)-TS(1,N-1))+E4*T(1,N)
0075              DO 103 J = 3,N2
0076              A(J)   = -E4
0077              B(J)   = E1
0078              C(J)   = -E4
0079              D(J)   = E3*TS(1,J) + E2*(TS(2,J)  -TS(1,J))
0080        103   CONTINUE
0081              CALL TRIMA (A,B,C,D,V1,N-1,2)
0082              DO 104 J = 2,N1
0083              T0(1,J)   = V1(J)
0084        104   CONTINUE
              C FOR ROWS I = 2,..M-1
0085              DO 105 I = 2,M1
0086              B(2) = E1
0087              C(2) = V(I,2)*E8 - E4
0088              D(2) = E3*TS(I,2) + (V(I,2)*E8+E4)*T(I,1)-U(I,2)*E8*(TS(I+1,2)-
                 1 TS(I-1,2))+E4*(TS(I-1,2) - 2.0*TS(I,2)+ TS(I+1,2))
0089              A(N-1) = (-V(I,N-1)*E8-E4)
0090              B(N-1) = E1
0091              D(N-1) = E3*TS(I,N-1)+(-V(I,N-1)*E8+E4)*T(I,N)-U(I,N-1)*E8*(
                 1 TS(I+1,N-1)-TS(I-1,N-1))+E4*(TS(I-1,N-1)-2.0*TS(I,N-1)
                 2 + TS(I+1,N-1))
0092              DO 106 J = 3,N2
0093              B(J) = E1
0094              C(J) = V(I,J)*E8 - E4
0095              A(J)   = -V(I,J)*E8 -E4
0096              D(J)   = E3*TS(I,J)-U(I,J)*E8*  (TS(I+1,J)-TS(I-1,J))+E4*(TS(I-1,
                 1 J) - 2.0*TS(I,J)+TS(I+1,J))
0097        106   CONTINUE
```

```
                      CALL TRIMA (A,B,C,D,V1,N-1,2)
                      DO 107 J = 2,N1
                      TD(I,J)   = V1(J)
              107     CONTINUE
              105     CONTINUE
              C FOR ROW I = M
                      B(2) = E1
                      C(2) = -E4
                      D(2) = E3*TS(M,2)+E2*(TS(M-1,2)-TS(M,2))+E4*T(M,1)
                      A(N-1) = -E4
                      B(N-1) = E1
                      D(N-1) = E3*TS(M,N-1)+E2*(TS(M-1,N-1)-TS(M,N-1))+E4*T(M,N)
                      DO 108 J = 3,N2
                      A(J)   = -E4
                      B(J)   = E1
                      C(J)   = -E4
                      D(J)   = E3*TS(M,J)+E2*(TS(M-1,J) - TS(M,J))
              108     CONTINUE
                      CALL TRIMA (A,B,C,D,V1,N-1,2)
                      DO 109 J = 2,N1
                      TD(M,J)   = V1(J)
              109     CONTINUE
              C CHECK FOR TEMP. CONVERGENCE  (OVERALL CONVERGENCE)
                      AMAX = 0.0
                      DO 300 I = 1,M
                      DO 300 J = 2,N1
                      DIFF = ABS( T(I,J) - TD(I,J))
                      IF (DIFF .LT. AMAX) GO TO 300
                      AMAX = DIFF
              300     CONTINUE
                      IF ( AMAX .LT. 0.0001 ) GO TO 400
                      IF ( K .EQ. 81 .AND. K5 .EQ.  1 ) GO TO 400
                      IF ( K .EQ. 50 .AND. K5 .GT. 1 ) GO TO 400
                      IF ( K .EQ. 100) GO TO 400
              C CALCULATE NEW INTERIOR VORTICITIES
              C FIRST HALF TIME STEP
                      DO 110 J = 2,N1
                      B(2) = E6
                      C(2) = U(2,J)*E8 -E7
                      D(2) = E5*(TD(2,J+1)-TD(2,J-1))+(V(2,J)*E8+E7)*Z(2,J-1)+E9*Z(2,J)
                     1 +(-V(2,J)*E8+E7)*Z(2,J+1)-(-U(2,J)*E8-E7)*Z(1,J)
                      A(M-1) = -U(M-1,J)*E8 - E7
                      B(M-1) = E6
                      D(M-1) = E5*(TD(M-1,J+1)-TD(M-1,J-1))+(V(M-1,J)*E8+E7)*Z(N-1,J-1)
                     1 +E9*Z(M-1,J)+(-V(M-1,J)*E8+E7)*Z(M-1,J+1)-(U(M-1,J)*E8-E7)*Z(M,J)
                      DO 111 I = 3,M2
                      A(I)   = (-U(I,J)*E8 - E7)
                      B(I)   = E6
                      C(I)   = U(I,J)*E8 - E7
                      D(I)   = E5*(TD(I,J+1)-TD(I,J-1))+(V(I,J)*E8+E7)*Z(I,J-1)
                     1 +E9*Z(I,J)+(-V(I,J)*E8+E7)*Z(I,J+1)
              111     CONTINUE
                      CALL TRIMA (A,B,C,D,V1,M-1,2)
                      DO 112 I = 2,M1
                      ZS(I,J)   = V1(I)
```

```
0146        112   CONTINUE
0147        110   CONTINUE
                  C SECOND HALF TIME STEP
0148              DO 113 I = 2,M1
0149              B(2) = E6
0150              C(2) = V(I,2)*E8 - E7
0151              D(2) = E5*(TD(I,3)-TD(I,1))+ (U(I,2)*E8+E7)*ZS(I-1,2)+E9*ZS(I,2)+
                 1 (-U(I,2)*E8+E7)*ZS(I+1,2)-(-V(I,2)*E8-E7)*Z(I,1)
0152              A(N-1) = -V(I,N-1)*E8 - E7
0153              B(N-1) = E6
0154              D(N-1) = E5*(TD(I,N)-TD(I,N-2))+(U(I,N-1)*E8+E7)*ZS(I-1,N-1)+E9*
                 1 ZS(I,N-1)+(-U(I,N-1)*E8+E7)*ZS(I+1,N-1)-(V(I,N-1)*E8-E7)*Z(I,N)
0155              DO 114 J = 3,N2
0156              A(J)   = -V(I,J)*E8 - E7
0157              B(J)   = E6
0158              C(J)   = V(I,J)*E8 - E7
0159              D(J)   = E5*(TD(I,J+1)-TD(I,J-1))+(U(I,J)*E8+E7)*ZS(I-1,J)
                 1 +E9*ZS(I,J)+(-U(I,J)*E8+E7)*ZS(I+1,J)
0160        114   CONTINUE
0161              CALL TRIMA (A,B,C,D,V1,N-1,2)
0162              DO 115  J = 2,N1
0163              ZD(I,J)   = V1(J)
0164        115   CONTINUE
0165        113   CONTINUE
                  C CONVERT NEW T AND VORT TO STANDARD NOTATION
0166              DO 116 I = 1,M
0167              DO 116 J = 2,N1
0168              T(I,J) = TD(I,J)
0169        116   CONTINUE
0170              DO 117 I = 2,M1
0171              DO 117 J = 2,N1
0172              Z(I,J) = ZD(I,J)
0173        117   CONTINUE
                  C COMPUTE NEW STREAM FUNCTION
0174              K1 = 0
                  C FIRST HALF OF TIME STEP FOR STM FCN
0175        120   K1 = K1 + 1
0176              IF ( K1 .GT. NUM ) GO TO 403
0177        305   DO 302 J = 2,N1
0178              B(2) = S1
0179              C(2) = -S3
0180              A(M-1) = -S3
0181              B(M-1) = S1
0182              D(2) = S2*S(2,J) + S3*(S(2,J-1) + S(2,J+1)) + Z(2,J)
0183              D(M-1) = Z(M-1,J) + S2*S(M-1,J) + S3*(S(M-1,J-1) + S(M-1,J+1))
0184              DO 303 I = 3,M2
0185              A(I) = -S3
0186              B(I) = S1
0187              C(I) = -S3
0188        303   D(I) = Z(I,J) + S2*S(I,J) + S3*(S(I,J+1) + S(I,J-1))
0189              CALL TRIMA (A,B,C,D,V1,M-1,2)
0190              DO 304 I = 2,M1
0191              SS(I,J) = V1(I)
0192        304   CONTINUE
0193        302   CONTINUE
```

```
C SECOND HALF TIME STEP FOR STM FCN
      DO 306 I = 2,M1
      B(2) = S1
      C(2) = -S3
      A(N-1) = -S3
      B(N-1) = S1
      D(2) = Z(I,2) + S2*SS(I,2) + S3*(SS(I-1,2) + SS(I+1,2))
      D(N-1) = Z(I,N-1) + S2*SS(I,N-1) + S3*(SS(I-1,N-1) + SS(I+1,N-1))
      DO 307 J = 3,N2
      A(J) = -S3
      B(J) = S1
      C(J) = -S3
  307 D(J) = Z(I,J) + S2*SS(I,J) + S3*(SS(I-1,J) + SS(I+1,J))
      CALL TRIMA (A,B,C,D,V1,N-1,2)
      DO 308 J = 2,N1
  308 S(I,J) = V1(J)
  306 CONTINUE
C CHECK FOR STRM FCN CONVERGENCE
      Z22 = S3*( 4.0*S(2,2) - S(3,2) - S(2,3))
      CHECK = ABS( (Z22 - Z(2,2)) / Z(2,2) )
      IF ( K .GT. 4 ) GO TO 311
      WRITE (6,312) K1, CHECK
  312 FORMAT (1H , ' K1 = ', I4, '  CHECK = ', 1PE16.6)
  311 CONTINUE
      IF ( CHECK .GT. SEC ) GO TO 120
      CONTINUE
C COMPUTE NEW VELOCITIES
C COMPUTE U
      DO 123 I = 2,M1
      U(I,2) = (-3.0*S(I,2)+6.0*S(I,3)-S(I,4))*E11
      U(I,N-1) =-(-3.0*S(I,N-1)+6.0*S(I,N-2)-S(I,N-3))*E11
      DO 124 J = 3,N2
      U(I,J) = (S(I,J-2)-8.0*(S(I,J-1)-S(I,J+1))-S(I,J+2))*E12
  124 CONTINUE
  123 CONTINUE
C COMPUTE V
      DO 125 J = 2,N1
      V(2,J) = (3.0*S(2,J)-6.0*S(3,J)+S(4,J))*E11
      V(M-1,J) =-(3.0*S(M-1,J)-6.0*S(M-2,J)+S(M-3,J))*E11
      DO 126 I = 3,M2
      V(I,J) = (-S(I-2,J)+8.0*(S(I-1,J)-S(I+1,J))+S(I+2,J))*E12
  126 CONTINUE
  125 CONTINUE
C COMPUTE NEW BOUNDARY VORTICITIES
      DO 127 I = 2,M1
      Z(I,1) = -E13 * S(I,2)
      Z(I,N) = -E13 * S(I,N-1)
  127 CONTINUE
      DO 128 J = 2,N1
      Z(1,J) = -E13 * S(2,J)
      Z(M,J) = -E13 * S(M-1,J)
  128 CONTINUE
      AVNU = 0.0
C COMPUTE NEW NUSSELT NUMBER
      DO 129 I = 1,M
```

```
0242                AN(I) = (-11.0*T(I,1)+18.0*T(I,2)-9.0*T(I,3)+2.0*T(I,4))*E12
0243                IF (I .NE. 1.AND.I .NE. M) GO TO 500
0244                F = AN(I) * DX / 2.0
0245                GO TO 501
0246          500   F = AN(I) * DX
0247          501   AVNU = AVNU + F
0248          129   CONTINUE
0249                WRITE (6,400) K, AVNU,AMAX
0250          400   FORMAT (1H , 'K = ',I4,'  AVG.NU = ',E16.6,'  AMAX = ',E16.6)
0251                GO TO 401
0252          402   WRITE (6,601) K, AMAX
0253          601   FORMAT (1HO,'K = ',I4,'  AMAX = ',E16.6,'  HAS NOT CONVERGED')
0254                GO TO 603
0255          403   WRITE (6,602) K1, CHECK
0256          602   FORMAT (1HO,'K1 = ',I4,' CHECK= ',E16.6,'  STM FCN UNCONVERGED')
0257                GO TO 603
0258          400   WRITE (6,605)
0259          605   FORMAT (1H1, 'TEMPERATURE  MATRIX')
0260                WRITE (6,604) (( T(I,J), J=1,N),I=1,M)
0261                WRITE (6,606)
0262          606   FORMAT (1H1, 'STREAM FUNCTION MATRIX')
0263                WRITE (6,604) (( S(I,J), J=1,N),I=1,M)
0264                WRITE (6,607)
0265          607   FORMAT (1H1, 'U VELOCITY MATRIX')
0266                WRITE (6,604) (( U(I,J), J=1,N),I=1,M)
0267                WRITE (6,608)
0268          608   FORMAT (1H1, 'V VELOCITY MATRIX')
0269                WRITE (6,604) (( V(I,J), J=1,N),I=1,M)
0270                WRITE (6,610)
0271          610   FORMAT (1H1,' VORTICITY MATRIX')
0272                WRITE (6,604) (( Z(I,J), J=1,N),I=1,M)
0273          604   FORMAT ( 1HO,1P11E11.3 / 1P10E11.3 )
0274                WRITE (6,609) ( AN(I),I=1,M)
0275          609   FORMAT (1HO,'LOCAL NUSSELT NUMBER'/ 1P11E11.3 / 1P10E11.3 )
0276                K = 0
0277                GO TO 170
0278          603   CONTINUE
0279                STOP
0280                END
```

TOTAL MEMORY REQUIREMENTS 006ED4 BYTES

```
FORTRAN IV G COMPILER        TRIMA          08-12-70        12:56:58        PAGE 0001

0001                  SUBROUTINE TRIMA (A,B,C,D,V1,L,K)
0002                  DIMENSION B(21),A(21),C(21),D(21),V1(21),BA(21),GA(21)
0003                  K1 = K + 1
0004                  LK = L - K
0005                  LI = L - I
0006                  BA(K) = B(K)
0007                  GA(K) = D(K) / BA(K)
0008                  DO 1 I =K1,L
0009                  BA(I) = B(I) -(A(I)*C(I-1))/ BA(I-1)
0010                  GA(I) = (D(I)-A(I)*GA(I-1)) / BA(I)
0011            1     CONTINUE
0012                  V1(L) = GA(L)
0013                  DO 2  I = 1,LK
0014                  J = L - I
0015                  V1(J) = GA(J) -(C(J)*V1(J+1))/ BA(J)
0016            2     CONTINUE
0017                  RETURN
0018                  END

 TOTAL MEMORY REQUIREMENTS 00C3AE BYTES
```

Errata

Page	Position	Original	Corrected
x	Figure 25	form	from
xii	Line 1	intial	initial
xvi	Table IV	the	to
1	Line 4	thsis	thesis
6	5 lines from bottom	1d	2c
83	2 lines from bottom	ξ	ζ
85	Line 11	ξ	ζ
124	Caption	(b) Pb - (d) Pb -	(b) Sn - (d) Sn -
125	Caption	(f) Pb - (h) Pb -	(f) Sn - (h) Sn -